Journal of Membrane Science 698 (2024) 122635

Contents lists available at ScienceDirect

Journal of Membrane Science

journal homepage: www.elsevier.com/locate/memsci

Fundamental insights into the variety of factors that influence water/alcohol membrane permeation selectivity

Rajamani Krishna *, Jasper M. van Baten

Van 't Hoff Institute for Molecular Sciences, University of Amsterdam, Science Park 904, 1098 XH, Amsterdam, the Netherlands

ARTICLE INFO

Keywords:
Mixture adsorption
Permeation selectivity
Microporous membrane
Selectivity reversal
Hydrogen bonding

ABSTRACT

The primary objective of this article is to develop a fundamental understanding of water/methanol and water/ethanol mixture permeation across microporous membrane constructs. Configurational-Bias Monte Carlo (CBMC) simulations were undertaken for water/methanol and water/ethanol mixture adsorption in all-silica zeolites (CHA, DDR, FAU, LTA) and ZIF-8. Additionally, Molecular Dynamics (MD) simulations were used to determine the intra-crystalline diffusivities in water/alcohol mixtures. The combination of CBMC and MD simulations allow the calculation of membrane permeation selectivities. This study provides insights into the influence of the structural properties of the microporous layer on the permeation selectivity. Another key result that emerges is that the water/alcohol permeation selectivity becomes increasingly in favor of water as the feed mixtures becomes richer in alcohol. The reason for the dependence can be traced to strong hydrogen bonding between water and alcohol molecular pairs resulting in cluster formation and enhanced water ingress; these results provide a rationalization of a number of membrane permeation studies in the literature. A corollary to the reported results is that the use of the Ideal Adsorbed Solution Theory (IAST) is unable to provide a quantitative description of mixture adsorption equilibrium and thermodynamic non-idealities need to be accounted for in modelling membrane permeation of water/alcohol mixtures.

1. Introduction

In the processing industries, distillation is the most common technology for separation of mixtures containing water and alcohols [1–3]. Due to the formation of water/alcohol azeotropes, the production of pure alcohols requires the addition of entrainers, such as cyclohexane, that alter the vapor/liquid equilibrium. The recovery of the entrainer requires an additional distillation processing step, placing additional energy demands because of vapor/liquid phase transformations in condensers, reboilers and solvent recovery sections. The use of membrane permeation devices in hybrid distillation-membrane processing schemes offers energy-efficient alternatives to azeotropic and extractive distillation operations in production of purified alcohols [4–8]. The membranes may be constructed as thin films of zeolites (e.g. CHA [6,9,10], DDR [11,12], LTA [13–16], MFI [17,18], FAU [19]) or zeolitic imidazolate frameworks (ZIFs) [20,21].

The water(1)/alcohol (2) membrane permeation selectivity, S_{perm}, is dictated by a combination of the adsorption selectivity, S_{ads}, and the diffusion selectivity, S_{diff}, defined as follows [22–27]

$$S_{perm} = S_{ads} \times S_{diff}; \quad S_{ads} = \frac{q_1/q_2}{f_1/f_2}; \quad S_{diff} = \frac{D_{1,self}}{D_{2,self}} \tag{1}$$

where q_1 and q_2 are the molar loadings of the water and alcohol in the adsorbed phase in equilibrium with the feed mixture with partial fugacities f_1 and f_2; $D_{1,\text{self}}$ and $D_{2,\text{self}}$ are the intra-crystalline self-diffusivities. Due to the narrow 3.3 Å – 4.1 Å window sizes of ZIF-8, CHA, DDR, and LTA zeolites, the diffusion selectivity, S_{diff}, strongly favors water transport [8,28]. Equation (1) is a fair approximation for membrane pervaporation processes wherein the downstream compartment is subject to vacuum, and component loadings at the downstream face of the membrane may be neglected.

Water-selective dehydration of water/ethanol feed mixtures of near-azeotropic composition (≈5% water) is carried out on a commercial scale using LTA-4A (=NaA) membranes [13].

In published works in which the composition of the water/alcohol mixture in the upstream compartment is varied, the permeation selectivity S_{perm} becomes increasingly in favor of water as the alcohol content in the feed mixture increases [14,16,29,30]. The first objective of this article is to provide the theoretical background and rationalization of

* Corresponding author.
E-mail address: r.krishna@uva.nl (R. Krishna).

https://doi.org/10.1016/j.memsci.2024.122635
Received 23 January 2024; Received in revised form 3 March 2024; Accepted 5 March 2024
Available online 6 March 2024

the influence of feed mixture compostion on S_{perm}. The second objective is to gain insights into the influence of the membrane framework structural properties on the permeation selectivity.

Towards this end, Configurational-Bias Monte Carlo (CBMC) simulations of water(1)/methanol(2), water(1)/ethanol(2), and water(1)/methanol(2)/ethanol(3) mixture adsorption equilibrium were performed for four all-silica zeolites (CHA, DDR, LTA, and FAU), along with ZIF-8.

CHA zeolite (all-silica), consists of cages of volume 316 Å^3, separated by 3.8 Å × 4.2 Å 8-ring windows. DDR consists of cages of 277.8 Å^3 volume, separated by 3.65 Å × 4.37 Å 8-ring windows. LTA (Linde Type A) all-silica zeolite consist of cages of 743 Å^3 volume, separated by 4.11 Å × 4.47 Å 8-ring windows. All-silica FAU (=faujasite) has cages of 786 Å^3 volume, separated by 12-ring windows of 7.3 Å size. ZIF-8 has a cage-window SOD (sodalite) topology with large cavities (≈11.6 Å) interconnected by small six-ring-openings (≈3.3 Å) that are flexible. The pore landscape and structural details are provided in Figs. S1–S10 of the Supplementary Material accompanying this publication. All the four zeolites considered are all-silica versions, i.e. not containing extra-framework cations. In practice, LTA and FAU zeolites are invariably employed in their ion-exchanged forms (LTA-4A, LTA-5A, NaX, NaY); therefore the CBMC results for all silica versions of LTA and FAU zeolites provide selectivity data that only afford the correct qualitative trends.

The CBMC simulation methodology used in this article follows published works [23,31–36]. All host materials are considered to be rigid in the simulations, performed at a temperature $T = 300$ K. The force field implementation follows earlier publications [11,27,37,38]. Water is modeled using the Tip5pEw potential [39]. The alcohols are described with the TraPPE force field [40]. Intramolecular potentials are included to describe the flexibility of alcohols, while the water molecules are kept rigid. The bond lengths are fixed for all molecules. Bond bending potentials are considered for methanol and ethanol, and a torsion potential is used for ethanol [40].

Four different simulation campaigns were performed. Firstly, the bulk fluid phase composition held constant at $y_1 = f_1/(f_1 + f_2) = 0.5$, and the bulk fluid phase fugacity $f_t = f_1 + f_2$ was varied over a wide range from the Henry regime of adsorption to pore saturation conditions, typically reached at $f_t = 1$ MPa. In the second campaign, the bulk fluid phase composition held constant at $y_1 = 0.05$, and the total fugacity f_t was varied. In the third campaign, for equimolar ($f_1 = f_2 = f_3$) water(1)/methanol(2)/ethanol(3) mixtures for which the total bulk fugacity $f_t = f_1 + f_2 + f_3$ is varied. In the fourth campaign for binary water(1)/methanol(2), and water(1)/ethanol(2) mixtures the bulk fluid phase fugacity $f_t = f_1 + f_2$ was held at a constant value of 10 kPa, and the bulk fluid phase mixture composition y_1 was varied in the range $0 < y_1 < 1$.

Additionally, Molecular Dynamics (MD) simulations were performed to determine the self-diffusivities, $D_{i,self}$, of each guest in water/methanol and water/ethanol mixtures of varying compositions in the adsorbed phase mixture.

Further simulation details, including force field parameters, are provided in the Supplementary Material accompanying this publication.

2. Thermodynamics of mixture adsorption

In developing our appreciation of the influence of the composition dependence of the adsorption selectivity, it is helpful to begin with the thermodynamics of mixture adsorption. The Gibbs adsorption equation relates the spreading pressure π to the molar chemical potential, μ_i, and the component molar loading, q_i, in the adsorbed phase as follows [41]

$$Ad\pi = \sum_{i=1}^{n} q_i d\mu_i \tag{2}$$

The quantity A is the surface area per kg of framework, with units of m^2 per kg of the framework of the crystalline material; q_i is the molar loading of component i in the adsorbed phase expressed as moles per kg of framework; μ_i is the molar chemical potential of component i. The spreading pressure π has the same units as surface tension, i.e. N m^{-1}.

At phase equilibrium, equating the component chemical potentials, μ_i, in adsorbed phase and in the bulk gas phase mixture in the upstream membrane compartment, we write

$$d\mu_i = RTd\ln f_i \tag{3}$$

where R is the gas constant (=8.314 J mol^{-1} K^{-1}).

Using the analogy with vapor/liquid equilibrium, Myers and Prausnitz [42] write the following expression relating the partial fugacities in the bulk gas mixture

$$f_i = P_i^0 \gamma_i x_i; \quad i = 1, 2, \ldots n \tag{4}$$

to the mole fractions, x_i, in the adsorbed phase mixture

$$x_i = \frac{q_i}{q_1 + q_2 + \ldots q_n}; \quad i = 1, 2, \ldots n \tag{5}$$

In eq (4), P_i^0 is the pressure for sorption of every component i, which yields the same spreading pressure, π for each of the pure components, as that for the n-component mixture:

$$\frac{\pi A}{RT} = \int_0^{P_1^0} \frac{q_1^0(f)}{f} df = \int_0^{P_2^0} \frac{q_2^0(f)}{f} df = \int_0^{P_3^0} \frac{q_3^0(f)}{f} df \tag{6}$$

In eq (6), $q_i^0(f)$ is the *pure* component adsorption isotherm. Since the surface area A is not directly accessible from experimental data, the surface potential $\pi A/RT \equiv \Phi$, with the units mol kg^{-1}, serves as a convenient and practical proxy for the spreading pressure π [24,43–45].

The surface potential Φ is a measure of the pore occupancy. As derived in detail in Chapter 5 of the Supplementary Material, the fractional pore occupancy, θ, is related to the surface potential by

$$\theta = 1 - \exp\left(-\frac{\Phi}{q_{sat,mix}}\right) \tag{7}$$

where $q_{sat,mix}$ is the saturation capacity for mixture adsorption. Eq (7) implies that Φ may also be interpreted as a proxy for the pore occupancy. For values of Φ larger than about 30, the pores are nearly saturated, i.e. $\theta \approx 1$, in the different host materials that have been investigated.

From eq (6), it is evident that the value of Φ depends on partial fugacities f_i of each of the guests, along with the unary isotherms; the isotherms reflect the specific guest/host interactions. In view of eq (4), we may express the adsorption selectivity for the i-j pair in n-component mixtures as follows

$$S_{ads,ij} = \frac{q_i/q_j}{f_i/f_j} = \frac{x_i/f_i}{x_j/f_j} = \frac{P_j^0 \gamma_j}{P_i^0 \gamma_i} \tag{8}$$

In the Ideal Adsorbed Solution Theory (IAST), we further assume that the activity coefficients of each of the components in the mixture are equal to unity, leading to the following simplification

$$\gamma_i = \gamma_j = 1; \quad S_{ads,ij} = \frac{P_j^0}{P_i^0}; \quad i,j = 1, 2 \ldots n \tag{9}$$

The applicability of eq (9) is contingent on the validity of three different tenets demanded by the IAST: (i) all of the adsorption sites within the microporous material are equally accessible to each of the guest molecules, implying a homogeneous distribution of guest adsorbates within the pore landscape, (ii) there are no preferential locations of any guest species in the pore landscape, and (iii) there is no molecular clustering [35,36,46–48].

In previous works [24,25,45] it has been established that eq (9) holds to a very good approximation selectivity of binary (CO_2/CH_4, CO_2/N_2, CH_4/N_2, CO_2/H_2), and ternary ($CO_2/CH_4/N_2$, $CO_2/CH_4/H_2$,

$CO_2/N_2/H_2$) mixtures in various zeolites, ZIFs, and MOFs.

Applying the restriction specified by eq (6), it follows that $S_{ads,ij}$ is uniquely determined by the surface potential Φ. It is important to note that eq (9) is valid irrespective of the total number of components in the mixture. The presence of component 3 in the ternary mixture influences the adsorption selectivity $S_{ads,12} = P_2^0/P_1^0$ for the 1–2 pair, *only* via the values of the sorption pressures P_i^0 which must satisfy eq (6) to yield the same value of surface potential Φ for each of the individual components in the mixture. A further point that requires to be underscored is that the calculation of the surface potential Φ does *not* mandate that $\gamma_i = 1$.

3. Composition dependence of adsorption selectivity

Fig. 1 presents CBMC simulation data for water/methanol, and water/ethanol selectivities, S_{ads}, for three different campaigns: 50/50 and 5/95 binary water/alcohol mixtures and 1/1/1 ternary water/methanol/ethanol mixture adsorption in CHA, DDR, and ZIF-8 at 300 K. The selectivities are plotted as function of the surface potential Φ.

In all cases, the selectivity is in favor of water at high values of Φ; this is due to entropy effects that manifest at high pore occupancies and favor the smaller guest (water) that has a higher saturation capacity [49,50]. In each case, at any specified value of the surface potential, Φ, the CBMC data shows that the hierarchy of selectivities is (1) binary mixture with $y_1 = 0.05$, (2) ternary mixture with $y_1 = 1/3$, and (3) binary mixture

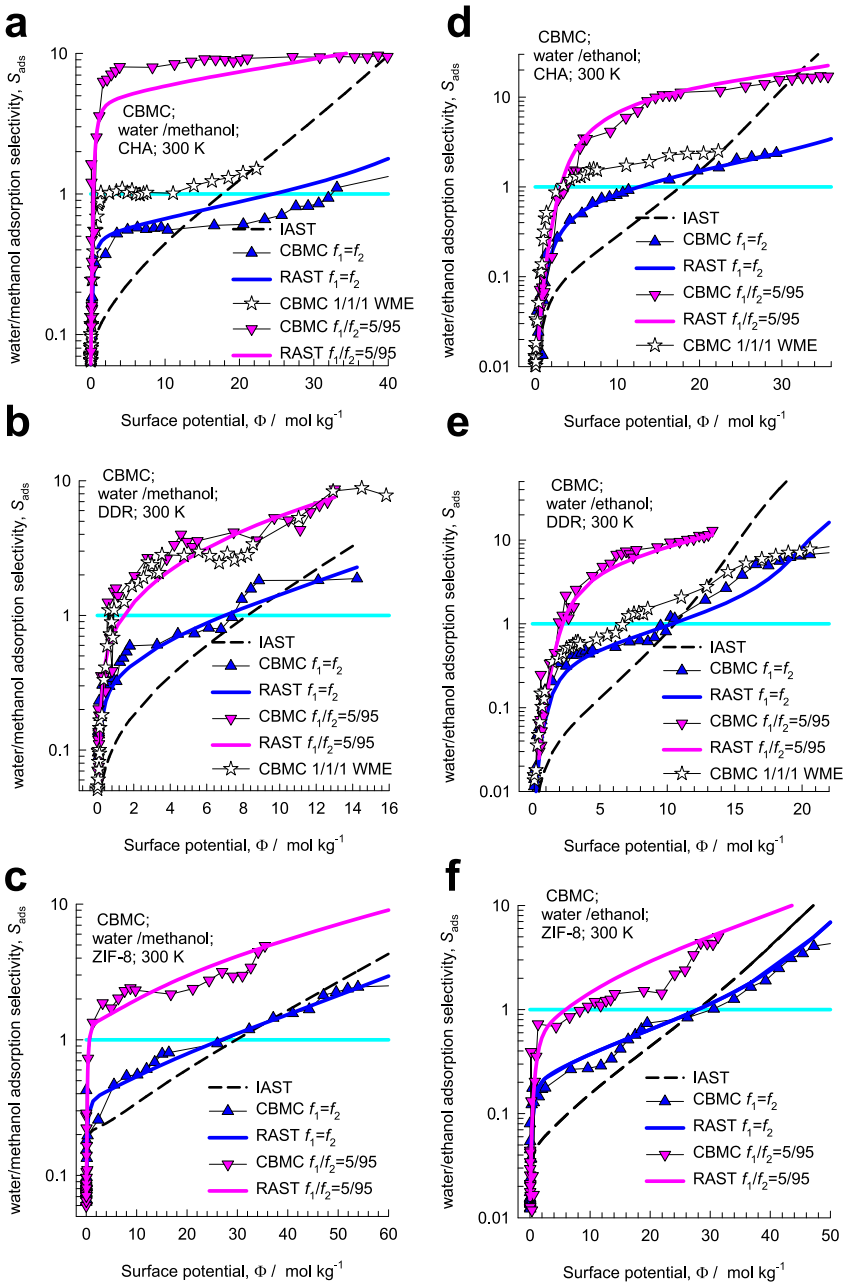

Fig. 1. CBMC simulations of (a, b, c) water(1)/methanol(2), and (d, e, f) water(1)/ethanol(2) selectivities, S_{ads}, for 50/50 and 5/95 binary water/alcohol mixtures and 1/1/1 ternary water(1)/methanol(2)/ethanol(3) mixture adsorption in (a, d) CHA, and (b, e) DDR, and (c, f) ZIF-8 at 300 K. The selectivities are plotted as function of the surface potential Φ. The continuous solid lines are RAST calculations. The dashed lines are the IAST calculations. Further information on the data inputs and calculations are provided in the Supplementary Material accompanying this publication. Plots of the selectivity versus the total fluid phase fugacity is provided in Fig. S44.

with $y_1 = 0.5$. The selectivity becomes increasingly in favor of water as the water composition in the bulk fluid mixture y_1 is lowered. The IAST calculations (indicated by the dashed line) anticipates the selectivity to be independent of bulk fluid phase composition, following eq (9); the IAST predictions fail miserably in all cases.

Results analogous to those presented in Fig. 1 are obtained for FAU (all-silica), LTA (all-silica); see Figs. S58–S61. For CHA and FER zeolites, the experiments of Arletti et al. [51] and Confalonieri et al. [52] provide confirmation that adsorption of water/ethanol mixtures is water-selective at high pore occupancies, i. e high values of Φ. The experiments of Van Assche et al. [53] demonstrate the selective uptake of water from liquid-phase aqueous acetonitriles mixtures using a wide variety of adsorbents such as LTA, FAU, and CHA.

Fig. 2a and b compares water/alcohol adsorption selectivity, S_{ads}, for (a) water/methanol, and (b) water/ethanol mixtures, determined from CBMC simulations in which the total fugacity is maintained constant at the value $f_t = f_1 + f_2 = 10$ kPa in five different host materials. The x-axis is the mole fraction of water(1) in the bulk fluid phase mixture, y_1. We note that for all guest/host combinations, the selectivity is in favor of water at sufficiently low values of y_1. When the bulk composition becomes increasingly rich in water, the selectivity tends to reverse in favor of the alcohol. Such selectivity reversals are not anticipated by the IAST for any guest/host combination; see Figs. S52–S61. The composition at which the selectivity reversal occurs reflects adsorption azeotropy [35, 36,54]. As illustration, Fig. 2c compares the CBMC simulated selectivity for water/methanol mixtures in DDR with the IAST (dashed line). We note that the IAST anticipates the water/methanol selectivity to favor methanol over the entire composition range. For water/ethanol mixture adsorption in CHA zeolite, the IAST anticipates the selectivity to favor water for the entire range of y_1 values; see Fig. 2d.

The failure of the IAST to match the CBMC data presented in Fig. 1, and Fig. 2 is a consequence of hydrogen bonding between guest molecules in water/alcohol mixtures [35,46–48]. One of the mandates of the IAST is violated because of the formation of water/alcohol clusters [35, 36]. In order to demonstrate the occurrence of hydrogen bonding in water/methanol, and water/ethanol mixtures, CBMC simulation data on the spatial locations of the guest molecules were sampled to determine the O····H distances of various pairs of molecular distances. By sampling a total of 10^6 simulation steps, the normalized radial distribution functions (RDF) of O····H distances were determined for water-water, water-alcohol, and alcohol-alcohol pairs. Fig. 3a shows the RDF of O···H distances for molecular pairs of water(1)/methanol(2) mixture adsorption in ZIF-8 at 300 K. We note the first peaks in the RDFs occur at a distance less than 2 Å, that is characteristic of hydrogen bonding [27, 55]. The heights of the first peaks are a direct reflection of the degree of hydrogen bonding between the molecular pairs, resulting in cluster formation and enhanced water ingress [36]. We may conclude, therefore that for water/methanol mixtures the degree of H-bonding between water-methanol pairs is significantly larger, by about an order of magnitude, than for water-water, and methanol-methanol pairs. Analogous set of conclusions can be drawn for water/ethanol mixtures, for which the RDF data are presented in Fig. 3b; the degree of H-bonding between water-ethanol pairs is larger than for water-water, and ethanol-ethanol pairs. Analogous RDF data for water/alcohol mixture

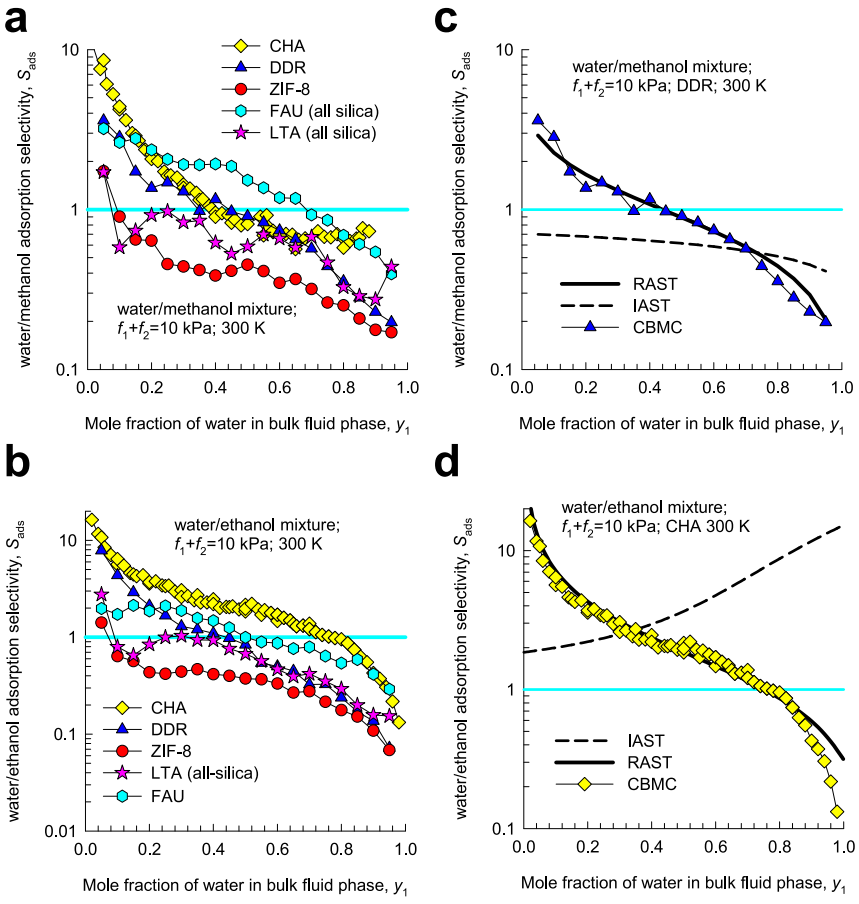

Fig. 2. (a, b) Water/alcohol adsorption selectivity, S_{ads}, for (a) water/methanol, and (b) water/ethanol mixtures in different host materials, determined from CBMC simulations in which $f_t = 10$ kPa. The x-axis is the mole fraction of water(1) in the bulk fluid phase mixture, y_1. (c) Comparison of water/methanol selectivity for DDR determined from CBMC simulations with IAST and RAST calculations. (d) Comparison of water/ethanol selectivity for CHA determined from CBMC simulations with IAST and RAST calculations. Further information on the data inputs and calculations are provided in the Supplementary Material accompanying this publication.

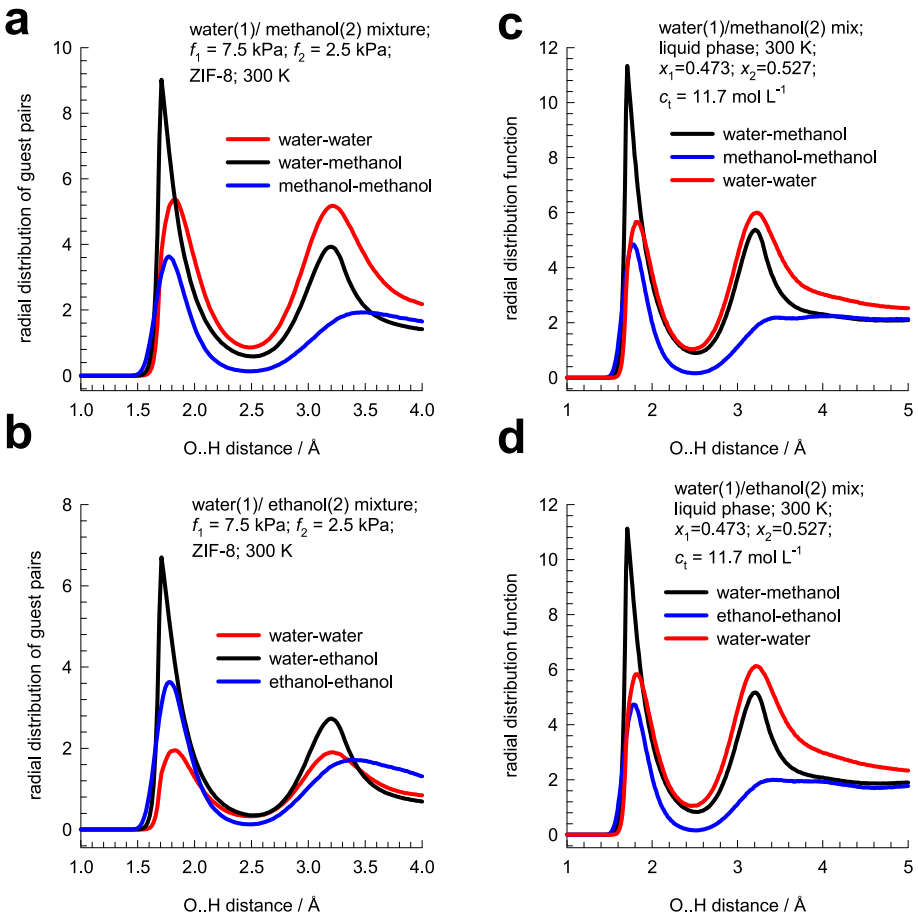

Fig. 3. RDF of O⋯H distances for molecular pairs of (a) water(1)/methanol(2), and (b) water(1)/ethanol(2) mixture adsorption in ZIF-8 zeolite at 300 K. For both sets of mixtures, the partial fugacities of components 1 and 2 are $f_1 = 7.5$ kPa, $f_2 = 2.5$ kPa. The *y*-axes are normalized in the same manner and, therefore, the magnitudes of the first peaks is a direct reflection of the degree of hydrogen bonding between the molecular pairs. (c) RDFs for binary liquid mixture of water and methanol at 300 K at a total molar concentration $c_t = 11.7$ mol L^{-1}. (d) RDFs for binary liquid mixture of water and ethanol at 300 K at total molar $c_t = 11.7$ mol L^{-1}.

adsorption is other hosts DDR, CHA, MFI, and FAU zeolites are presented in Figs. S14–S19.

Fig. 3c and d shows the RDFs for O–H bond distances for binary water/methanol and water/ethanol liquid phase mixtures at a total molar concentration $c_t = 11.7$ mol L^{-1} [27]. As is the case within micropores, the water-alcohol peak values are the highest, and can be traced to much stronger water-alcohol bonding.

4. The RAST for mixture adsorption equilibrium

To quantify non-ideality effects and departures from the IAST, we need to adopt the Real Adsorbed Solution Theory (RAST) that includes an appropriate model to describe the dependence of the activity coefficients γ_i introduced in eq (4). Following previous works we use the Margules model [35,36]

$$\begin{aligned}\ln(\gamma_1) &= x_2^2(A_{12} + 2(A_{21} - A_{12})x_1)(1 - \exp(-C\Phi)) \\ \ln(\gamma_2) &= x_1^2(A_{21} + 2(A_{12} - A_{21})x_2)(1 - \exp(-C\Phi))\end{aligned} \tag{10}$$

In eq (10) C is a constant with the units kg mol^{-1}. In view of eq (7), we note that the factor $(1 - \exp(-C\Phi))$ reflects the fractional pore occupancy; the inclusion of this correction factor imparts the correct limiting behaviors for the activity coefficients in the Henry regime: $\Phi \to 0$; $\theta \to 0$; $\gamma_i \to 1$. As pore saturation conditions are approached, this correction factor tends to unity: $(1 - \exp(-C\Phi)) \to 1$. The parameters A_{12}, A_{21}, C are fitted to match the CBMC data on activity coefficients; the fitting procedure is detailed in the Supplementary Material accompanying this publication. The continuous solid lines in Fig. 1, and Fig. 2 are RAST calculations with the fitted Margules parameters. As should be anticipated, the RAST model quantitatively captures the dependence of the selectivities on both bulk fluid phase mixture compositions and the surface potential Φ; see comparisons in Figs. S52–S61 for all guest/host combinations that are investigated.

We note, in passing, that this correction factor $(1 - \exp(-C\Phi))$ is often ignored in the RAST implementations in some published works [56–59]. In order to highlight the importance of this correction factor, Fig. 4a and b presents CBMC simulations of the activity coefficients for water(1)/ethanol(2) adsorption in CHA zeolite for (a) 50/50 mixtures and, (b) 5/95 mixtures with varying bulk fluid phase fugacity $f_t = f_1 + f_2$. The continuous black colored solid lines are RAST Margules model calculations taking due account of the $(1 - \exp(-C\Phi))$ correction with fitted constants $C = 0.131; A_{12} = -7.717; A_{21} = -4.083$; these calculations are in good agreement with the CBMC simulations for both simulation sets. It is important to note that both the activity coefficients tend to unity at vanishingly small values of the surface potential, i.e. $\gamma_i \to 1$; $\Phi \to 0$. The introduction of $(1 - \exp(-C\Phi))$ imparts the correct limiting behaviors.

The blue colored solid lines are the RAST calculations in which the correction factor $(1 - \exp(-C\Phi))$ is assumed to be unity; it is noteworthy that the activity coefficient of water $\gamma_1 \to 0$; $\Phi \to 0$, in striking nonconformity with the CBMC limiting value of $\gamma_1 \to 1$; $\Phi \to 0$.

Fig. 4c presents the activity coefficients for binary water(1)/ethanol(2) mixtures in which the total bulk fluid phase fugacity $f_t = 10$ kPa and the bulk fluid phase composition y_1 is varied. For these set of conditions, the surface potential lies in the range $16 < \Phi < 26$ mol kg^{-1}, and the

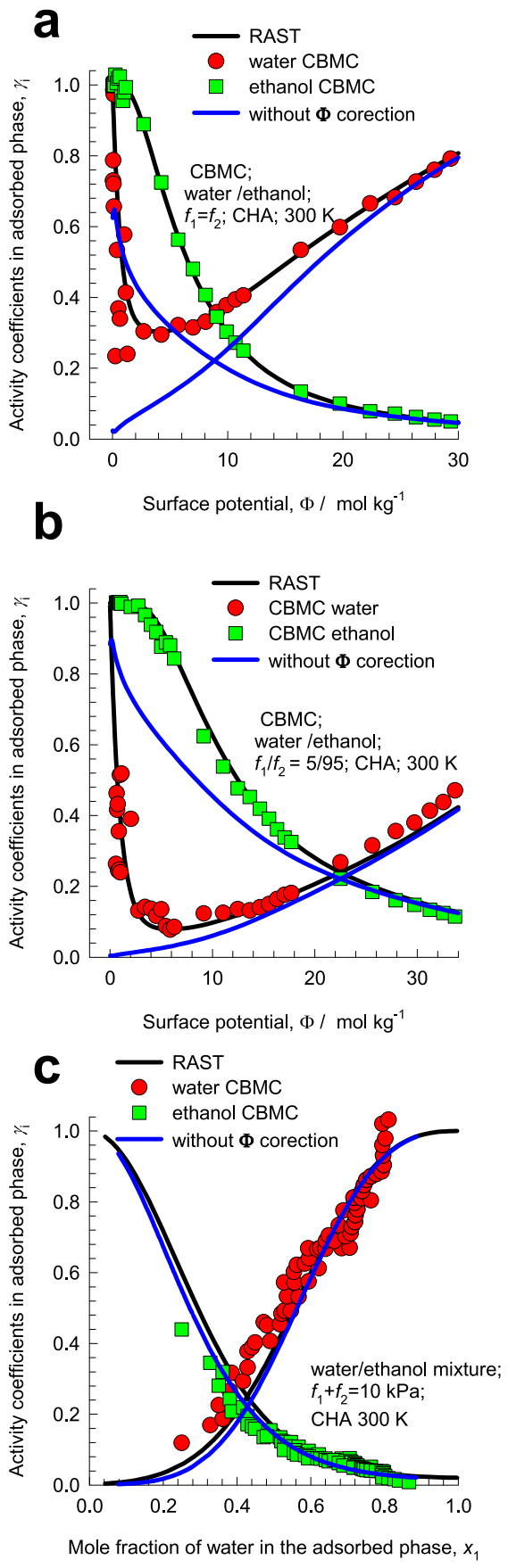

(caption on next column)

Fig. 4. CBMC simulations of water(1)/ethanol(2) adsorption selectivities, S_{ads}, in CHA zeolite for (a) 50/50 mixtures, (b) 5/95 mixtures, (c) binary mixtures in which the total bulk fluid phase fugacity $f_t = 10$ kPa and the bulk fluid phase composition y_1 is varied. The continuous black solid lines are RAST Margules model calculations with fitted constants $C = 0.131; A_{12} = -7.717; A_{21} = -4.083$. The blue lines are the RAST calculations in which the correction factor $(1 - \exp(-C\Phi))$ is assumed to be unity. Further information on the data inputs and calculations are provided in the Supplementary Material accompanying this publication. (For interpretation of the references to color in this figure legend, the reader is referred to the Web version of this article.)

correction factor lies in the range $0.9 < (1 - \exp(-C\Phi)) < 0.965$; the blue colored lines, taking $(1 - \exp(-C\Phi)) = 1$ is of good accuracy.

It must be stressed that in pervaporation of water/alcohol mixtures across microporous membranes, the upstream face of the membrane in contact with the liquid phase bulk feed mixture will correspond to near pore saturation conditions, and $(1 - \exp(-C\Phi)) = 1$ is a reasonably good approximation, as illustrated in Fig. 4c. However, the downstream face of the membrane is in contact with a fluid mixture at low pressures, or vacuum; therefore, $\Phi \to 0$. Along the thickness of the membrane the surface potential will vary in the range $16 < \Phi < 26$ mol kg^{-1} at the upstream face, to $\Phi \approx 0$ at the downstream face, requiring the proper accounting of $(1 - \exp(-C\Phi))$ correction in RAST modelling of mixture adsorption equilibrium.

5. Diffusion and membrane permeation selectivities

Fig. 5a and b presents data for self-diffusivities $D_{i,self}$ in water/ethanol mixtures of varying compositions in the adsorbed phase mixture in CHA and DDR zeolites, maintaining the total loading at a constant value. Fig. 5 show that the diffusivities of each guest decreases with increasing proportion of partner species; this mutual slowing-down effect is accordance with published experimental data [37]. Analogous MD data for other guest/host combinations are presented in Figs. S62–S65.

The MD data in Fig. 5 allows the calculation of the diffusion selectivity S_{diff} as function of the composition. We note that the water/ethanol diffusion selectivity is higher for DDR zeolite (with 3.65 Å × 4.37 Å windows) as compared to CHA zeolite (with 3.8 Å × 4.2 Å windows) because the guest molecules are more strongly constricted in the window regions. The data on S_{diff} may be combined with the CBMC data on S_{ads} in Fig. 2a and b to determine the permeation selectivity S_{perm} using eq (1); the results are provided in Fig. 6 for water/ethanol permeation in CHA and DDR zeolites; the precise calculation procedures are discussed in the Supplementary Material. The permeation selectivity increases in favor of water as the composition of the bulk fluid mixture becomes poorer in water. The important point to note is that this trend is a direct consequence of the variation of S_{ads} with feed mixture composition presented in Fig. 2. These data, representative of all materials investigated (see Figs. S32–S42), provide a rationalization of experimental observations showing S_{perm} increases as y_1 decreases [14,16,29,30]. On the basis of the data presented in Fig. 6 we may conclude that DDR zeolite has a superior permeation selectivity; experimental confirmation of the efficacy of DDR is available in the papers of Kuhn et al. [11,12].

The permeation selectivity increases in favor of water as the composition of the bulk fluid mixture becomes poorer in water. The important point to note is that this trend is a direct consequence of the variation of S_{ads} with feed mixture composition presented in Fig. 2. These data, representative of all materials investigated (see Figs. S32–S42), provide a rationalization of experimental observations showing S_{perm} increases as y_1 decreases [14,16,29,30].

6. Conclusions

The primary thrust of this article has been on providing fundamental

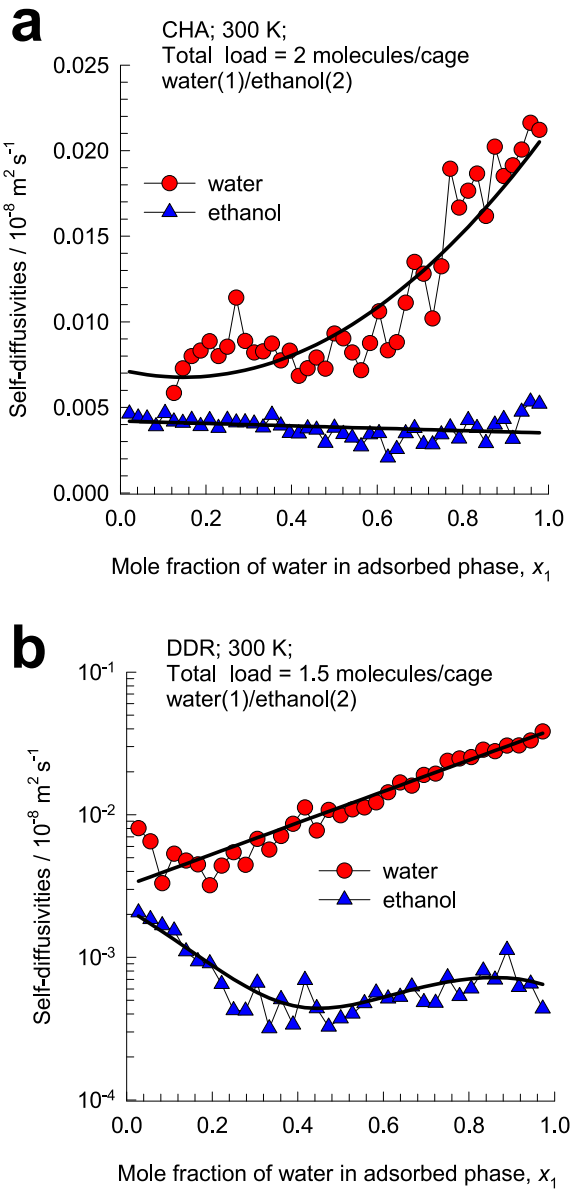

Fig. 5. (a, b) MD simulations of self-diffusivities, $D_{i,self}$, in binary (a) water(1)/methanol(2), and (b) water(1)/ethanol(2) mixtures at a total loading, Θ_t, that is held constant at a value of 1.5 molecules cage^{-1}, plotted as function of the mole fraction of water in the adsorbed phase mixture. Further information on the data inputs and calculations are provided in the Supplementary Material accompanying this publication.

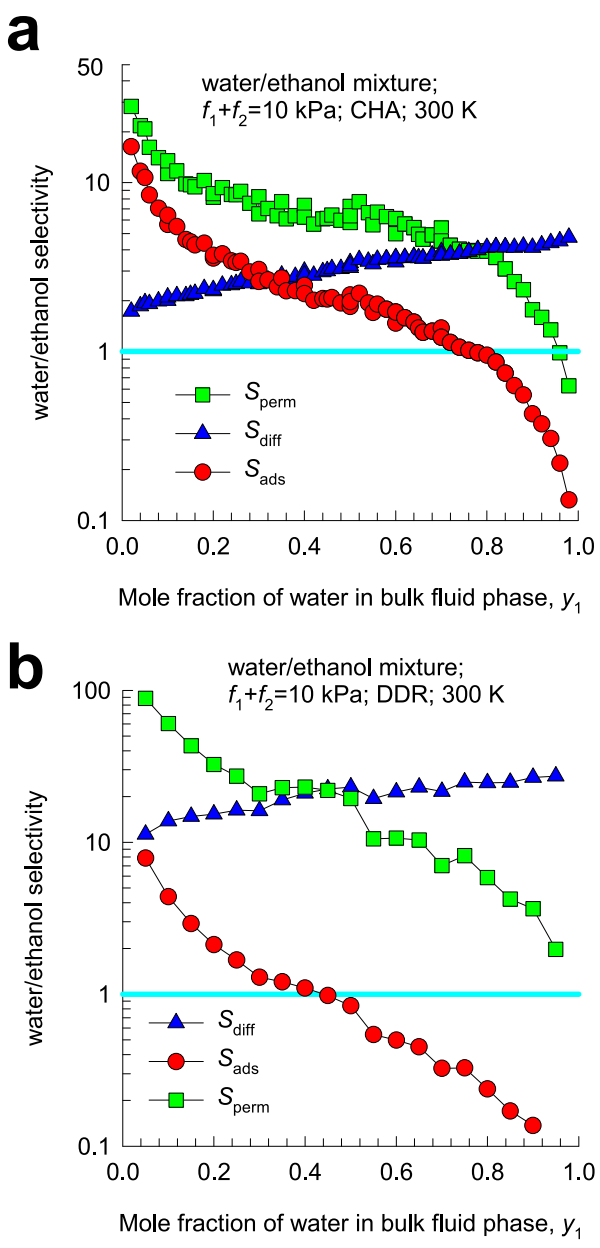

Fig. 6. (a, b) Combined data from CBMC and MD simulations for S_{ads}, S_{diff}, and S_{perm} in binary water(1)/ethanol(2) mixtures at a total pressure of 10 kPa in (a) CHA, and (b) DDR zeolites, plotted as function of the mole fraction of water in the bulk fluid mixture. Further information on the data inputs and calculations are provided in the Supplementary Material accompanying this publication.

thermodynamic insights into the influence of feed mixture composition on water/methanol and water/ethanol permeation across membrane constructs with microporous crystalline layers of CHA, DDR, FAU, LTA and ZIF-8. Four different CBMC campaigns were conducted to demonstrate that the water(1)/alcohol (2) adsorption selectivity S_{ads} is a function of both surface potential, Φ, a proxy for the pore occupancy, and the composition of water in the feed mixture, y_1. The CBMC data show that at sufficiently high values of Φ, the adsorption selectivity favors water. Furthermore, at any specified value of Φ, the selectivity becomes increasingly in favor of water as the water composition in the feed mixture y_1 is lowered. This influence of water content in the feed mixture is a direct consequence of strong hydrogen bonding between water-alcohol molecular pairs resulting in cluster formation and enhanced water ingress, and consequent failure of the IAST to provide a quantitative description of mixture adsorption equilibrium.

MD simulations for water/alcohol mixtures were undertaken to determine the diffusion selectivities S_{diff} as function of the mixture composition. Combination of the CBMC and MD data show that the water/alcohol permeation selectivity, $S_{perm} = S_{ads} \times S_{diff}$, increases with decreasing values of water mole fraction in the feed mixture, primarily due to the dependence of S_{ads} on y_1. The data such as presented in Fig. 6 affords insights into the influence of the structural properties of the microporous membrane material on the adsorption, diffusion, and permeation selectivities. Water-selective permeation is beneficial for alcohol dehydration membrane constructs. Remarkably, this benefit derives from thermodynamic non-idealities resulting from hydrogen bonding. A corollary of this result is that we need to use the RAST, in combination with the Maxwell-Stefan diffusion formulation for modelling of water/alcohol membrane permeation; this aspect is illustrated in

Figs. S66–S72.

Notes

The authors declare no competing financial interest.

CRediT authorship contribution statement

Rajamani Krishna: Writing – review & editing, Writing – original draft, Validation, Resources, Project administration, Methodology, Investigation, Formal analysis, Data curation, Conceptualization. **Jasper M. van Baten:** Writing – review & editing, Visualization, Software, Methodology.

Declaration of competing interest

The authors declare that they have no known competing financial interests or personal relationships that could have appeared to influence the work reported in this paper.

Data availability

All data are included in the Supplementary Material (e-component)

Nomenclature

Latin alphabet

A	surface area per kg of framework, $m^2\ kg^{-1}$
A_{12}, A_{21}	Margules parameters, dimensionless
C	constant used in eq (10), $kg\ mol^{-1}$
$D_{i,self}$	self-diffusivity of species i, $m^2\ s^{-1}$
f_i	partial fugacity of species i, Pa
f_t	total fugacity of bulk gas mixture, Pa
n	number of species in the mixture, dimensionless
P_i^0	sorption pressure, Pa
q_i	component molar loading of species i, $mol\ kg^{-1}$
$q_{sat,mix}$	saturation capacity of mixture, $mol\ kg^{-1}$
R	gas constant, 8.314 $J\ mol^{-1}\ K^{-1}$
S_{ads}	adsorption selectivity, dimensionless
S_{diff}	diffusion selectivity, dimensionless
S_{perm}	permeation selectivity, dimensionless
T	absolute temperature, K
x_1	mole fraction of water in adsorbed phase, dimensionless
y_1	mole fraction of water in bulk fluid mixture, dimensionless

Greek alphabet

γ_i	activity coefficient of component i in adsorbed phase, dimensionless
μ_i	molar chemical potential of component i, $J\ mol^{-1}$
π	spreading pressure, $N\ m^{-1}$
θ	fractional pore occupancy, dimensionless
ρ	crystal framework density, $kg\ m^{-3}$
Φ	surface potential, $mol\ kg^{-1}$

Subscripts

i	referring to component i
t	referring to total mixture
sat	referring to saturation condition

Appendix A. Supplementary data

Supplementary data to this article can be found online at https://doi.org/10.1016/j.memsci.2024.122635.

References

[1] P.A.M. Springer, B. Buttinger, R. Baur, R. Krishna, Crossing of the distillation boundary in homogeneous azeotropic distillation: influence of interphase mass transfer, Ind. Eng. Chem. Res. 41 (2002) 1621–1631, https://doi.org/10.1021/ie010388m.

[2] R. Krishna, Highlighting diffusional coupling effects in ternary liquid extraction and comparisons with distillation, Ind. Eng. Chem. Res. 55 (2016) 1053–1063, https://doi.org/10.1021/acs.iecr.5b04236.

[3] R. Krishna, Diffusing uphill with James Clerk Maxwell and Josef Stefan, Chem. Eng. Sci. 195 (2019) 851–880, https://doi.org/10.1016/j.ces.2018.10.032.

[4] P. Peng, B. Shi, Y. Lan, A review of membrane materials for ethanol recovery by pervaporation, Separ. Sci. Technol. 46 (2011) 234–246.

[5] K. Sato, K. Aoki, K. Sugimoto, K. Izumi, S. Inoue, J. Saito, S. Ikeda, T. Nakane, Dehydrating performance of commercial LTA zeolite membranes and application to fuel grade bio-ethanol production by hybrid distillation/vapor permeation process, Microporous Mesoporous Mater. 115 (2008) 184–188.

[6] K. Sato, K. Sugimoto, N. Shimosuma, T. Kikuchi, T. Kyotani, T. Kurata, Development of practically available up-scaled high-silica CHA-type zeolite membranes for industrial purpose in dehydration of N-methyl pyrrolidone solution, J. Membr. Sci. 409–410 (2012) 82–95.

[7] R. Krishna, Highlighting thermodynamic coupling effects in alcohol/water pervaporation across polymeric membranes, ACS Omega 4 (2019) 15255–15264, https://doi.org/10.1021/acsomega.9b02255.

[8] R. Krishna, J.M. van Baten, Investigating the influence of diffusional coupling on mixture permeation across porous membranes, J. Membr. Sci. 430 (2013) 113–128, https://doi.org/10.1016/j.memsci.2012.12.004.

[9] Y. Hasegawa, C. Abe, A. Ikeda, Pervaporative dehydration of organic solvents using high-silica CHA-type zeolite membrane, Membranes 11 (2021) 229, https://doi.org/10.3390/membranes11030229.
[10] Y. Hasegawa, C. Abe, M. Nishioka, K. Sato, T. Nagase, T. Hanaoka, Formation of high flux CHA-type zeolite membranes and their application to the dehydration of alcohol solutions, J. Membr. Sci. 364 (2010) 318–324.
[11] J. Kuhn, J.M. Castillo-Sanchez, J. Gascon, S. Calero, D. Dubbeldam, T.J.H. Vlugt, F. Kapteijn, J. Gross, Adsorption and diffusion of water, methanol, and ethanol in all-silica DD3R: experiments and simulation, J. Phys. Chem. C 113 (2009) 14290–14301.
[12] J. Kuhn, K. Yajima, T. Tomita, J. Gross, F. Kapteijn, Dehydration performance of a hydrophobic DD3R zeolite membrane, J. Membr. Sci. 321 (2008) 344–349.
[13] Y. Morigami, M. Kondo, J. Abe, H. Kita, K. Okamoto, The first large-scale pervaporation plant using tubular-type module with zeolite NaA membrane, Sep. Purif. Technol. 25 (2001) 251–260.
[14] M. Pera-Titus, C. Fité, V. Sebastián, E. Lorente, J. Llorens, F. Cunill, Modeling pervaporation of ethanol/water mixtures within 'real' zeolite NaA membranes, Ind. Eng. Chem. Res. 47 (2008) 3213–3224.
[15] M. Pera-Titus, J. Llorens, J. Tejero, F. Cunill, Description of the pervaporation dehydration performance of A-type zeolite membranes: a modeling approach based on the Maxwell–Stefan theory, Catal. Today 118 (2006) 73–84.
[16] B. Liu, H. Kita, K. Yogo, Preparation of Si-rich LTA membrane using organic template-free solution for methanol dehydration Sep, Purif. Technol. 239 (2020) 116533, https://doi.org/10.1016/j.seppur.2020.116533.
[17] M. Yu, J.L. Falconer, R.D. Noble, R. Krishna, Modeling transient permeation of polar organic mixtures through a MFI zeolite membrane using the maxwell-stefan equations, J. Membr. Sci. 293 (2007) 167–173.
[18] N. Mittal, P. Bai, J.I. Siepmann, P. Daoutidis, M. Tsapatsis, Bioethanol enrichment using zeolite membranes: molecular modeling, conceptual process design and techno-economic analysis, J. Membr. Sci. 540 (2017) 464–476.
[19] K. Sawamura, T. Furuhata, Y. Sekine, E. Kikuchi, B. Subramanian, M. Matsukata, Zeolite membrane for dehydration of isopropylalcohol-water mixture by vapor permeation, ACS Appl. Mater. Interfaces 7 (2015) 13728–13730, https://doi.org/10.1021/acsami.5b04085.
[20] J. Yao, H. Wang, Zeolitic imidazolate framework composite membranes and thin films: synthesis and applications, Chem. Soc. Rev. 43 (2014) 4470–4493, https://doi.org/10.1039/C3CS60480B.
[21] K. Zhang, R.P. Lively, C. Zhang, W.J. Koros, R.R. Chance, Investigating the intrinsic ethanol/water separation capability of ZIF-8: an adsorption and diffusion study, J. Phys. Chem. C 117 (2013) 7214–7225, https://doi.org/10.1021/jp401548b.
[22] R. Krishna, J.M. van Baten, In silico screening of zeolite membranes for CO_2 capture, J. Membr. Sci. 360 (2010) 323–333, https://doi.org/10.1016/j.memsci.2010.05.032.
[23] R. Krishna, J.M. van Baten, In silico screening of metal-organic frameworks in separation applications, Phys. Chem. Chem. Phys. 13 (2011) 10593–10616, https://doi.org/10.1039/C1CP20282K.
[24] R. Krishna, Thermodynamic insights into the characteristics of unary and mixture permeances in microporous membranes, ACS Omega 4 (2019) 9512–9521, https://doi.org/10.1021/acsomega.9b00907.
[25] R. Krishna, J.M. van Baten, Using the spreading pressure to inter-relate the characteristics of unary, binary and ternary mixture permeation across microporous membranes, J. Membr. Sci. 643 (2022) 120049, https://doi.org/10.1016/j.memsci.2021.120049.
[26] R. Krishna, J.M. Van Baten, Highlighting the anti-synergy between adsorption and diffusion in cation-exchanged faujasite zeolites, ACS Omega 7 (2022) 13050–13056, https://doi.org/10.1021/acsomega.2c00427.
[27] R. Krishna, J.M. van Baten, Hydrogen bonding effects in adsorption of water-alcohol mixtures in zeolites and the consequences for the characteristics of the maxwell-stefan diffusivities, Langmuir 26 (2010) 10854–10867, https://doi.org/10.1021/la100737c.
[28] R. Krishna, The maxwell-stefan description of mixture diffusion in nanoporous crystalline materials, Microporous Mesoporous Mater. 185 (2014) 30–50, https://doi.org/10.1016/j.micromeso.2013.10.026.
[29] J.Y. Wu, Q.L. Liu, Y. Xiong, A.M. Zhu, Y. Chen, Molecular simulation of water/alcohol mixtures adsorption and diffusion in zeolite 4A membranes, J. Phys. Chem. B 113 (2009) 4267–4274.
[30] S. Guo, C. Yua, X. Gua, W. Jin, J. Zhong, C.-J. Chen, Simulation of adsorption, diffusion, and permeability of water and ethanol in NaA zeolite membranes, J. Membr. Sci. 376 (2011) 40–49, https://doi.org/10.1016/j.memsci.2011.03.043.
[31] R. Krishna, J.M. van Baten, A comparison of the CO_2 capture characteristics of zeolites and metal-organic frameworks, Sep. Purif. Technol. 87 (2012) 120–126, https://doi.org/10.1016/j.seppur.2011.11.031.
[32] D. Frenkel, B. Smit, Understanding Molecular Simulations: from Algorithms to Applications, second ed., Academic Press, San Diego, 2002.
[33] B. Smit, R. Krishna, Molecular simulations in zeolitic process design, Chem. Eng. Sci. 58 (2003) 557–568.
[34] T.J.H. Vlugt, R. Krishna, B. Smit, Molecular simulations of adsorption isotherms for linear and branched alkanes and their mixtures in silicalite, J. Phys. Chem. B 103 (1999) 1102–1118, https://doi.org/10.1021/jp982736c.
[35] R. Krishna, J.M. Van Baten, How reliable is the ideal adsorbed solution theory for estimation of mixture separation selectivities in microporous crystalline adsorbents? ACS Omega 6 (2021) 15499–15513, https://doi.org/10.1021/acsomega.1c02136.
[36] R. Krishna, J.M. Van Baten, Water/alcohol mixture adsorption in hydrophobic materials: enhanced water ingress caused by hydrogen bonding, ACS Omega 5 (2020) 28393–28402, https://doi.org/10.1021/acsomega.0c04491.
[37] R. Krishna, J.M. van Baten, Mutual slowing-down effects in mixture diffusion in zeolites, J. Phys. Chem. C 114 (2010) 13154–13156, https://doi.org/10.1021/jp105240c.
[38] R. Krishna, J.M. van Baten, Highlighting pitfalls in the maxwell-stefan modeling of water-alcohol mixture permeation across pervaporation membranes, J. Membr. Sci. 360 (2010) 476–482, https://doi.org/10.1016/j.memsci.2010.05.049.
[39] S.W. Rick, A reoptimization of the five-site water potential (TIP5P) for use with ewald sums, J. Chem. Phys. 120 (2004) 6085–6093.
[40] B. Chen, J.J. Potoff, J.I. Siepmann, Monte Carlo calculations for alcohols and their mixtures with alkanes. Transferable potentials for phase equilibria. 5. United-atom description of primary, secondary, and tertiary alcohols, J. Phys. Chem. B 105 (2001) 3093–3104.
[41] D.M. Ruthven, Principles of Adsorption and Adsorption Processes, John Wiley, New York, 1984.
[42] A.L. Myers, J.M. Prausnitz, Thermodynamics of mixed gas adsorption, A.I.Ch, E.J 11 (1965) 121–130.
[43] O. Talu, A.L. Myers, Rigorous thermodynamic treatment of gas-adsorption, A.I.Ch, E.J 34 (1988) 1887–1893.
[44] F.R. Siperstein, A.L. Myers, Mixed-gas adsorption, A.I.Ch, E.J 47 (2001) 1141–1159.
[45] R. Krishna, J.M. Van Baten, Using molecular simulations to unravel the benefits of characterizing mixture permeation in microporous membranes in terms of the spreading pressure, ACS Omega 5 (2020) 32769–32780, https://doi.org/10.1021/acsomega.0c05269.
[46] R. Krishna, J.M. van Baten, Segregation effects in adsorption of CO_2 containing mixtures and their consequences for separation selectivities in cage-type zeolites, Sep. Purif. Technol. 61 (2008) 414–423, https://doi.org/10.1016/j.seppur.2007.12.003.
[47] R. Krishna, J.M. Van Baten, Investigating the non-idealities in adsorption of CO_2-bearing mixtures in cation-exchanged zeolites, Sep. Purif. Technol. 206 (2018) 208–217, https://doi.org/10.1016/j.seppur.2018.06.009.
[48] R. Krishna, J.M. van Baten, R. Baur, Highlighting the origins and consequences of thermodynamic nonidealities in mixture separations using zeolites and metal-organic frameworks, Microporous Mesoporous Mater. 267 (2018) 274–292, https://doi.org/10.1016/j.micromeso.2018.03.013.
[49] R. Krishna, Elucidation and characterization of entropy effects in mixture separations with micro-porous crystalline adsorbents, Sep. Purif. Technol. 215 (2019) 227–241, https://doi.org/10.1016/j.seppur.2019.01.014.
[50] R. Krishna, Separating mixtures by exploiting molecular packing effects in microporous materials, Phys. Chem. Chem. Phys. 17 (2015) 39–59, https://doi.org/10.1039/C4CP03939D.
[51] R. Arletti, G. Vezzalini, S. Quartieri, F. Di Renzo, V. Dmitriev, Pressure-induced water intrusion in FER-type zeolites and the influence of extraframework species on structural deformations, Microporous Mesoporous Mater. 191 (2014) 27–37.
[52] G. Confalonieri, S. Quartieri, G. Vezzalini, G. Tabacchi, E. Fois, T. Jean Daoue, R. Arletti, Differential penetration of ethanol and water in Si-chabazite: high pressure dehydration of azeotrope solution, Microporous Mesoporous Mater. 284 (2019) 161–169.
[53] T.R.C. Van Assche, T. Remy, G. Desmet, G.V. Baron, J.F.M. Denayer, Adsorptive separation of liquid water/acetonitrile mixtures, Sep. Purif. Technol. 82 (2011) 76–86, https://doi.org/10.1016/j.seppur.2011.08.027.
[54] R. Krishna, J.M. Van Baten, Elucidation of selectivity reversals for binary mixture adsorption in microporous adsorbents, ACS Omega 5 (2020) 9031–9040, https://doi.org/10.1021/acsomega.0c01051.
[55] C. Zhang, X. Yang, Molecular dynamics simulation of ethanol/water mixtures for structure and diffusion properties, Fluid Phase Equil. 231 (2005) 1–10.
[56] S. Sochard, N. Fernandes, J.-M. Reneaume, Modeling of adsorption isotherm of a binary mixture with real adsorbed solution theory and nonrandom two-liquid model, AIChE J. 56 (2010) 3109–3119.
[57] N. Mittal, P. Bai, I. Siepmann, P. Daoutidis, M. Tsapatsis, Bioethanol enrichment using zeolite membranes: molecular modeling, conceptual process design and techno-economic analysis, J. Membr. Sci. 540 (2017) 464–476.
[58] G. Calleja, A. Jimenez, J. Pau, L. Domínguez, P. Pérez, Multicomponent adsorption equilibrium of ethylene, propane, propylene and CO_2 on 13X zeolite, Gas Sep. Purif. 8 (1994) 247–256.
[59] H. Kaur, B.D. Marshall, Real adsorbed solution theory model for the adsorption of CO_2 from humid gas on CALF-20, Chem (2023) 1–18, https://doi.org/10.26434/chemrxiv-2023-2cp2c.

Supplementary Material

Fundamental Insights into the Variety of Factors that Influence Water/Alcohol Membrane Permeation Selectivity

Rajamani Krishna* and Jasper M. van Baten

Van 't Hoff Institute for Molecular Sciences
University of Amsterdam
Science Park 904
1098 XH Amsterdam, The Netherlands
email: r.krishna@uva.nl; r.krishna@contact.uva.nl
ORCID 0000-0002-4784-8530

Contents

1 Structural Details and CBMC Methodology

1.1 Structural details of host materials and pore landscapes

CHA zeolite (all-silica), consists of cages of volume 316 $Å^3$, separated by 3.8 Å × 4.2 Å 8-ring windows; the pore landscape and structural details are provided in Figure S1, and Figure S2.[1-4]

DDR consists of cages of 277.8 $Å^3$ volume, separated by 3.65 Å × 4.37 Å 8-ring windows; the pore landscapes and structural details are provided in Figure S3, and Figure S4. The DDR structure is an orthorhombic reconstruction of the monoclinic geometry in the original paper of Gies[5], using larger unit cell dimensions.

ZIF-8 ($Zn(MeIm)_2$, MeIm = 2-methylimidazole) has a cage-window SOD (sodalite) topology with large cavities (≈ 11.6 Å) interconnected by small six-ring-openings (≈ 3.3 Å) (see pore landscapes in Figure S5, and Figure S6). Though the crystallographic size of the windows of ZIF-8 is 3.3 Å, the windows are flexible.

All-silica FAU (= faujasite) has cages of 786 $Å^3$ volume, separated by 7.3 Å 12-ring windows; see structural information in Figure S7, and Figure S8.

LTA (Linde Type A) all-silica zeolite consist of cages of 743 $Å^3$ volume, separated by 4.11 Å × 4.47 Å 8-ring windows; the pore landscapes and structural details are provided in Figure S9, and Figure S10.

CuBTC (= $Cu_3(BTC)_2$ with BTC = 1,3,5-benzenetricarboxylate, also known as HKUST-1) framework is composed of copper atoms connected by benzene-1,3,5-tricarboxylate (BTC) linkers, which form a characteristic paddle-wheel structure: two copper atoms bonded to the oxygen atoms of four BTC linkers, generating four-connected square-planar vertexes; see Figure S11, and Figure S12.

The structural information for CuBTC simulations have been taken from Chui et al.[6] and Yang and Zhong.[7] The crystal structure of Chui et al. [6] includes axial oxygen atoms weakly bonded to the Cu atoms,

which correspond to water ligands; our simulations have been performed on the dry CuBTC with these oxygen atoms removed.

The framework contains two types of large cavities (9 Å diameter) and small cavities (of 5 Å diameter). The larger cavities (L_2 and L_3) are similar in size and shape but as a result of the paddle-wheel, the copper atoms are only accessible from the L_3 cages. L_2 and L_3 cavities are connected through triangular-shaped windows. The small cavities (T_1) are tetrahedral pockets enclosed by the benzene rings; these are connected to L_3 cages by small triangular windows (3.5 Å in size), as shown in Figure S13.

The CuBTC framework is composed of copper atoms connected by benzene-1,3,5-tricarboxylate (BTC) linkers, which form a characteristic paddle-wheel structure: two copper atoms bonded to the oxygen atoms of four BTC linkers, generating four-connected square-planar vertexes. The framework contains two types of large cavities (9 Å diameter) and small cavities (of 5 Å diameter). The larger cavities (L_2 and L_3) are similar in size and shape but as a result of the paddle-wheel, the copper atoms are only accessible from the L_3 cages. L_2 and L_3 cavities are connected by windows. The small cavities (T_1) are tetrahedral pockets enclosed by the benzene rings. They are connected to L_3 cages by small triangular windows as shown in Figure S11, Figure S12, and Figure S13. The tetrahedral pockets can accommodate about 9 molecules of water, but only about 1 molecule of 1-propanol.

Watch also the presentations titled **Guest Mobility in CuBTC, Diffusion in LTA-4A and 5A Zeolites, Diffusion in Cage-Type Zeolites, Inter-cage Hopping in DDR Zeolite, Inter-cage Hopping in CHA Zeolite, ZIF-8 Membranes, Visualizing Motion of Guest Molecules in ZIF-8, Diffusion in LTA Zeolite, Diffusion in CHA Zeolite, Diffusion in DDR Zeolite, Diffusion in ZIF-8**

on YouTube https://www.youtube.com/@rajamanikrishna250/videos

1.2 Force fields and CBMC simulation methodology

For simulations of adsorption of guest molecules water, methanol, and ethanol, the force field implementation follows earlier publications.[8-11] Water is modeled using the Tip5pEw potential.[12] The alcohols are described with the TraPPE force field.[13] Intramolecular potentials are included to describe

the flexibility of alcohols, while the water molecules are kept rigid. The bond lengths are fixed for all molecules. Bond bending potentials are considered for methanol and ethanol, and a torsion potential is used for ethanol.[13] The force field parameters are summarized in Table S1.

Following Kiselev and co-workers,[14] the zeolite is modeled as a rigid crystal. The interactions of the guest (pseudo) atoms with the host zeolite atoms aredominated by the dispersive interactions with the oxygen atoms, these interactions are described with a Lennard-Jones potential; see Table S2.

ZIF-8 is also modelled as a rigid structure. The Lennard-Jones potentials for the framework atoms of ZIF-8 were taken from the combined works of Mayo et al.[15], Yang and Zhong [16], and Jorgensen et al.[17] as was reported in the computational study of Zhou et al.[18] The framework charges of ZIF-8 were estimated using the group-contribution procedure based on quantum mechanical calculations described in the recent paper by Xu and Zhong.[19] Table S3 provides a summary of the force fields for ZIF-8 framework atoms.

The Lorentz-Berthelot mixing rules were applied for calculating the Lennard-Jones parameters describing guest-host interactions

$$\sigma_{guest-host} = \frac{\left(\sigma_{guest} + \sigma_{host}\right)}{2}$$
$$\frac{\varepsilon_{guest-host}}{k_B} = \sqrt{\frac{\varepsilon_{guest}}{k_B} \times \frac{\varepsilon_{host}}{k_B}} \qquad \text{(S1)}$$

The Lennard-Jones potentials are shifted and cut at 12 Å. Periodic boundary conditions were employed. The Configurational-Bias Monte Carlo (CBMC) simulation technique used is identical to that used by Kuhn et al.,[11] and is described in detail by Frenkel and Smit.[20] The CBMC simulations were performed using the BIGMAC code developed by T.J.H. Vlugt, University of Amsterdam, as basis.

Also included in the simulations are re-analyses of CBMC data for polar guests in CuBTC as provided in our earlier works, wherein the force fields are specified.[21, 22]

1.3 List of Tables for Structural Details and CBMC Methodology

Table S1. Lennard-Jones parameters for guest pseudo-atoms. as provided in Table 1 of Kuhn et al.[11] The water model has two off-center charges that are labeled M in the Table. The name "alcohol" refers to both methanol and ethanol molecules.

Molecule	(pseudo-) atom	σ / Å	ε/k_B / K	charge
water	O	3.097	89.516	0
water	H	0	0	0.241
water	M	0	0	-0.241
methanol	CH3	3.75	98	0.265
ethanol	CH3	3.75	98	0
ethanol	CH2	3.95	46	0.265
alcohol	O	3.02	93	-0.7
alcohol	H	0	0	0.435

Table S2. Lennard-Jones parameters for host atoms in all-silica zeolites.

(pseudo-) atom	σ / Å	ε/k_B / K	charge
Si			2.05
O	3	93.53	-1.025

Table S3. The Lennard-Jones potentials for the host framework atoms of ZIF-8 were taken from the combined works of Mayo et al.[15] Yang and Zhong,[16] and Jorgensen et al.[17] as was reported in the computational study of Zhou et al.[18] The framework charges of ZIF-8 were estimated using the group-contribution procedure based on quantum mechanical calculations described by Xu and Zhong.[19]

(pseudo-) atom	σ / Å	ε/k_B / K	charge
Zn	4.54	27.59	0.749
N	3.25	85.29	-0.387
Ca	2.25	25.08	0.698
Cb	3.55	35.12	-0.0093
Cc	3.5	20.03	0.0117
Ha	2.5	15.05	-0.139
Hb	3.19	7.53	0.0627

See Cartoon below for further explanation:

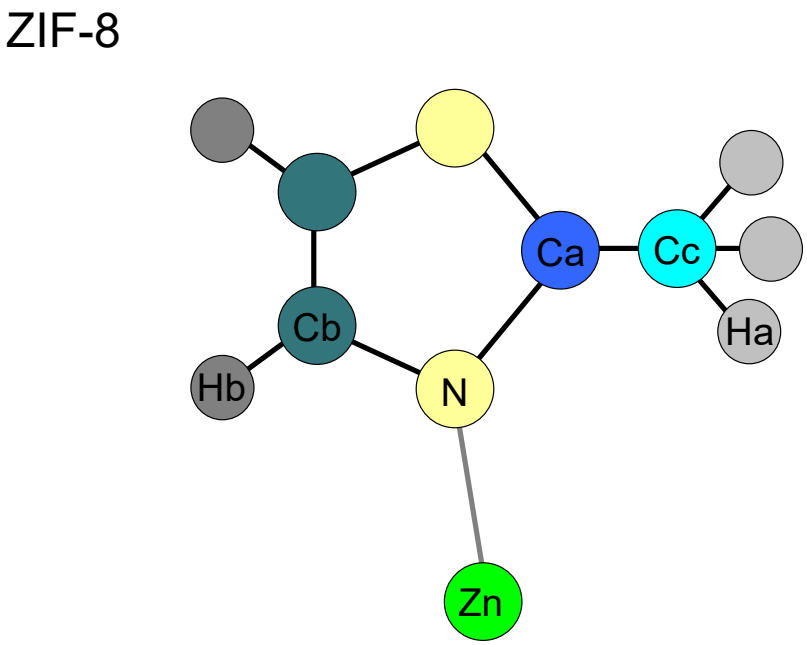

1.4 List of Figures for Structural Details and CBMC Methodology

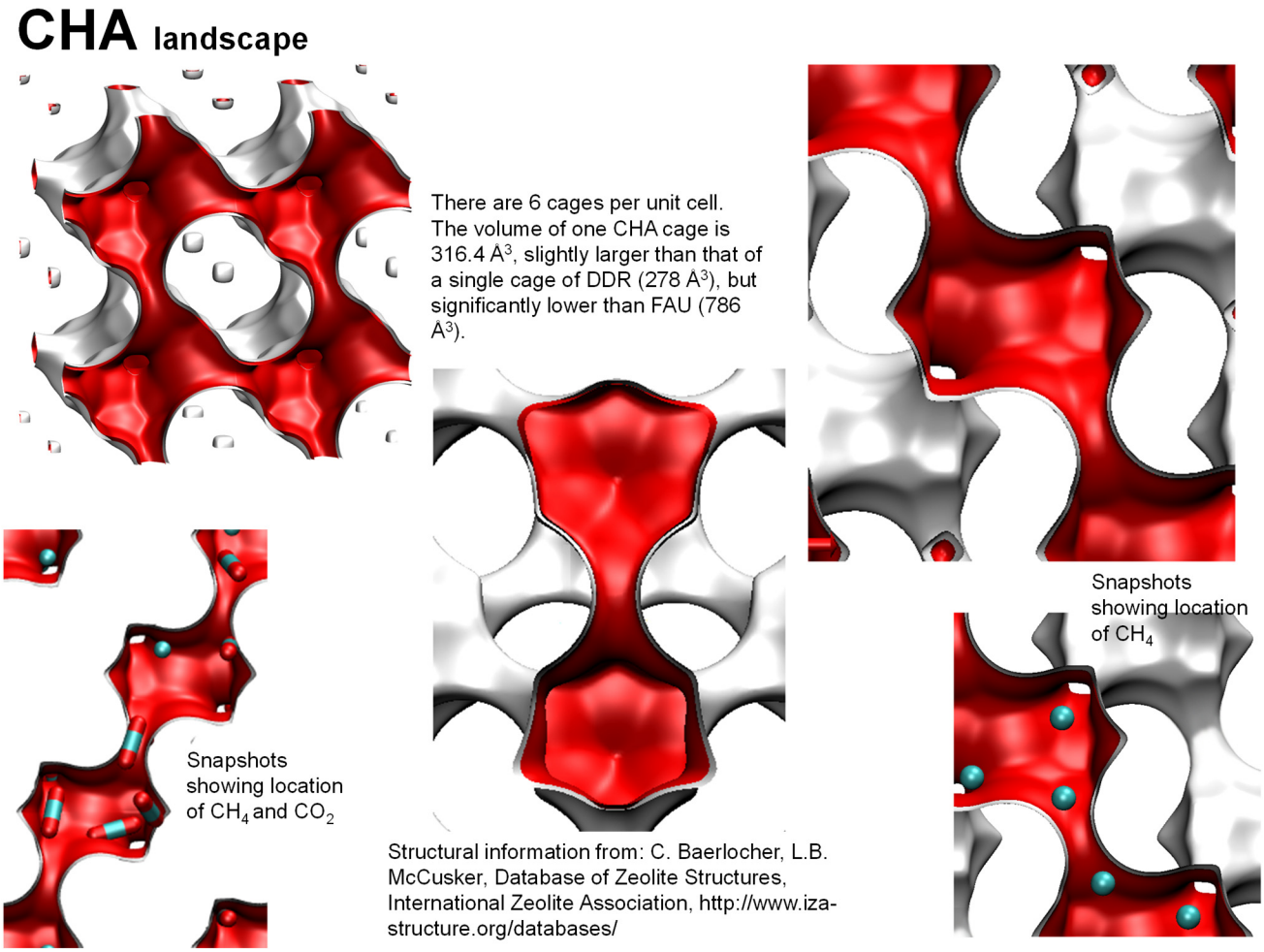

Figure S1. Pore landscape and structural details of all-silica CHA zeolite, also called SiCHA.

CHA window and pore dimensions

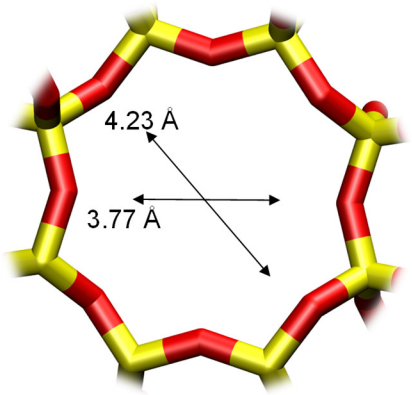

CHA

The window dimensions calculated using the van der Waals diameter of framework atoms = 2.7 Å are indicated above by the arrows.

	CHA
a /Å	15.075
b /Å	23.907
c /Å	13.803
Cell volume / Å^3	4974.574
conversion factor for [molec/uc] to [mol per kg Framework]	0.2312
conversion factor for [molec/uc] to [kmol/m^3]	0.8747
ρ [kg/m3]	1444.1
MW unit cell [g/mol(framework)]	4326.106
ϕ, fractional pore volume	0.382
open space / Å^3/uc	1898.4
Pore volume / cm^3/g	0.264
Surface area /m^2/g	758.0
DeLaunay diameter /Å	3.77

Figure S2. Pore landscape and structural details of all-silica CHA zeolite, also called SiCHA.

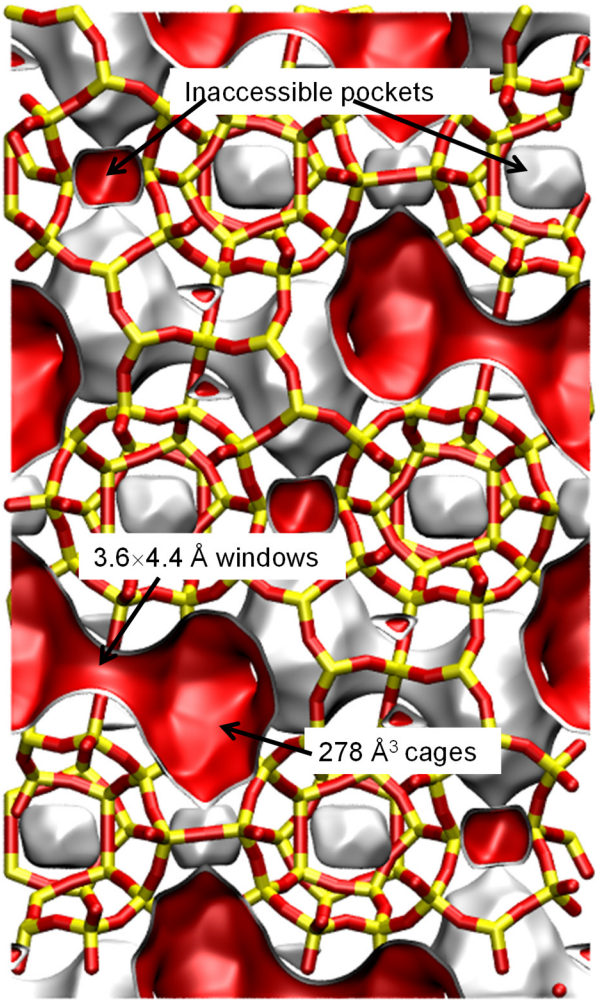

DDR landscape

To convert from molecules per unit cell to mol kg^{-1}, multiply by 0.06936.
The pore volume is 0.182 cm^3/g.

There are 12 cages per unit cell. The volume of one DDR cage is 278 Å^3, significantly smaller than that of a single cage of FAU (786 Å^3), or ZIF-8 (1168 Å^3).

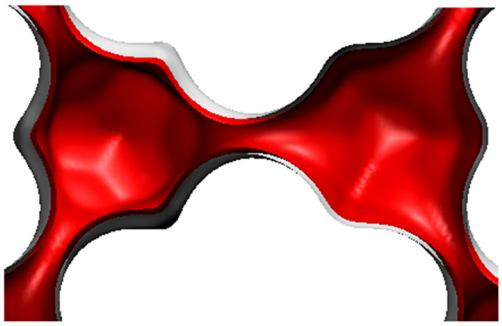

Structural information from: C. Baerlocher, L.B. McCusker, Database of Zeolite Structures, International Zeolite Association, http://www.iza-structure.org/databases/

Figure S3. Pore landscape of all-silica DDR zeolite.

DDR window and pore dimensions

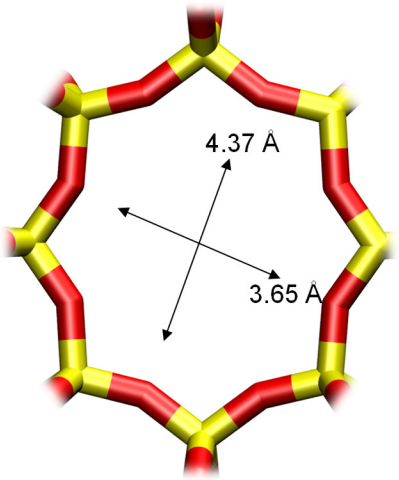

DDR

The window dimensions calculated using the van der Waals diameter of framework atoms = 2.7 Å are indicated above by the arrows.

	DDR
a /Å	24.006
b /Å	13.86
c /Å	40.892
Cell volume / Å^3	13605.72
conversion factor for [molec/uc] to [mol per kg Framework]	0.0693
conversion factor for [molec/uc] to [kmol/m^3]	0.4981
ρ [kg/m3]	1759.991
MW unit cell [g/mol(framework)]	14420.35
ϕ, fractional pore volume	0.245
open space / Å^3/uc	3333.5
Pore volume / cm^3/g	0.139
Surface area /m^2/g	350.0
DeLaunay diameter /Å	3.65

Figure S4. Structural details for DDR zeolite.

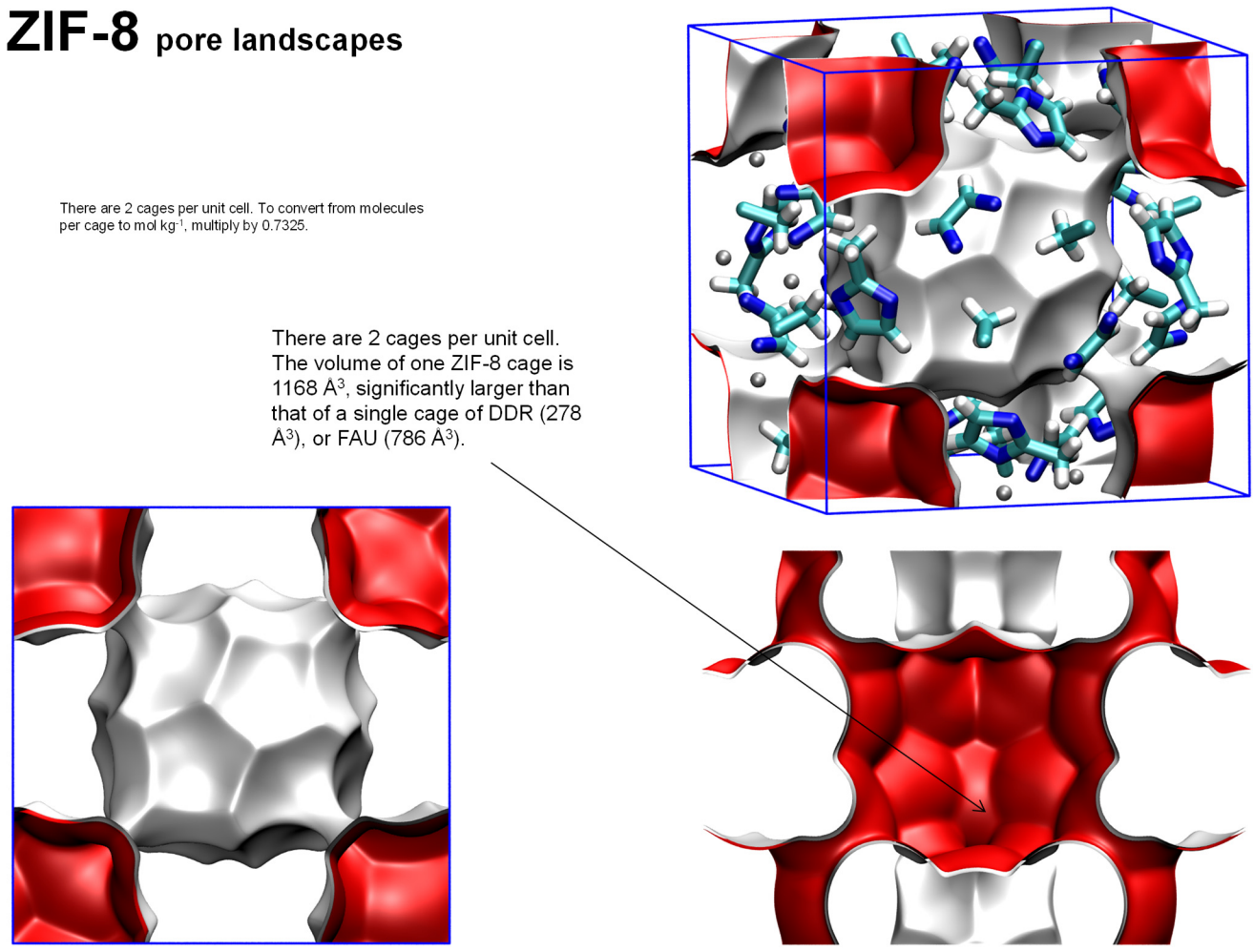

Figure S5. Pore landscape and structural details of ZIF-8.

ZIF-8 dimensions

	ZIF-8
a /Å	16.991
b /Å	16.991
c /Å	16.991
Cell volume / Å^3	4905.201
conversion factor for [molec/uc] to [mol per kg Framework]	0.3663
conversion factor for [molec/uc] to [kmol/m^3]	0.7106
ρ [kg/m3]	924.253
MW unit cell [g/mol(framework)]	2730.182
ϕ, fractional pore volume	0.476
open space / Å^3/uc	2337.0
Pore volume / cm^3/g	0.515
Surface area /m^2/g	1164.7
DeLaunay diameter /Å	3.26

Figure S6. Pore landscape and structural details of ZIF-8.

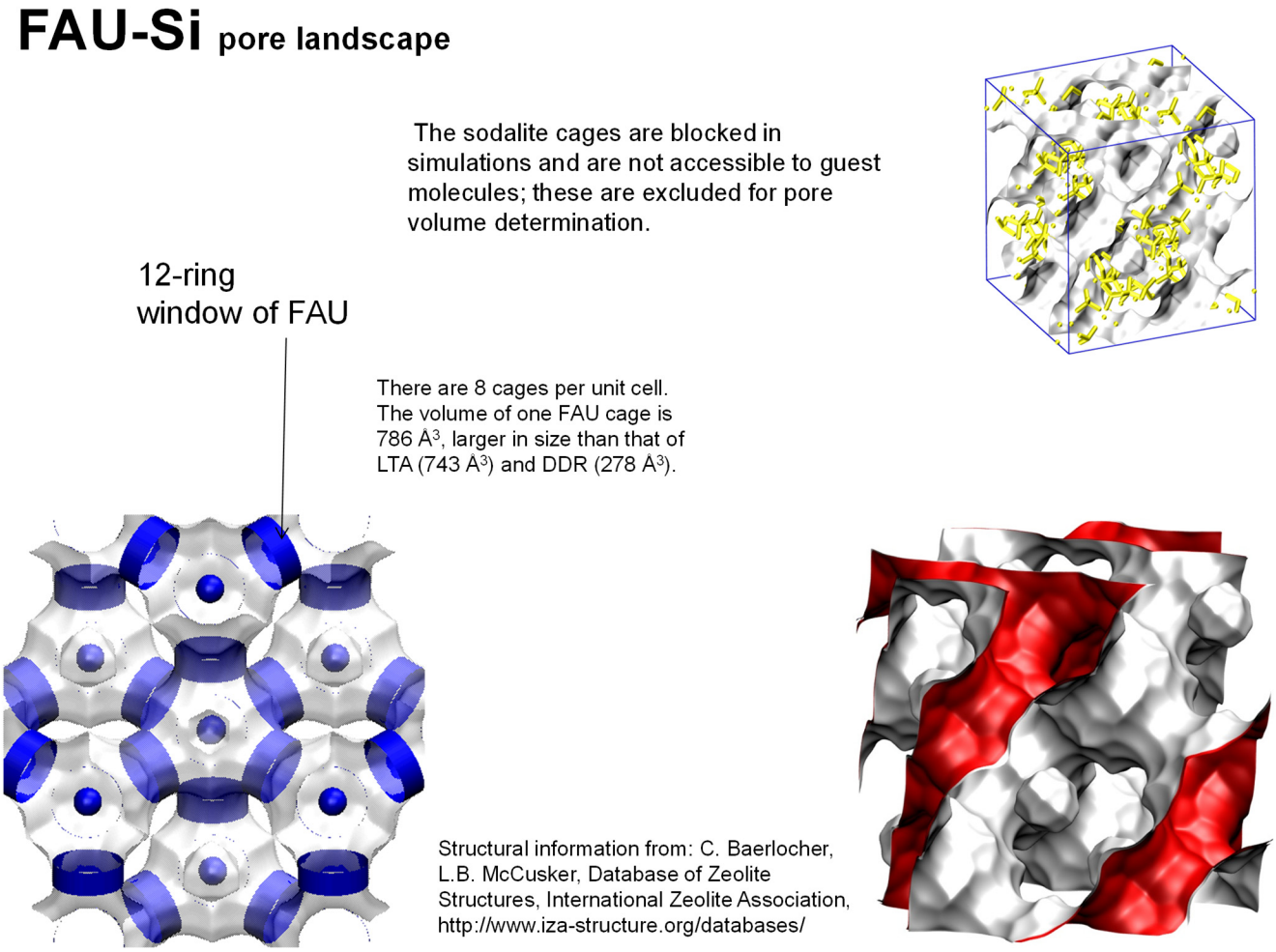

Figure S7. Pore landscape of all-silica FAU zeolite.

FAU-Si window and pore dimensions

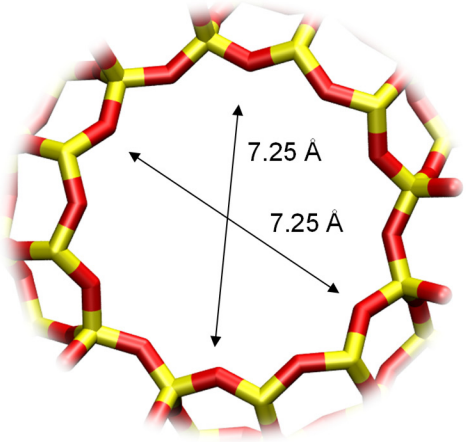

	FAU-Si
a /Å	24.28
b /Å	24.28
c /Å	24.28
Cell volume / Å^3	14313.51
conversion factor for [molec/uc] to [mol per kg Framework]	0.0867
conversion factor for [molec/uc] to [kmol/m^3]	0.2642
ρ [kg/m3]	1338.369
MW unit cell [g/mol (framework)]	11536.28
ϕ, fractional pore volume	0.439
open space / Å^3/uc	6285.6
Pore volume / cm^3/g	0.328
Surface area /m^2/g	1086.0
DeLaunay diameter /Å	7.37

Figure S8. Structural details for FAU zeolite.

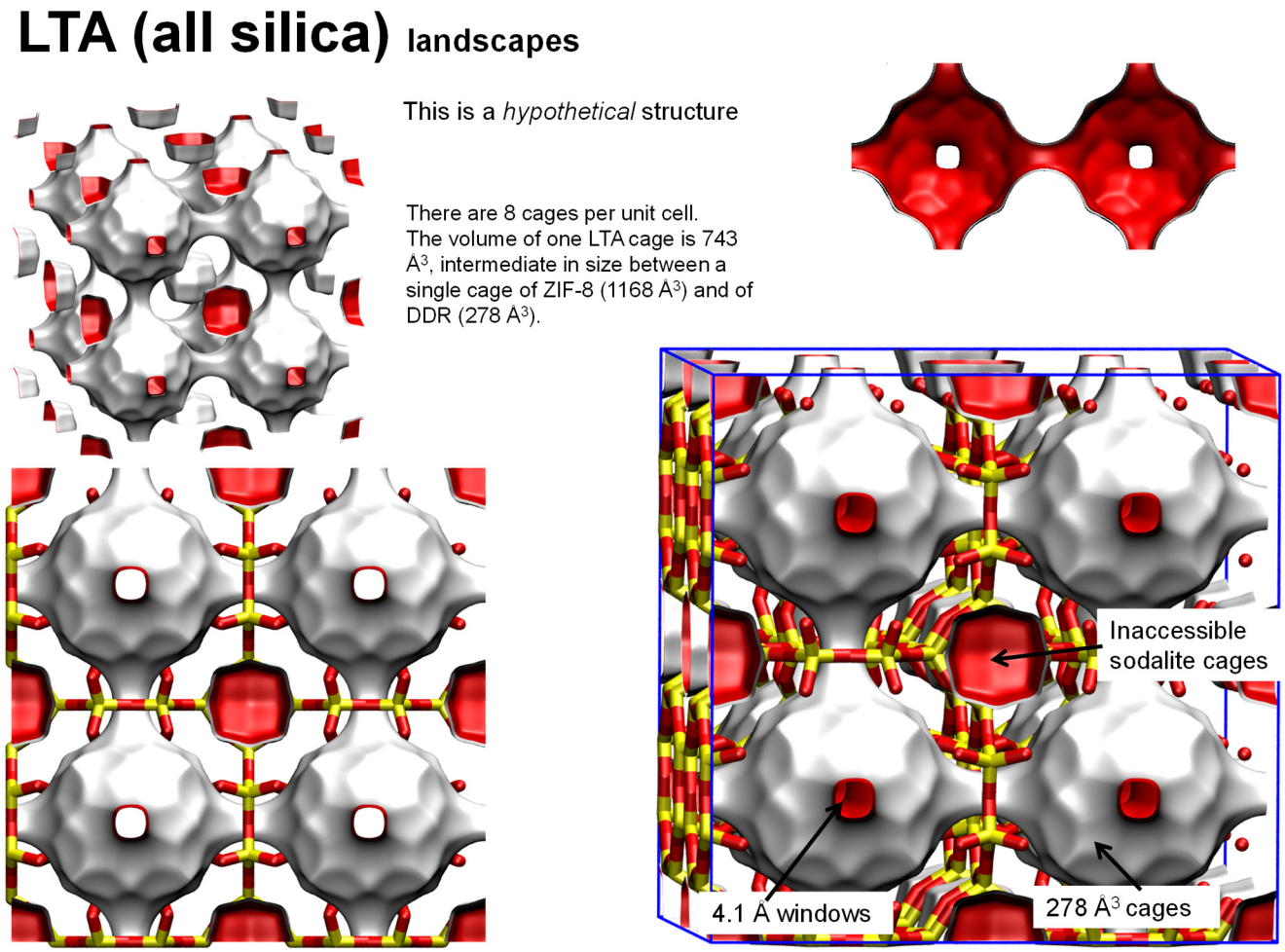

Figure S9. Pore landscape of all-silica LTA zeolite.

LTA (all-silica) window and pore dimensions

8-ring window of LTA

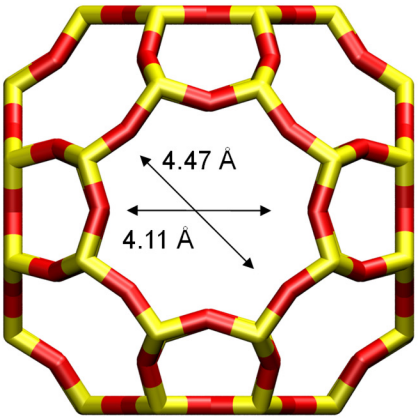

The window dimension calculated using the van der Waals diameter of framework atoms = 2.7 Å is indicated above by the arrows.

This plot of surface area versus pore dimension is determined using a combination of the DeLaunay triangulation method for pore dimension determination, and the procedure of Düren for determination of the surface area.

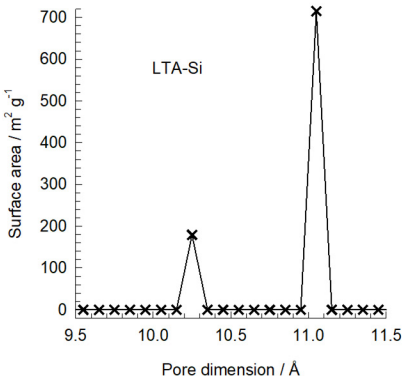

	LTA-Si
a /Å	24.61
b /Å	24.61
c /Å	24.61
Cell volume / Å^3	14905.1
conversion factor for [molec/uc] to [mol per kg Framework]	0.0867
conversion factor for [molec/uc] to [kmol/m^3]	0.2794
ρ [kg/m3]	1285.248
MW unit cell [g/mol(framework)]	11536.28
ϕ, fractional pore volume	0.399
open space / Å^3/uc	5944.4
Pore volume / cm^3/g	0.310
Surface area /m^2/g	896.0
DeLaunay diameter /Å	4.10

Figure S10. Structural details for all-silica LTA zeolite.

CuBTC pore landscapes

The structural information for CuBTC (= $Cu_3(BTC)_2$ with BTC = 1,3,5-benzenetricarboxylate) have been taken from

S.S.Y. Chui, S.M.F. Lo, J.P.H. Charmant, A.G. Orpen, I.D. Williams, A chemically functionalizable nanoporous material $[Cu_3(TMA)_2(H2O)_3]_n$, Science 283 (1999) 1148-1150.
The crystal structure of Chui et al. includes axial oxygen atoms weakly bonded to the Cu atoms, which correspond to water ligands. Our simulations have been performed on the dry CuBTC with these oxygen atoms removed.

Q. Yang, C. Zhong, Electrostatic-Field-Induced Enhancement of Gas Mixture Separation in Metal-Organic Frameworks: A Computational Study, ChemPhysChem 7 (2006) 1417-1421.

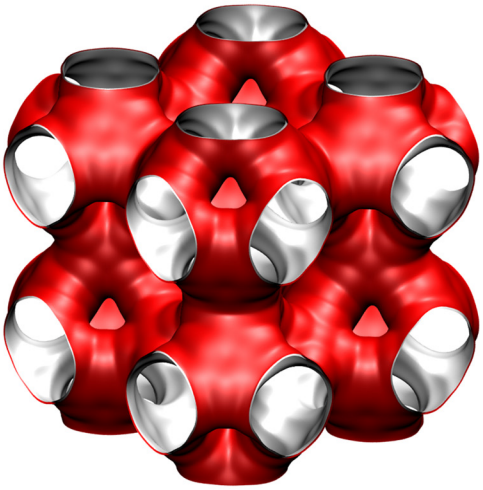

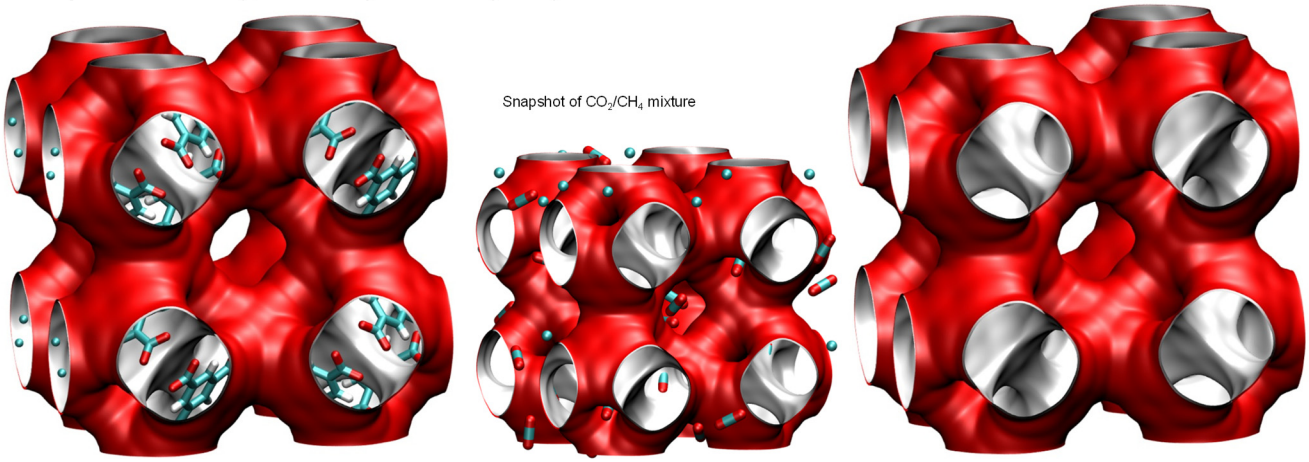

Figure S11. Structural details and pore landscape for CuBTC.

CuBTC pore dimensions

	CuBTC
a /Å	26.343
b /Å	26.343
c /Å	26.343
Cell volume / Å^3	18280.82
conversion factor for [molec/uc] to [mol per kg Framework]	0.1034
conversion factor for [molec/uc] to [kmol/m^3]	0.1218
ρ [kg/m3]	878.8298
MW unit cell [g/mol(framework)]	9674.855
ϕ, fractional pore volume	0.746
open space / Å^3/uc	13628.4
Pore volume / cm^3/g	0.848
Surface area /m^2/g	2097.0
DeLaunay diameter /Å	6.23

The CuBTC structure consists of two types of “cages” and two types of “windows” separating these cages. Large cages are inter-connected by 9 Å windows of square cross-section. The large cages are also connected to tetrahedral-shaped pockets of ca. 5 Å size through triangular-shaped windows of ca. 4.6 Å size

Figure S12. Structural details and pore landscape for CuBTC.

CuBTC framework

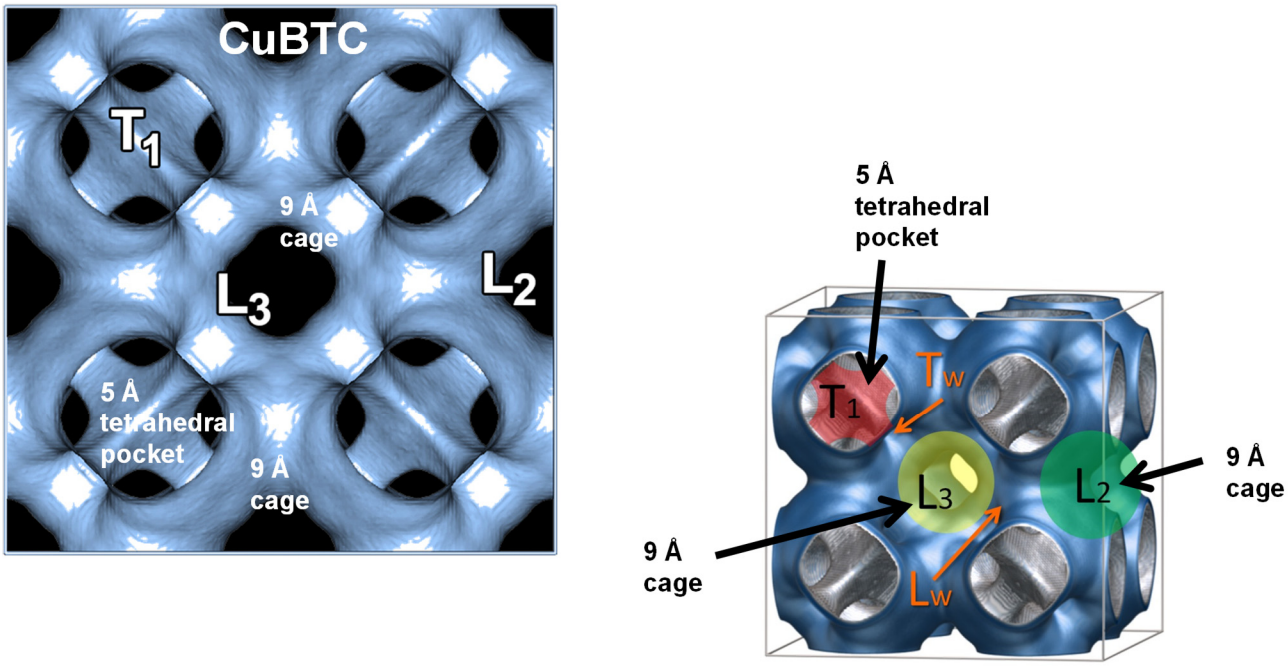

Figure S13. Structural details and pore landscape for CuBTC.

2 Radial Distribution Functions of O···H distances

In order to demonstrate the occurrence of hydrogen bonding in water/methanol, and water/ethanol mixtures CBMC simulation data on the spatial locations of the guest molecules were sampled to determine the O···H distances of various pairs of molecules. By sampling a total of 10^6 simulation steps, the radial distribution functions (RDF) of O···H distances were determined for water-water, water-alcohol, and alcohol-alcohol pairs.

Figure S14a shows the RDF of O…H distances for molecular pairs of water(1)/methanol(2) mixture adsorption in CHA zeolite at 300 K. The partial fugacities of components 1 and 2 are f_1= 2.5 kPa, f_2= 7.5 kPa. We note the first peaks in the RDFs occur at a distance less than 2 Å, that is characteristic of hydrogen bonding.[8, 23] The heights of the first peaks are a direct reflection of the degree of hydrogen bonding between the molecular pairs. We may conclude, therefore that for water/methanol mixtures the degree of H-bonding between water-methanol pairs is significantly larger, by about an order of magnitude, than for water-water, and methanol-methanol pairs. Analogous set of conclusions can be drawn for water/ethanol mixtures, for which the RDF data are presented in Figure S14b, i.e. the degree of H-bonding between water-ethanol pairs is larger than for water-water, and ethanol-ethanol pairs. For comparison purposes, the RDF data for adsorption of methanol/ethanol mixtures are shown in Figure S14c. The magnitude of the first peaks for methanol-ethanol, methanol-methanol, ethanol-ethanol pairs are significantly lower than the water-alcohol peaks in Figure S14a,b. Therefore, the H-bonding effects should be expected to be of less importance for methanol/ethanol mixture adsorption in CHA than for water/methanol and water/ethanol mixtures.

A visual appreciation of hydrogen bonding is gleaned from the snapshots in Figure S15 for mixture adsorption in CHA.

Figure S16 shows the corresponding results for RDF of O···H distances for molecular pairs of water(1)/ethanol(2) mixture adsorption in DDR zeolite at 300 K. The H-bonding between water/ethanol pairs is much stronger than for water/water and ethanol/ethanol pairs; these conclusions are in line with those for CHA zeolite.

A visual appreciation of hydrogen bonding is gleaned from the snapshots in Figure S17 for mixture adsorption in DDR.

Figure S18a shows the data on RDF of O···H distances for molecular pairs of water(1)/ethanol(2) mixture adsorption in MFI zeolite at 300 K. We again conclude that H-bonding between water/ethanol pairs is more significant than for other pairs. Computational snapshots for water/methanol and water/ethanol mixture adsorption in MFI are provided in Figure S18b,c.

Figure S19a,b presents RDF of O···H distances for molecular pairs of water(1)/methanol(2) (total loading = 72 molecules per unit cell), water(1)/ethanol(2) (total loading = 56 molecules per unit cell) mixture adsorption in FAU zeolite at 300 K; these mixture are equimolar in the adsorbed phase.[8] The degree of molecular clustering due to hydrogen bonding can be characterized by the magnitudes of the first peaks.[8, 23] The RDF data for water/methanol, and water/ethanol mixtures in FAU (all silica) were determined for a range of adsorbed phase compositions.[8] Collecting the data on the magnitude of the first peaks for water-alcohol mixtures in FAU, Figure S19c,d presents plots of the first-peak heights as function of the mole fraction of the alcohol. We observe that molecular clustering effects are higher for water-alcohol pairs, as compared to water-water, and alcohol-alcohol pairs.

Figure S20a shows the RDF of O…H distances for molecular pairs of water(1)/methanol(2) mixture adsorption in ZIF-8 at 300 K. We note the first peaks in the RDFs occur at a distance less than 2 Å, that is characteristic of hydrogen bonding. [8, 23] The heights of the first peaks are a direct reflection of the degree of hydrogen bonding between the molecular pairs, resulting in cluster formation and enhanced water ingress.[24] We may conclude, therefore that for water/methanol mixtures the degree of H-bonding between water-methanol pairs is significantly larger, by about an order of magnitude, than for water-water, and methanol-methanol pairs. Analogous set of conclusions can be drawn for water/ethanol mixtures, for

which the RDF data are presented in Figure S20b; the degree of H-bonding between water-ethanol pairs is larger than for water-water, and ethanol-ethanol pairs.

Computational snapshots for water/methanol and water/ethanol mixture adsorption in ZIF-8 are provided in Figure S21a,b.

Watch also the presentations titled **Hydrogen Bonding Influences on Adsorption, Visualizing Motion of Guest Molecules in ZIF-8**

on YouTube https://www.youtube.com/@rajamanikrishna250/videos

2.1 List of Figures for Radial Distribution Functions of O···H distances

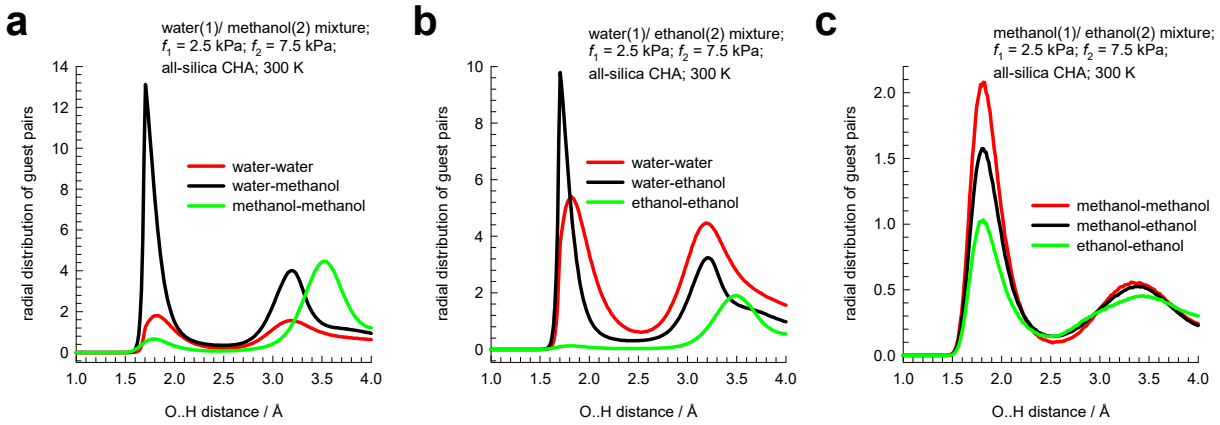

Figure S14. RDF of O···H distances for molecular pairs of (a) water(1)/methanol(2), (b) water(1)/ethanol(2), and (c) methanol(1)/ethanol(2) mixture adsorption in CHA zeolite at 300 K. For all three sets of mixtures, the partial fugacities of components 1 and 2 are f_1= 2.5 kPa, f_2= 7.5 kPa. The *y*-axes are normalized in the same manner and, therefore, the magnitudes of the first peaks is a direct reflection of the degree of hydrogen bonding between the molecular pairs.

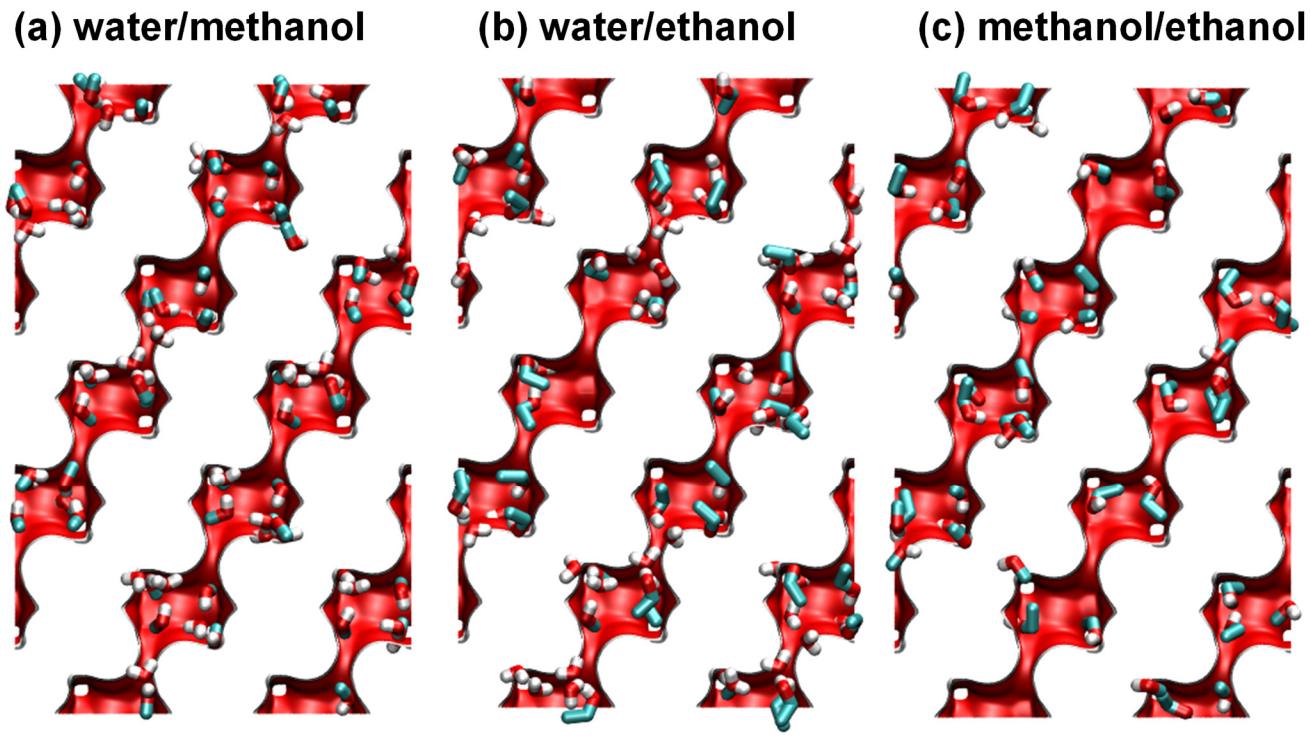

Figure S15. Snapshots showing location and conformations of guest molecules for adsorption of (a) water(1)/methanol(2), (b) water(1)/ethanol(2), and (c) methanol(1)/ethanol(2) mixture adsorption in CHA zeolite at 300 K. The partial fugacities of components 1 and 2 are f_1= 2.5 kPa, f_2= 7.5 kPa.

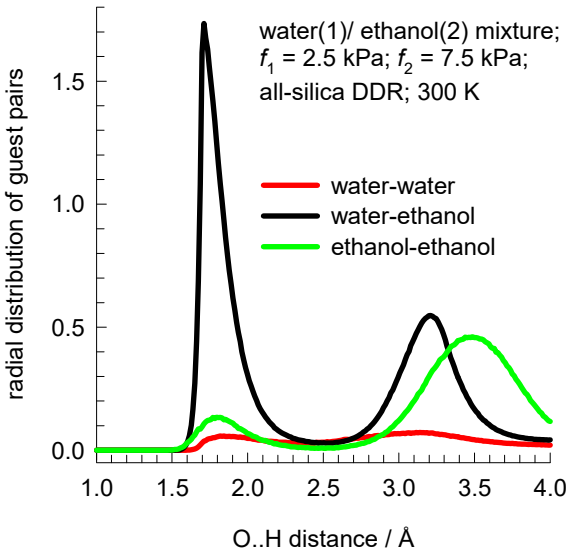

Figure S16. RDF of O···H distances for molecular pairs of water(1)/ethanol(2) mixture adsorption in DDR zeolite at 300 K. The partial fugacities of components 1 and 2 are f_1= 2.5 kPa, f_2= 7.5 kPa.

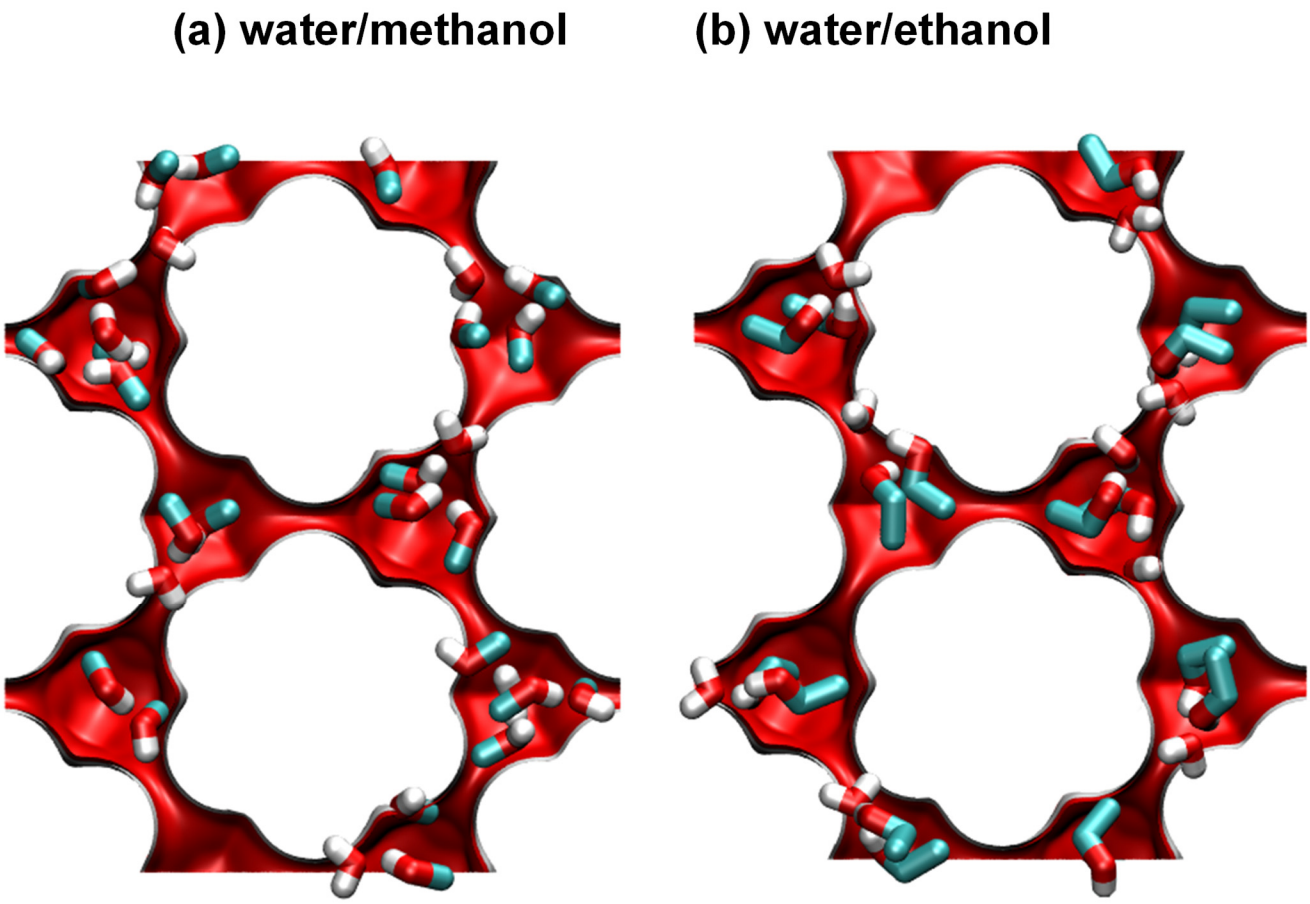

Figure S17. Snapshots showing location and conformations of guest molecules for adsorption of (a) water(1)/methanol(2), and (b) water(1)/ethanol(2) mixture adsorption in DDR zeolite at 300 K. The partial fugacities of components 1 and 2 are f_1= 2.5 kPa, f_2= 7.5 kPa.

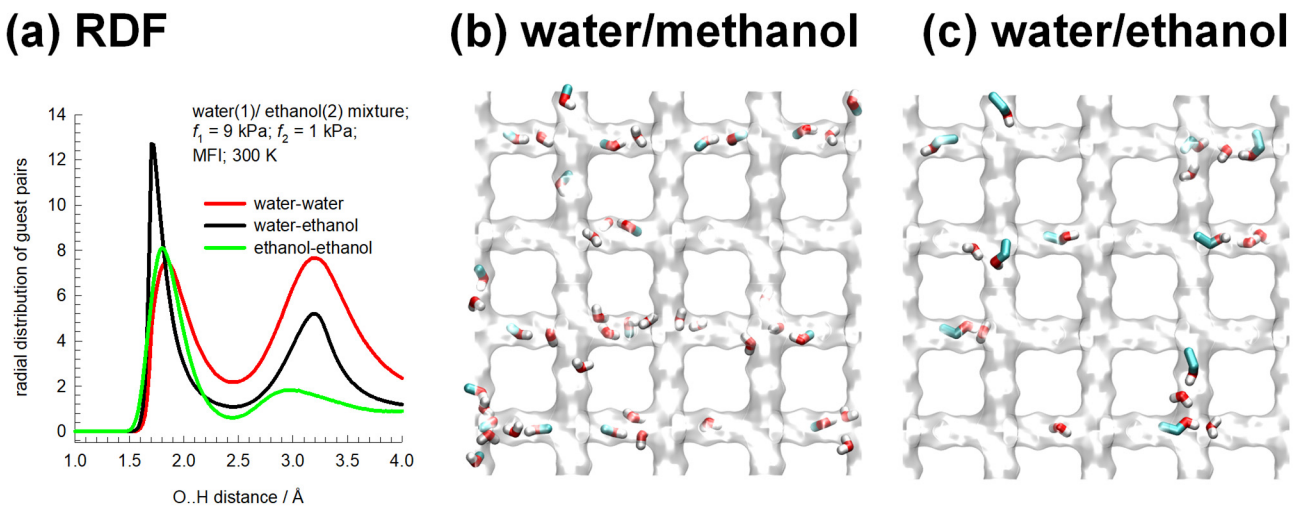

Figure S18. (a) RDF of O···H distances for molecular pairs of water(1)/ethanol(2) mixture adsorption in MFI zeolite at 300 K. The partial fugacities of components 1 and 2 are f_1= 9 kPa, f_2= 1 kPa. (b, c) Snapshots showing location and conformations of guest molecules for adsorption of (b) water(1)/methanol(2), and (c) water(1)/ethanol(2) mixture adsorption in MFI zeolite at 300 K.

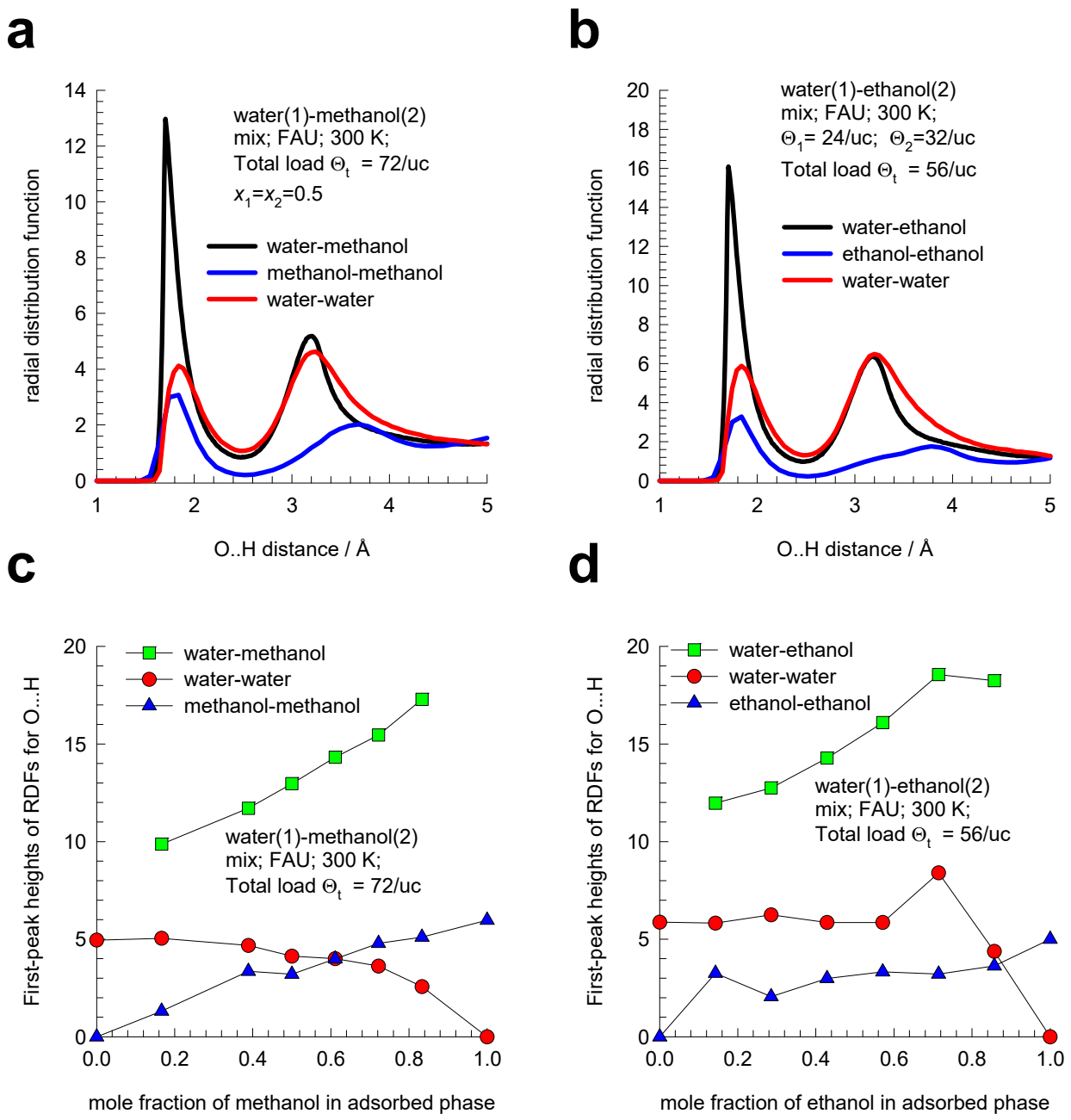

Figure S19. (a, b) RDF of O···H distances for molecular pairs of water(1)/methanol(2) (total loading = 72 molecules per unit cell), water(1)/ethanol(2) (total loading = 56 molecules per unit cell) mixture adsorption in FAU zeolite at 300 K; these mixture are equimolar in the adsorbed phase. (c, d) Plots of the first-peak heights of the RDFs, from data such as those presented in (a, b) for varying compositions in the adsorbed phase.

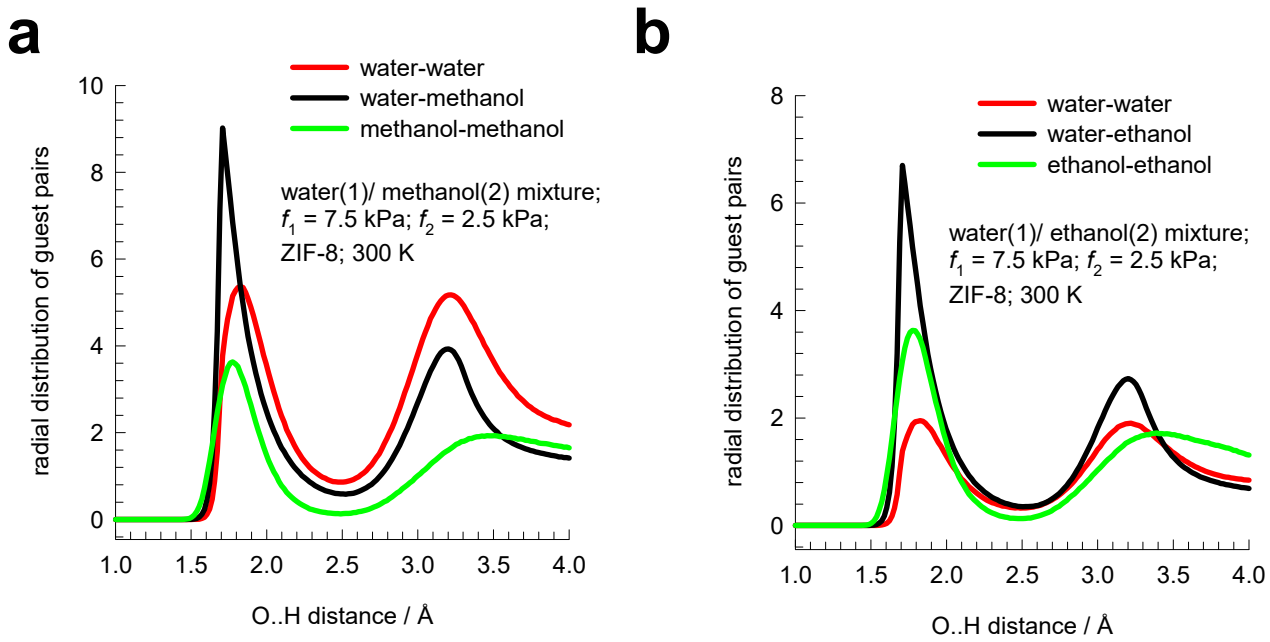

Figure S20. RDF of O···H distances for molecular pairs of (a) water(1)/methanol(2), and (b) water(1)/ethanol(2) mixture adsorption in ZIF-8 at 300 K. For both mixtures, the partial fugacities of components 1 and 2 are f_1= 7.5 kPa, f_2= 2.5 kPa. The *y*- axes are normalized in the same manner and, therefore, the magnitudes of the first peaks is a direct reflection of the degree of hydrogen bonding between the molecular pairs.

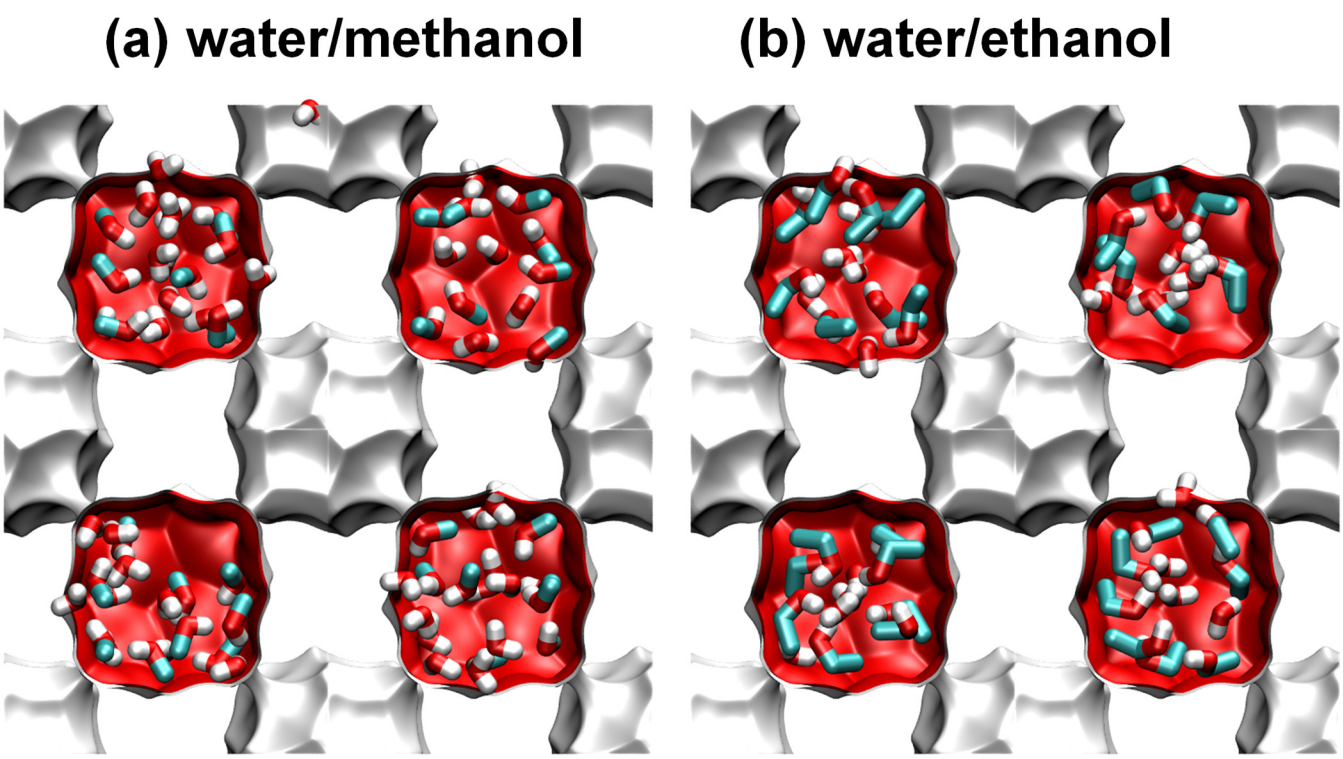

Figure S21. Snapshots showing location and conformations of guest molecules for adsorption of (a) water(1)/methanol(2), and (b) water(1)/ethanol(2) mixture adsorption in ZIF-8 at 300 K.

3 Molecular Dynamics (MD) Simulation Methodology

Diffusion is simulated using Newton's equations of motion until the system properties, on average, no longer change in time. The Verlet algorithm is used for time integration. A time step of 1 fs was used in all simulations. For each simulation, *initializing* CBMC moves are used to place the molecules in the domain, minimizing the energy. Next, follows an *equilibration* stage. These are essentially the same as the production cycles, only the statistics are not yet taken into account. This removes any initial large disturbances in the system that do not affect statistics on molecular displacements. After a fixed number of initialization and equilibrium steps, the MD simulation *production* cycles start. For every cycle, the statistics for determining the mean square displacements (MSDs) are updated. The MSDs are determined for time intervals ranging from 2 fs to 1 ns. In order to do this, an order-*N* algorithm, as detailed in Chapter 4 of Frenkel and Smit[20] is implemented. The Nosé-Hoover thermostat is applied to all the diffusing particles.

For all the MD simulation results presented in this article, the DLPOLY code[25] was used along with the force field implementation as described in the previous section. DL_POLY is a molecular dynamics simulation package written by W. Smith, T.R. Forester and I.T. Todorov and has been obtained from CCLRCs Daresbury Laboratory via the website.[25]

All MD simulations were carried out using Snellius, the National Supercomputer in the Netherlands. The MD simulations were carried out for a variety of loadings. Each MD simulation, for a specified loading, was run for a time duration that is sufficiently long to obtain reliable statistics for determination of the diffusivities. In several cases the campaigns were replicated and the results averaged.

The self-diffusivities $D_{i,self}$ are computed from MD simulations by analyzing the mean square displacement of each species *i* for each coordinate direction

$$D_{i,self} = \frac{1}{2n_i} \lim_{\Delta t \to \infty} \frac{1}{\Delta t} \left\langle \left(\sum_{l=1}^{n_i} \left(\mathbf{r}_{l,i}(t + \Delta t) - \mathbf{r}_{l,i}(t) \right)^2 \right) \right\rangle \tag{S2}$$

In this expression n_i represents the number of molecules of species i, and $\mathbf{r}_{l,i}(t)$ is the position of molecule l of species i at any time t.

For three-dimensional pore networks (e.g. FAU, LTA, ZIF-8, CHA) the arithmetic average of the diffusivities in the three coordinate directions were used in further analysis and reported. For DDR the reported diffusivities are the averages in x- and y- directions.

MD simulations were performed to determine the self-diffusivities $D_{i,self}$ in a variety of equimolar. $(q_1 = q_2)$. binary and ternary $(q_1 = q_2 = q_3)$ mixtures. In a few cases, the MD simulations were performed for mixtures in which the total loading $q_t = q_1 + q_2$ was held constant and the mole fraction of the adsorbed phase mixture, $x_1 = \frac{q_1}{q_1 + q_2}$ was varied from 0 to 1. All MD simulations reported in this work were conducted at a temperature $T = 300$ K.

Watch also the presentations titled **Diffusion in LTA-4A and 5A Zeolites, Diffusion in Cage-Type Zeolites, Inter-cage Hopping in DDR Zeolite, Inter-cage Hopping in CHA Zeolite, Mutual Slowing-Down in Water/Alcohol Mixture Diffusion, Visualizing Motion of Guest Molecules in ZIF-8, Diffusion in LTA Zeolite, Diffusion in CHA Zeolite, Diffusion in DDR Zeolite, Diffusion in ZIF-8**

on YouTube https://www.youtube.com/@rajamanikrishna250/videos

For the interpretation and analysis of the MD simulations for mixture diffusion in microporous host materials, the RAST calculation procedure (details are provided in a subsequent chapter) needs to be performed differently because in the MD simulations, the molar loadings q_i in the mixture are specified, and the partial fugacities in the bulk fluid mixture are not known *a priori*. Also, in this case, the equalities in eq (S7) must be satisfied in conjunction with eq (S10). The entire set of eqs (S5) to (S12) need to be solved numerically to obtain the partial fugacities, f_i of the individual components in the mixture, that yield the same loadings as chosen in the MD simulations. The RAST calculations also determine the

surface potential Φ. In all of the calculations presented in this article, the set of equations were solved using an Excel macro that was developed for this specific purpose.

4 The IAST for mixture adsorption equilibrium

Within microporous crystalline materials, the guest molecules exist in the adsorbed phase, and the thermodynamics of mixture adsorption has an important bearing on the diffusion characteristics of guest molecules. For that reason, we provide below a brief summary of the Ideal Adsorbed Solution Theory (IAST) theory of Myers and Prausnitz.[26]

4.1 Brief outline of theory

The Gibbs adsorption equation[27] in differential form is

$$Ad\pi = \sum_{i=1}^{n} q_i d\mu_i \tag{S3}$$

The quantity A is the surface area per kg of framework, with units of m^2 per kg of the framework of the crystalline material; q_i is the molar loading of component i in the adsorbed phase with units moles per kg of framework; μ_i is the molar chemical potential of component i. The spreading pressure π has the same units as surface tension, i.e. N m^{-1}.

The chemical potential of any component in the adsorbed phase, μ_i, equals that in the bulk fluid phase. If the partial fugacities in the bulk fluid phase are f_i, we have

$$d\mu_i = RTd\ln f_i \tag{S4}$$

where R is the gas constant (= 8.314 J mol^{-1} K^{-1}).

Briefly, the basic equation of Ideal Adsorbed Solution Theory (IAST) theory of Myers and Prausnitz[26] is the analogue of Raoult's law for vapor-liquid equilibrium, i.e.

$$f_i = P_i^0 x_i; \quad i = 1, 2, ...n \tag{S5}$$

where x_i is the mole fraction in the adsorbed phase

$$x_i = \frac{q_i}{q_1 + q_2 + ...q_n} \tag{S6}$$

and P_i^0 is the pressure for sorption of every component *i*, which yields the same spreading pressure, π for each of the pure components, as that for the mixture:

$$\frac{\pi A}{RT} = \int_0^{P_1^0} \frac{q_1^0(f)}{f} df = \int_0^{P_2^0} \frac{q_2^0(f)}{f} df = \int_0^{P_3^0} \frac{q_3^0(f)}{f} df = \ldots \tag{S7}$$

where $q_i^0(f)$ is the *pure* component adsorption isotherm. The units of $\Phi \equiv \frac{\pi A}{RT}$, also called the surface potential, [24, 28-31] are mol kg^{-1}.

The unary isotherm may be described by say the 1-site Langmuir isotherm

$$q^0(f) = q_{sat} \frac{bf}{1+bf}; \quad \theta = \frac{bf}{1+bf} \tag{S8}$$

where we define the fractional *occupancy* of the adsorbate molecules, $\theta = q^0(f)/q_{sat}$. The superscript 0 is used to emphasize that $q^0(f)$ relates the *pure component* loading to the bulk fluid fugacity. For all of the guest/host combinations considered in this article, the unary isotherms need to be described by the dual-Langmuir-Freundlich model

$$q^0(f) = q_{A,sat} \frac{b_A f^{\nu A}}{1+b_A f^{\nu A}} + q_{B,sat} \frac{b_B f^{\nu B}}{1+b_B f^{\nu B}} \tag{S9}$$

Each of the integrals in eq (S7) can be evaluated analytically. For the dual-site Langmuir-Freundlich isotherm, for example, the integration yields for component *i*,

$$\begin{aligned} \Phi \equiv \frac{\pi A}{RT} &= \int_{f=0}^{P_i^0} \frac{q_i^0(f)}{f} df = \frac{q_{A,sat}}{\nu_A} \ln\left(1+b_A\left(P_i^0\right)^{\nu_A}\right) + \frac{q_{B,sat}}{\nu_B} \ln\left(1+b_B\left(P_i^0\right)^{\nu_B}\right); \\ \Phi \equiv \frac{\pi A}{RT} &= \int_{f=0}^{P_i^0} \frac{q_i^0(f)}{f} df = \frac{q_{A,sat}}{\nu_A} \ln\left(1+b_A\left(\frac{f_i}{x_i}\right)^{\nu_A}\right) + \frac{q_{B,sat}}{\nu_B} \ln\left(1+b_B\left(\frac{f_i}{x_i}\right)^{\nu_B}\right) \end{aligned} \tag{S10}$$

The right hand side of eq (S10) is a function of P_i^0. For multicomponent mixture adsorption, each of the equalities on the right hand side of Eq (S7) must be satisfied. These constraints may be solved using a suitable equation solver, to yield the set of values of , P_2^0, P_3^0,.. P_n^0, each of which satisfy eq (S7). The

corresponding values of the integrals using these as upper limits of integration must yield the same value of . Φ . for each component; this ensures that the obtained solution is the correct one.

Watch also the presentations titled **Fitting of Unary Isotherms, 3-site Langmuir-Freundlich fit?** on YouTube https://www.youtube.com/@rajamanikrishna250/videos

The adsorbed phase mole fractions x_i are then determined from

$$x_i = \frac{f_i}{P_i^0}; \quad i = 1, 2, ...n \tag{S11}$$

The applicability of eqs (S5) and (S11) mandates that all of the adsorption sites within the microporous material are equally accessible to each of the guest molecules, implying a homogeneous distribution of guest adsorbates within the pore landscape, with no preferential locations of any guest species. The circumstances in which this mandate is not fulfilled are highlighted in recent works.[30-32]

A key assumption of the IAST is that the adsorption enthalpies and surface areas of the adsorbed molecules do not change upon mixing. If the total mixture loading is q_t, the area covered by the adsorbed mixture is $\frac{A}{q_t}$ with units of m^2 (mol mixture)$^{-1}$. Therefore, the assumption of no surface area change due to mixture adsorption translates as $\frac{A}{q_t} = \frac{Ax_1}{q_1^0\left(P_1^0\right)} + \frac{Ax_2}{q_2^0\left(P_2^0\right)} + \cdots \frac{Ax_n}{q_n^0\left(P_n^0\right)}$; the total mixture loading is q_t is calculated from

$$q_t = q_1 + q_2 ... + q_n = \frac{1}{\frac{x_1}{q_1^0(P_1^0)} + \frac{x_2}{q_2^0(P_2^0)} + ... + \frac{x_n}{q_n^0(P_n^0)}} \tag{S12}$$

in which $q_1^0(P_1^0)$, $q_2^0(P_2^0)$,… $q_n^0(P_n^0)$ are determined from the unary isotherm fits, using the sorption pressures for each component P_1^0, P_2^0, P_3^0,.. P_n^0 that are available from the solutions to equations Eqs (S7), and (S10).

The occurrence of molecular clustering and hydrogen bonding should be expected to applicability of eq (S12) because the surface area occupied by a molecular cluster is different from that of each of the un-clustered guest molecules in the adsorbed phase.

The entire set of eqs (S5) to (S12) need to be solved numerically to obtain the loadings, q_i of the individual components in the mixture.

Watch also the presentations titled **The IAST for Mixture Adsorption Equilibrium, Dependence of Adsorption Selectivity on Mixture Composition, Adsorption Selectivity vs Total Pressure, Significance of the Spreading Pressure Concept, Hydrogen Bonding Influences on Adsorption, Langmuir Model for Binary Mixture Adsorption, Reversals in Adsorption Selectivity, The Spreading Pressure Concept for Microporous Membranes** on YouTube https://www.youtube.com/@rajamanikrishna250/videos

For the interpretation and analysis of the MD simulations for binary mixture diffusion in microporous host materials, the IAST calculation procedure has to be performed differently because in the MD simulations, the molar loadings q_1, and q_2 in the mixture are specified, and the partial fugacities in the bulk fluid mixture are not known *a priori*. Also in this case, the equalities in eq (S10) must be satisfied in conjunction with eq (S12). The entire set of eqs (S5) to (S12) need to be solved numerically to obtain the partial fugacities, f_i of the individual components in the mixture, that yield the same loadings as chosen in the MD simulations. In all of the calculations presented in this article, the set of equations were solved using an Excel macro that was developed for this specific purpose.

4.2 Selectivity for mixture adsorption

For *n*-component mixture adsorption, the selectivity of guest constituent *i* with respect to another guest constituent *j*, in that mixture, $S_{ads,ij}$, is defined by

$$S_{ads,ij} = \frac{q_i/q_j}{f_i/f_j} = \frac{x_i/f_i}{x_j/f_j} \tag{S13}$$

where q_i, q_j are the molar loadings of the constituents *i* and *j*, in the adsorbed phase in equilibrium with a bulk fluid phase mixture with partial fugacities f_i, f_j, and mole fractions $y_i = f_i/f_t$; $f_t = \left(\sum_{k=1}^{n} f_k\right)$. In view of eqs (S11), and (S12), we may re-write eq (S13) as the ratio of the sorption pressures

$$S_{ads,ij} = \frac{P_j^0}{P_i^0} \tag{S14}$$

Applying the restriction specified by eq (S7), it follows that $S_{ads,ij}$ is uniquely determined by the surface potential Φ. It is important to note that eq (S14) is valid irrespective of the total number of components in the mixture. Put another way, the presence of component 3 in the ternary mixture has no influence of the adsorption selectivity $S_{ads,12} = \frac{P_2^0}{P_1^0}$ for the 1-2 pair, except insofar as the presence of component 3 alters the value of the surface potential Φ for the 1-2-3 mixture. Therefore, for an ideal adsorbed phase mixture, the presence of additional guest constituents, say species 3, 4, 5, do not influence the selectivity of the 1-2 pair.

In Figure S22a,b, the CO_2/CH_4, and CO_2/N_2 adsorption selectivities in MFI and FAU zeolites determined from CBMC simulations data for binary mixtures[33] are compared with the values determined for $CO_2/CH_4/N_2$ and $CO_2/CH_4/N_2/H_2$ mixtures. The CBMC data for each binary pair on S_{ads} displays a unique dependence on the surface potential Φ, as anticipated from the application of eq (S14), Also, the CBMC data are in excellent agreement with the IAST estimates.

Figure S23a,b plots the selectivities for CO_2/CH_4, CO_2/N_2, CO_2/H_2, and CH_4/N_2 pairs in CHA, and DDR zeolites determined from CBMC data for adsorption of binary, ternary and quaternary mixtures of a variety of compositions. Each of the individual pair selectivities displays a unique dependence on Φ, irrespective of the number of components in the mixture. The IAST calculations (indicated by dashed lines in Figure S23a,b) show small deviations from the CBMC simulated data due to non-idealities caused by preferential perching of CO_2 at the window regions of CHA and DDR; detailed explanations are provided in our earlier works [32, 34-36].

The inescapable conclusion to be drawn is that for the adsorption of light gaseous molecules (CO_2, CH_4, N_2, H_2) in the four host materials (CHA, DDR, MFI, FAU) considered in this article, the uniqueness of the S_{ads} vs Φ relationship is not affected by non-idealities in mixture adsorption. Further detailed confirmation for other mixture/host combination are provided by Krishna and van Baten.[33]

4.3 The IAST model for 1-site Langmuir isotherms

The IAST procedure will be applied for binary mixture adsorption in which the unary isotherms are described by the 1-site Langmuir model in which the saturation capacities of components 1 and 2 are identical to each other, i.e. $q_{1,sat} = q_{2,sat} = q_{sat}$:

$$q_i^0\left(f\right) = q_{sat}\frac{b_i f}{1+b_i f} \tag{S15}$$

For unary adsorption, the surface potential for a 1-site Langmuir isotherm can be calculated analytically

$$\Phi \equiv \frac{\pi A}{RT} = q_{sat}\ln\left(1+bP^0\right) \tag{S16}$$

The objective is to determine the molar loadings, q_1, and q_2, in the adsorbed phase. Performing the integration of eq (S7) results in an expression relating the sorption pressures P_i^0 of the two species

$$\begin{aligned}&\Phi \equiv \frac{\pi A}{RT} = q_{sat}\ln\left(1+b_1P_1^0\right) = q_{sat}\ln\left(1+b_2P_2^0\right)\\ &b_1P_1^0 = b_2P_2^0 = \exp\left(\frac{\pi A}{q_{sat}RT}\right)-1\end{aligned} \tag{S17}$$

The adsorbed phase mole fractions of component 1, and component 2 are given by eq (S11)

$$x_1 = \frac{f_1}{P_1^0};\quad x_2 = 1-x_1 = \frac{f_2}{P_2^0} \tag{S18}$$

Combining eqs (S17), and (S18):

$$\exp\left(\frac{\pi A}{q_{sat}RT}\right)-1 = b_1\frac{f_1}{x_1} = b_2\frac{f_2}{1-x_1} \tag{S19}$$

The adsorbed phase mole fractions can be determined

$$\frac{x_1}{x_2} = \frac{q_1}{q_2} = \frac{b_1f_1}{b_2f_2};\quad x_1 = \frac{q_1}{q_t} = \frac{b_1f_1}{b_1f_1+b_2f_2};\quad x_2 = \frac{q_2}{q_t} = \frac{b_2f_2}{b_1f_1+b_2f_2} \tag{S20}$$

Once x_1, and $x_2 = 1-x_1$ are determined, the sorption pressures can be calculated:

$$P_1^0 = \frac{f_1}{x_1};\quad P_2^0 = \frac{f_2}{x_2} = \frac{f_2}{1-x_1} \tag{S21}$$

From eqs (S17), and (S21) we get

$$b_i P_1^0 = \frac{b_1 f_1}{x_1} = b_2 P_2^0 = \frac{b_2 f_2}{x_2} = b_1 f_1 + b_2 f_2$$
$$1 + b_i P_1^0 = 1 + b_2 P_2^0 = 1 + b_1 f_1 + b_2 f_2 \tag{S22}$$

Combining eqs (S17), and (S22) we obtain the following explicit expression for the surface potential

$$\Phi = q_{sat} \ln\left(1 + b_1 f_1 + b_2 f_2\right) \tag{S23}$$

The total amount adsorbed, $q_t = q_1 + q_2$ can be calculated from Eq (S12)

$$q_t = q_1 + q_2 = q_{sat} \frac{b_1 P_1^0}{1 + b_1 P_1^0} = q_{sat} \frac{b_2 P_2^0}{1 + b_2 P_2^0} = q_{sat} \frac{b_1 f_1 + b_2 f_2}{1 + b_1 f_1 + b_2 f_2} \tag{S24}$$

Combining eqs (S20), and (S24) we obtain the following explicit expressions for the component loadings, and fractional occupancies

$$\theta_1 = \frac{q_1}{q_{sat}} = \frac{b_1 f_1}{1 + b_1 f_1 + b_2 f_2}; \quad \theta_2 = \frac{q_2}{q_{sat}} = \frac{b_2 f_2}{1 + b_1 f_1 + b_2 f_2} \tag{S25}$$

Eq (S25) is commonly referred to as the mixed-gas Langmuir model.

From eqs (S17), (S24), and (S25) we derive the following expression for the total occupancy of the mixture

$$\theta = \theta_1 + \theta_2 = \frac{q_t}{q_{sat}} = 1 - \exp\left(-\frac{\Phi}{q_{sat}}\right) = \frac{b_1 f_1 + b_2 f_2}{1 + b_1 f_1 + b_2 f_2} \tag{S26}$$

For *unary* adsorption of component *i*, say, $f_i = P_i^0$, the occupancy of component 1 is

$$\theta_i = 1 - \exp\left(-\frac{\Phi}{q_{i,sat}}\right) = \frac{b_i f_i}{1 + b_i f_i}; \quad \text{unary adsorption of species i} \tag{S27}$$

From eqs (S26), and (S27) we may also conclude the *occupancy* may be considered to be the appropriate *proxy* for the spreading pressure. The conclusion that we draw from the foregoing analysis is that the equalities of spreading pressures for unary adsorption of component 1, unary adsorption of component 2, and binary 1-2 mixture adsorption also implies the corresponding equalities of the corresponding *occupancies* for unary adsorption of component 1, unary adsorption of component 2, and binary 1-2 mixture adsorption.

For *n*-component mixtures, eq (S23) may be generalized to

$$\Phi = q_{sat} \ln\left(1 + \sum_{i=1}^{n} b_i f_i\right) \tag{S28}$$

4.4 Generalized expression for fractional occupancy

From knowledge of the surface potential, Φ, the fractional occupancy for *n*-component mixture adsorption is then calculated using

$$\theta = 1 - \exp\left(-\frac{\pi A}{q_{sat,mix} RT}\right) = 1 - \exp\left(-\frac{\Phi}{q_{sat,mix}}\right) \tag{S29}$$

For an *n*-component mixture, the saturation capacity $q_{sat,mix}$ is calculated from the saturation capacities of the constituent guests

$$q_{sat,mix} = \frac{1}{\frac{x_1}{q_{1,sat}} + \frac{x_2}{q_{2,sat}} + ... \frac{x_n}{q_{n,sat}}}; \quad q_{i,sat} = q_{i,A,sat} + q_{i,B,sat}; \quad i = 1, 2...n \tag{S30}$$

where

$$x_i = \frac{q_i}{q_1 + q_2 + ... q_n}; \quad i = 1, 2, ... n \tag{S31}$$

are the mole fractions in the adsorbed mixture. The fundamental justification of Eq (S30) is provided by invoking eq (S12).

For binary mixtures, eq (S30) simplifies to yield $q_{sat,mix} = \frac{1}{\frac{x_1}{q_{1,sat}} + \frac{x_2}{q_{2,sat}}}$.

It is also to be noted that eq (15) of our earlier publication[37] has a typographical error in the calculation of $q_{sat,mix}$; the correct form is given by eq (S30).

As an example, let consider the adsorption of water(1)/ethanol(2) mixtures in CHA zeolite at 300 K. The Dual-site Langmuir-Freundlich isotherm fit parameters are specified in Table S4. The saturation capacity of water (1) $q_{1,sat} = q_{1,A,sat} + q_{1,B,sat}$ =16.8 + 4.6 = 21.4 mol kg^{-1}. The saturation capacity of ethanol

(2) $q_{2,sat} = q_{2,A,sat} + q_{2,B,sat}$ =2.5 + 2.9 = 5.4 mol kg^{-1}. The saturation capacity of the mixture for adsorbed phase compositions, $x_1 = x_2 = 0.5$ is $q_{sat,mix} = \dfrac{1}{\dfrac{x_1}{q_{1,sat}} + \dfrac{x_2}{q_{2,sat}}}$ = 8.62 mol kg^{-1}.

For binary CO_2(1)/CH_4(2) mixture adsorption in CHA, DDR, MFI, and all-silica FAU zeolite at 300 K, the pore occupancies for each host, calculated using eq (S29) are below as function of the corresponding surface potential Φ.

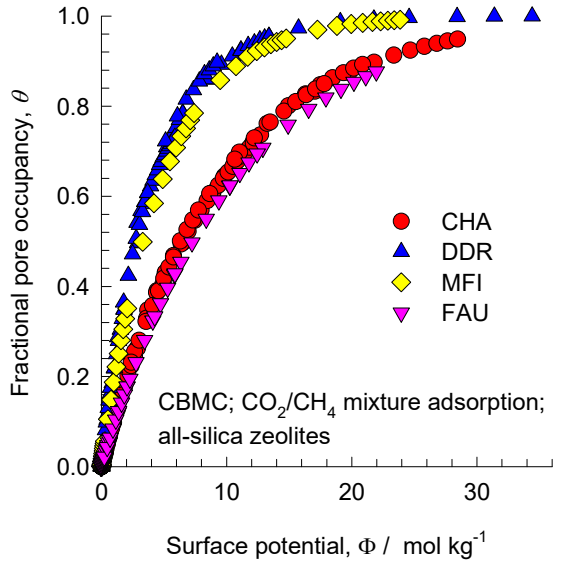

We note that for all four hosts, the pore occupancy $\theta \to 1$ as $\Phi >> 30$ mol kg^{-1}.

4.5 List of Figures for The IAST for mixture adsorption equilibrium

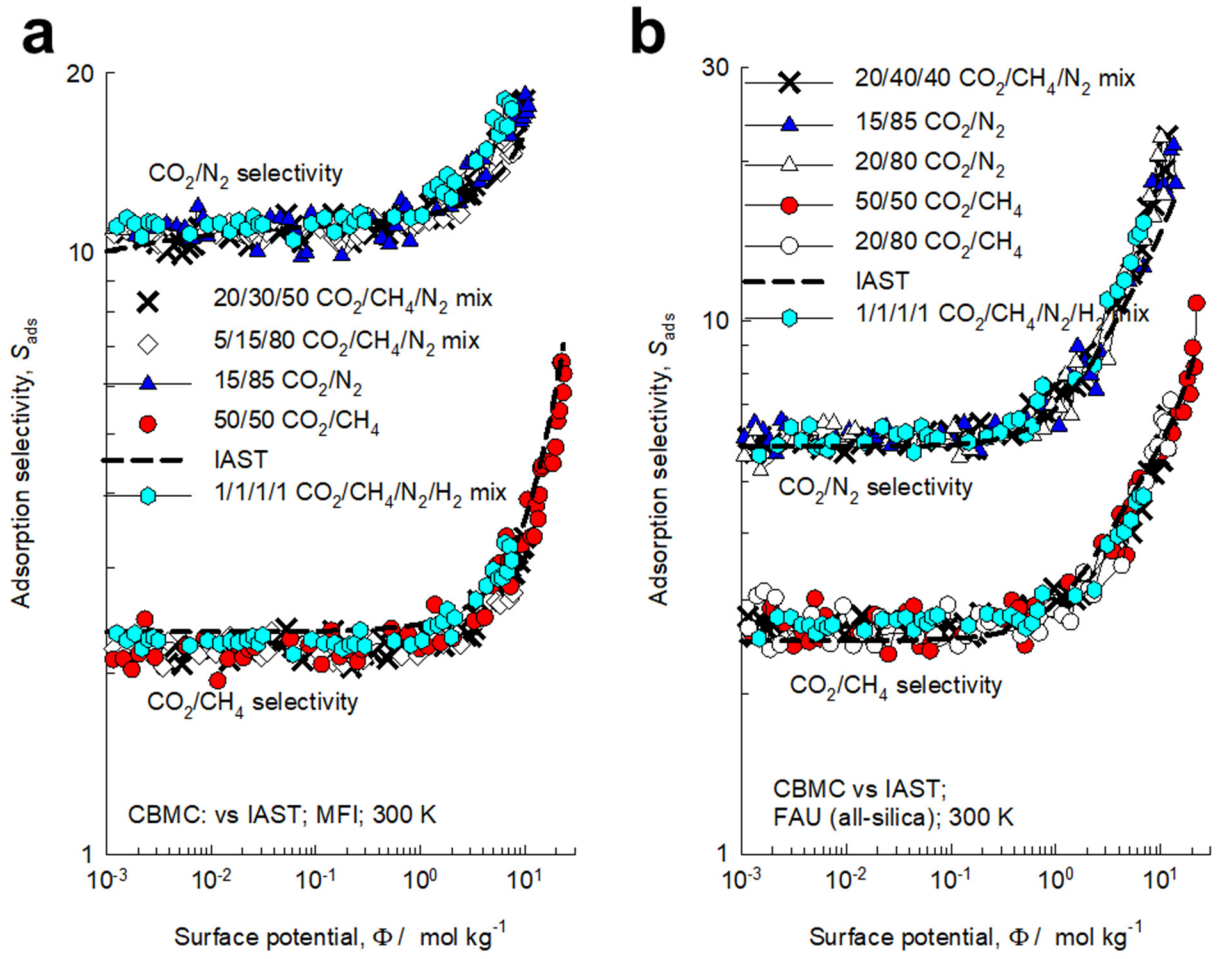

Figure S22. (a, b) CBMC simulations of CO_2/CH_4, and CO_2/N_2 adsorption selectivities, S_{ads}, in (a) MFI, (b) FAU zeolites at 300 K, plotted as function of the surface potential, Φ. The pair selectivities are determined from CBMC data for binary, ternary, and quaternary mixtures. The dashed lines are IAST estimates of $S_{ads,ij}$.

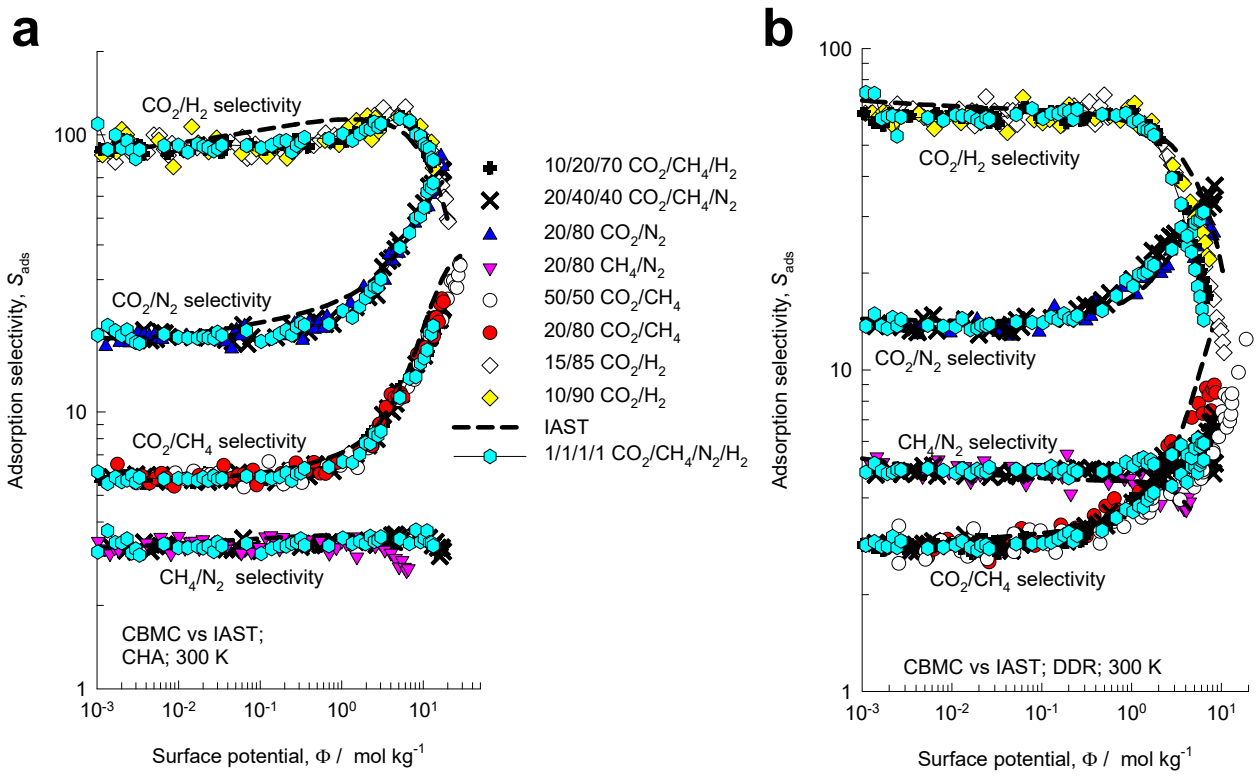

Figure S23. (a, b) CBMC simulations of CO_2/CH_4, CO_2/H_2, CO_2/N_2, and CH_4/N_2 adsorption selectivities, S_{ads}, in (a) CHA, and (b) DDR zeolites at 300 K, plotted as function of the surface potential, Φ. The pair selectivities are determined from CBMC data for binary, ternary, and quaternary mixtures. The dashed lines are IAST estimates of S_{ads}.

5 The Real Adsorbed Solution Theory (RAST)

To account for non-ideality effects in mixture adsorption, we introduce activity coefficients γ_i into eEq (S5) [26]

$$f_i = P_i^0 x_i \gamma_i \tag{S32}$$

Following the approaches of Myers, Talu, and Siperstein[28, 29, 38] we model the excess Gibbs free energy for binary mixture adsorption as follows

$$\frac{G^{excess}}{RT} = x_1 \ln(\gamma_1) + x_2 \ln(\gamma_2) \tag{S33}$$

For calculation of the total mixture loading $q_t = q_1 + q_2$ we need to replace eq (S12) by

$$\frac{1}{q_t} = \frac{x_1}{q_1^0(P_1^0)} + \frac{x_2}{q_2^0(P_2^0)} + \left(\frac{1}{q_t}\right)^{excess} \tag{S34}$$

The excess reciprocal loading for the mixture can be related to the partial derivative of the Gibbs free energy with respect to the surface potential at constant composition

$$\left(\frac{1}{q_t}\right)^{excess} = \left.\frac{\partial\left(\frac{G^{excess}}{RT}\right)}{\partial\Phi}\right|_{T,x} \tag{S35}$$

5.1 Margules model for activity coefficients

The Margules model for activity coefficients in binary liquid mixtures needs to be modified to include the influence of pore occupancy on the activity coefficients

$$\begin{aligned} \ln(\gamma_1) &= x_2^2\left(A_{12} + 2\left(A_{21} - A_{12}\right)x_1\right)\theta \\ \ln(\gamma_2) &= x_1^2\left(A_{21} + 2\left(A_{12} - A_{21}\right)x_2\right)\theta \end{aligned} \tag{S36}$$

The introduction of the multiplier θ will ensure that the activity coefficients tend to unity at vanishingly small pore occupancies $\gamma_i \to 1; \quad \theta \to 0$. In view of eq (S29)

$$\begin{aligned} \ln(\gamma_1) &= x_2^2\left(A_{12} + 2\left(A_{21} - A_{12}\right)x_1\right)\left(1 - \exp\left(-\frac{\Phi}{q_{sat,mix}}\right)\right) \\ \ln(\gamma_2) &= x_1^2\left(A_{21} + 2\left(A_{12} - A_{21}\right)x_2\right)\left(1 - \exp\left(-\frac{\Phi}{q_{sat,mix}}\right)\right) \end{aligned} \tag{S37}$$

where the saturation capacity of the mixture $q_{sat,mix}$ is calculated using eq (S30):

$$q_{sat,mix} = \frac{1}{\frac{x_1}{q_{1,sat}} + \frac{x_2}{q_{2,sat}}}; \quad q_{i,sat} = q_{i,A,sat} + q_{i,B,sat}; \quad i = 1,2.$$

The Margules coefficients A_{12}, A_{21} may assume either positive or negative values.

In our implementation of the RAST in this work, we adopt a somewhat simplified approach by introducing a constant C that is essentially the inverse of the saturation capacity of the mixture, $C = 1/q_{sat,mix}$, but assumed to be independent of the composition of the adsorbed phase mixture. The Margules model we use in the RAST calculations is

$$\begin{aligned} \ln(\gamma_1) &= x_2^2\left(A_{12} + 2\left(A_{21} - A_{12}\right)x_1\right)\left(1 - \exp\left(-C\Phi\right)\right) \\ \ln(\gamma_2) &= x_1^2\left(A_{21} + 2\left(A_{12} - A_{21}\right)x_2\right)\left(1 - \exp\left(-C\Phi\right)\right) \end{aligned} \tag{S38}$$

In eq (S38) C is a constant with the units kg mol^{-1}. The introduction of $\left(1 - \exp\left(-C\Phi\right)\right)$ imparts the correct limiting behaviors $\Phi \to 0; \quad \theta \to 0; \quad \gamma_i \to 1$ for the activity coefficients in the Henry regime, $f_t \to 0; \quad \Phi \to 0$, as the pore occupancy tends to vanishingly small values. As pore saturation conditions are approached, this correction factor tends to unity $\left(1 - \exp\left(-C\Phi\right)\right) \to 1$. The choice of $A_{12} = A_{21} = 0$ in eq (S38), yields unity values for the activity coefficients. We note, in passing, that this correction factor $\left(1 - \exp\left(-C\Phi\right)\right)$ is often ignored in the RAST implementations in some published works.[39-42]

From eq (S29), we note that the expression for the fractional pore occupancy is $\theta = 1 - \exp\left(-\frac{\Phi}{q_{sat,mix}}\right)$.

We should therefore expect that the factor C may well be identified with the inverse of the saturation capacity of the mixture $q_{sat,mix} = \frac{1}{\frac{x_1}{q_{1,sat}} + \frac{x_2}{q_{2,sat}}}$. One approach is to estimate C by assuming $C = \frac{x_1}{q_{1,sat}} + \frac{x_2}{q_{2,sat}}$, assuming, say, $x_1 = x_2 = 0.5$.

As an example, let consider the adsorption of water(1)/ethanol(2) mixtures in CHA zeolite at 300 K. The Dual-site Langmuir-Freundlich isotherm fit parameters are specified in Table S4. The saturation capacity of water (1) $q_{1,sat} = q_{1,A,sat} + q_{1,B,sat}$ =16.8 + 4.6 = 21.4 mol kg^{-1}. The saturation capacity of ethanol (2) $q_{2,sat} = q_{2,A,sat} + q_{2,B,sat}$ =2.5 + 2.9 = 5.4 mol kg^{-1}. The estimated value of C for adsorbed phase compositions, $x_1 = x_2 = 0.5$ is $C = \frac{x_1}{q_{1,sat}} + \frac{x_2}{q_{2,sat}}$ = 0.116 kg mol^{-1}. The value of C obtained by fitting the entire set of three different CBMC campaigns for water(1)/ethanol(2) mixture adsorption in CHA zeolite at 300 K is 0.131 kg mol^{-1}, remarkably close to the value of 0.116 kg mol^{-1} estimated from the saturation capacities.

The experimental data of Sakuth et al.[43, 44] for toluene(1)/1-propanol(2) mixture adsorption in DAY-13 (dealuminated Y zeolite, with FAU topology) at T = 298.15 K and two different total pressures of 0.36 kPa, and 1.06 kPa are presented below.

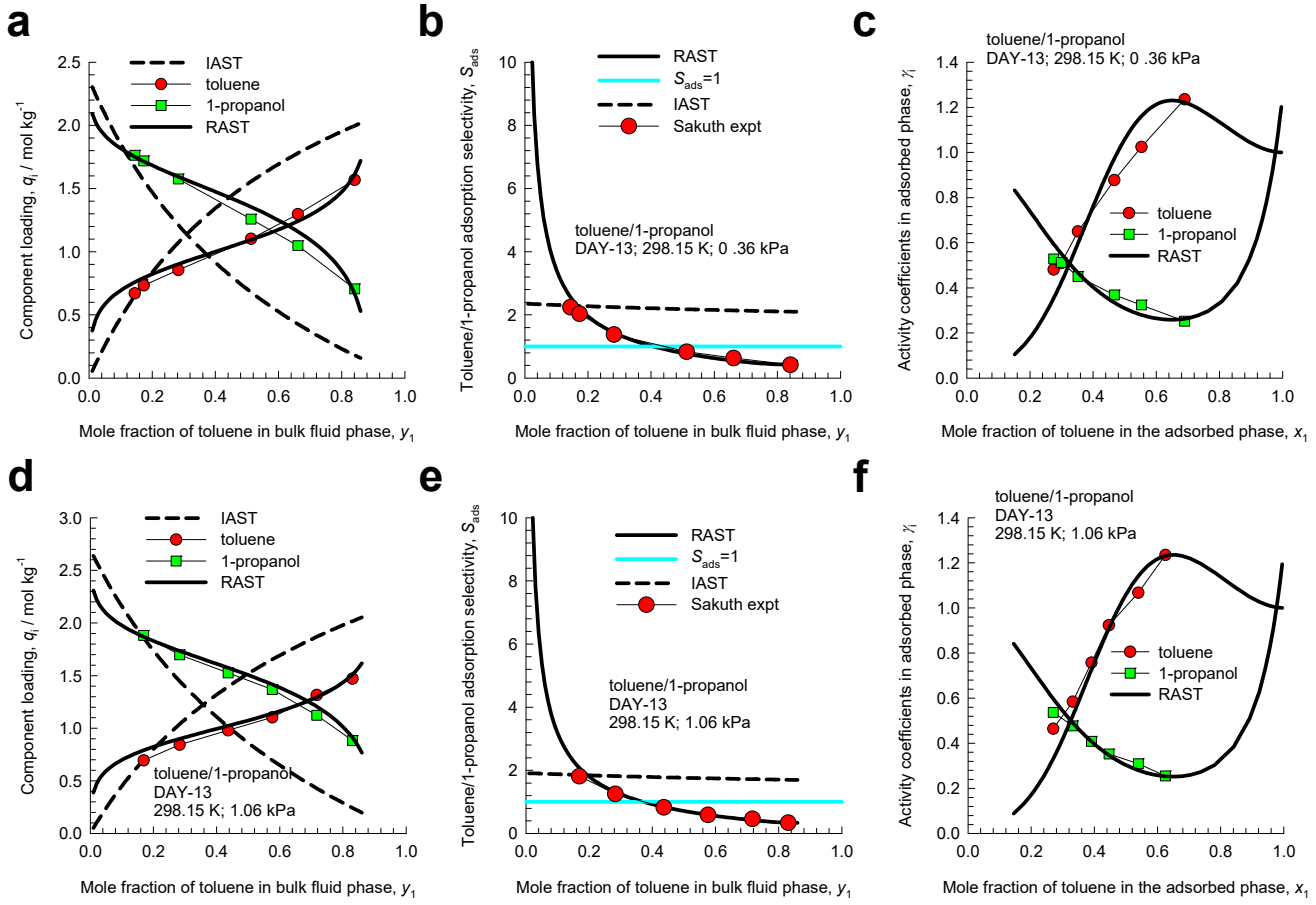

The IAST calculations anticipate that the selectivity is in favor of toluene for the entire range of bulk fluid phase compositions. The experimental data, on the other hand, displays selectivity reversal in favor of 1-propanol for bulk fluid phase compositions $y_1 > 0.4$. The IAST does not anticipate the reversal in the toluene/1-propanol selectivity with increased mole fraction of the aromatic in the bulk fluid mixture.

The unary isotherm data are provided in Table S13. The saturation capacity of toluene (1) $q_{1,sat}$ = 2.26 mol kg^{-1}. The saturation capacity of 1-propanol (2) $q_{2,sat}$ = 3.26 mol kg^{-1}. The estimated value of C for adsorbed phase compositions, $x_1 = x_2 = 0.5$ is $C = \frac{x_1}{q_{1,sat}} + \frac{x_2}{q_{2,sat}} = 0.375$ kg mol^{-1}. The RAST calculations of the component loadings, selectivity and activity coefficients are obtained by the choice of the Margules parameters: $C = 0.375; A_{12} = -4.818; A_{21} = 0.232$. The fitted parameter values are obtained by minimizing the sum of squares of the deviations between the experimentally determined activity coefficients

$\gamma_{1,\exp t} = \dfrac{f_1}{P_1^0 x_{1,\exp t}}; \gamma_{2,\exp t} = \dfrac{f_2}{P_2^0 x_{2,\exp t}}$, from the RAST calculations using eq (S38). The excellent match between experiments and RAST Margules model is a testament to the validity of the calculations of C using $C = \dfrac{x_1}{q_{1,sat}} + \dfrac{x_2}{q_{2,sat}}$.

For calculation of the total mixture loading $q_t = q_1 + q_2$ we need to replace eq (S12) by

$$\frac{1}{q_t} = \frac{x_1}{q_1^0(P_1^0)} + \frac{x_2}{q_2^0(P_2^0)} + x_1 x_2 \left[A_{12} x_2 + A_{21} x_1\right] C \exp\left(-C\Phi\right) \tag{S39}$$

With the introduction of activity coefficients, the expression for the adsorption selectivity for binary mixtures is

$$S_{ads} = \frac{q_1/q_2}{y_1/y_2} = \frac{q_1/y_1}{q_2/y_2} = \frac{x_1/f_1}{x_2/f_2} = \frac{P_2^0 \gamma_2}{P_1^0 \gamma_1} \tag{S40}$$

Since the activity coefficients are composition dependent, the adsorption selectivity is also composition dependent, and S_{ads} is not uniquely related to the surface potential, Φ. Siperstein and Myers[29] report experimental data for adsorption of CO_2(1)/C_3H_8(2) mixtures in NaX zeolite at 293 K. The adsorption selectivity, S_{ads}, plotted as a function of the surface potential, Φ, does not exhibit a unique dependence as anticipated by the IAST, indicated by the dashed lines in (a) below.

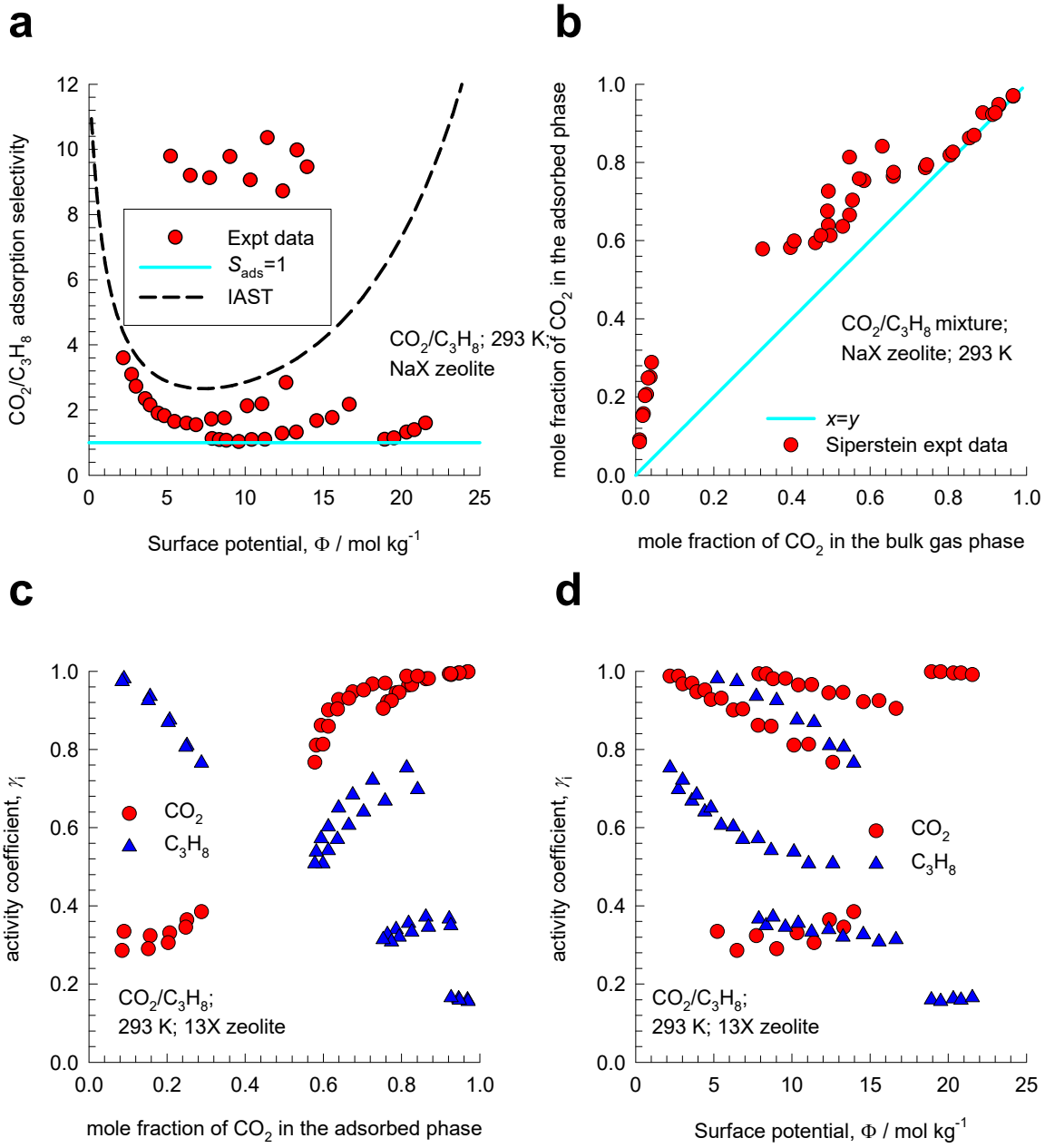

In (b), the adsorbed phase mole fraction of $CO_2(1)$, x_1, is plotted as function of mole fraction of $CO_2(1)$ in the bulk gas phase mixture, y_1. It is noteworthy that at high mole fractions of $CO_2(1)$ in the bulk gas phase mixture, y_1, there is a tendency towards adsorption azeotropy, i.e. $x_1 = y_1$. The analysis of azeotropic adsorption and the rationalization of the Siperstein experiments are provided by Krishna and van Baten.[30] The activity coefficients of $CO_2(1)$, and $C_3H_8(2)$ mixtures in NaX zeolite at 293 K are functions of both

adsorbed phase compositions, and the surface potential; see (c) and (d). Particularly noteworthy is that $\Phi \to 0; \quad \theta \to 0; \quad \gamma_i \to 1.$

To underscore the fact that mixture compositions influence the water/alcohol adsorption selectivity, Figure S50a,b present CBMC simulations of the water(1)/methanol(2) selectivities, S_{ads}, for binary equimolar $(f_1 = f_2)$ water(1)/methanol(2) and ternary equimolar $(f_1 = f_2 = f_3)$ water(1)/methanol(2)/ethanol(3) mixture adsorption in (a) CHA , and (b) DDR zeolites at 300 K. The selectivities are plotted as function of the surface potential Φ. The dashed lines are the IAST calculations. For the same value of the surface potential, that is a proxy for the pore occupancy, the water(1)/methanol(2) selectivity, S_{ads}, is higher for the ternary mixture for which the water composition in the bulk fluid mixture $y_1 = f_1/f_t = 1/3$ is lower than for the binary mixture for $y_1 = f_1/f_t = 1/2$. The IAST (indicated by the dashed line) anticipates the selectivity to be independent of bulk fluid phase composition. Another point to note is that the selectivity becomes in favor of water at sufficiently higher pore occupancies, i.e. increasing surface potential Φ.

Figure S51a,b,c present CBMC simulations of the water(1)/ethanol(2) selectivities, S_{ads}, for binary equimolar $(f_1 = f_2)$ water(1)/ethanol(2) and ternary equimolar $(f_1 = f_2 = f_3)$ water(1)/methanol(2)/ethanol(3) mixture adsorption in (a) CHA , (b) DDR , and (c) ZIF-8 at 300 K. We note that the water(1)/ethanol(2) selectivities, S_{ads}, in the equimolar $(f_1 = f_2 = f_3)$ ternary water(1)/ methanol(2)/ethanol(3) mixtures are higher than those for the corresponding binary equimolar $(f_1 = f_2)$ water(1)/ethanol(2) mixtures, when compared at the same value of the surface potential Φ. This is because for the ternary mixture the water composition in the bulk fluid mixture $y_1 = f_1/f_t = 1/3$ is lower than for the binary mixture for $y_1 = f_1/f_t = 1/2$.

Also included in Figure S51a,b for (a) CHA, and (b) DDR zeolites are the selectivities for binary equimolar 5/95 water(1)/ethanol(2) mixtures $(f_1/f_2 = 5/95)$. At any specified value of the surface

potential, Φ, the CBMC data shows that the hierarchy of selectivities is (1) binary mixture with $y_1 = 0.05$, (2) ternary mixture with $y_1 = 0.33333$, and (3) binary mixture with $y_1 = 0.5$. The selectivity becomes increasingly in favor of water as the water composition is lowered.

Watch also the presentations titled **Dependence of Adsorption Selectivity on Mixture Composition, Hydrogen Bonding Influences on Adsorption, How Reliable is the IAST?, The Real Adsorbed Solution Theory, Co-operative Mixture Adsorption in Zeolites & MOFs, The Spreading Pressure Concept for Microporous Membranes**

on YouTube https://www.youtube.com/@rajamanikrishna250/videos

6 CBMC vs IAST for mixture adsorption

6.1 CBMC simulation campaigns

A comprehensive campaign of CBMC simulations for adsorption of binary mixtures (water/methanol, water/ethanol) was undertaken to investigate hydrogen bonding effects in all-silica zeolites (CHA, DDR, FAU, LTA), and ZIF-8. Two types of mixture adsorption campaigns were conducted.

Campaign A. The bulk fluid phase composition held constant at $y_1 = y_2 = 0.5$, and the bulk fluid phase fugacity $f_t = f_1 + f_2$ was varied over a wide range from the Henry regime of adsorption, , to pore saturation conditions, typically $\Phi > 30$. For CHA, DDR and ZIF-8 additional campaigns for water/methanol, and water/ethanol mixtures were conducted in which the bulk fluid phase composition held constant at $y_1 = 0.05$. For CHA and DDR, CBMC campaigns were also conducted for equimolar $\left(f_1 = f_2 = f_3\right)$ ternary water(1)/ methanol(2)/ethanol(3) mixtures for which the total bulk fugacity $f_t = f_1 + f_2 + f_3$ is varied from the Henry regime of adsorption, $f_t \to 0;\ \Phi \to 0$, to pore saturation conditions, typically $\Phi > 30$.

Campaign B. The bulk fluid phase fugacity $f_t = f_1 + f_2$ was held at a constant value of 10 kPa, and the bulk fluid phase mixture composition y_1 was varied $0 < y_1 < 1$.

Each CBMC simulation data point, for specified partial fugacities in the bulk fluid phase, f_1, f_2, yields the component loadings, $q_{1,CBMC}; q_{2,CBMC}$, and the total mixture loading $q_{t,CBMC} = q_{1,CBMC} + q_{2,CBMC}$.

For each guest/host combination, CBMC simulations of the unary isotherms of the constituent guest molecules were also carried out.

Also included in the simulations are re-analyses of CBMC data for polar guests in CuBTC as published in our earlier works.[21, 22]

6.2 Vapor-liquid phase transitions

To understand the CBMC simulations, it is essential to gain an understanding of vapor/liquid phase transitions for water/methanol and water/ethanol mixtures. Figure S24a,b presents calculations of the molar densities of the vapor and liquid phases as a function of the bulk fluid phase fugacity; these calculations are based on the Peng-Robinson equation of state. For fugacities below about 10 kPa, the bulk fluid is predominantly in the vapor phase. For fugacities in excess of 1 MPa, the bulk fluid phase is predominantly in the liquid phase. For fugacities in the range of 10 kPa to 1 MPa, both vapor and liquid phases co-exist.

Figure S24c,d present CBMC simulations of the fractional pore occupancies for 50/50 water/methanol and 50/50 water/ethanol mixtures as function of the bulk fluid phase fugacity, f_i for adsorption in CHA, DDR, FAU, LTA, and ZIF-8. It is interesting to note that for bulk fluid phase fugacities exceeding 10 kPa, the fractional pore occupancies approach unity. Comparison with Figure S24a,b leads us to conclude that the fractional pore occupancies are close to unity when the bulk fluid phase consists of a mixture of vapor and liquid phases.

In our molecular simulations, we consistently use fugacities rather than "pressures" when plotting unary adsorption isotherms. This is vital because the bulk fluid phase could be either in the vapor phase, in the liquid phase, or a mixture of vapor and liquid phases.

6.3 Unary isotherm fit parameters

The CBMC simulated unary isotherms were fitted with the dual-site Langmuir-Freundlich model, eq (S9). The unary isotherm for water adsorption in ZIF-8, and CuBTC required the use of the 3-site Langmuir-Freundlich model to capture the steep isotherm characteristics.

The unary isotherm fit parameters are provided in the following set of Tables.

Unary isotherms for water, methanol, and ethanol in CHA: Table S4

Unary isotherms for water, methanol, and ethanol in DDR: Table S5

Unary isotherms for water, methanol, and ethanol in ZIF-8: Table S6

Unary isotherms for water, methanol, and ethanol in all-silica FAU: Table S7

Unary isotherms for water, methanol, and ethanol in all-silica LTA: Table S8

Unary isotherms for water, methanol, and ethanol in CuBTC: Table S9, Table S10.

Figure S25a,b,c,d,e,f compare CBMC simulations of unary isotherms in different microporous host materials, (a) CHA, (b) DDR, (c) ZIF-8, (d) FAU (all-silica), (e) LTA (all-silica), and (f) CuBTC, plotted as function of the fugacity of guest species in the bulk fluid phase. Molecular clustering

Due to cluster formation, the unary isotherms of water displays step-like characteristics.[45-51] Besides the RDF data on O-H distances (see our earlier works[8, 24]), another way of underscoring the manifestation of molecular clustering is by examining the unary isotherms and calculating the inverse thermodynamic factor, $1/\Gamma_i$, defined by

$$\frac{1}{\Gamma_i} \equiv \frac{\partial \ln q_i}{\partial \ln f_i} = \frac{f_i}{q_i}\frac{\partial q_i}{\partial f_i} \tag{S41}$$

Figure S26 presents the calculations of $1/\Gamma_i$ for adsorption of water, methanol, and ethanol in in different microporous host materials, (a) CHA, (b) DDR, (c) ZIF-8, (d) FAU (all-silica), (e) LTA (all-silica), and (f) CuBTC, plotted as function of the fugacity of guest species in the bulk fluid phase. The values of $1/\Gamma_i$ exceeds unity for a range of fugacities f_i. Values of $1/\Gamma_i \geq 1$ is indicative of molecular clustering. For all hosts, the molecular clustering is strongest for water, than for methanol and ethanol.

Figure S27 compares the calculations of $1/\Gamma_i$ for water, methanol, and ethanol in in different microporous host materials, plotted as function of (a) fugacity in the bulk fluid phase, f (b) surface potential, Φ , and (c) pore occupancy, θ, determined from eq (S29).

In order to fully appreciate the import of $1/\Gamma_i > 1$, it is best to first discuss the simple case for which the adsorbed phase loading follows a single-site Langmuir isotherm $q_i = q_{i,sat}\frac{b_i f_i}{1+b_i f_i}$, whose differentiation yields

$$\frac{1}{\Gamma_i} = 1 - \theta_i \tag{S42}$$

where we define the fractional *occupancies* $\theta_i \equiv q_i / q_{i,sat}$. Eq (S42) shows that inverse thermodynamic factor, $1/\Gamma_i$, equals the fractional *vacancy* $\theta_V = \left(1 - \theta_i\right)$ for a Langmuirian adsorbed phase, and in this case we must have $1/\Gamma_i \leq 1$. When there is no molecular clustering, increasing the loading, q_i, by increasing the bulk fluid phase fugacity, leads to *linear decrease* in the number of vacant sites. For the data presented in Figure S26 and Figure S27 there is an *increase* in the number of vacant sites with increasing pore occupancy; this deserves further explanation. We present below the arguments as put forward by Krishna and van Baten;[52] the explanation is based on a simple lattice model for unary adsorption. Consider a square lattice containing 64 adsorption sites; see Figure S28a. If the molecular species, 10 in total, are all unclustered the fractional occupancy is $\theta_i = 10/64$, and the fractional vacancy $\theta_V = 1 - \theta_i = 54/64$. A molecular cluster can be regarded as a *k*-mer. A *k*-mer occupies the same vacant adsorbed site as a normal, unclustered, molecule. As a consequence, it is feasible to have the fractional vacancy exceed unity, i.e. $1/\Gamma_i > 1$. If clustering occurs and dimers are formed, the same number of molecules will occupy only 5 sites; see Figure S28b. The remaining number of vacant locations, 59, are still available for occupation. Even if no more clusters are formed, this would imply that a total of 10 + 59 = 69 molecules could be accommodated on the square lattice. Cluster formation has the effect of increasing the fractional vacancy θ_V to the value of 69/64. Therefore, it is possible to have $1/\Gamma_i > 1$ when clustering occurs. Equivalently, the occurrence of $1/\Gamma_i > 1$ can be taken to imply the existence of molecular clusters.

Experimental confirmation of clustering effects is provided by the experimental data of Tsotsalas et al.[53] for adsorption of methanol in CuBTC.

6.4 Water/ethanol adsorption in LTA-4A zeolite

The use of LTA-4A zeolite in a hybrid distillation-membrane separation scheme is illustrated in Figure S29. Distillation can produce ethanol with a purity close to 95 wt% owing to azeotrope formation. For

obtaining say 99.5% pure ethanol, we need to feed the obtained 95 wt% ethanol product to an azeotropic distillation column with an entrainer such as benzene, or cyclohexane. A better alternative, avoiding the use of entrainers, is to adopt a hybrid scheme (see Figure S29) in which the 95 wt% ethanol top product is fed to a hydrophilic LTA-4A zeolite membrane pervaporation unit. LTA-4A zeolite has 11 Å sized cages separated by windows with an aperture of 4 Å. Water has a significantly higher diffusivity than ethanol due to the narrow window aperture; diffusion selectivity strongly favors water. The desired 99.5% pure ethanol product is recovered as retentate. The water-rich permeate is returned to the distillation column. We now analyze water/ethanol separations with LTA-4A membranes.

Watch also the presentations titled **Water/Ethanol Distillation and Membrane Pervaporation Hybrid, Hydrogen Bonding Influences on Adsorption, Co-operative Mixture Adsorption in Zeolites & MOFs**

on YouTube https://www.youtube.com/@rajamanikrishna250/videos

Figure S30a,b shows the experimental data of Pera-Titus et al.[54] for pure component isotherms for water and ethanol in LTA-4A zeolite at a variety of temperatures. The data sets were fitted with good accuracy using the dual-site Langmuir-Freundlich model, where we distinguish two distinct adsorption sites A and B:

$$q = \frac{q_{sat,A} b_A p^{\nu A}}{1 + b_A p^{\nu A}} + \frac{q_{sat,B} b_B p^{\nu B}}{1 + b_B p^{\nu B}} \tag{S43}$$

In eq (S43), the Langmuir-Freundlich parameters b_A, b_B are both temperature dependent

$$b_A = b_{A0} \exp\left(\frac{E_A}{RT}\right); \quad b_b = b_{B0} \exp\left(\frac{E_B}{RT}\right) \tag{S44}$$

In eq (S44), E_A, E_B are the energy parameters associated with sites A, and B, respectively. The unary fit parameters are specified in Table S12.

Pera-Titus et al.[54] also published experimental data of the component loadings for water/ethanol mixtures at 2.1 kPa and 333 K as a function of mole fraction of water in the bulk vapor phase; see Figure S31.The experimental data on component loadings in the mixture were used to determine the Wilson

parameters, as reported in Table S12.. The continuous solid lines in Figure S31.are RAST estimations, that offer improvement over the corresponding IAST estimations (shown by the dashed lines).

6.5 Summary of CBMC simulation data

The CBMC simulated data are presented graphically in the following set of Figures.

Figure S32: Water/methanol mixture in CHA

Figure S33:Water/ethanol mixture in CHA

Figure S34: Water/methanol mixture in DDR

Figure S35:Water/ethanol mixture in DDR

Figure S36: Water/methanol mixture in ZIF-8

Figure S37: Water/ethanol mixture in ZIF-8

Figure S38: Water/methanol mixture in all-silica FAU

Figure S39: Water/ethanol mixture in all-silica FAU

Figure S40: Water/2-propanol mixture in all-silica FAU

Figure S41: Water/methanol mixture in all-silica LTA

Figure S42: Water/ethanol mixture in all-silica LTA

For each of the guest/host combinations:

(a) provides CBMC simulation data on component loadings, q_1, q_2, for Campaign A (y_1= 0.5), plotted as a function of the bulk fluid phase fugacity $f_t = f_1 + f_2$. The dashed lines are IAST estimates of component loadings.

(b) provides CBMC simulation data on component loadings q_1, q_2, for Campaign B (f_t = 10 kPa), plotted as a function of the bulk fluid phase mixture composition y_1. The dashed lines are IAST estimates of component loadings.

(c) provides adsorption selectivities S_{ads} (left *y*-axis) and pore occupancies (right *y*-axis) for Campaign B (f_t = 10 kPa), plotted as a function of the bulk fluid phase mixture composition y_1

(d) compares CBMC data for S_{ads}, for both Campaigns A and B plotted as function of pore occupancy, θ. The pore occupancy is calculated using eq (S29)

(e) compares CBMC data for mole fraction in the adsorbed phase, x_1, for both Campaigns A and B plotted as function of pore occupancy, θ. The pore occupancy is calculated using eq (S29).

(f) provides the selectivities for adsorption, S_{ads}, diffusion, S_{diff}, and permeation, $S_{perm} = S_{ads} \times S_{diff}$, for Campaign B ($f_t$ = 10 kPa), plotted as a function of the bulk fluid phase mixture composition y_1. The values of diffusion, S_{diff} are based on MD simulation data for self-diffusivities, $D_{i,self}$, determined for binary water(1)/methanol(2), and water(1)/ethanol(2) mixtures. The MD data are presented in the following Figures.

CHA: Figure S62

DDR: Figure S63

LTA (all silica) Figure S64

FAU (all silica) Figure S65

The values of the diffusion selectivities thus determined are multiplied by the adsorption selectivity $S_{ads} = \frac{q_1/q_2}{f_1/f_2}$ for mixture adsorption at total fugacity of 10 kPa in order to determine the permeation selectivities $S_{perm} = S_{ads} \times S_{diff}$.

Figure S43 summarize the CBMC simulation data on adsorption selectivities, S_{ads}, for equimolar water/methanol, water/methanol, methanol/ethanol, water/1-propanol, water/benzene, methanol/benzene, ethanol/benzene, and acetone/benzene mixtures (Campaign A, y_1= 0.5) in CuBTC at 298 K. The selectivity data are plotted as a function of the surface potential Φ. The dashed lines are the IAST estimates. The continuous solid blue lines are the RAST calculations, with fitted Margules parameters specified in Table S11. For all eight mixtures, the selectivity reverses in favor of the smaller molecules as pore saturation conditions are approached, i.e. $\Phi >> 100$; the selectivity reversals are due to entropy effects.[55, 56]

Figure S44a,b compares the adsorption selectivity, S_{ads}, for (a) water/methanol, and (b) water/ethanol mixtures, determined from CBMC simulations (Campaign A, y_1= 0.5), in various host materials, using the bulk fugacity f_t as *x*-axis. Figure S44c,d present the adsorption selectivity data for Campaign A using the surface potential Φ as *x*-axis. The IAST estimates of the adsorption selectivity are plotted in Figure S45a,b. The IAST predicts the selectivity reversals in favor of water with increase in the total bulk fluid phase fugacity.

Figure S46a,b,c,d compares water/alcohol adsorption selectivity, S_{ads}, and pore occupancies, θ, and for (a, c) water/methanol, and (b, d) water/ethanol mixtures, determined from CBMC simulations (Campaign B, f_t = 10 kPa), in various host materials. The *x*-axis is the mole fraction of water(1) in the bulk fluid phase mixture, y_1. We note that for all guest/host combinations, the selectivity is in favor of water at low values of y_1. When the bulk composition becomes increasing rich in the alcohol, the selectivity tends to reverse in favor of the alcohol.

6.6 List of Tables for CBMC vs IAST for mixture adsorption

Table S4. Dual-site Langmuir-Freundlich parameters for pure component water, methanol, and ethanol in CHA zeolite at 300 K. The fit parameters are based on the CBMC simulations of pure component isotherms presented in earlier work.[57]

$$q = \frac{q_{sat,A} b_A p^{\nu A}}{1 + b_A p^{\nu A}} + \frac{q_{sat,B} b_B p^{\nu B}}{1 + b_B p^{\nu B}}$$

	Site A			Site B		
	$\frac{q_{A,sat}}{\text{mol kg}^{-1}}$	$\frac{b_A}{\text{Pa}^{-\nu_A}}$	ν_A	$\frac{q_{B,sat}}{\text{mol kg}^{-1}}$	$\frac{b_B}{\text{Pa}^{-\nu_B}}$	ν_B
water	16.8	3.031E-54	15.6	4.6	2.218E-05	1
methanol	3.7	4.281E-11	3.37	3.7	4.545E-04	1
ethanol	2.5	8.578E-06	1.07	2.9	3.505E-03	1.1

Fitted Margules non-ideality parameters for binary mixture adsorption in CHA at 300 K. The fits are based on combining CBMC Campaigns A and B for each mixture.

	C / kg mol^{-1}	A_{12}	A_{21}
water/methanol	1.617	-6.337	-0.798
water/ethanol	0.131	-7.717	-4.083

Table S5. Dual-site Langmuir-Freundlich parameters for pure component water, methanol, and ethanol at 300 K in all-silica DDR zeolite. The fit parameters are based on the CBMC simulations of pure component isotherms presented in earlier work.[8]

	Site A			Site B		
	$\frac{q_{A,sat}}{\text{mol kg}^{-1}}$	$\frac{b_A}{\text{Pa}^{-\nu_A}}$	ν_A	$\frac{q_{B,sat}}{\text{mol kg}^{-1}}$	$\frac{b_B}{\text{Pa}^{-\nu_B}}$	ν_B
water	6.45	2.776E-17	4.3	2.4	1.300E-05	1.06
methanol	1.7	1.186E-04	1.3	1.7	6.055E-04	0.78
ethanol	1.6	9.962E-03	0.88	1.2	9.160E-05	0.66

Fitted Margules non-ideality parameters for binary mixture adsorption in DDR at 300 K. The fits are based on combining CBMC Campaigns A and B for each mixture.

	C / kg mol^{-1}	A_{12}	A_{21}
water/methanol	5.696	-1.937	-1.489
water/ethanol	0.293	-7.066	-1.858

Table S6. 3-site and 2-site Langmuir-Freundlich parameters for adsorption of water, methanol, and ethanol at 300 K in ZIF-8.

	Site A			Site B			Site C		
	$\frac{q_{A,sat}}{\text{mol kg}^{-1}}$	$\frac{b_A}{\text{Pa}^{-\nu_A}}$	ν_A	$\frac{q_{B,sat}}{\text{mol kg}^{-1}}$	$\frac{b_B}{\text{Pa}^{-\nu_B}}$	ν_B	$\frac{q_{c,sat}}{\text{mol kg}^{-1}}$	$\frac{b_c}{\text{Pa}^{-\nu_C}}$	ν_C
water	22	2.08×10^{-57}	13.4	3.6	1.327×10^{-15}	3.2	69	1.20×10^{-7}	1

Adsorbate	Site A			Site B		
	$\frac{q_{A,sat}}{\text{mol kg}^{-1}}$	$\frac{b_A}{\text{Pa}^{-\nu_A}}$	ν_A	$\frac{q_{B,sat}}{\text{mol kg}^{-1}}$	$\frac{b_B}{\text{Pa}^{-\nu_B}}$	ν_B
methanol	8.4	1.736E-43	12	3.9	2.920E-05	1
ethanol	4.6	2.372E-12	3.9	2.3	2.396E-04	1

Fitted Margules non-ideality parameters for binary mixture adsorption in ZIF-8 at 300 K. The fits are based on combining CBMC Campaigns A and B for each mixture.

	C / kg mol^{-1}	A_{12}	A_{21}
water/methanol	1.335	-1.190	-0.949
water/ethanol	1.246	-2.515	-0.688

Table S7. Dual-site Langmuir-Freundlich parameters for adsorption of water, methanol, and ethanol at 300 K in all-silica FAU zeolite. The fit parameters are based on the CBMC simulations of pure component isotherms presented in earlier work.[8]

Adsorbate	Site A			Site B		
	$\frac{q_{A,sat}}{\text{mol kg}^{-1}}$	$\frac{b_A}{\text{Pa}^{-\nu_A}}$	ν_A	$\frac{q_{B,sat}}{\text{mol kg}^{-1}}$	$\frac{b_B}{\text{Pa}^{-\nu_B}}$	ν_B
water	15.4	1.850E-121	32.6	7.4	3.555E-05	1
methanol	3.4	6.362E-16	4.6	5.8	1.679E-04	1
ethanol	2.5	3.189E-13	4.9	2.9	1.000E-03	1.05
2-propanol	1.5	3.906E-06	2.45	2.8	1.951E-03	1

Fitted Margules non-ideality parameters for binary mixture adsorption in all-silica FAU at 300 K. The fits are based on combining CBMC Campaigns A and B for each mixture.

	C / kg mol^{-1}	A_{12}	A_{21}
water/methanol	1.041	-1.287	-2.764
water/ethanol	0.152	-1.241	-1.790

Table S8. Dual-site Langmuir-Freundlich parameters for adsorption of water, methanol, and ethanol at 300 K in all-silica LTA zeolite. The fit parameters are based on the CBMC simulations of pure component isotherms presented in earlier work.[8]

Adsorbate	Site A			Site B		
	$\frac{q_{A,sat}}{\text{mol kg}^{-1}}$	$\frac{b_A}{\text{Pa}^{-\nu_A}}$	ν_A	$\frac{q_{B,sat}}{\text{mol kg}^{-1}}$	$\frac{b_B}{\text{Pa}^{-\nu_B}}$	ν_B
water	18	3.35353E-68	16	4.3	8.75008E-07	1.06
methanol	6.2	8.07492E-53	14.6	2.4	9.73382E-06	1.09
ethanol	3.6	2.94176E-17	5.4	1.2	0.000111202	1

Fitted Margules non-ideality parameters for binary mixture adsorption in all-silica LTA zeolite at 300 K. The fits are based on combining CBMC Campaigns A and B for each mixture.

	C / kg mol^{-1}	A_{12}	A_{21}
water/methanol	14.355	-0.693	-3.094
water/ethanol	22.657	-1.328	-2.451

Table S9. 3-site Langmuir-Freundlich isotherm fits for adsorption of water in CuBTC at 298 K.

	Site A			Site B			Site C		
	$\frac{q_{A,sat}}{\text{mol kg}^{-1}}$	$\frac{b_A}{\text{Pa}^{-\nu_A}}$	ν_A	$\frac{q_{B,sat}}{\text{mol kg}^{-1}}$	$\frac{b_B}{\text{Pa}^{-\nu_B}}$	ν_B	$\frac{q_{c,sat}}{\text{mol kg}^{-1}}$	$\frac{b_c}{\text{Pa}^{-\nu_C}}$	ν_C
water	22	5.48×10^{-4}	1	22	6.24×10^{-32}	10	10	2.51×10^{-4}	0.6

Table S10. Dual-site Langmuir-Freundlich parameters for adsorption of methanol, ethanol, 1-propanol, acetone, and benzene at 298 K in CuBTC.

Adsorbate	Site A			Site B		
	$\frac{q_{A,sat}}{\text{mol kg}^{-1}}$	$\frac{b_A}{\text{Pa}^{-\nu_A}}$	ν_A	$\frac{q_{B,sat}}{\text{mol kg}^{-1}}$	$\frac{b_B}{\text{Pa}^{-\nu_B}}$	ν_B
methanol	8.4	3.82×10^{-4}	1.03	11.5	9.3×10^{-16}	6.5
ethanol	5	2.29×10^{-3}	0.97	8	6.41×10^{-7}	3.2
1-propanol	8	4.83×10^{-4}	2.7	2	2.07×10^{-2}	0.5
acetone	5	4.83×10^{-17}	7.5	4.9	1.39×10^{-2}	0.7
benzene	4.6	2.76×10^{-6}	3.1	2.1	3.96×10^{-3}	1

Table S11. Fitted Margules non-ideality parameters for binary mixture adsorption in CuBTC at 298 K.

	C / kg mol^{-1}	A_{12}	A_{21}
water/methanol	0.005	-20.565	-10.590
water/ethanol	0.068	-12.427	-5.443
methanol/ethanol	0.002	-12.500	-8.068
water/1-propanol	0.049	-18.882	-6.752
water/benzene	0.002	-144.760	-70.527
methanol/benzene	0.019	-7.821	-13.592
ethanol/benzene	0.019	-10.220	-9.023
acetone/benzene	0.029	-7.791	-5.977

Table S12. Dual-site Langmuir-Freundlich parameters for adsorption of water, and ethanol in LTA-4A zeolite. The isotherm fits are based on the experimental data of Pera-Titus et al.[54]

$$q = \frac{q_{sat,A} b_A p^{\nu A}}{1 + b_A p^{\nu A}} + \frac{q_{sat,B} b_B p^{\nu B}}{1 + b_B p^{\nu B}}; \quad b_A = b_{A0} \exp\left(\frac{E_A}{RT}\right); \quad b_b = b_{B0} \exp\left(\frac{E_B}{RT}\right)$$

	Site A				Site B			
	$\frac{q_{A.sat}}{\text{mol kg}^{-1}}$	$\frac{b_{A,0}}{\text{Pa}^{-\nu_A}}$	$\frac{E_A}{\text{kJ mol}^{-1}}$	ν_A	$\frac{q_{B.sat}}{\text{mol kg}^{-1}}$	$\frac{b_{B,0}}{\text{Pa}^{-\nu_B}}$	$\frac{E_B}{\text{kJ mol}^{-1}}$	ν_B
water	2.1	2.1×10^{-60}	269	7.26	9.7	5.81×10^{-8}	33	0.83
ethanol	1.85	5.24×10^{-13}	43.3	1.9	1.4	2.65×10^{-10}	40	1.7

The fitted Wilson parameters for water/ethanol/LTA-4A using the experimental data of Pera-Titus et al.[54] The units of C are kg mol^{-1}.

	Λ_{12}	Λ_{21}	C / kg mol^{-1}
water/ethanol/LTA-4A	10.3	3.2×10^{-6}	0.036

Table S13. Langmuir-Freundlich fits of the unary isotherms of toluene, and 1-propanol in DAY-13 zeolite at 298 K. The parameters were obtained by fitting the unary isotherm data in Table 1 of Sakuth et al.[43]

	$\frac{q_{sat}}{\text{mol kg}^{-1}}$	$\frac{b}{\text{Pa}^{-\nu}}$	ν
toluene	2.26	0.2585	0.74
1-propanol	3.26	0.09743	0.56

The fitted Margules parameters for toluene/1-propanol mixture adsorption in DAY-13.

	C / kg mol^{-1}	A_{12}	A_{21}
Toluene/1-propanol	0.375	-4.818	0.232

6.7 List of Figures for CBMC vs IAST for mixture adsorption

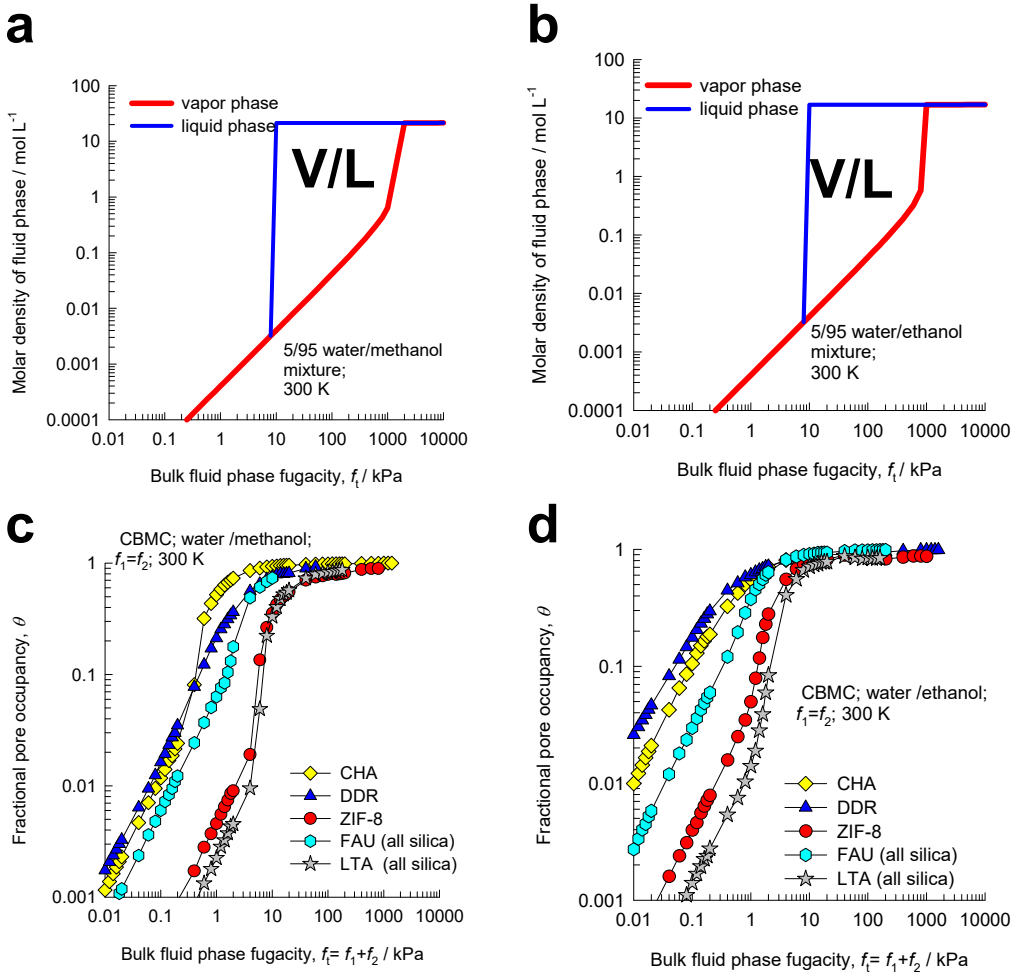

Figure S24. (a, b) Molar densities of the vapor and liquid phases for 5/95 water/methanol and 5/95 water/ethanol mixtures as function of the bulk fluid phase fugacity, f_t. These calculations are based on the Peng-Robinson equation of state. (c, d) CBMC simulations of the fractional pore occupancies for 50/50 water/methanol and 50/50 water/ethanol mixtures as function of the bulk fluid phase fugacity, f_t for adsorption in CHA, DDR, FAU, LTA, and ZIF-8.

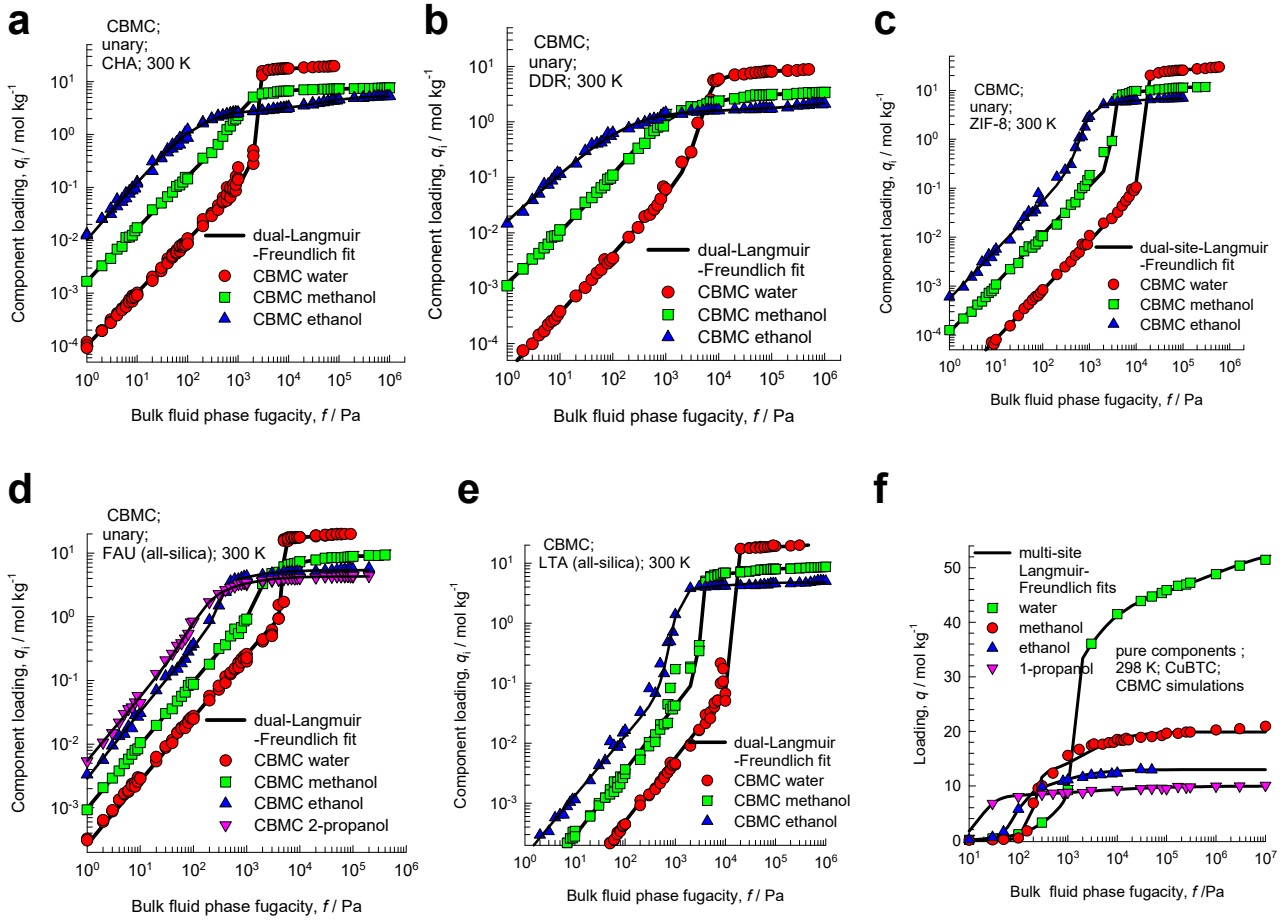

Figure S25. CBMC simulations of unary isotherms in different microporous host materials (a) CHA, (b) DDR, (c) ZIF-8, (d) FAU, (e) LTA, and (f) CuBTC, plotted as function of the fugacity in the bulk fluid phase.

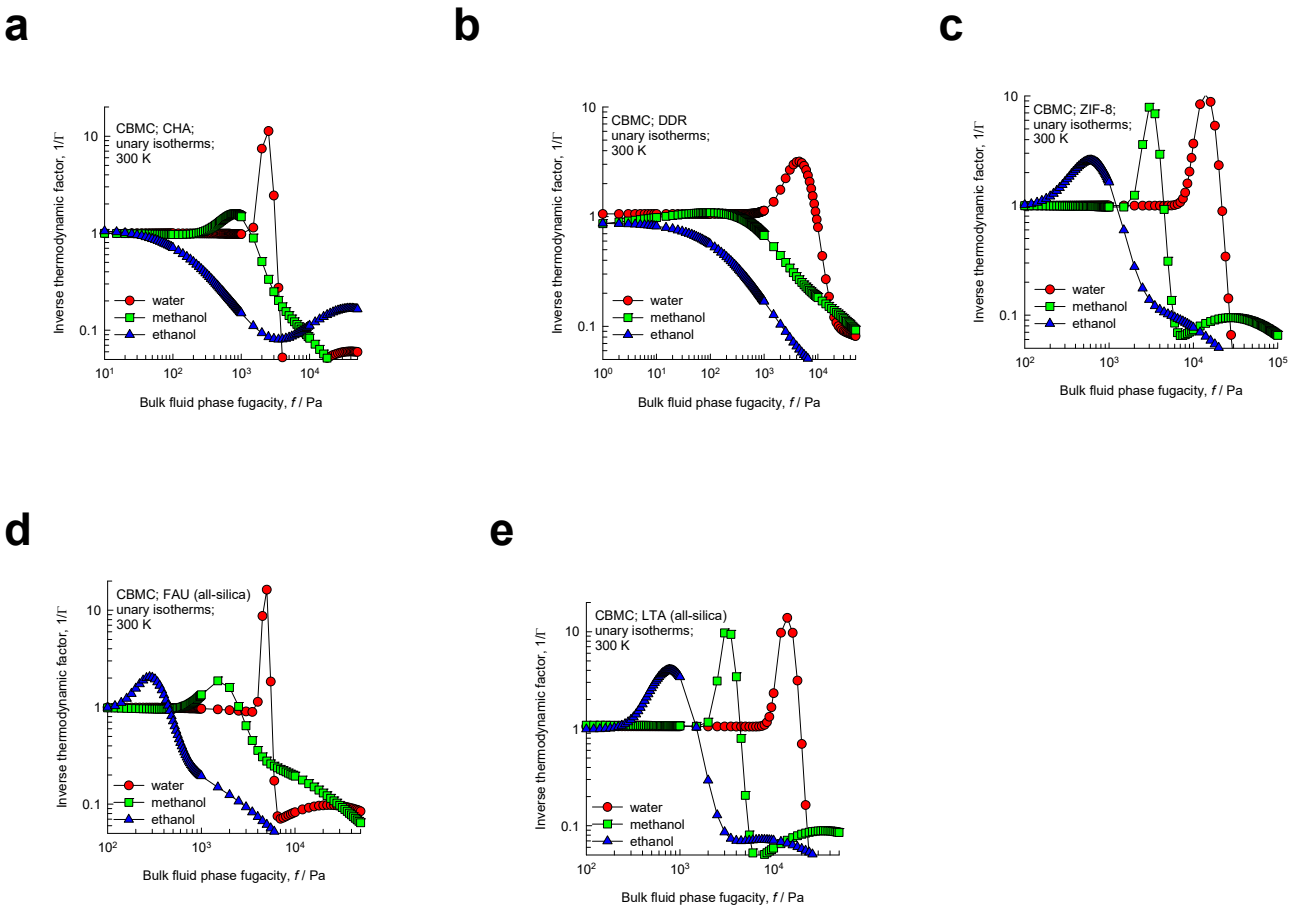

Figure S26. Inverse thermodynamic factors for water, methanol, and ethanol in different microporous host materials (a) CHA, (b) DDR, (c) ZIF-8, (d) FAU, (e) LTA, plotted as function of the fugacity in the bulk fluid phase.

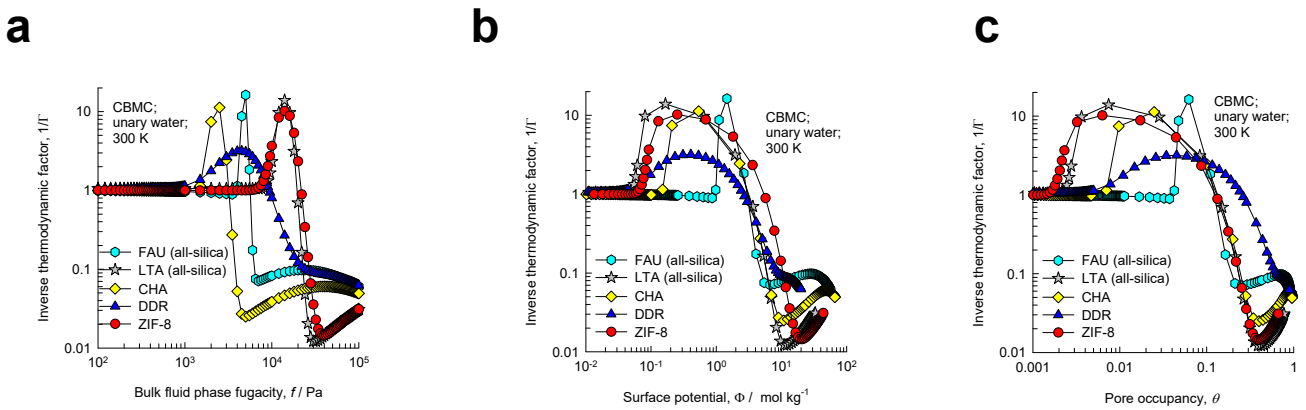

Figure S27. Comparison of the inverse thermodynamic factors for water in different microporous host materials, plotted as function of (a) fugacity in the bulk fluid phase, f (b) surface potential, Φ , and (c) pore occupancy, θ, determined from eq (S29).

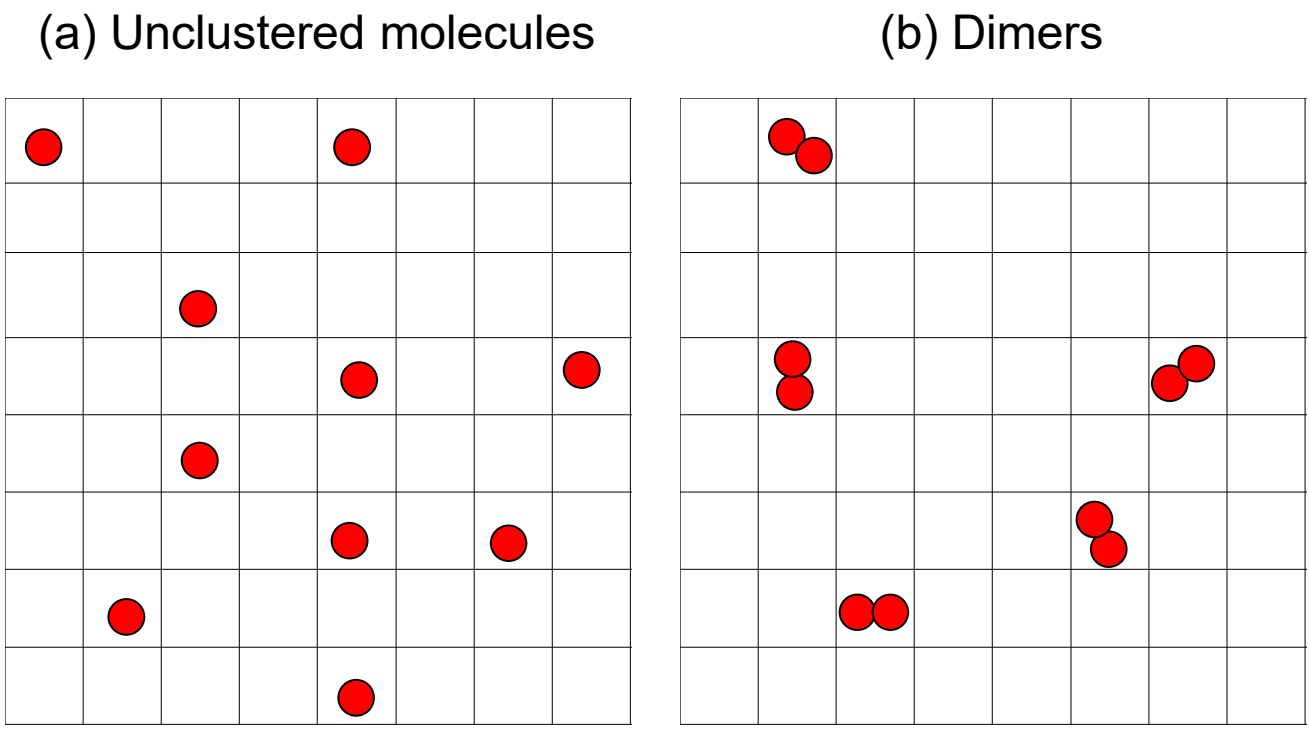

Figure S28. (a) Adsorption of 10 unclustered molecular species on a square lattice containing 64 adsorption sites. (b) Adsorption of dimers.

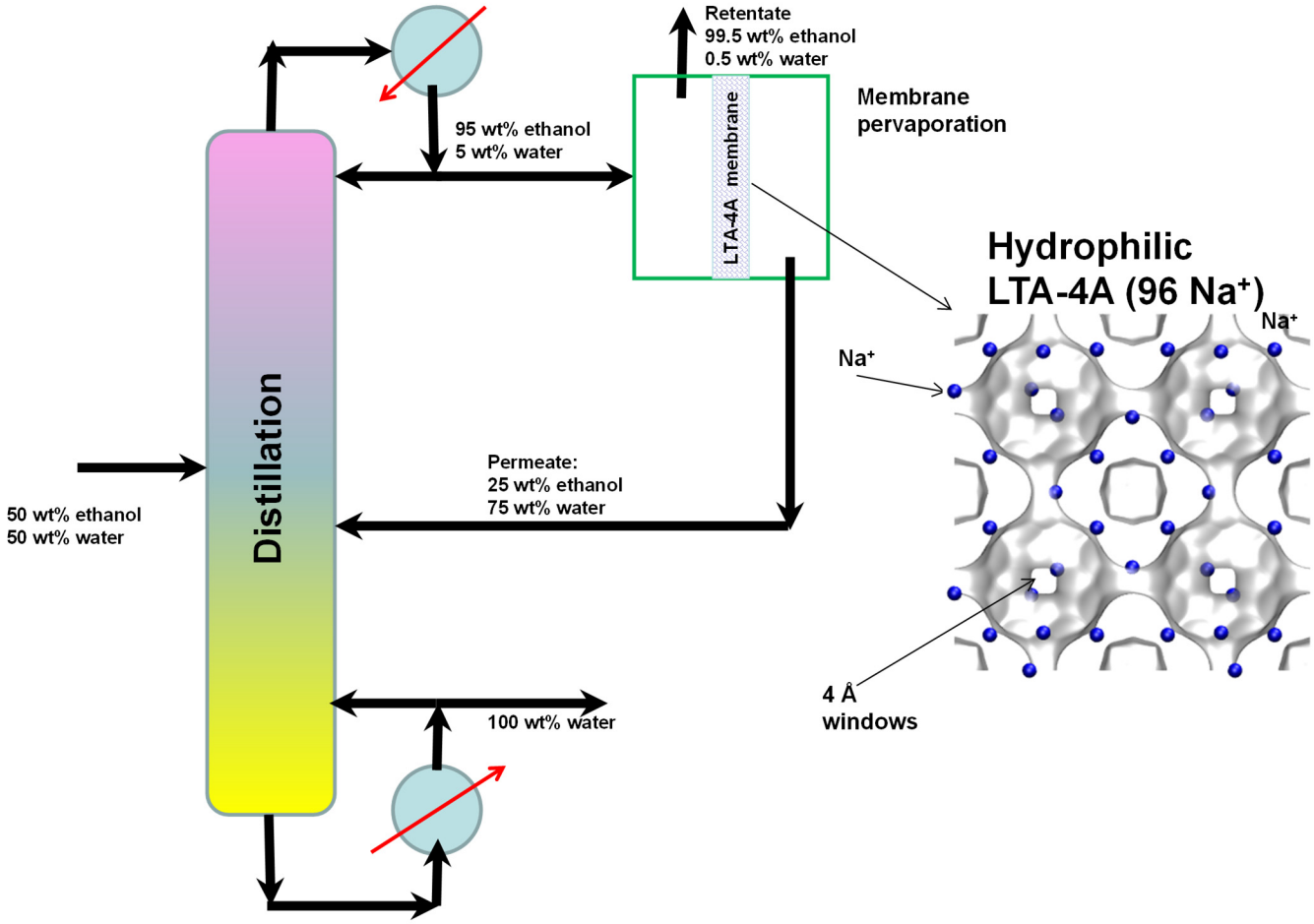

Figure S29. Water permeates preferentially across LTA-4A zeolite membrane used in hybrid scheme for production of 99.5% pure ethanol.

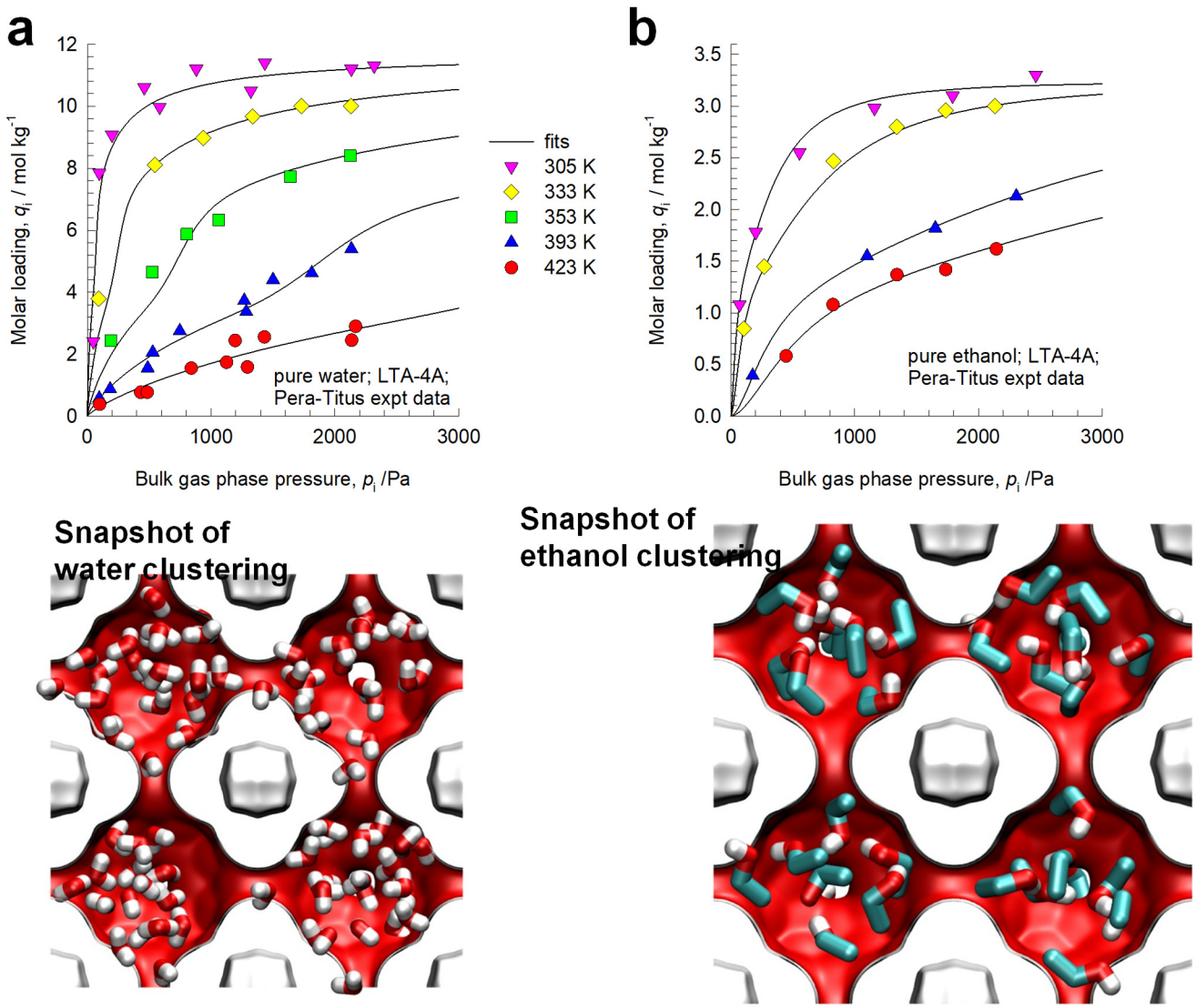

Figure S30. (a, b) Pure component isotherms for (a) water, and (b) ethanol in LTA-4A zeolite. Experimental data of Pera-Titus.[54] The unary isotherm fit parameters are specified in Table S12.

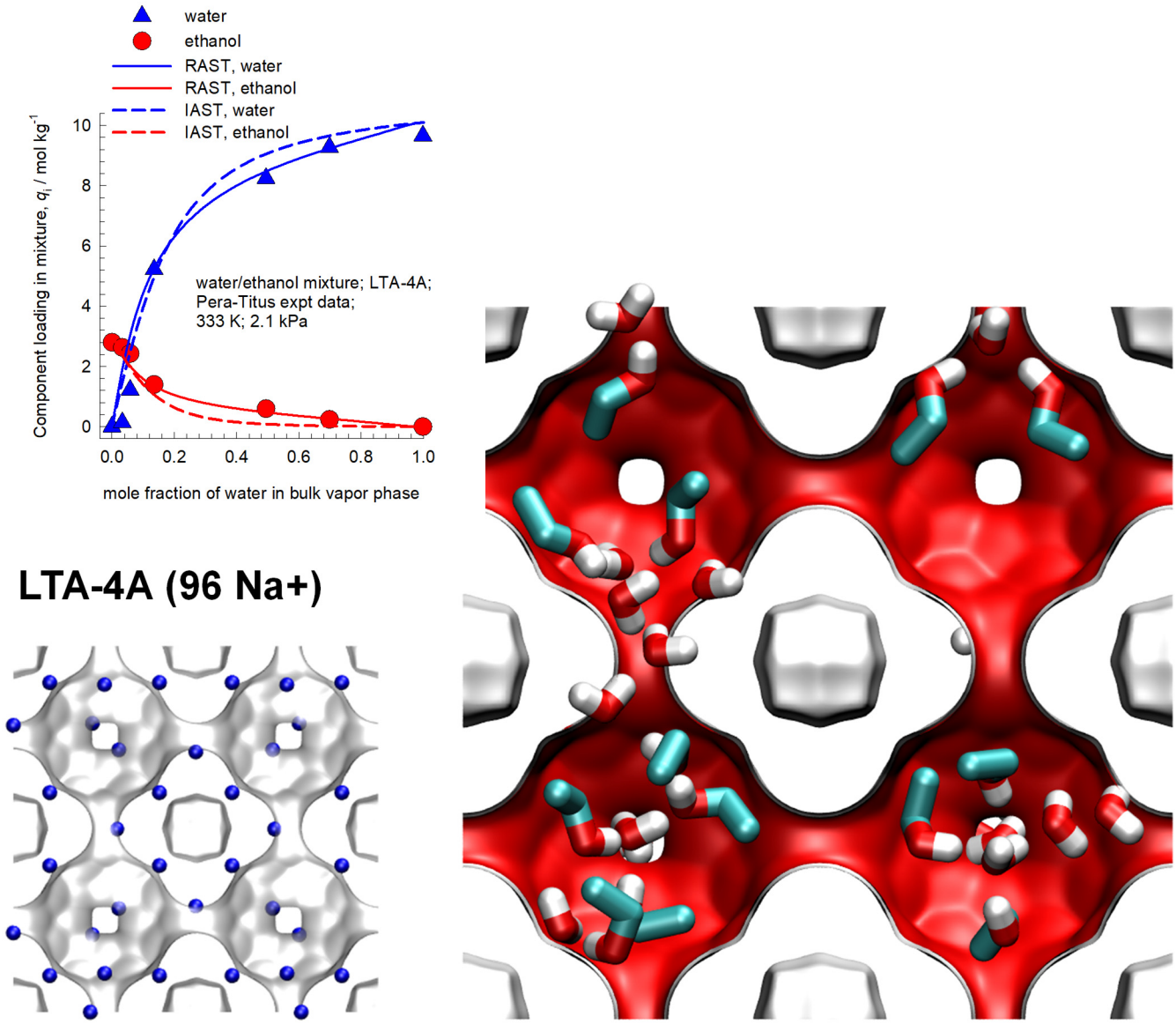

Figure S31. Experimental data of Pera-Titus[54] for component loadings for water and ethanol in LTA-4A zeolite at 2.1 kPa and 333 K as a function of the mole fraction of water in the bulk vapor phase. The dashed lines are IAST estimations. The continuous solid lines are RAST estimations. The unary isotherm fit parameters are specified in Table S12, along with the Wilson parameters.

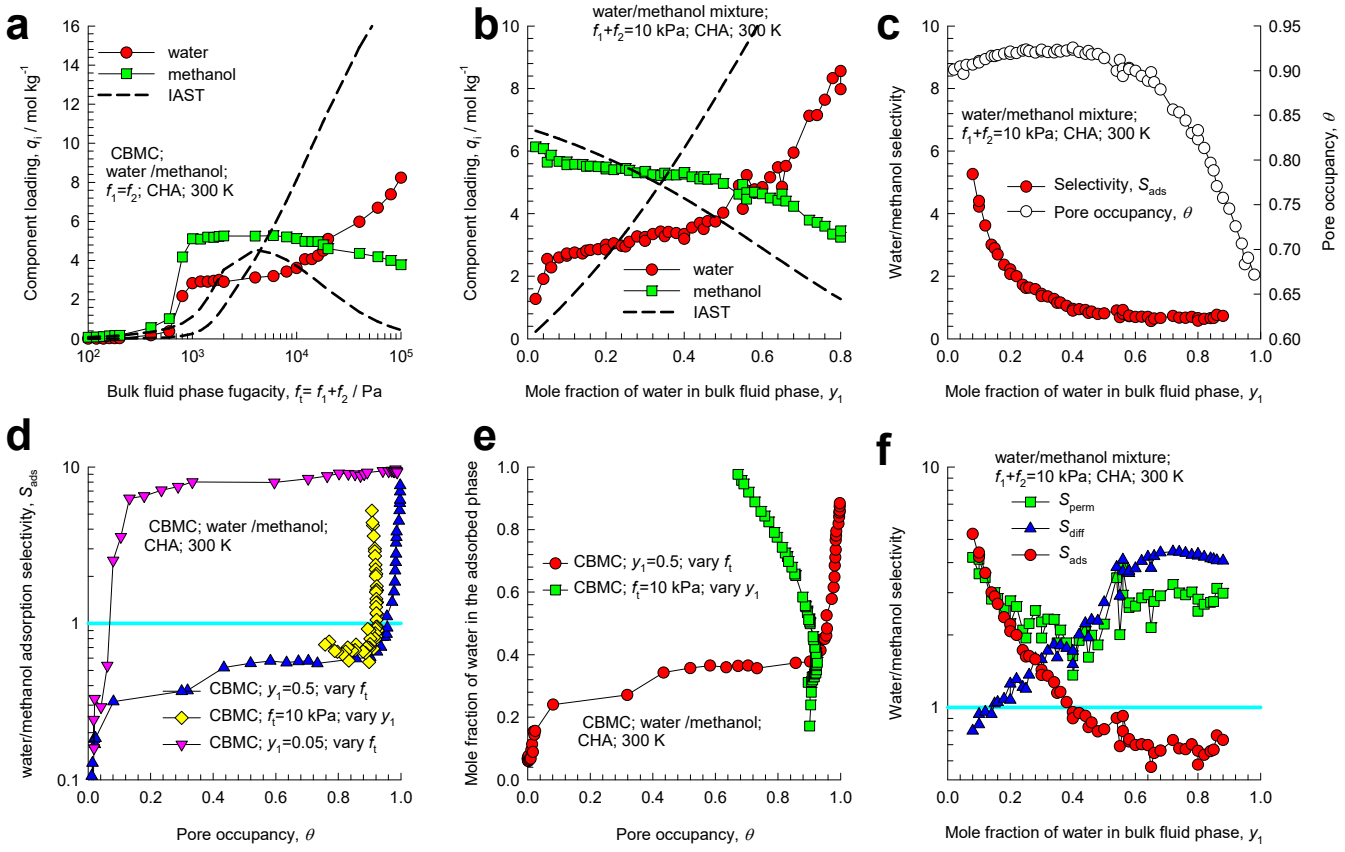

Figure S32. (a) CBMC simulation data on component loadings q_1, q_2 for Campaign A (y_1= 0.5) for water(1)/methanol(2) mixture in CHA at 300 K. (b, c) CBMC simulation data on (b) component loadings q_1, q_2, and (c) adsorption selectivities S_{ads} for Campaign B (f_t = 10 kPa) for water/methanol mixture in CHA at 300 K. (d) CBMC data for S_{ads} in Campaign A and B plotted as function of pore occupancy, θ. (e) CBMC data for mole fraction in the adsorbed phase, x_1, in Campaign A and B plotted as function of pore occupancy, θ. (f) Selectivities $S_{ads}, S_{diff}, S_{perm}$ for Campaign B.

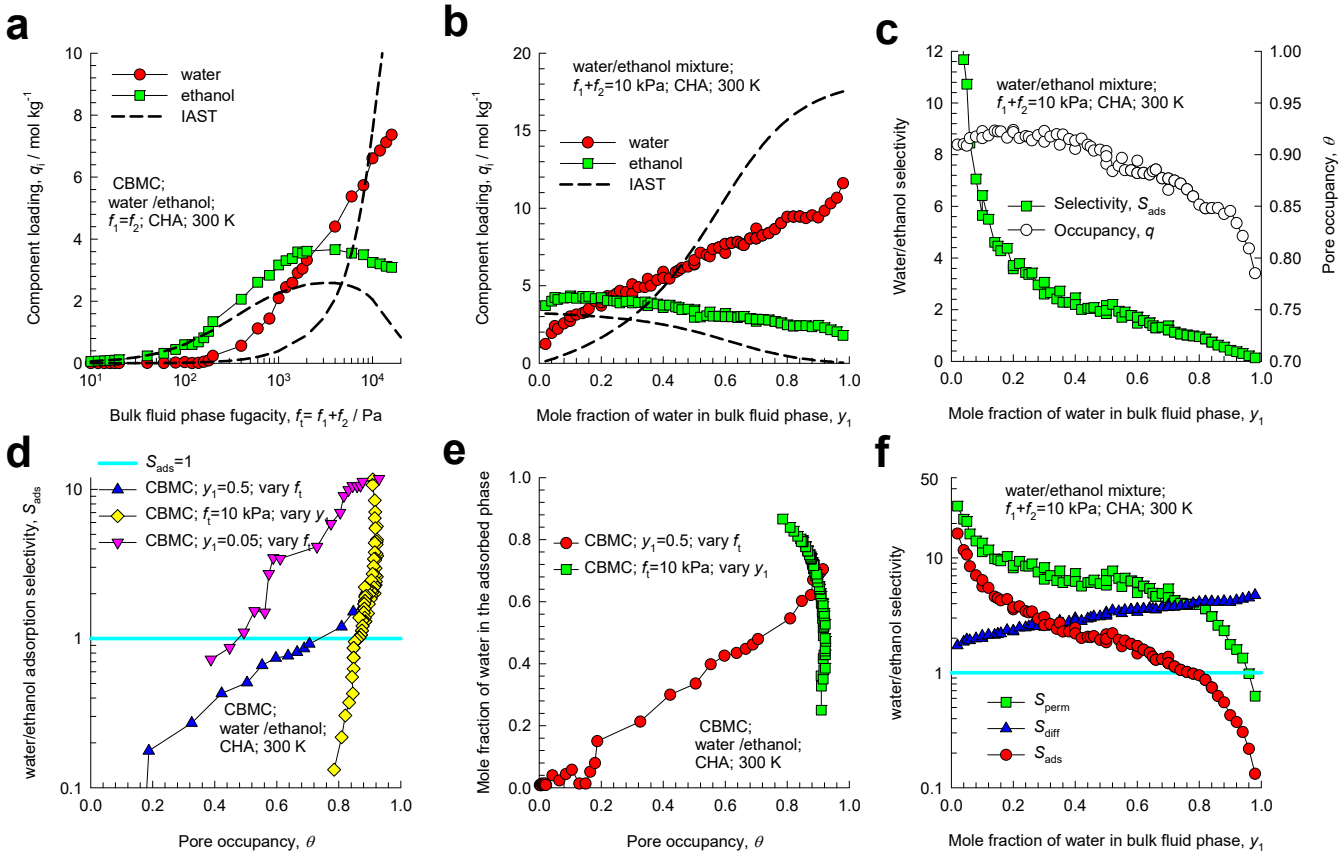

Figure S33. (a) CBMC simulation data on component loadings q_1, q_2 for Campaign A (y_1= 0.5) for water(1)/ethanol(2) mixture in CHA at 300 K. (b, c) CBMC simulation data on (b) component loadings q_1, q_2, and (c) adsorption selectivities S_{ads} for Campaign B (f_t = 10 kPa) for water/methanol mixture in CHA at 300 K. (d) CBMC data for S_{ads} in Campaign A and B plotted as function of pore occupancy, θ. (e) CBMC data for mole fraction in the adsorbed phase, x_1, in Campaign A and B plotted as function of pore occupancy, θ. (f) Selectivities $S_{ads}, S_{diff}, S_{perm}$ for Campaign B.

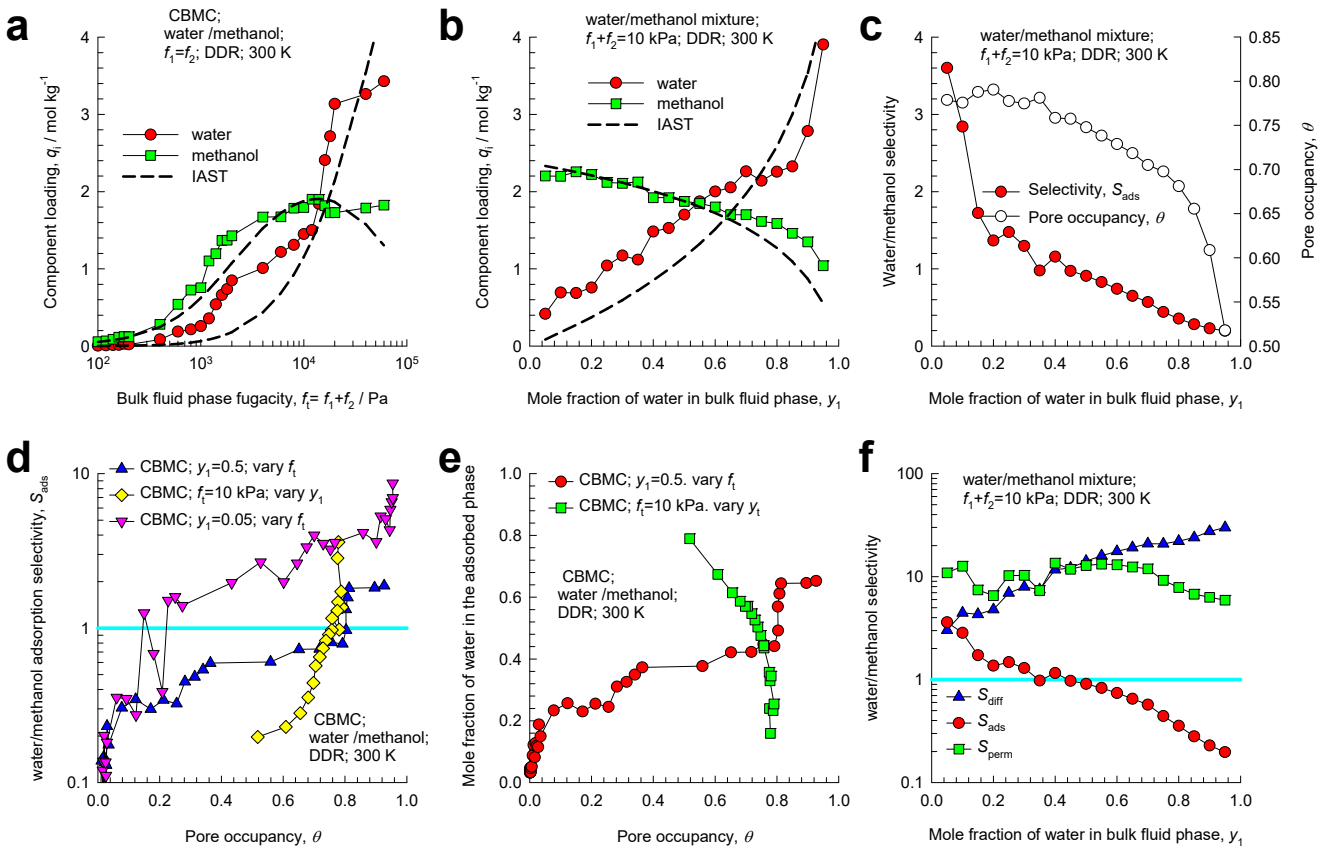

Figure S34. (a) CBMC simulation data on component loadings q_1, q_2 for Campaign A (y_1= 0.5) for water(1)/methanol(2) mixture in DDR at 300 K. (b, c) CBMC simulation data on (b) component loadings q_1, q_2, and (c) adsorption selectivities S_{ads} for Campaign B (f_t = 10 kPa) for water/methanol mixture in CHA at 300 K. (d) CBMC data for S_{ads} in Campaign A and B plotted as function of pore occupancy, θ. (e) CBMC data for mole fraction in the adsorbed phase, x_1, in Campaign A and B plotted as function of pore occupancy, θ. (f) Selectivities $S_{ads}, S_{diff}, S_{perm}$ for Campaign B.

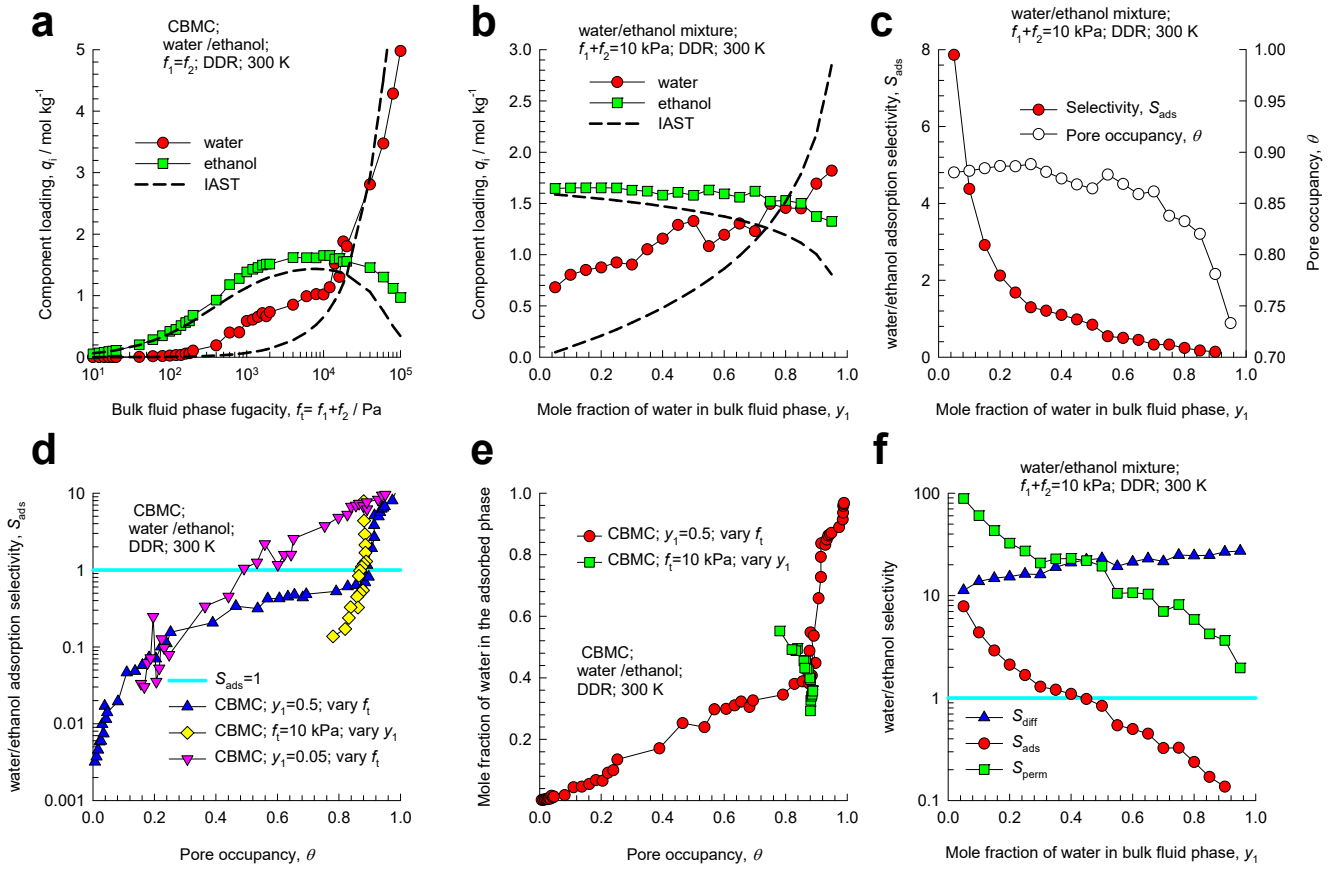

Figure S35. (a) CBMC simulation data on component loading q_1, q_2 for Campaign A (y_1= 0.5) for water(1)/ethanol(2) mixture in DDR at 300 K. (b, c) CBMC simulation data on (b) component loadings q_1, q_2, and (c) adsorption selectivities S_{ads} for Campaign B (f_t = 10 kPa) for water/methanol mixture in CHA at 300 K. (d) CBMC data for S_{ads} in Campaign A and B plotted as function of pore occupancy, θ. (e) CBMC data for mole fraction in the adsorbed phase, x_1, in Campaign A and B plotted as function of pore occupancy, θ. (f) Selectivities $S_{ads}, S_{diff}, S_{perm}$ for Campaign B.

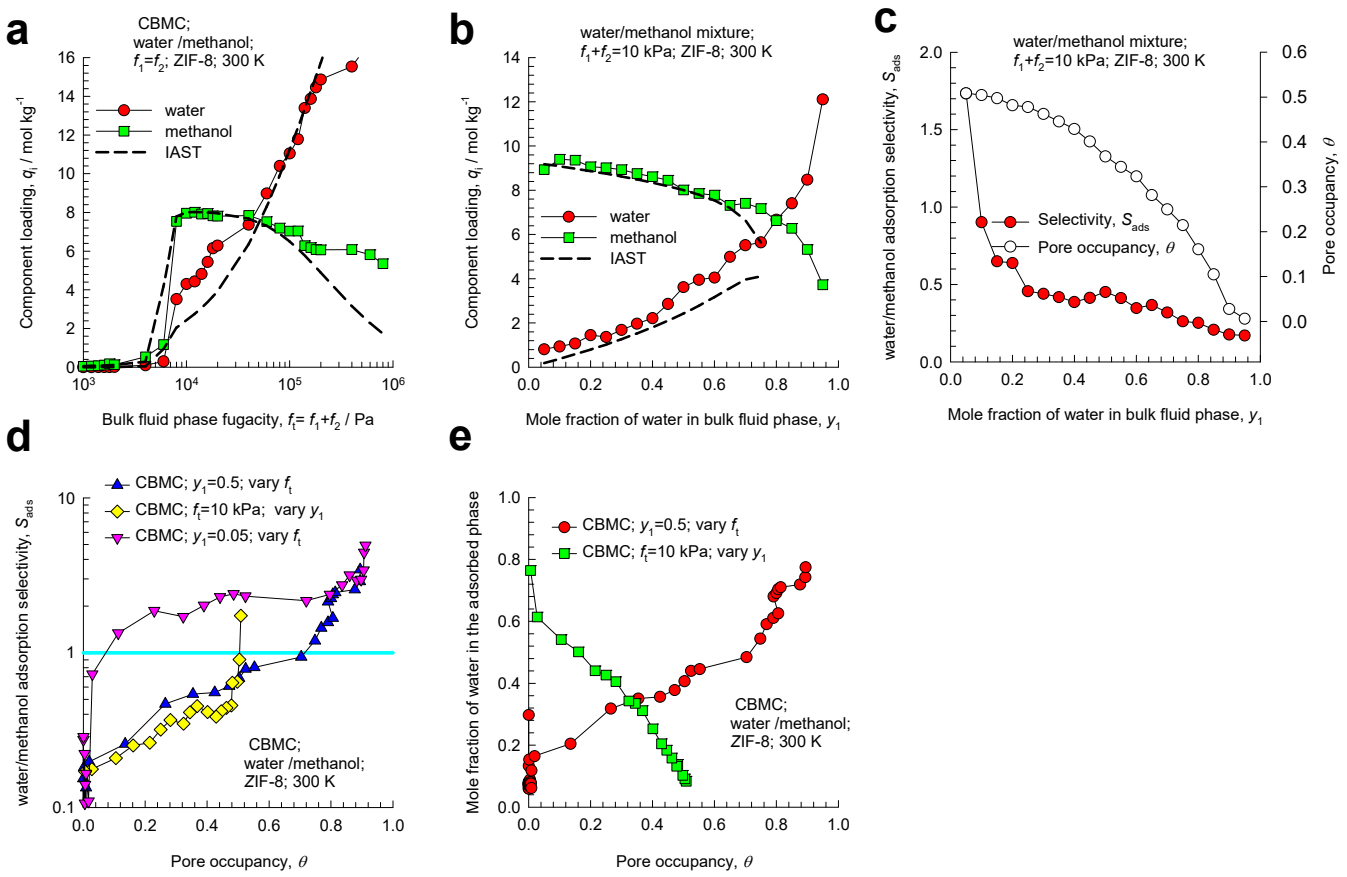

Figure S36. (a) CBMC simulation data on component loadings q_1, q_2 for Campaign A (y_1= 0.5) for water(1)/methanol(2) mixture in ZIF-8 at 300 K. (b, c) CBMC simulation data on (b) component loadings q_1, q_2, and (c) adsorption selectivities S_{ads} for Campaign B (f_t = 10 kPa) for water/methanol mixture in CHA at 300 K. (d) CBMC data for S_{ads} in Campaign A and B plotted as function of pore occupancy, θ. (e) CBMC data for mole fraction in the adsorbed phase, x_1, in Campaign A and B plotted as function of pore occupancy, θ.

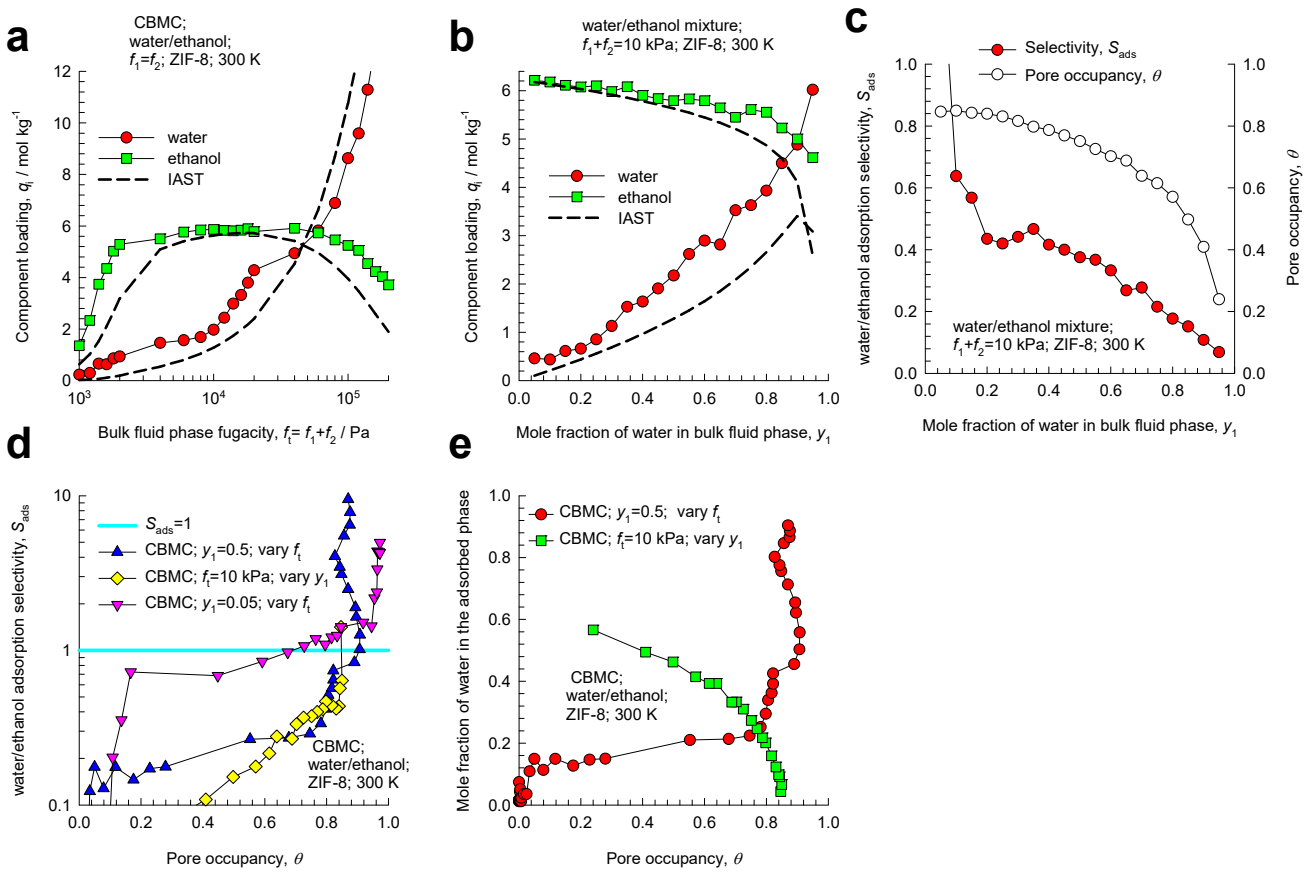

Figure S37. (a) CBMC simulation data on component loadings q_1, q_2 for Campaign A (y_1= 0.5) for water(1)/ethanol(2) mixture in ZIF-8 at 300 K. (b, c) CBMC simulation data on (b) component loadings q_1, q_2, and (c) adsorption selectivities S_{ads} for Campaign B (f_t = 10 kPa) for water/methanol mixture in CHA at 300 K. (d) CBMC data for S_{ads} in Campaign A and B plotted as function of pore occupancy, θ. (e) CBMC data for mole fraction in the adsorbed phase, x_1, in Campaign A and B plotted as function of pore occupancy, θ.

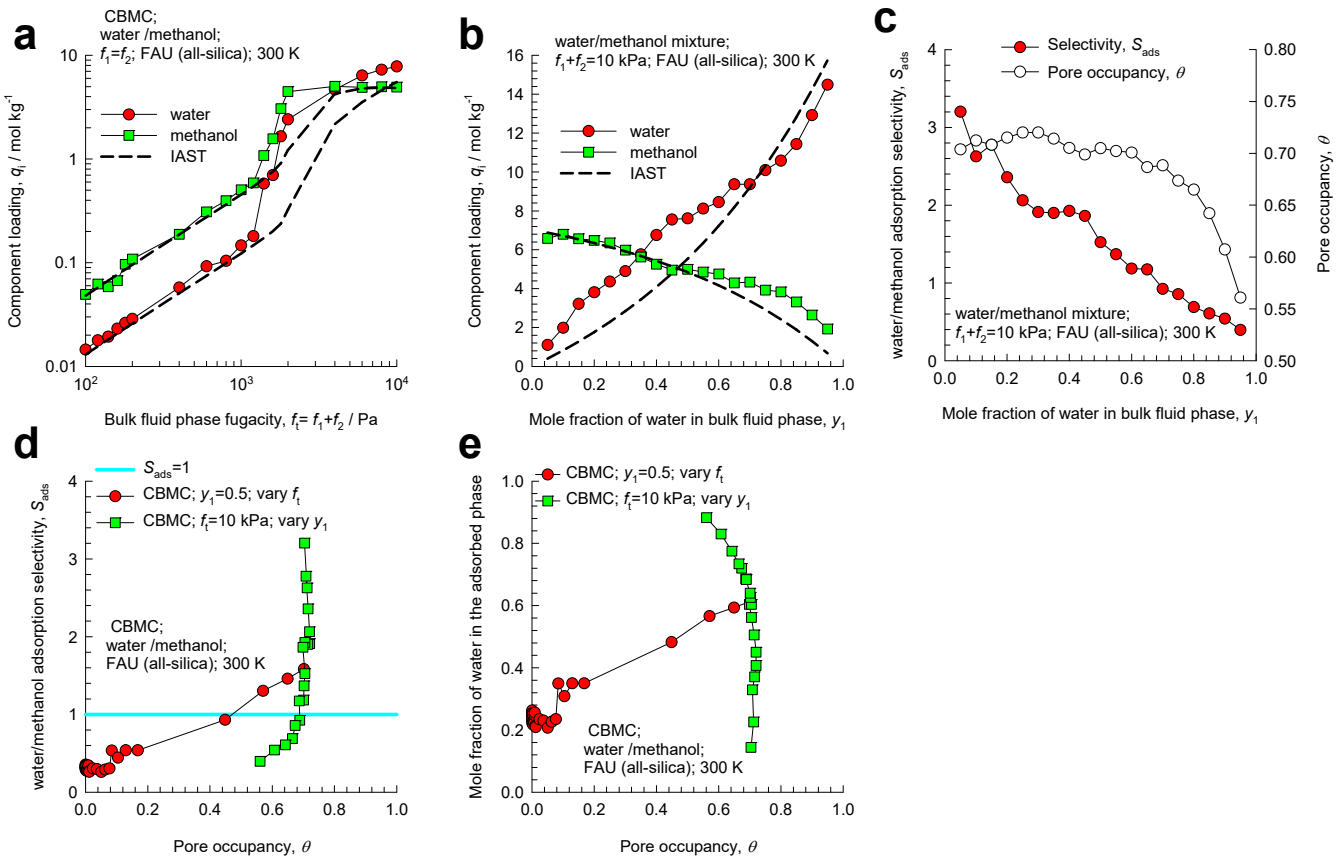

Figure S38. (a) CBMC simulation data on component loadings q_1, q_2 for Campaign A (y_1= 0.5) for water(1)/methanol(2) mixture in all-silica FAU at 300 K. (b, c) CBMC simulation data on (b) component loadings q_1, q_2, and (c) adsorption selectivities S_{ads} for Campaign B (f_t = 10 kPa) for water/methanol mixture in all-silica FAU at 300 K. (d) CBMC data for S_{ads} in Campaign A and B plotted as function of pore occupancy, θ. (e) CBMC data for mole fraction in the adsorbed phase, x_1, in Campaign A and B plotted as function of pore occupancy, θ.

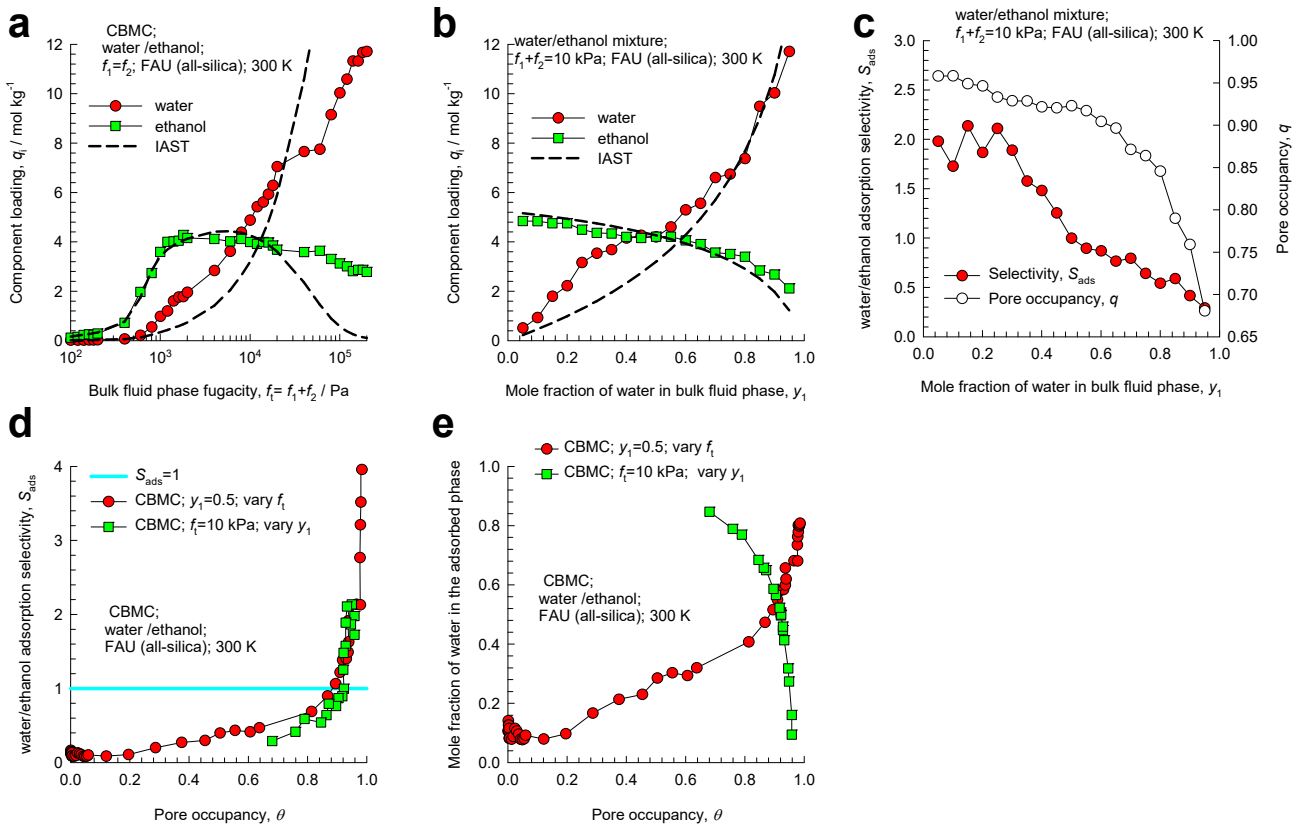

Figure S39. (a) CBMC simulation data on component loadings q_1, q_2 for Campaign A (y_1= 0.5) for water(1)/ethanol(2) mixture in all-silica FAU at 300 K. (b, c) CBMC simulation data on (b) component loadings q_1, q_2, and (c) adsorption selectivities S_{ads} for Campaign B (f_t = 10 kPa) for water/methanol mixture in all-silica FAU at 300 K. (d) CBMC data for S_{ads} in Campaign A and B plotted as function of pore occupancy, θ. (e) CBMC data for mole fraction in the adsorbed phase, x_1, in Campaign A and B plotted as function of pore occupancy, θ.

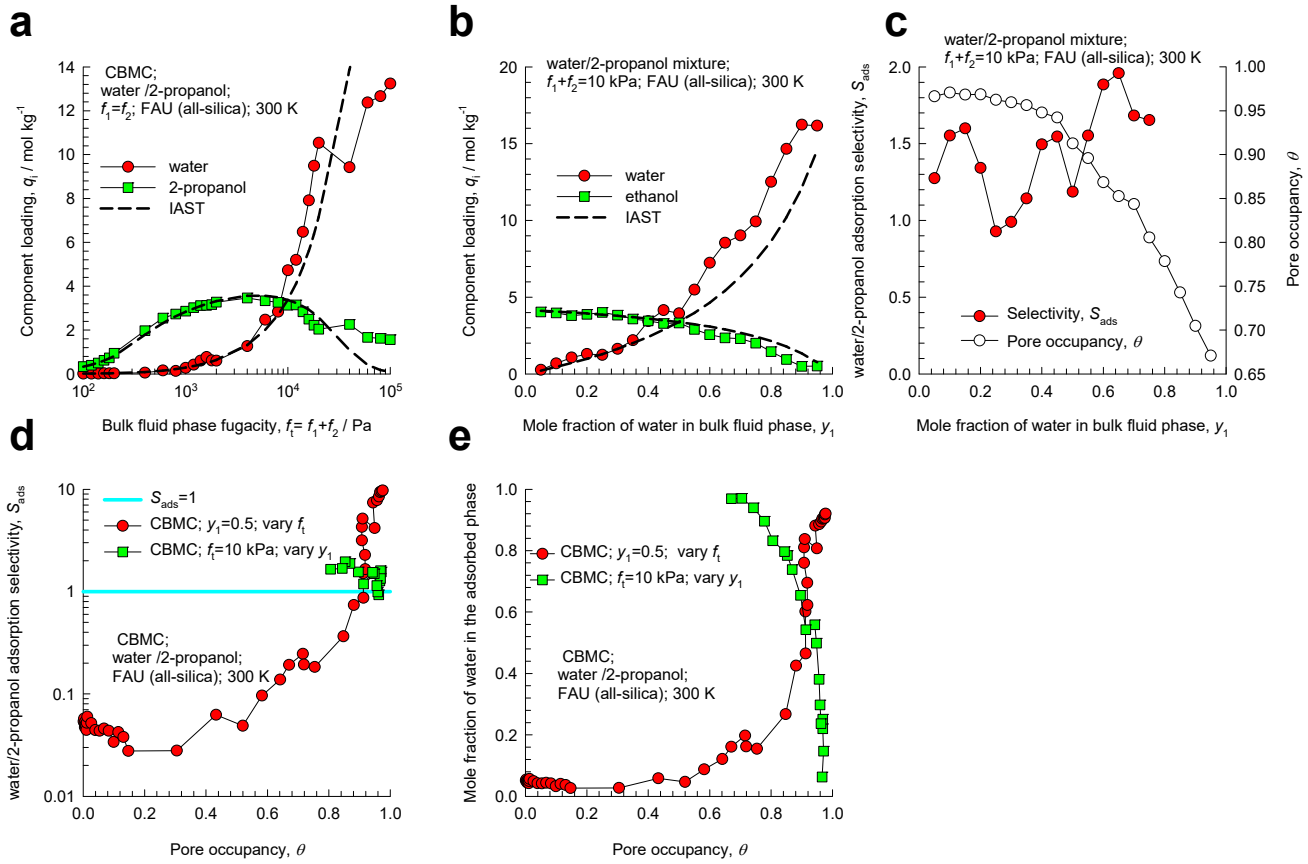

Figure S40. (a) CBMC simulation data on component loadings q_1, q_2 for Campaign A (y_1= 0.5) for water(1)/2-propanol(2) mixture in all-silica FAU at 300 K. (b, c) CBMC simulation data on (b) component loadings q_1, q_2, and (c) adsorption selectivities S_{ads} for Campaign B (f_t = 10 kPa) for water/methanol mixture in all-silica FAU at 300 K. (d) CBMC data for S_{ads} in Campaign A and B plotted as function of pore occupancy, θ. (e) CBMC data for mole fraction in the adsorbed phase, x_1, in Campaign A and B plotted as function of pore occupancy, θ.

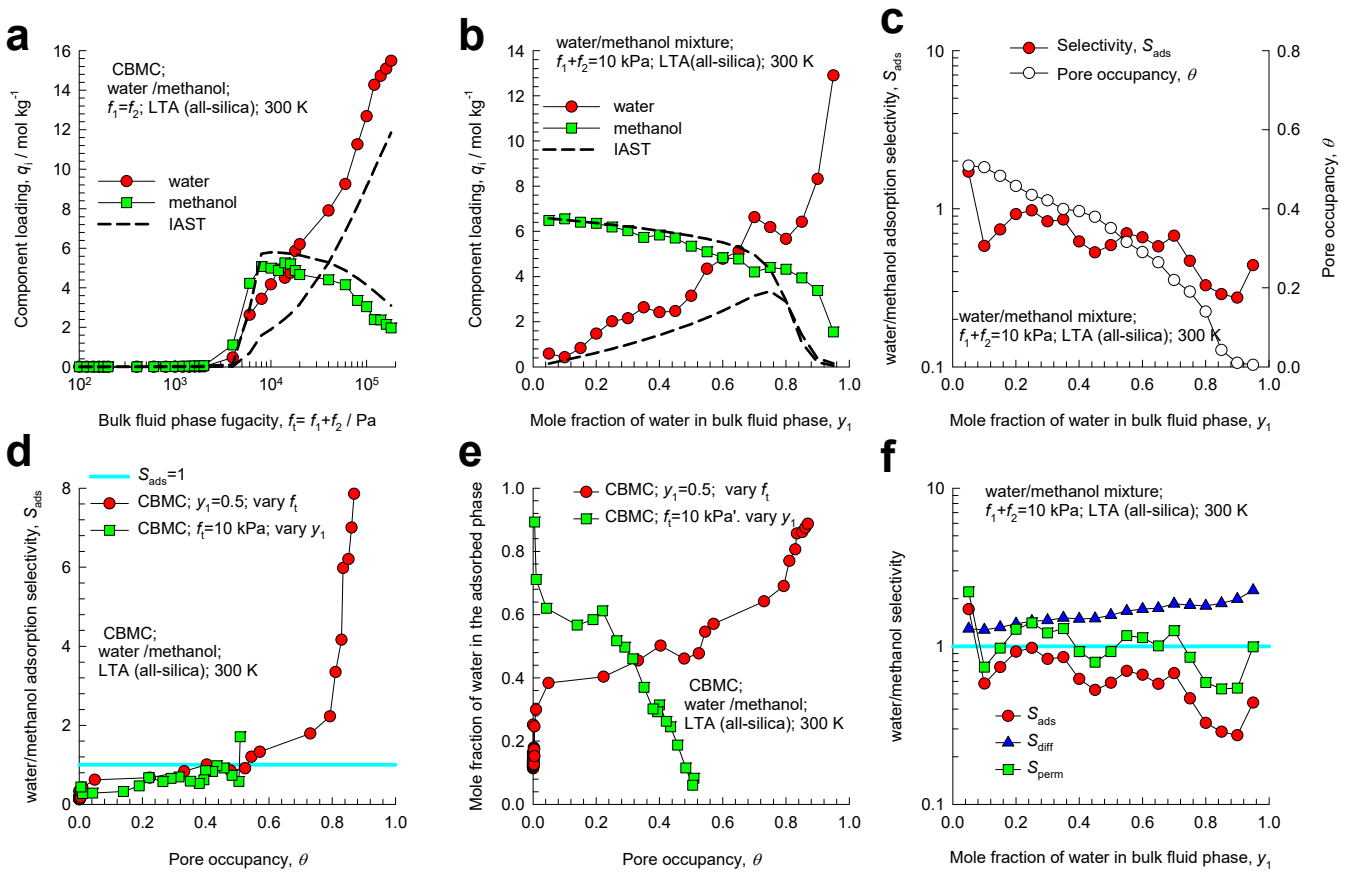

Figure S41. (a) CBMC simulation data on component loadings, q_1, q_2, for Campaign A (y_1= 0.5) for water(1)/methanol(2) mixture in all-silica LTA at 300 K. (b, c) CBMC simulation data on (b) component loadings q_1, q_2, and (c) adsorption selectivities S_{ads} for Campaign B (f_t = 10 kPa) for water/methanol mixture in all-silica LTA at 300 K. (d) CBMC data for S_{ads} in Campaign A and B plotted as function of pore occupancy, θ. (e) CBMC data for mole fraction in the adsorbed phase, x_1, in Campaign A and B plotted as function of pore occupancy, θ. (f) Selectivities $S_{ads}, S_{diff}, S_{perm}$ for Campaign B.

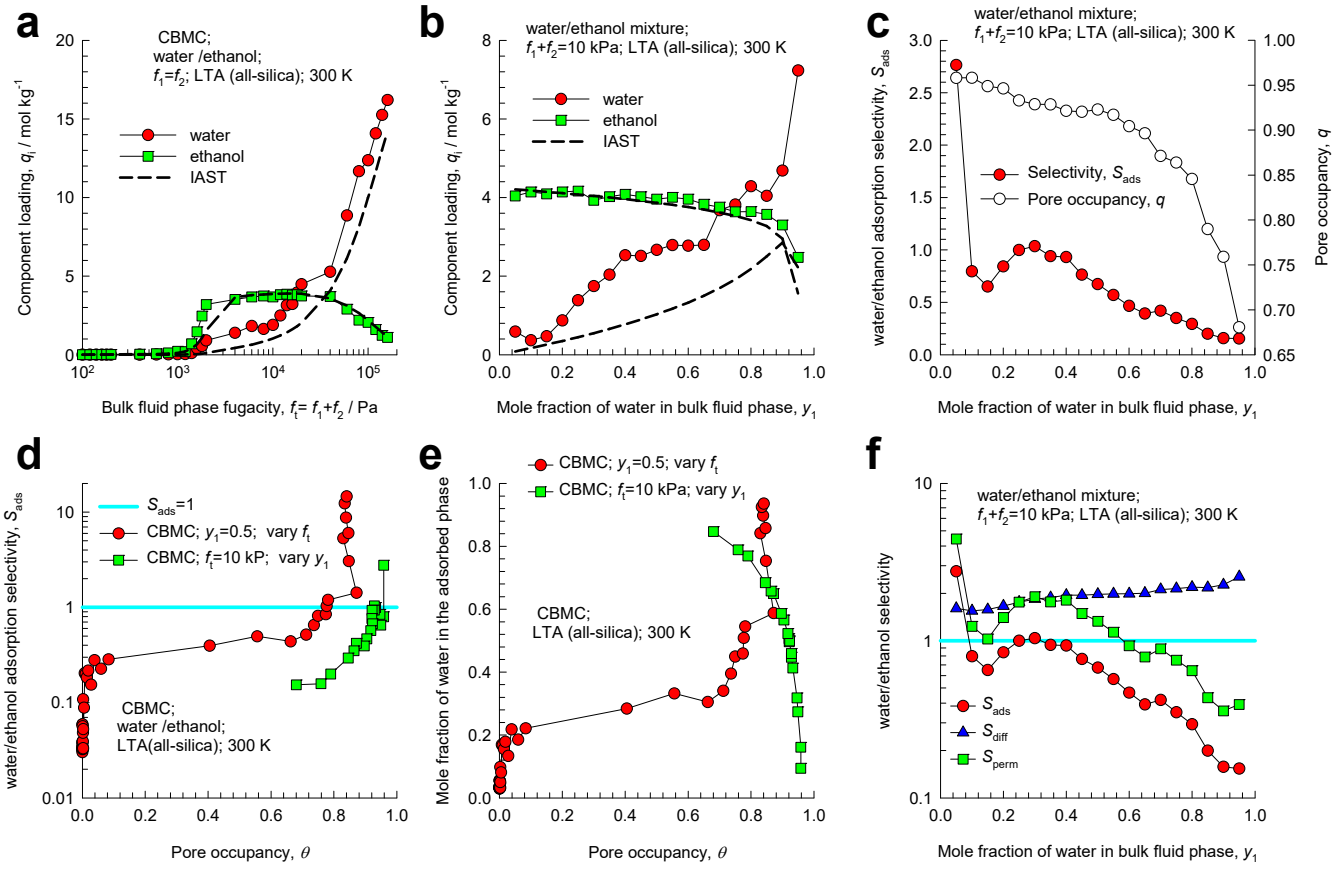

Figure S42. (a) CBMC simulation data on component loadings, q_1, q_2, for Campaign A (y_1= 0.5) for water(1)/ethanol(2) mixture in all-silica LTA at 300 K. (b, c) CBMC simulation data on (b) component loadings q_1, q_2, and (c) adsorption selectivities S_{ads} for Campaign B (f_t = 10 kPa) for water/methanol mixture in all-silica LTA at 300 K. (d) CBMC data for S_{ads} in Campaign A and B plotted as function of pore occupancy, θ. (e) CBMC data for mole fraction in the adsorbed phase, x_1, in Campaign A and B plotted as function of pore occupancy, θ. (f) Selectivities $S_{ads}, S_{diff}, S_{perm}$ for Campaign B.

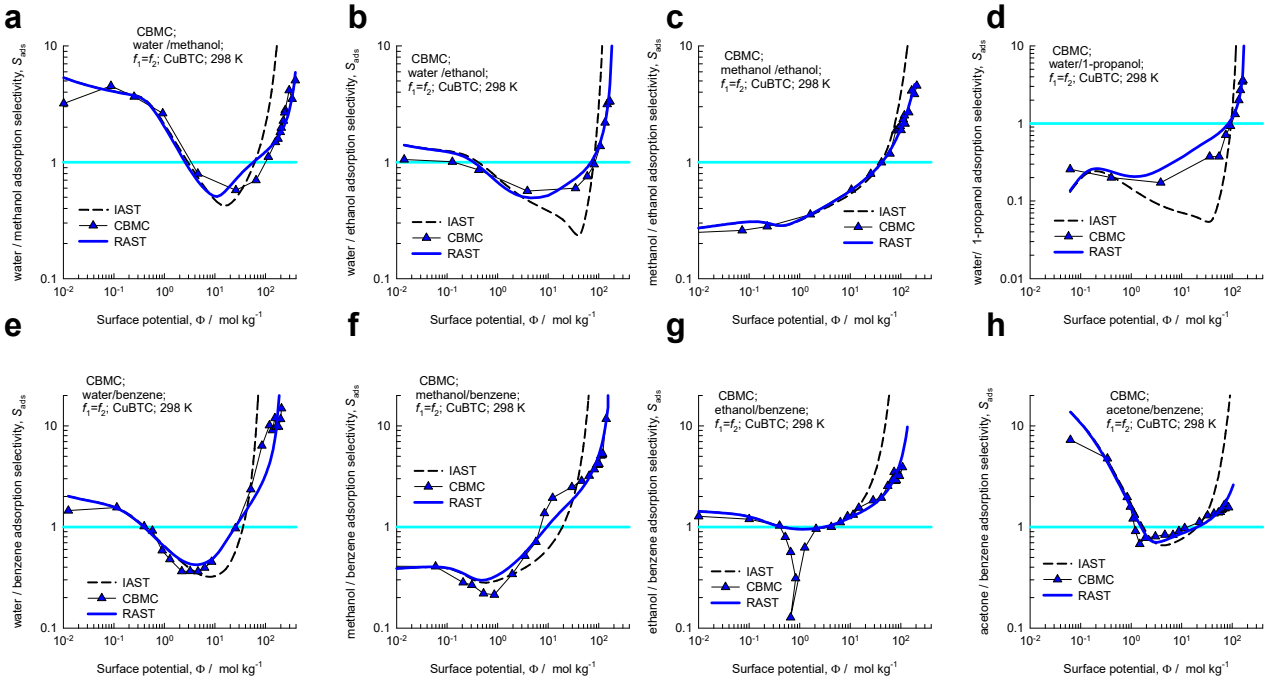

Figure S43. CBMC simulation data on adsorption selectivities, S_{ads}, for equimolar water/methanol, water/methanol, methanol/ethanol, water/1-propanol, water/benzene, methanol/benzene, ethanol/benzene, and acetone/benzene mixtures (Campaign A, y_1= 0.5) in CuBTC at 298 K. The selectivity data are plotted as a function of the surface potential Φ. The dashed lines are the IAST estimates. The continuous solid blue lines are the RAST calculations, with fitted Margules parameters specified in Table S11.

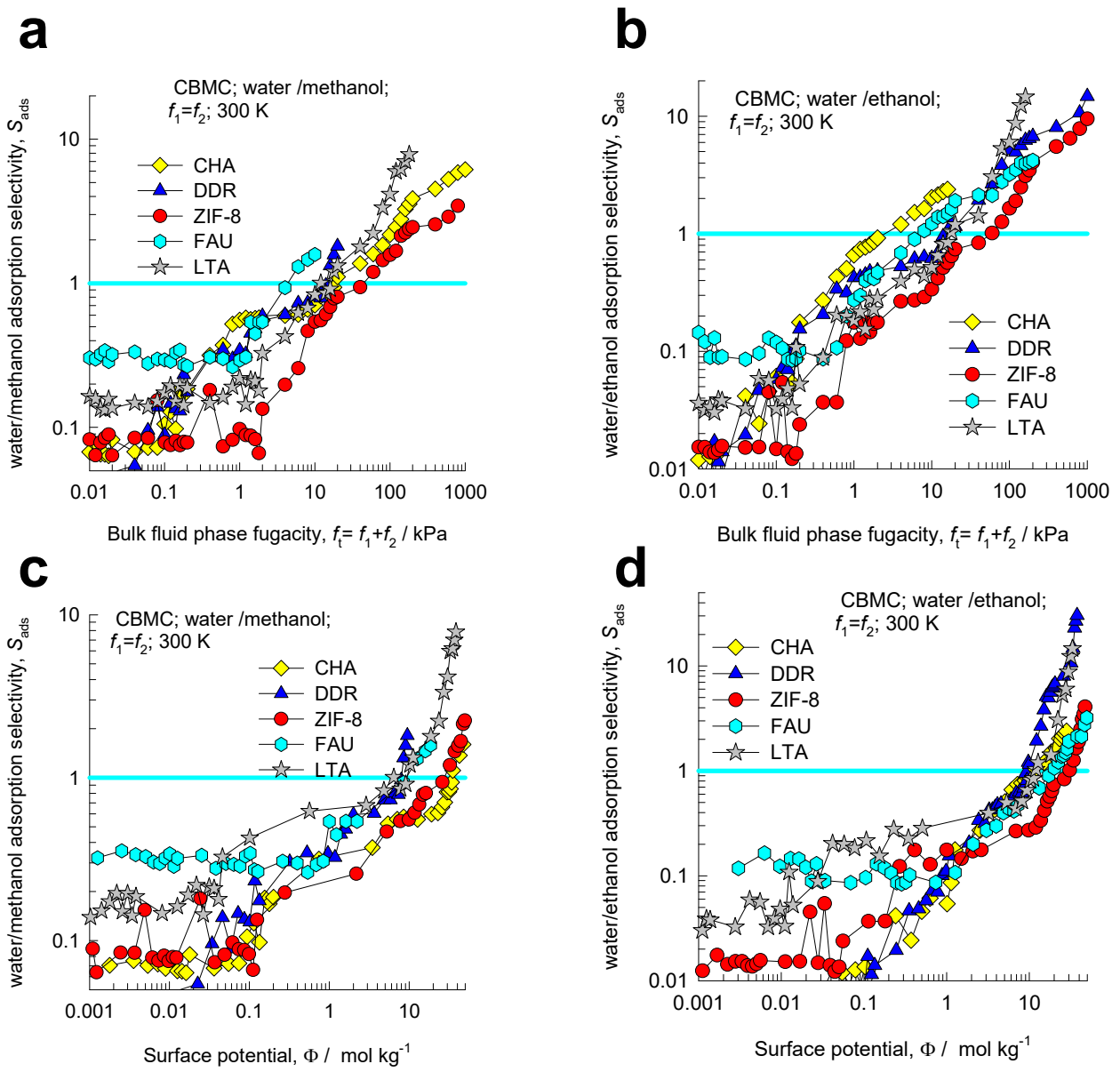

Figure S44. (a, b) Water/alcohol adsorption selectivity, S_{ads}, for (a) water/methanol, and (b) water/ethanol mixtures, determined from CBMC simulations (Campaign A, y_1= 0.5), in various host materials, using the bulk fugacity f_t as x-axis. (c, d) Water/alcohol adsorption selectivity, S_{ads}, for Campaign A using the surface potential Φ as x-axis.

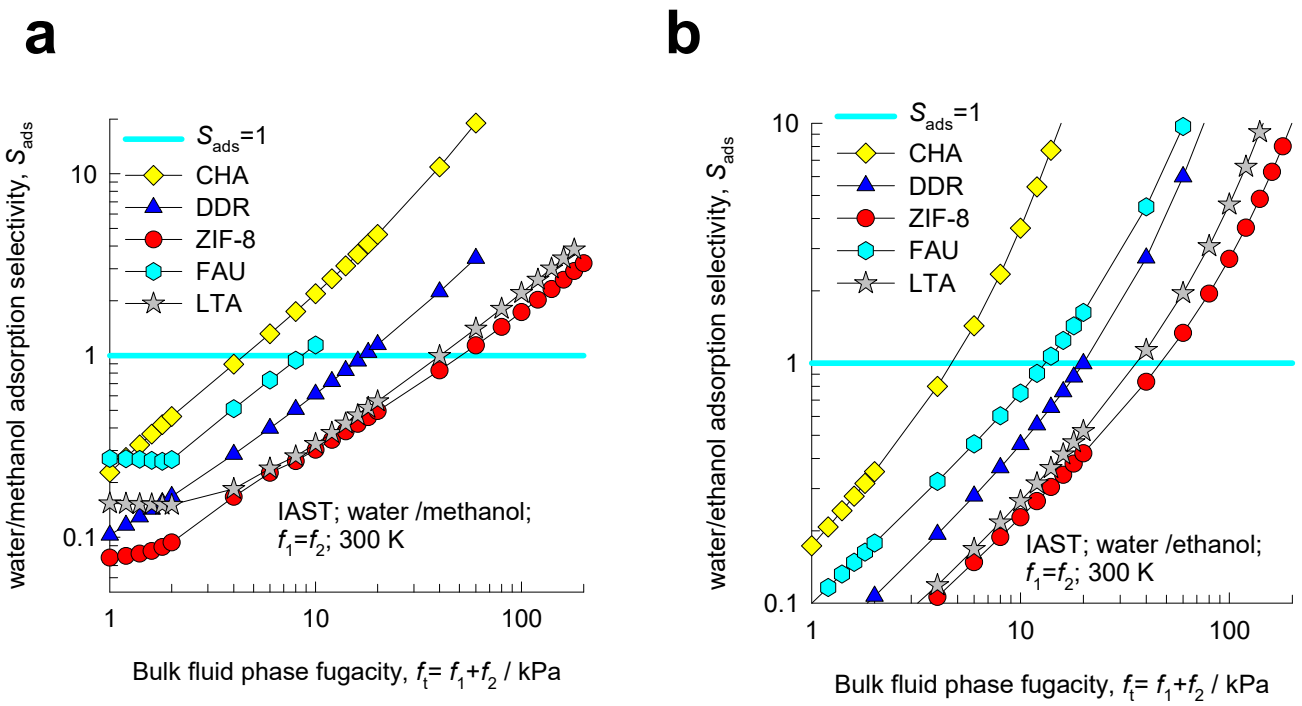

Figure S45. Water/alcohol adsorption selectivity, S_{ads}, for (a) water/methanol, and (b) water/ethanol mixtures, estimated from IAST calculations (Campaign A, y_1= 0.5), in various host materials, using the bulk fugacity f_t as x-axis.

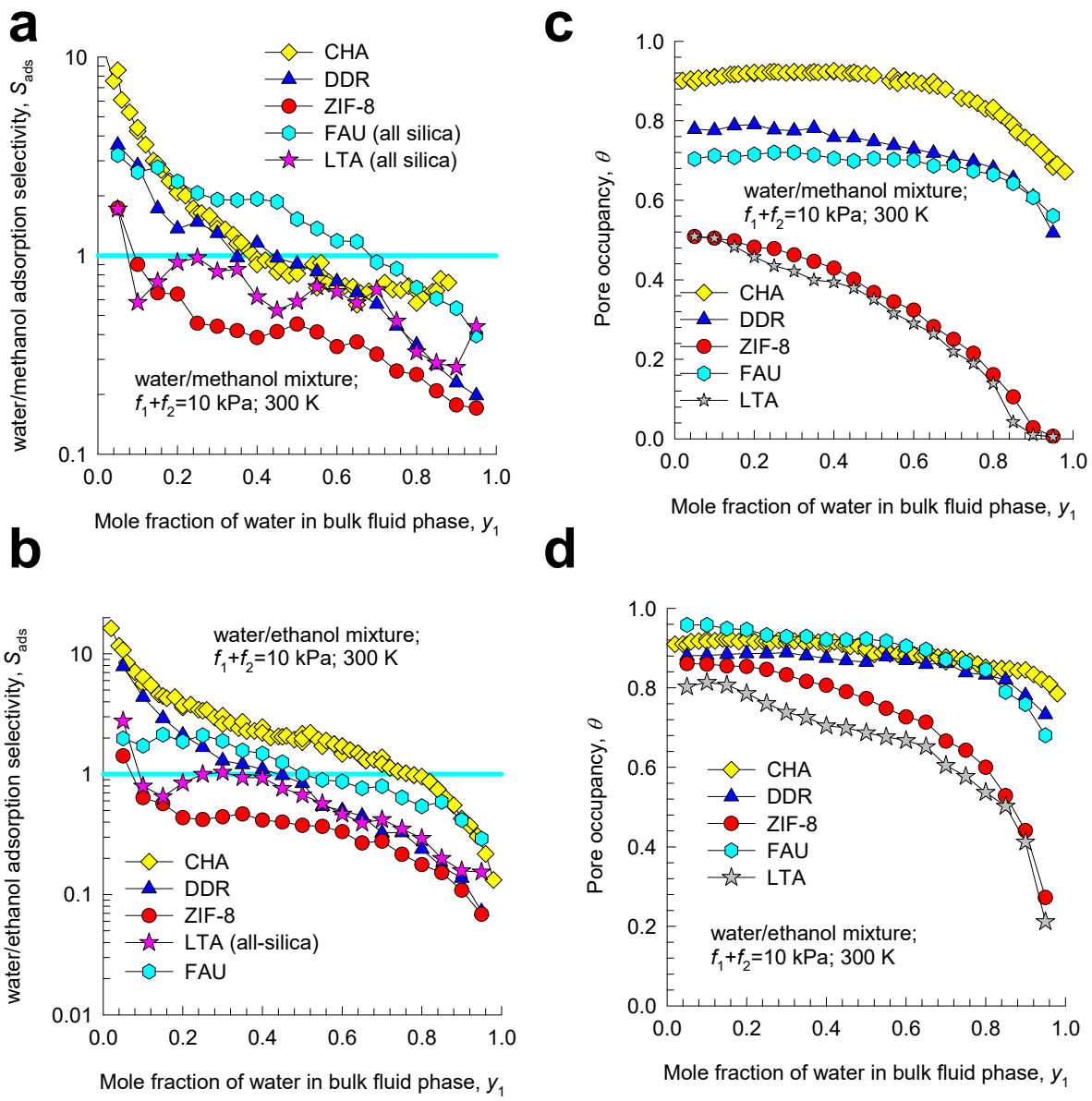

Figure S46. (a, b) Water/alcohol adsorption selectivity, S_{ads}, (c, d) pore occupancies, θ, for (a) water/methanol, and (b) water/ethanol mixtures in different host materials, determined from CBMC simulations in which f_t= 10 kPa. The x-axis is the mole fraction of water(1) in the bulk fluid phase mixture, y_1.

7 CBMC vs RAST for mixture adsorption

Having established the failure of the IAST to provide a quantitative description of mixture adsorption equilibrium for water/alcohol mixtures, we now proceed to quantify the departures from the IAST.

7.1 Determination of activity coefficients from CBMC mixture adsorption data

For each CBMC mixture simulation campaign (Campaign A, or Campaign B), the mole fractions of the adsorbed phase, $x_1 = \frac{q_{1,CBMC}}{q_{t,CBMC}}; x_2 = \frac{q_{2,CBMC}}{q_{t,CBMC}}; q_{t,CBMC} = q_{1,CBMC} + q_{2,CBMC}$ are determined. The sorption pressures P_1^0, P_2^0, each of which satisfying eq (S7), can be determined from using the unary isotherm fits for each of the components in the binary mixture.

The activity coefficients of the two components $\gamma_{1,CBMC}; \gamma_{2,CBMC}$ are determined from eq (S32):

$$\gamma_{1,CBMC} = \frac{f_1}{P_1^0 x_{1,CBMC}}; \gamma_{2,CBMC} = \frac{f_2}{P_2^0 x_{2,CBMC}} \tag{S45}$$

The activity coefficients of the two components $\gamma_{1,CBMC}; \gamma_{2,CBMC}$, determined using eq (S45) are subject to a degree of scatter that is inherent in the CBMC mixture simulation data.

As illustration, let consider the adsorption of water(1)/ethanol(2) mixtures in CHA zeolite at 300 K. The CBMC simulation data for three different simulation campaigns are used in conjunction with eq (S45) to determine the activity coefficients of both guests in the adsorbed phase mixture

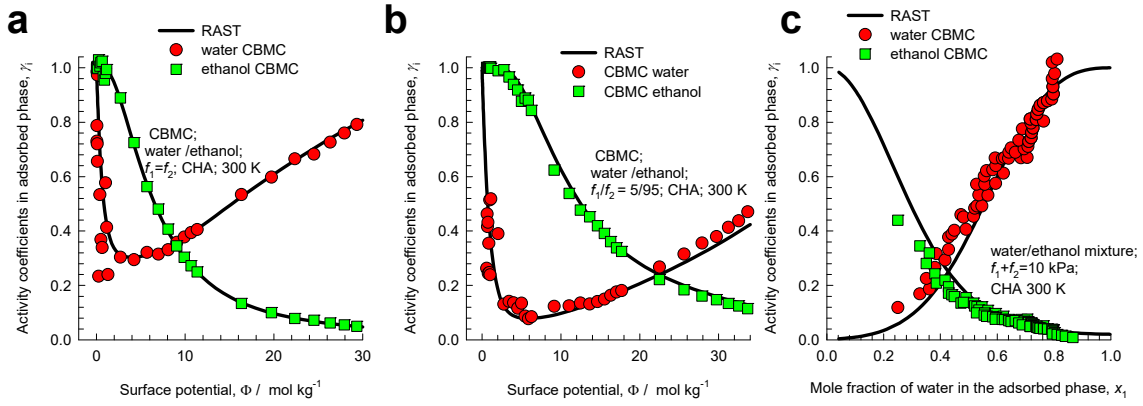

The continuous solid black lines are the RAST model calculations using the Margules model fits specified in Table S4.

It is important to note that both the activity coefficients tend to unity at vanishingly small values of the surface potential, i.e. $\gamma_i \to 1; \quad \Phi \to 0$. The introduction of $\left(1-\exp\left(-C\Phi\right)\right)$ imparts the correct limiting behaviors.

With the same set of Margules parameters $C = 0.131; A_{12} = -7.717; A_{21} = -4.083$, as specified in Table S4, if the correction factor $\left(1-\exp\left(-C\Phi\right)\right)$ were to be ignored completely, we obtain for the same three CBMC simulation campaigns for water(1)/ethanol(2) mixtures in CHA zeolite the blue lines indicated below.

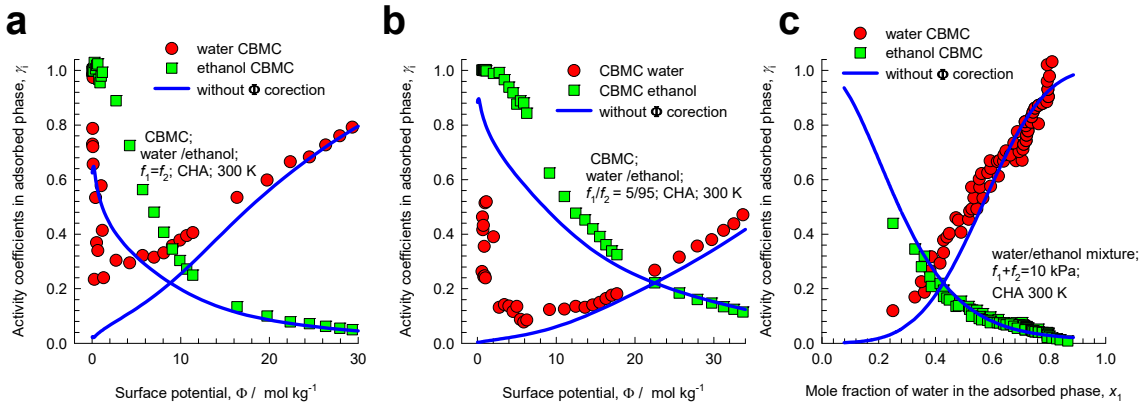

For the first two campaigns in which the bulk fluid phase compositions are held constant at $y_1 = y_2 = 0.5$, or $y_1 = 0.05$, and the bulk fluid phase fugacity $f_t = f_1 + f_2$ is varied over a wide range to saturation, it is noteworthy that the activity coefficient of water, ignoring the correction factor $\left(1-\exp\left(-C\Phi\right)\right)$, is $\gamma_1 \to 0; \quad \Phi \to 0$, in total non-conformity with the CBMC limiting value of $\gamma_1 \to 1; \quad \Phi \to 0$.

For the third campaign, wherein $f_t = 10$ kPa, and the bulk fluid phase composition y_1 is varied, the neglect of the correction factor has a minor effect because the conditions correspond nearly to pore saturation, implying that $\left(1-\exp\left(-C\Phi\right)\right) \approx 1$.

To stress the importance of the correction factor $\left(1-\exp\left(-C\Phi\right)\right)$ we plot the activity coefficients of guest components for equimolar water/methanol, water/methanol, methanol/ethanol, water/1-propanol, water/benzene, methanol/benzene, ethanol/benzene, and acetone/benzene mixtures (Campaign A, y_1= 0.5) in CuBTC at 298 K. The RAST Margules parameters are specified in Table S11.

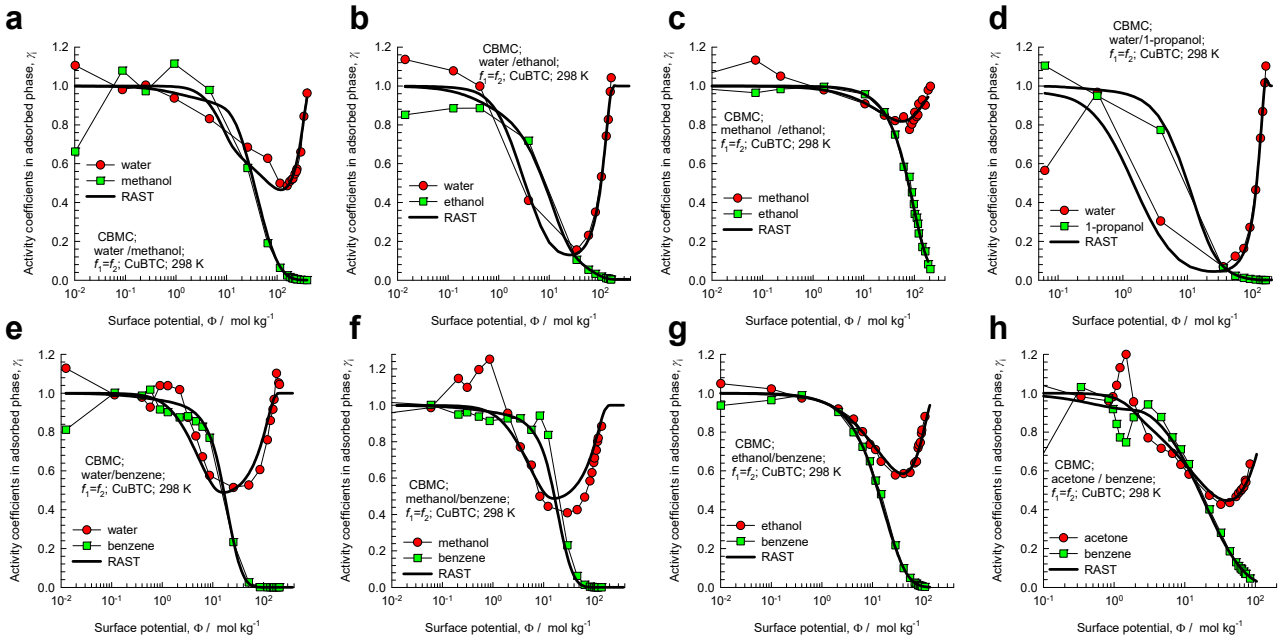

For all eight mixtures, we note that CBMC limiting value of $\gamma_1 \to 1; \quad \Phi \to 0$. To satisfy this limiting condition, we need to incorporate the correction factor $\left(1-\exp\left(-C\Phi\right)\right)$.

A further interesting point to note is that the activity coefficients of water and ethanol in the adsorbed phase mixture in CHA are both less than unity. The corresponding activity coefficients in the bulk phase liquid mixture at 300 K are both larger than unity.

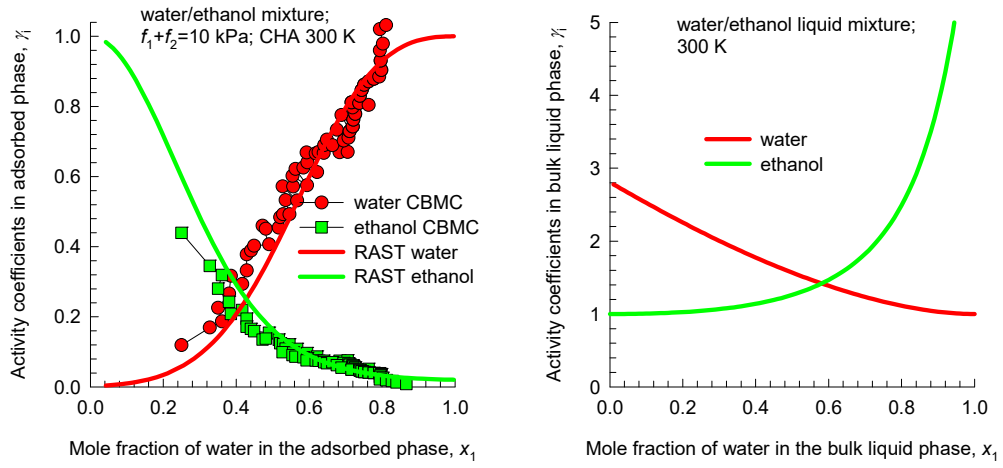

Figure S47 plots the activity coefficients $\gamma_{1,CBMC}, \gamma_{2,CBMC}$ for CBMC simulations Campaigns A, and B for (a, b) water/methanol, and (c, d) water/ethanol mixtures in various host materials, plotted as function of the surface potential, Φ.

In view of the fact that the IAST anticipates the selectivity to be described by eq (S14), we may also use the CBMC data on the adsorption selectivity $S_{ads} = \frac{q_1/q_2}{y_1/y_2}$ to be back-out the values of the ratios of activity coefficients of water with respect to alcohol:

$$\frac{\gamma_{1,CBMC}}{\gamma_{2,CBMC}} = \frac{S_{ads,IAST}}{S_{ads,CBMC}} \tag{S46}$$

Figure S48a,b plot the values of $\frac{\gamma_{1,CBMC}}{\gamma_{2,CBMC}} = \frac{S_{ads,IAST}}{S_{ads,CBMC}}$ for CBMC simulations (Campaign A, y_1= 0.5), in various host materials, plotted as function of the surface potential, Φ.

Figure S49a,b plot the mole fraction of water in the adsorbed phase, determined from CBMC simulations, $x_{1,CBMC}$ for both Campaigns A, and B for (a) water/methanol, and (b) water/ethanol mixtures at 300 K in various host materials. The *x*-axis is the corresponding mole fractions of water in the adsorbed phase determined from the IAST, $x_{1,IASTC}$. The data in Figure S49a,b demonstrate that thermodynamic

non-idealities and departures from the IAST favor water(1) in both (a) water/methanol, and (b) water/ethanol mixtures. Conversely, the non-idealities favor the alcohol in dilute aqueous mixtures.

7.2 Determination of Margules fit parameters from mixture adsorption data

For each mixture/host combination, the set of three Margules parameters A_{12}, A_{21}, C that yield the minimum value for the objective function calculated as the sum of the mean-squared deviations between the CBMC simulated component loadings, and those predicted using RAST

$$\text{Objective Function} = \left(q_{1,CBMC} - q_{1,RAST}\right)^2 + \left(q_{2,CBMC} - q_{2,RAST}\right)^2 \quad \text{(S47)}$$

The A_{12}, A_{21}, C were determined using the Excel solver function. For determination of the Margules parameters A_{12}, A_{21}, C, the CBMC data for both Campaigns A, and B were employed. The values of the fitted Margules parameters A_{12}, A_{21}, C are tabulated in

CHA: Table S4

DDR: Table S5

ZIF-8: Table S6

FAU (all silica): Table S7

LTA (all-silica): Table S8

The Margules parameters are not precisely the same as reported in our earlier works[24, 35] because additional CBMC simulation campaigns and data were obtained and analyzed in the present work.

7.3 Summary of CBMC simulation data and comparison with RAST.

The CBMC simulated data for both Campaigns A, and B , and comparison with the RAST model, with fitted Margules parameters are presented graphically in the following set of Figures.

CHA: Figure S52 and Figure S53

DDR: Figure S54 and Figure S55

ZIF-8: Figure S56 and Figure S57

FAU (all silica): Figure S58 and Figure S59

LTA (all-silica): Figure S60 and Figure S61

The dashed lines in these Figures are the IAST calculations. For all the mixtures considered the Margules model for activity coefficients and the use of the RAST provide a quantitative description of water/alcohol mixture adsorption equilibrium.

To underscore the fact that both mixture composition and surface potential influence the water/alcohol adsorption selectivity, Figure S50a,b,c present CBMC simulations of the water(1)/methanol(2) selectivities, S_{ads}, for adsorption in (a) CHA , (b) DDR , and (c) ZIF-8 at 300 K of

binary equimolar $\left(f_1 = f_2\right)$ water(1)/methanol(2) mixtures

binary $\left(f_1/f_2 = 5/95\right)$ water(1)/methanol(2) mixtures

ternary equimolar $\left(f_1 = f_2 = f_3\right)$ water(1)/methanol(2)/ethanol(3) mixtures.

The selectivities are plotted as function of the surface potential Φ.

At any specified value of the surface potential, Φ, the CBMC data shows that the hierarchy of selectivities is (1) binary mixture with $y_1 = 0.05$, (2) ternary mixture with $y_1 = 0.33333$, and (3) binary mixture with $y_1 = 0.5$. The selectivity becomes increasingly in favor of water as the water composition is lowered.

Figure S51a,b,c present CBMC simulations of the water(1)/ethanol(2) selectivities, S_{ads}, for adsorption in (a) CHA , (b) DDR , and (c) ZIF-8 at 300 K of

binary equimolar $\left(f_1 = f_2\right)$ water(1)/ethanol(2) mixtures

binary 5/95 water(1)/ethanol(2) $\left(f_1/f_2 = 5/95\right)$ mixtures

ternary equimolar $\left(f_1 = f_2 = f_3\right)$ water(1)/methanol(2)/ethanol(3) mixtures.

The selectivities are plotted as function of the surface potential Φ.

At any specified value of the surface potential, Φ, the CBMC data shows that the hierarchy of selectivities is (1) binary mixture with $y_1 = 0.05$, (2) ternary mixture with $y_1 = 0.33333$, and (3) binary

mixture with $y_1 = 0.5$. The selectivity becomes increasingly in favor of water as the water composition is lowered.

Figure S51d,e,f presents CBMC simulations of the water(1)/ethanol(2) selectivities, S_{ads}, for binary equimolar $\left(f_1 = f_2\right)$ water(1)/ethanol(2) mixtures plotted as a function of the total bulk fluid phase fugacity, $f_t = f_1 + f_2$.

7.4 List of Figures for CBMC vs RAST for mixture adsorption

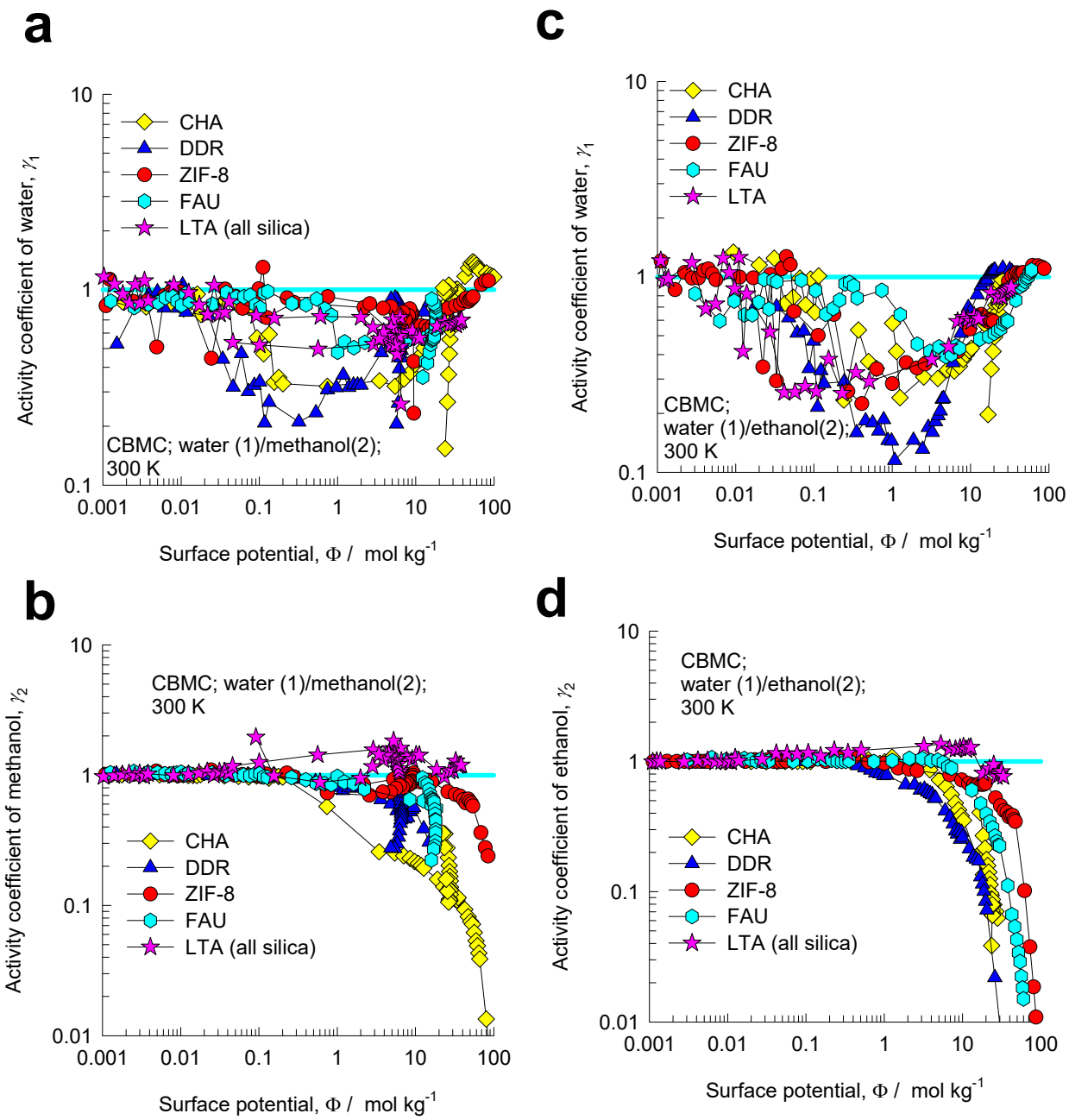

Figure S47. Activity coefficients $\gamma_{1,CBMC}, \gamma_{2,CBMC}$ for CBMC simulations Campaigns A, and B for (a, b) water/methanol, and (c, d) water/ethanol mixtures in various host materials, plotted as function of the surface potential, Φ.

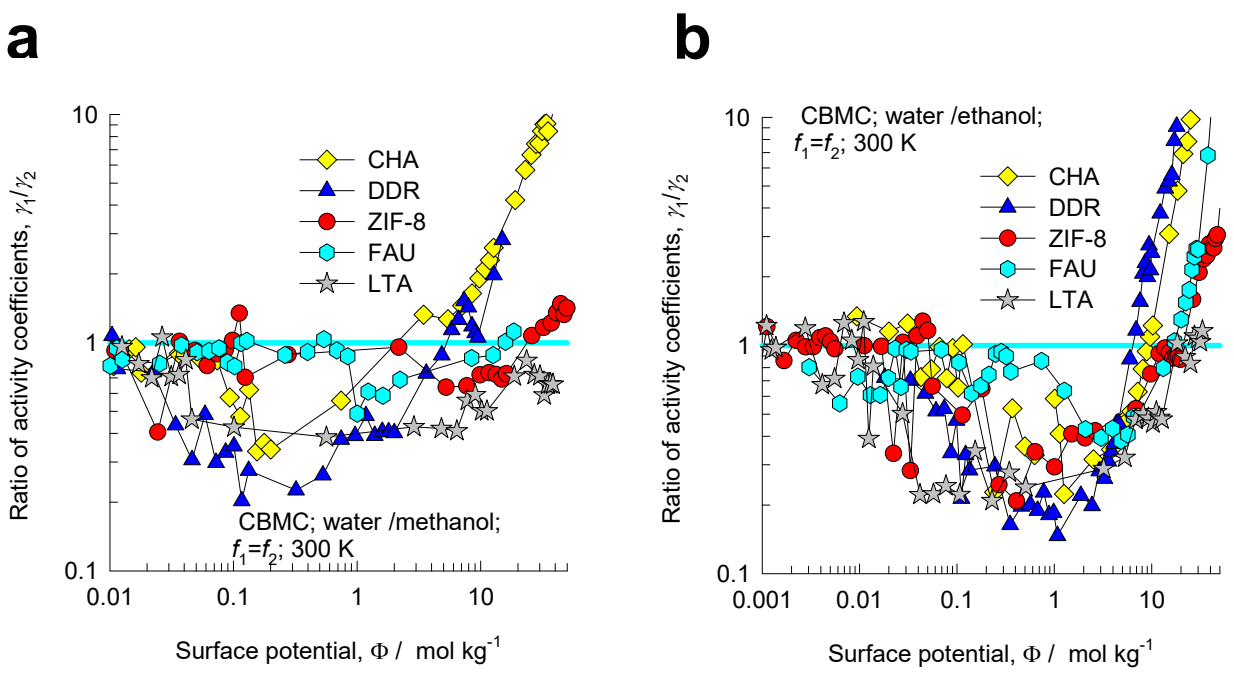

Figure S48. (a, b) Ratio of activity coefficients $\frac{\gamma_{1,CBMC}}{\gamma_{2,CBMC}} = \frac{S_{ads,IAST}}{S_{ads,CBMC}}$ for CBMC simulations (Campaign A, y_1= 0.5), in various host materials, plotted as function of the surface potential, Φ.

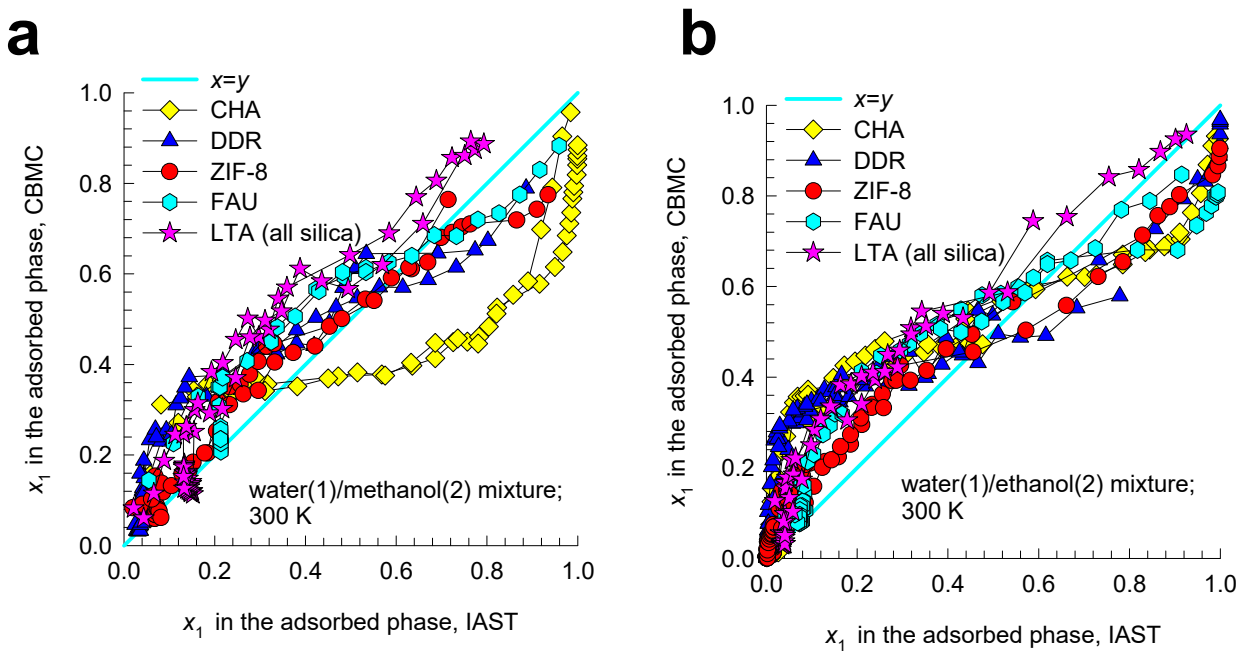

Figure S49. (a, b) Mole fraction of water in the adsorbed phase, determined from CBMC simulations, $x_{1,CBMC}$ for both Campaigns A, and B for (a) water/methanol, and (b) water/ethanol mixtures at 300 K in various host materials. The *x*-axis is the corresponding mole fractions of water in the adsorbed phase determined from the IAST, $x_{1,IASTC}$.

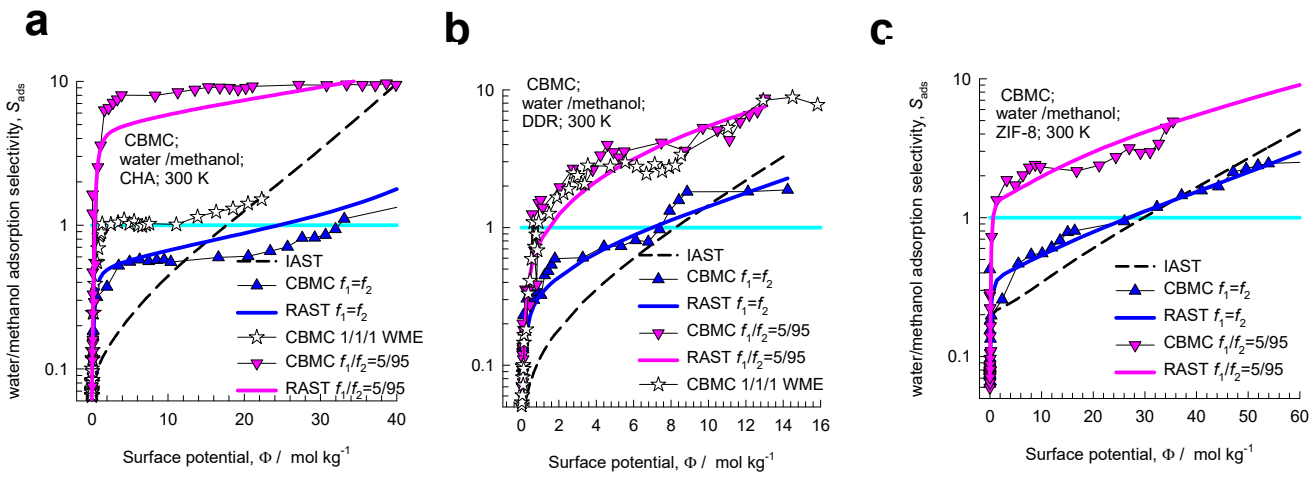

Figure S50. (a, b, c) CBMC simulations of the water(1)/methanol(2) selectivities, S_{ads}, for binary equimolar $(f_1 = f_2)$ water(1)/methanol(2) and ternary equimolar $(f_1 = f_2 = f_3)$ water(1)/methanol(2)/ethanol(3) mixture adsorption in (a) CHA , (b) DDR , and (c) ZIF-8 at 300 K. The selectivities are plotted as function of the surface potential Φ. Also included for (a) CHA, and (b) DDR zeolites are the selectivities for binary 5/95 water(1)/methanol(2) mixtures $(f_1/f_2 = 5/95)$. The dashed lines are the IAST calculations.

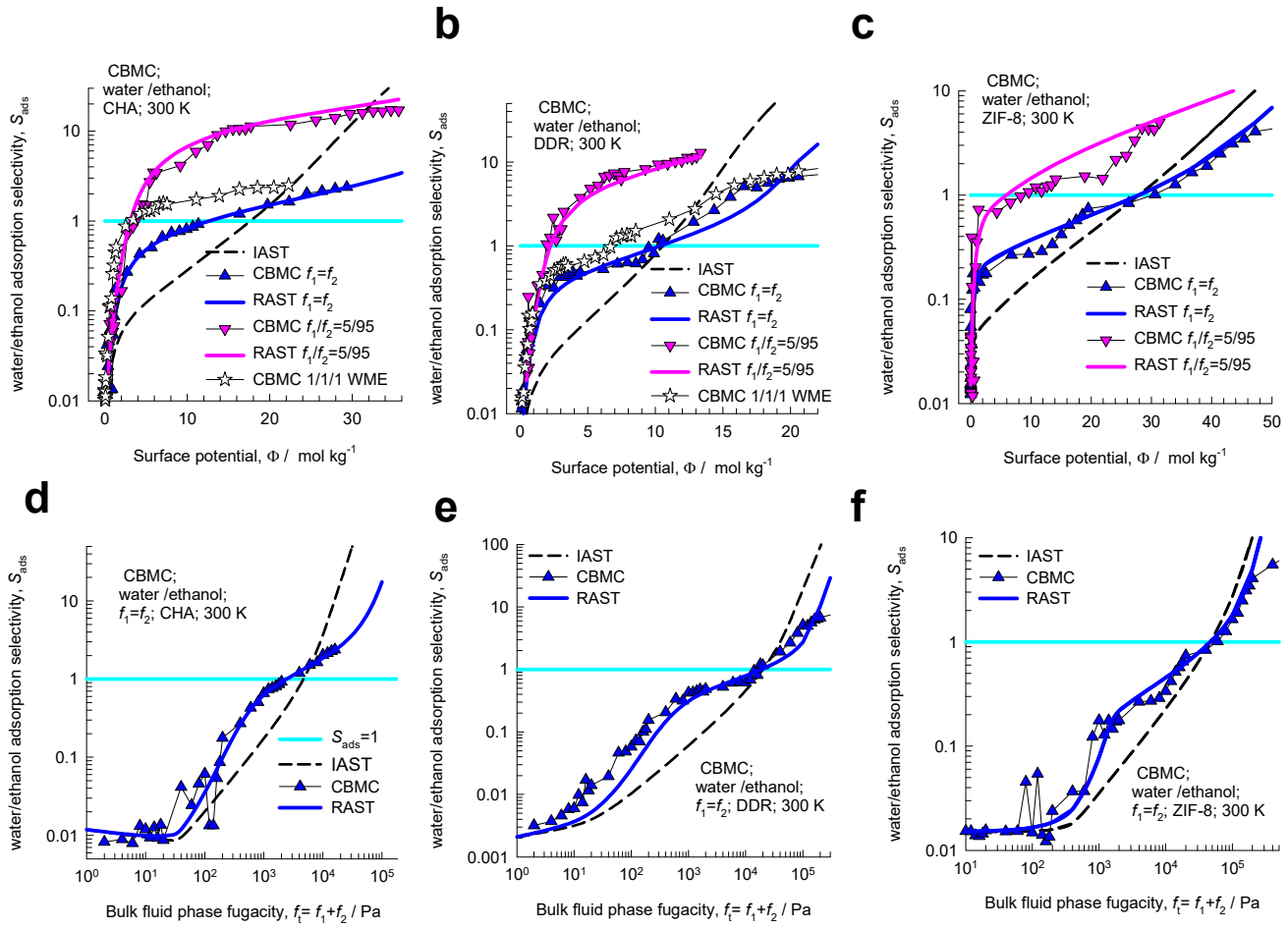

Figure S51. (a, b, c) CBMC simulations of the water(1)/ethanol(2) selectivities, S_{ads}, for binary equimolar $(f_1 = f_2)$ water(1)/ethanol(2) and ternary equimolar $(f_1 = f_2 = f_3)$ water(1)/methanol(2)/ethanol(3) mixture adsorption in (a) CHA , (b) DDR , and (c) ZIF-8 at 300 K. The selectivities are plotted as function of the surface potential Φ. Also included for (a) CHA, and (b) DDR zeolites are the selectivities for binary 5/95 water(1)/ethanol(2) mixtures $(f_1/f_2 = 5/95)$. The dashed lines are the IAST calculations. (d, e, f) CBMC simulations of the water(1)/ethanol(2) selectivities, S_{ads}, for binary equimolar $(f_1 = f_2)$ water(1)/ethanol(2) mixtures plotted as a function of the total bulk fluid phase fugacity, $f_t = f_1 + f_2$.

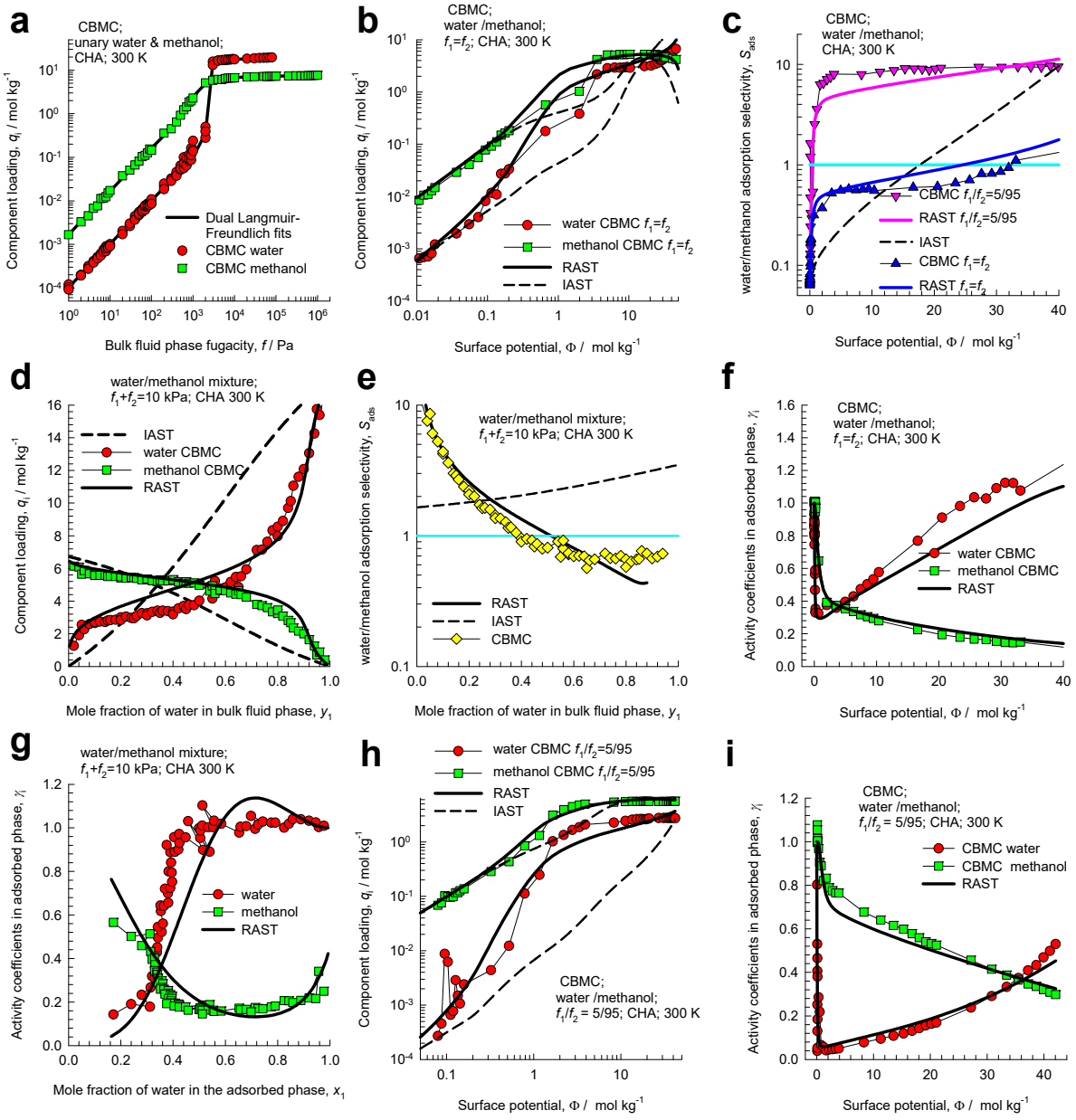

Figure S52. CBMC simulation data on component loadings, selectivities, and activity coefficients for Campaign A (y_1= 0.5 and y_1= 0.05) and Campaign B (f_i= 10 kPa) for water(1)/methanol(2) mixtures in CHA zeolite at 300 K The CBMC data are compared with RAST calculations using fitted Margules parameters. The dashed lines are IAST calculations.

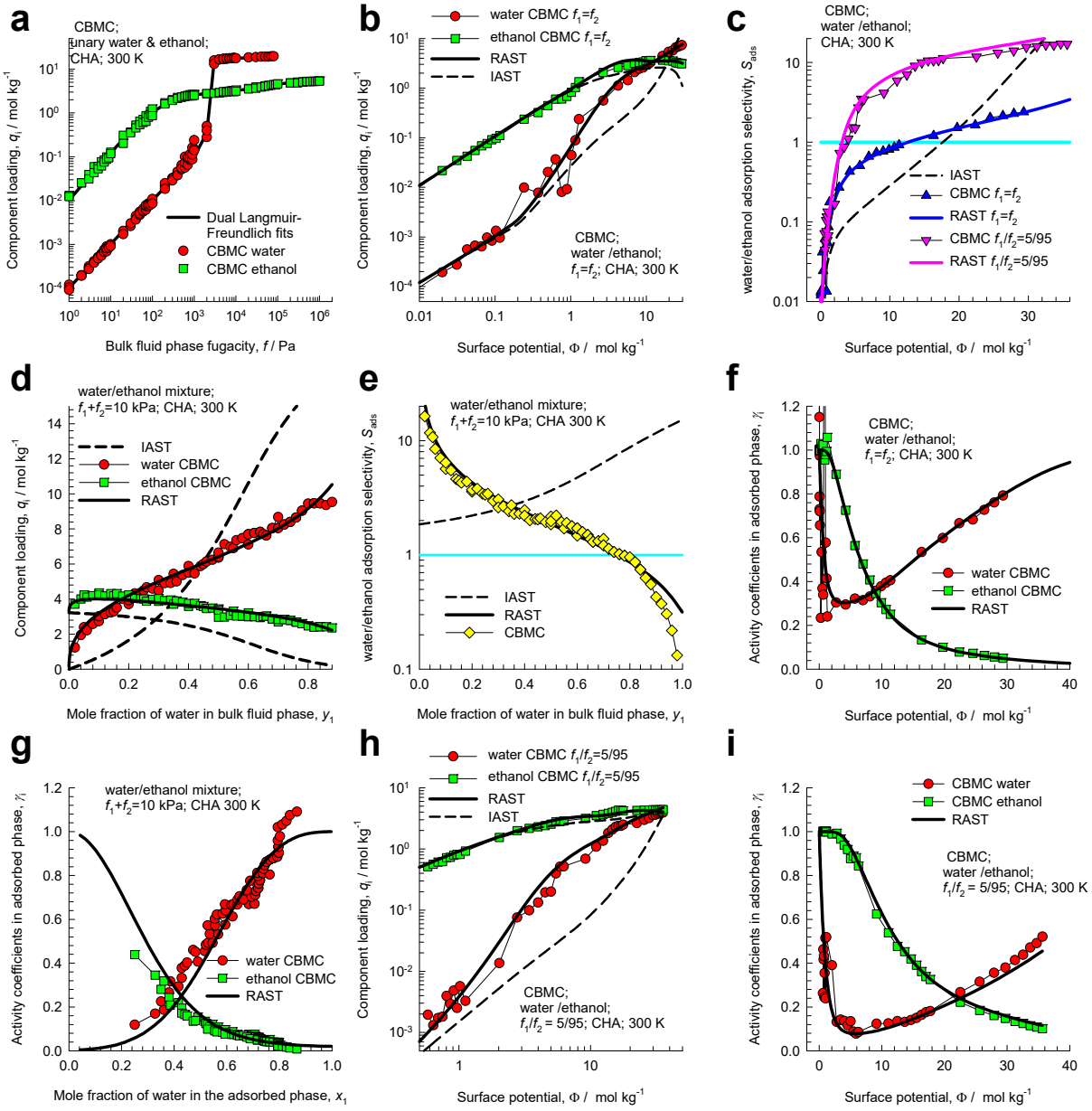

Figure S53. CBMC simulation data on component loadings, selectivities, and activity coefficients for Campaigns A (y_1= 0.5 and y_1= 0.05) and Campaign B (f_t= 10 kPa) for water(1)/ethanol(2) mixtures in CHA zeolite at 300 K The CBMC data are compared with RAST calculations using fitted Margules parameters. The dashed lines are IAST calculations.

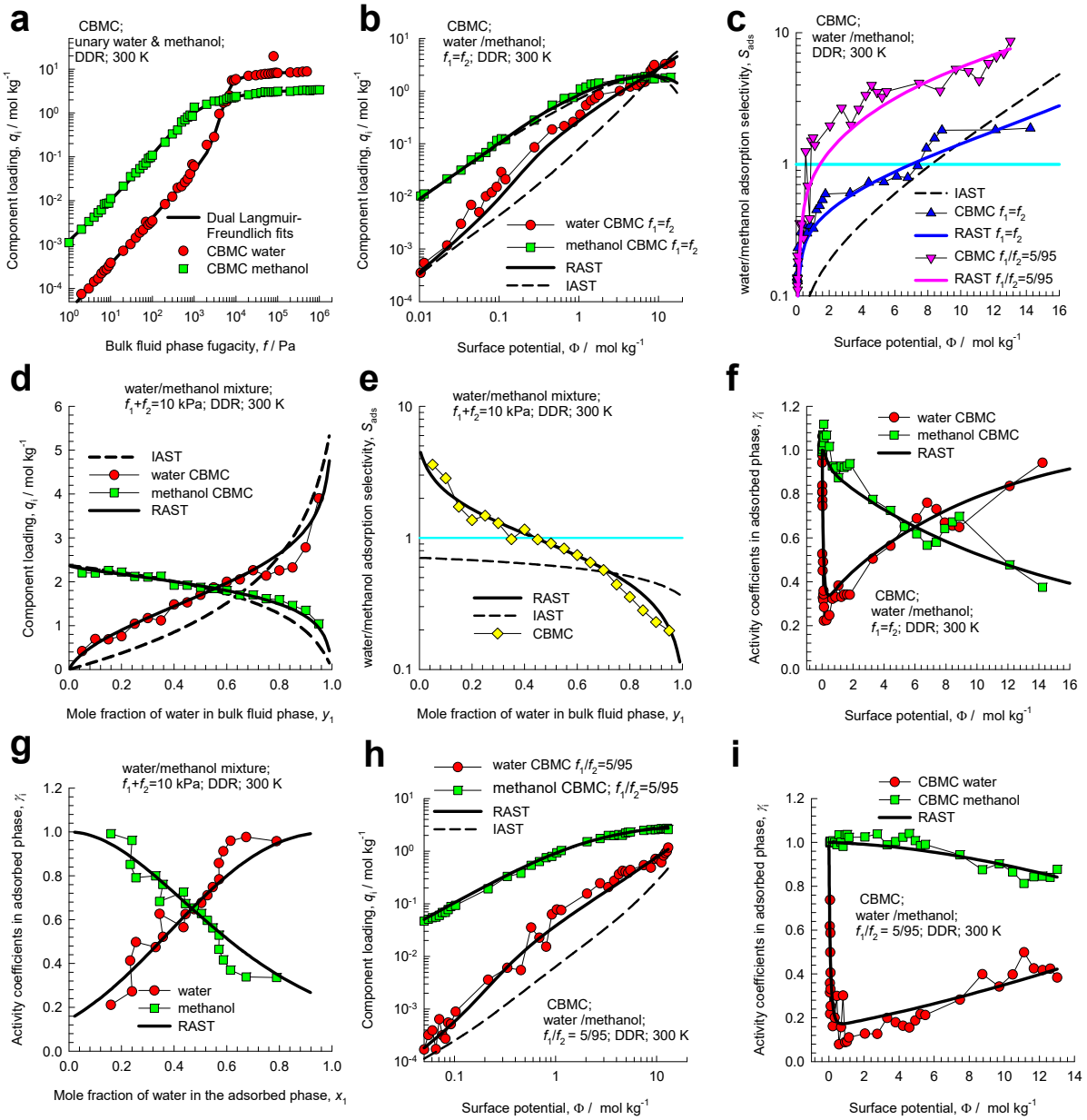

Figure S54. CBMC simulation data on component loadings, selectivities, and activity coefficients for Campaign A (y_1= 0.5 and y_1= 0.05) and Campaign B (f_i= 10 kPa) for water(1)/methanol(2) mixtures in DDR zeolite at 300 K The CBMC data are compared with RAST calculations using fitted Margules parameters. The dashed lines are IAST calculations.

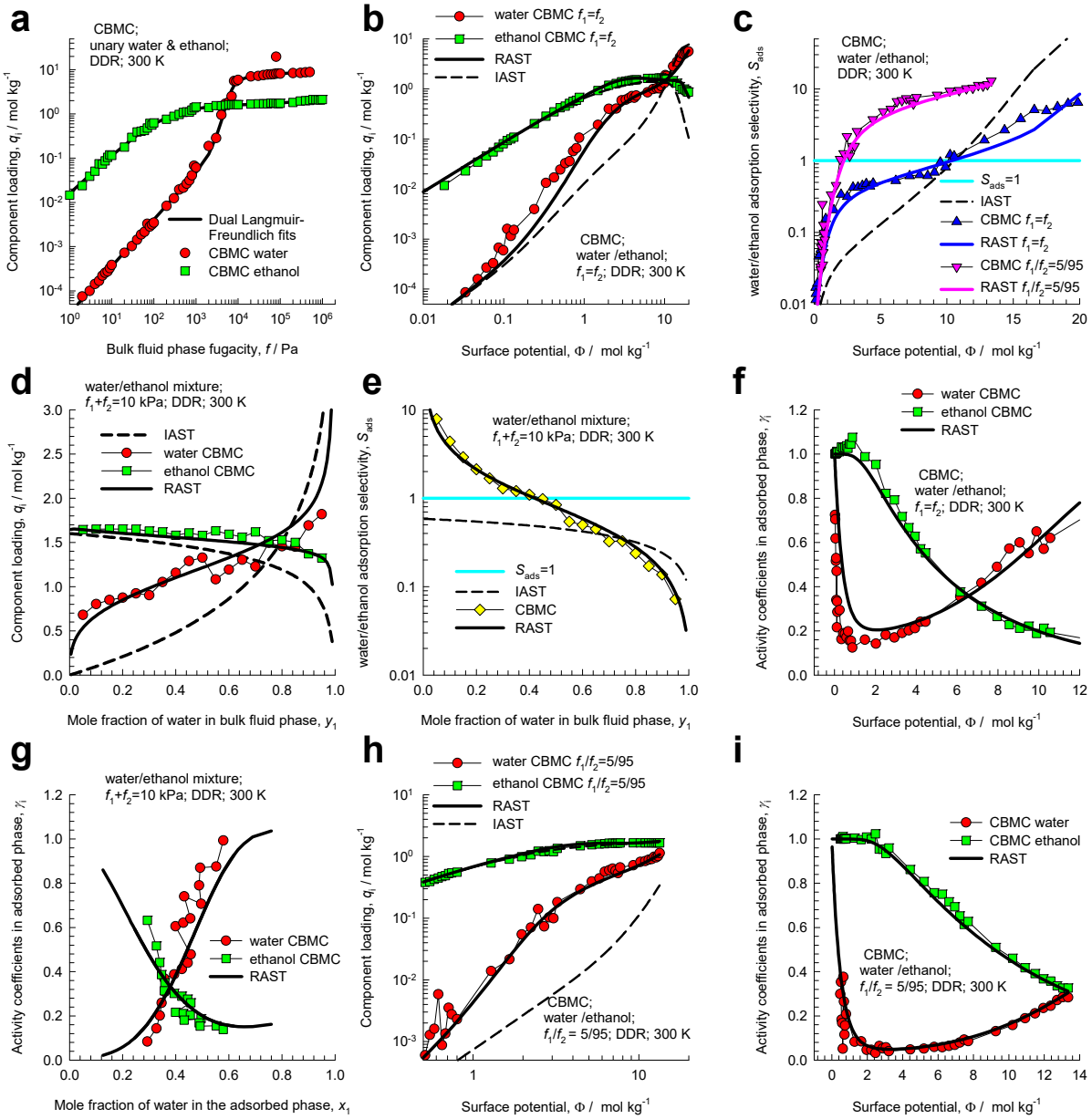

Figure S55. CBMC simulation data on component loadings, selectivities, and activity coefficients for Campaigns A (y_1= 0.5 and y_1= 0.05) and Campaign B (f_t= 10 kPa) for water(1)/ethanol(2) mixtures in DDR zeolite at 300 K The CBMC data are compared with RAST calculations using fitted Margules parameters. The dashed lines are IAST calculations.

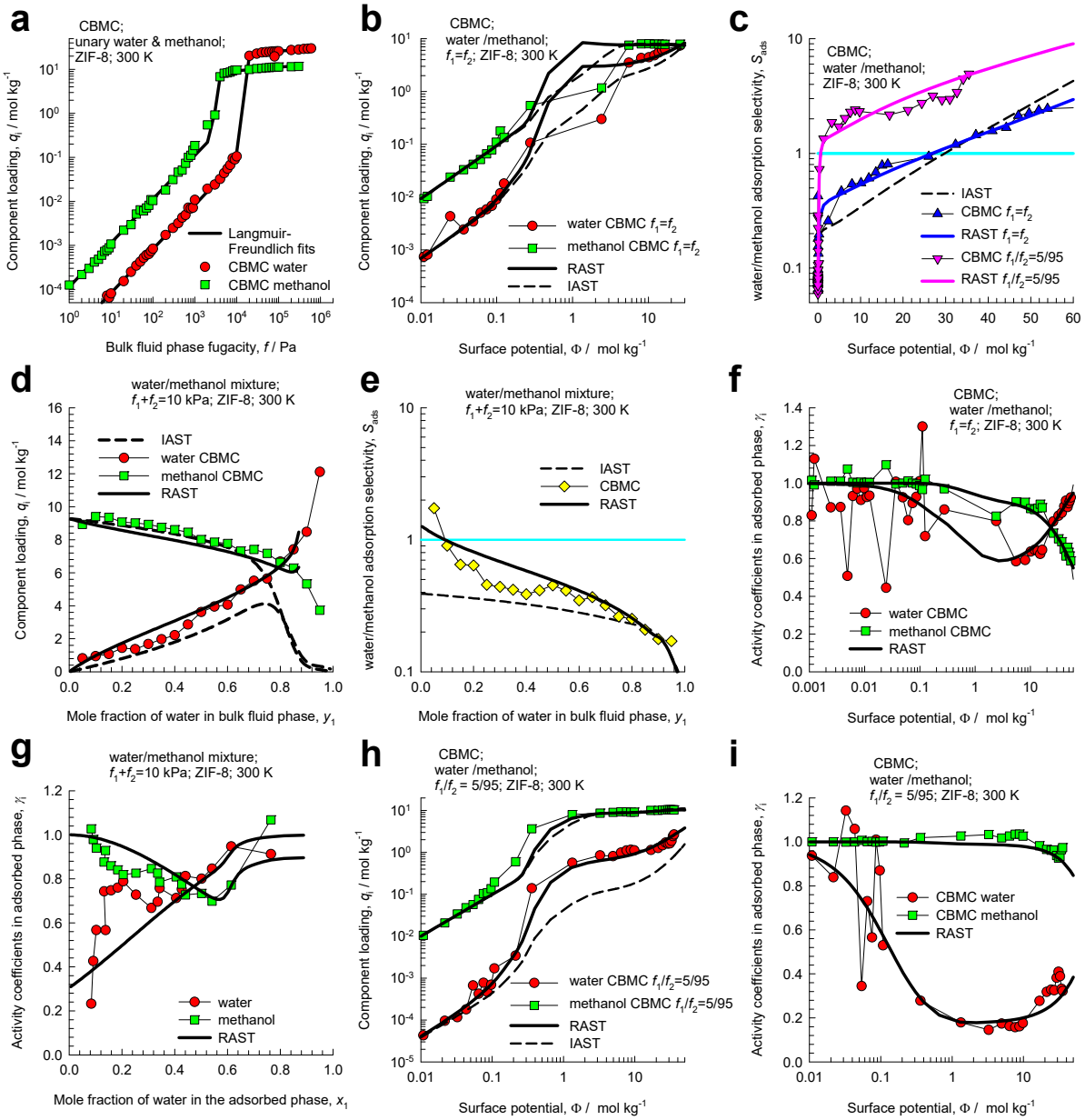

Figure S56. CBMC simulation data on component loadings, selectivities, and activity coefficients for Campaign A (y_1= 0.5 and y_1= 0.05) and Campaign B (f_t= 10 kPa) for water(1)/methanol(2) mixtures in ZIF-8 at 300 K The CBMC data are compared with RAST calculations using fitted Margules parameters. The dashed lines are IAST calculations.

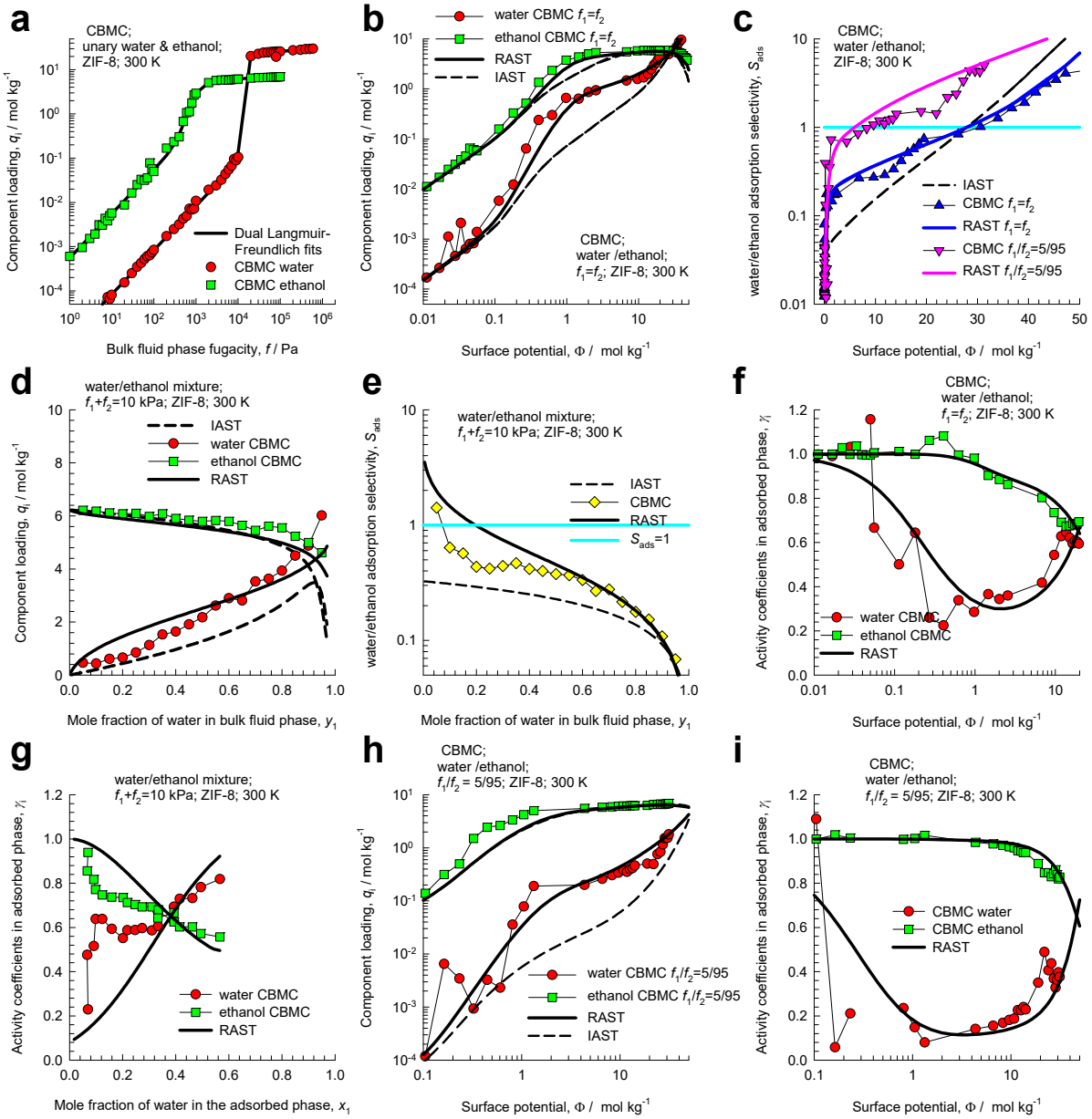

Figure S57. CBMC simulation data on component loadings, selectivities, and activity coefficients for Campaigns A (y_1= 0.5 and y_1= 0.05) and Campaign B (f_t= 10 kPa) for water(1)/ethanol(2) mixtures in ZIF-8 at 300 K The CBMC data are compared with RAST calculations using fitted Margules parameters. The dashed lines are IAST calculations.

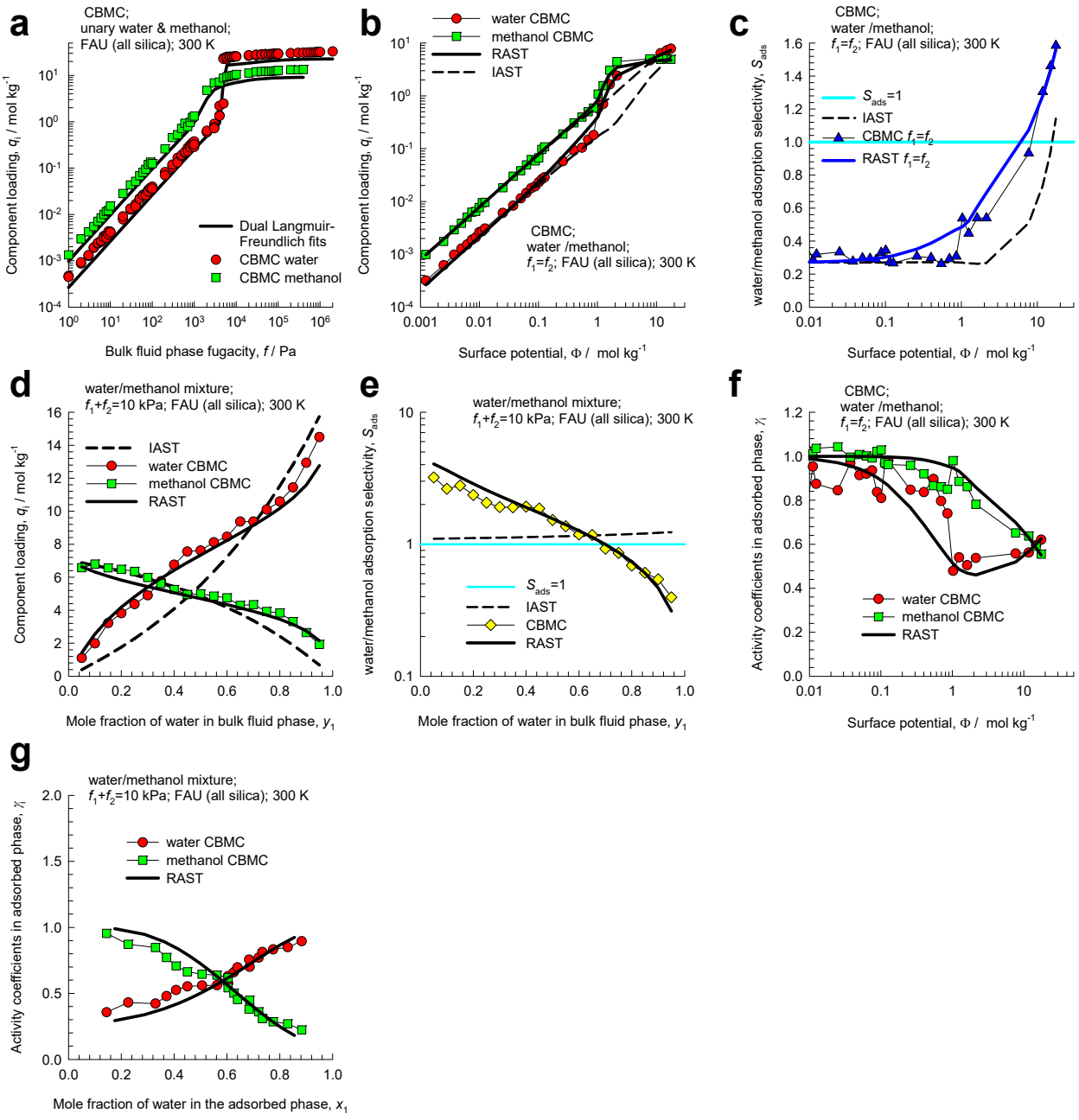

Figure S58. CBMC simulation data on component loadings, selectivities, and activity coefficients for Campaign A (y_1= 0.5) and Campaign B (f_t= 10 kPa) for water(1)/methanol(2) mixtures in FAU (all silica) at 300 K The CBMC data are compared with RAST calculations using fitted Margules parameters. The dashed lines are IAST calculations.

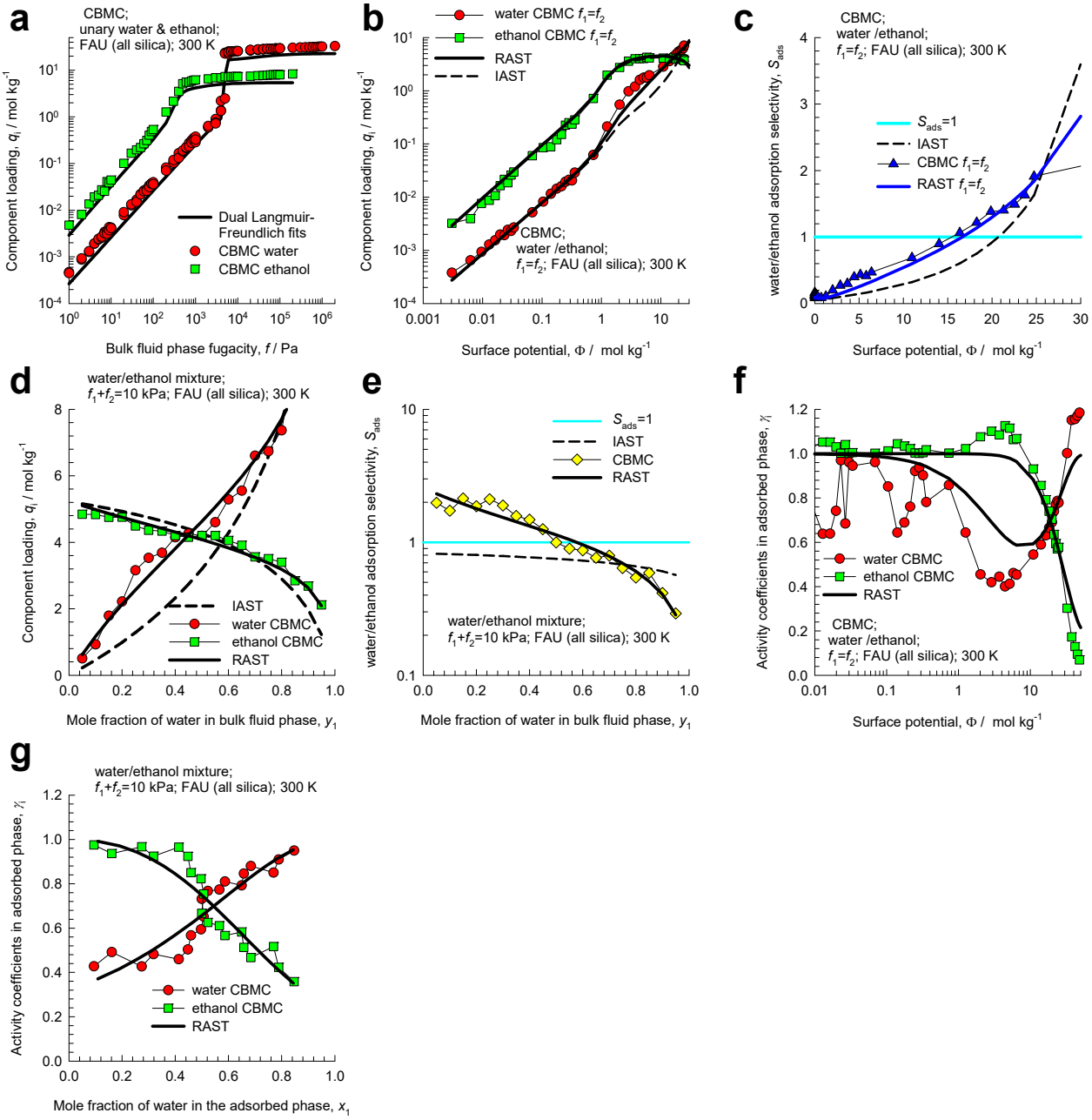

Figure S59. CBMC simulation data on component loadings, selectivities, and activity coefficients for Campaign A (y_1= 0.5) and Campaign B (f_t= 10 kPa) for water(1)/ethanol(2) mixtures in FAU (all silica) at 300 K The CBMC data are compared with RAST calculations using fitted Margules parameters. The dashed lines are IAST calculations.

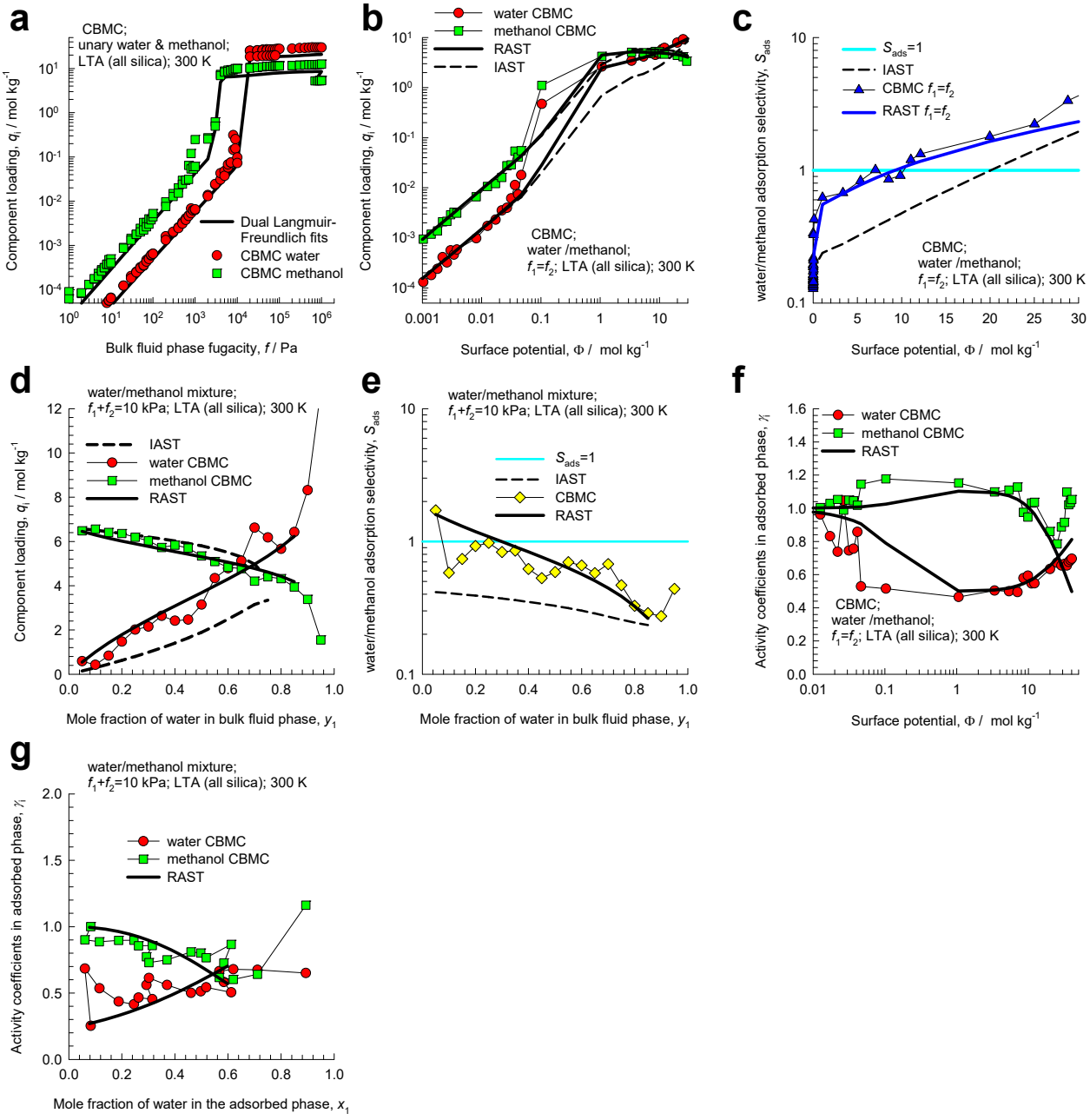

Figure S60. CBMC simulation data on component loadings, selectivities, and activity coefficients for Campaign A (y_1= 0.5) and Campaign B (f_t= 10 kPa) for water(1)/methanol(2) mixtures in LTA (all silica) at 300 K The CBMC data are compared with RAST calculations using fitted Margules parameters. The dashed lines are IAST calculations.

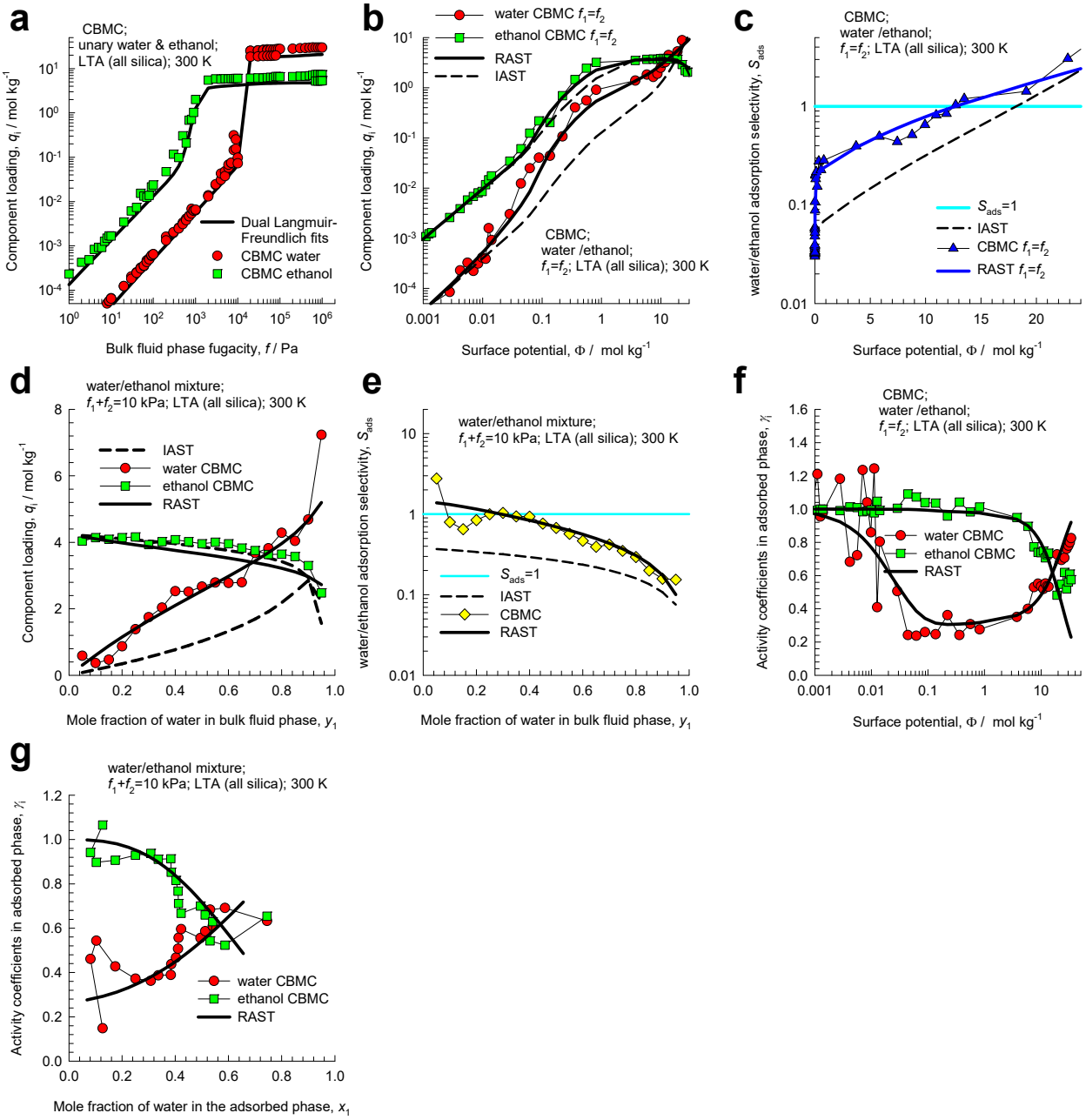

Figure S61. CBMC simulation data on component loadings, selectivities, and activity coefficients for Campaign A (y_1= 0.5) and Campaign B (f_t= 10 kPa) for water(1)/ethanol(2) mixtures in LTA (all silica) at 300 K The CBMC data are compared with RAST calculations using fitted Margules parameters. The dashed lines are IAST calculations.

8 MD Simulations of Water/Alcohol Diffusion

MD simulations were carried to determine the self-diffusivities, $D_{i,self}$, of water, methanol, and ethanol in four different zeolites: CHA, DDR, LTA (all silica), and FAU (all silica) at 300 K. For each zeolite, the $D_{i,self}$ were determined for unary water, methanol, and ethanol as a function of the total loading, expressed as molecules per cage. For a fixed total mixture loading, the self-diffusivities, $D_{i,self}$, were also determined for binary water(1)/methanol(2) , and water(1)/ethanol(2) mixtures. The MD data are presented in the following Figures.

CHA: Figure S62

DDR: Figure S63

LTA (all silica) Figure S64

FAU (all silica) Figure S65

From the self-diffusivities in binary mixtures, the diffusion selectivity $S_{diff} = \frac{D_{1,self}}{D_{2,self}}$ is determined for each binary mixture as a function of the adsorbed phase mole fractions.

The values of the diffusion selectivities thus determined are multiplied by the adsorption selectivity $S_{ads} = \frac{q_1/q_2}{f_1/f_2}$ for mixture adsorption at total fugacity of 10 kPa in order to determine the permeation selectivities $S_{perm} = S_{ads} \times S_{diff}$; $S_{ads} = \frac{q_1/q_2}{f_1/f_2}$ in the following Figures.

Figure S32f: Water/methanol mixture in CHA

Figure S33f:Water/ethanol mixture in CHA

Figure S34f: Water/methanol mixture in DDR

Figure S35f:Water/ethanol mixture in DDR

Figure S41f: Water/methanol mixture in all-silica LTA

Figure S42f: Water/ethanol mixture in all-silica LTA

Watch also the presentations titled **Diffusion in LTA-4A and 5A Zeolites, Diffusion in Cage-Type Zeolites, Inter-cage Hopping in DDR Zeolite, Inter-cage Hopping in CHA Zeolite, Mutual Slowing-Down in Water/Alcohol Mixture Diffusion, Hydrogen Bonding Influences on Adsorption, ZIF-8 Membranes, Visualizing Motion of Guest Molecules in ZIF-8, Diffusion in Micropores, Zeolite Membrane Permeation, Unary Diffusivities in Micropores, Water/Alcohol Membrane Pervaporation, Co-operative Mixture Adsorption in Zeolites & MOFs**

on YouTube https://www.youtube.com/@rajamanikrishna250/videos

8.1 List of Figures for MD Simulations of Water/Alcohol Diffusion

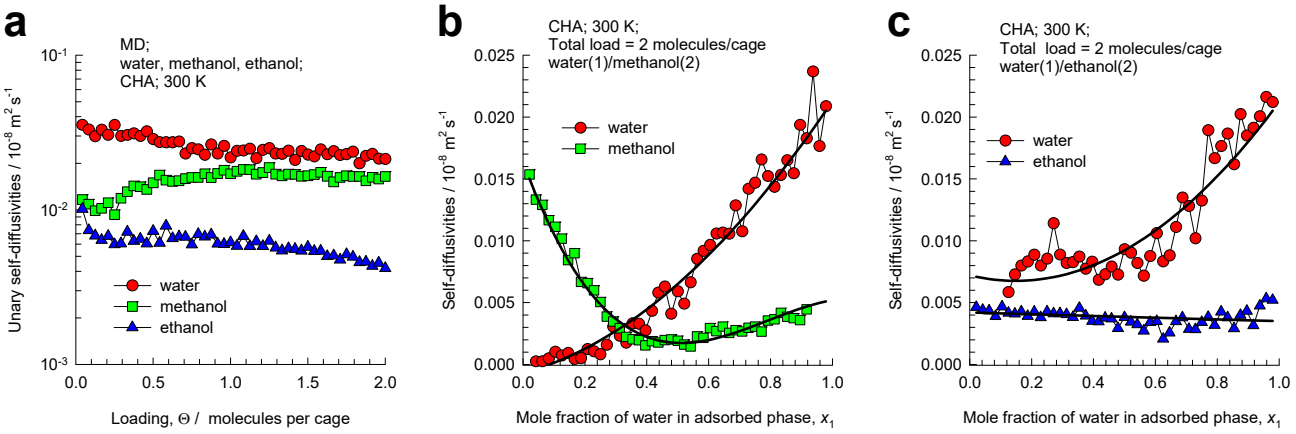

Figure S62. (a) MD simulations of unary self-diffusivities for water, methanol, and ethanol in CHA zeolite at 300 K as function of the loadings expressed in molecules per cage. (b, c) MD simulations of self-diffusivities, $D_{i,self}$, in binary (b) water(1)/methanol(2), and (c) water(1)/ethanol(2) mixtures at a total loading, Θ_t, that is held constant at a value of 2 molecules cage^{-1}, plotted as function of the mole fraction of water in the adsorbed phase mixture.

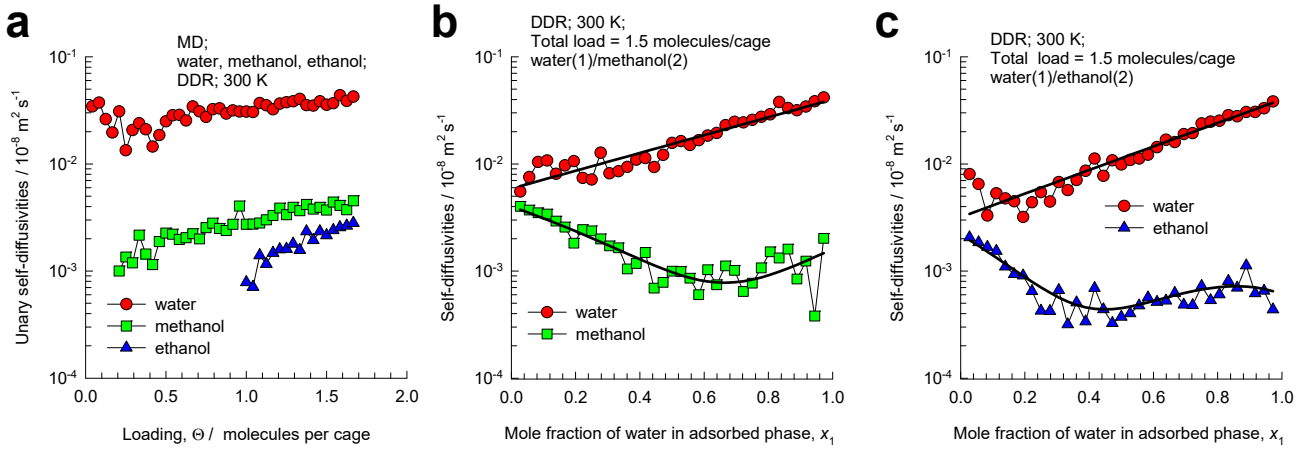

Figure S63. (a) MD simulations of unary self-diffusivities for water, methanol, and ethanol in DDR zeolite at 300 K as function of the loadings expressed in molecules per cage. (b, c) MD simulations of self-diffusivities, $D_{i,self}$, in binary (b) water(1)/methanol(2), and (c) water(1)/ethanol(2) mixtures at a total loading, Θ_t, that is held constant at a value of 1.5 molecules cage^{-1}, plotted as function of the mole fraction of water in the adsorbed phase mixture.

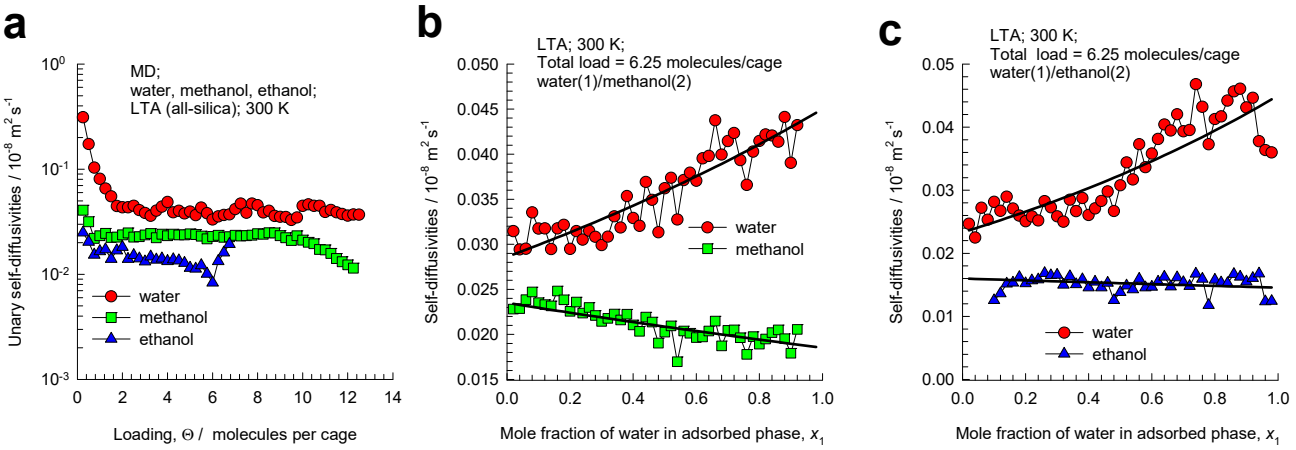

Figure S64. (a) MD simulations of unary self-diffusivities for water, methanol, and ethanol in LTA (all-silica) zeolite at 300 K as function of the loadings expressed in molecules per cage. (b, c) MD simulations of self-diffusivities, $D_{i,self}$, in binary (b) water(1)/methanol(2), and (c) water(1)/ethanol(2) mixtures at a total loading, Θ_t, that is held constant at a value of 6.25 molecules cage^{-1}, plotted as function of the mole fraction of water in the adsorbed phase mixture.

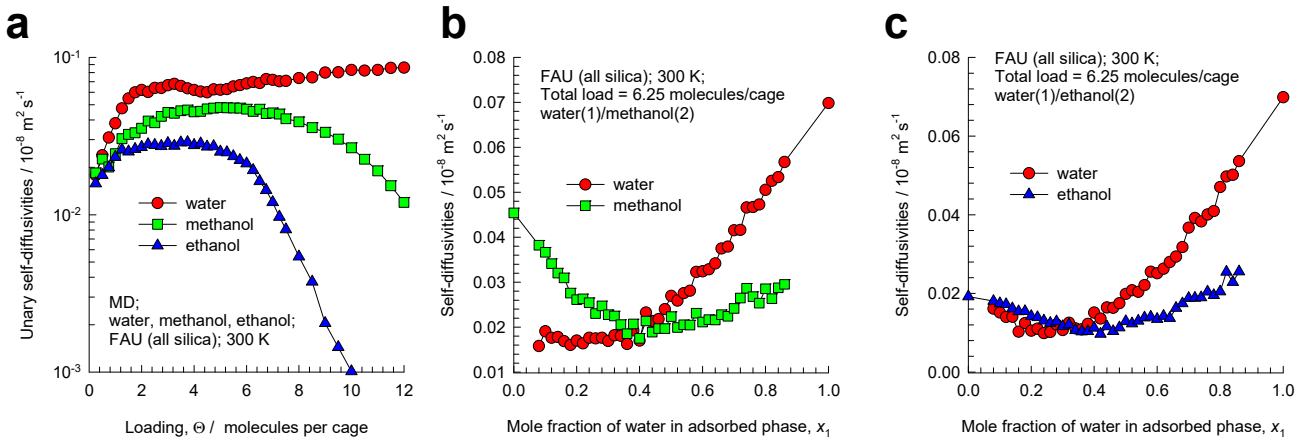

Figure S65. (a) MD simulations of unary self-diffusivities for water, methanol, and ethanol in FAU (all-silica) zeolite at 300 K as function of the loadings expressed in molecules per cage. (b, c) MD simulations of self-diffusivities, $D_{i,self}$, in binary (b) water(1)/methanol(2), and (c) water(1)/ethanol(2) mixtures at a total loading, Θ_t, that is held constant at a value of 6.25 molecules cage^{-1}, plotted as function of the mole fraction of water in the adsorbed phase mixture.

9 Maxwell-Stefan Modeling of Membrane Permeation

9.1 The Maxwell-Stefan (M-S) description of intra-crystalline diffusion

Within micro-porous crystalline materials, such as zeolites, metal-organic frameworks (MOFs), and zeolitic imidazolate frameworks (ZIFs), the guest molecules exist in the adsorbed phase. The Maxwell-Stefan (M-S) equations for *n*-component diffusion in porous materials is applied in the following manner[58-65]

$$-\rho\frac{q_i}{RT}\frac{\partial\mu_i}{\partial r}=\sum_{\substack{j=1\\ j\neq i}}^{n}\frac{x_jN_i-x_iN_j}{Đ_{ij}}+\frac{N_i}{Đ_i};\qquad i=1,2,..n \tag{S48}$$

where ρ is the framework density with units of kg m^{-3}, q_i is the molar loading of adsorbate, and the adsorbed phase mole fractions are $x_i=q_i/q_t$ where q_t is the *total* mixture loading $q_t=\sum_{i=1}^{n}q_i$. The fluxes N_i in equations (S48) are defined in terms of the moles transported per m^2 of the *total surface of crystalline material*.

An important, persuasive, argument for the use of the M-S formulation for mixture diffusion is that the M-S diffusivity $Đ_i$ in mixtures can be estimated using information on the loading dependence of the corresponding unary diffusivity values, provided the comparison is made at the same value of the adsorption potential, calculated from IAST usingEquation (S7), or its proxy the occupancy, θ, calculated using equations (S29), (S30), (S31). Essentially this implies that the M-S diffusivity $Đ_i$ can be estimated from experimental data on *unary* diffusion in the porous material.

The *exchange coefficients* $Đ_{ij}$, defined by the first right member equations (S48), are introduced to quantify the coupling between species diffusion. At the molecular level, the $Đ_{ij}$ reflect how the facility for transport of species *i correlates* with that of species *j*.

The Maxwell-Stefan diffusion formulation is consistent with the theory of irreversible thermodynamics. The Onsager Reciprocal Relations imply that the M-S pair diffusivities are symmetric

$$Đ_{ij} = Đ_{ji} \tag{S49}$$

For mixture diffusion in cage-type zeolites with 8-ring windows (CHA, LTA, DDR, ERI) and in ZIF-8.MD simulations[24, 33, 34, 62, 66-72] have established that correlation effects are of negligible importance, and therefore eq (S48) simplifies to yield

$$N_i = -\rho Đ_i \frac{q_i}{RT}\frac{\partial \mu_i}{\partial r}; \qquad i = 1, 2, ..n \tag{S50}$$

9.2 Thermodynamic correction factors

At thermodynamic equilibrium, the chemical potential of component *i* in the bulk fluid mixture equals the chemical potential of that component in the adsorbed phase. For the bulk fluid phase mixture we have

$$\frac{1}{RT}\frac{\partial \mu_i}{\partial r} = \frac{\partial \ln f_i}{\partial r} = \frac{1}{f_i}\frac{\partial f_i}{\partial r}; \qquad i = 1, 2, ..n \tag{S51}$$

The chemical potential gradients $\partial \mu_i / \partial r$ can be related to the gradients of the molar loadings, q_i, by defining thermodynamic correction factors Γ_{ij}

$$\frac{q_i}{RT}\frac{\partial \mu_i}{\partial r} = \sum_{j=1}^{n} \Gamma_{ij}\frac{\partial q_j}{\partial r}; \quad \Gamma_{ij} = \frac{q_i}{f_i}\frac{\partial f_i}{\partial q_j}; \qquad i, j = 1, ...n \tag{S52}$$

The thermodynamic correction factors Γ_{ij} can be calculated by differentiation of the model describing mixture adsorption equilibrium. For water/alcohol permeation, the Real Adsorbed Solution Theory (RAST) is the preferred method for estimation of mixture adsorption equilibrium.

Watch also the presentations titled **Diffusion in Micropores, Zeolite Membrane Permeation, Unary Diffusivities in Micropores, Water/Alcohol Membrane Pervaporation, Transient Mixture Permeation across Microporous Membranes, Transient Mixture Permeation across Microporous Membranes, A Tutorial on Membrane Permeation, Membrane Selectivity vs Permeance, Diffusion in Microporous Materials, The Spreading Pressure Concept for Microporous Membranes**

on YouTube https://www.youtube.com/@rajamanikrishna250/videos

9.3 M-S formulation for binary mixture diffusion

For binary mixture diffusion inside microporous crystalline materials the Maxwell-Stefan equations (S50) are written

$$N_1 = -\rho Đ_1 \frac{q_1}{RT}\frac{\partial \mu_1}{\partial r}$$
$$N_2 = -\rho Đ_2 \frac{q_2}{RT}\frac{\partial \mu_2}{\partial r} \quad \text{(S53)}$$

In two-dimensional matrix notation, eq (S52) take the form

$$\begin{pmatrix} \frac{q_1}{RT}\frac{\partial \mu_1}{\partial r} \\ \frac{q_2}{RT}\frac{\partial \mu_2}{\partial r} \end{pmatrix} = [\Gamma] \begin{pmatrix} \frac{\partial q_1}{\partial r} \\ \frac{\partial q_2}{\partial r} \end{pmatrix} \quad \text{(S54)}$$

. Equation (S53) can be re-cast into 2-dimensional matrix notation

$$\begin{pmatrix} N_1 \\ N_2 \end{pmatrix} = -\rho \begin{bmatrix} Đ_1 & 0 \\ 0 & Đ_2 \end{bmatrix} \begin{bmatrix} \Gamma_{11} & \Gamma_{12} \\ \Gamma_{21} & \Gamma_{22} \end{bmatrix} \begin{pmatrix} \frac{\partial q_1}{\partial r} \\ \frac{\partial q_2}{\partial r} \end{pmatrix} \quad \text{(S55)}$$

9.4 Simulation methodology for transient membrane permeation

Pervaporation of water/alcohol mixtures is an important process in the processing industry, and a wide variety of membrane materials has been used, including polymers, zeolites (e.g. CHA, LTA, MFI, FAU, DDR), ZIF-8, and mixed matrix membranes.[11, 73-75]

The transient permeation fluxes N_i, defined in terms of the cross-sectional area of the membrane, are obtained by solving the set of partial differential equations

$$\frac{\partial q_i(z,t)}{\partial t} = -\frac{1}{\rho}\frac{\partial}{\partial r}\left(N_i\right) \quad \text{(S56)}$$

where r is the distance coordinate along the direction of membrane thickness. In the general case when correlations are of importance, we need to use the M-S eq (S52) to describe the permeation fluxes.

For host materials such as DDR, CHA, ZIF-8, LTA-4A, correlations are of negligible importance because the guest molecules jump one-at-a-time across the narrow windows; in these circumstances, the simplified eq (S55) used to describe permeation fluxes.

The boundary conditions are the partial fugacities and component molar loadings at the upstream (z = 0) and downstream ($r = \delta$) faces of the membrane; see schematic in Figure S66

$$\begin{aligned} r &= 0; \quad f_i = f_{i0}; \quad q_i = q_{i0} \\ r &= \delta; \quad f_i = f_{i\delta}; \quad q_i = q_{i\delta} \end{aligned} \tag{S57}$$

The permeability of component i is defined as

$$\Pi_i = \frac{N_i}{\Delta f_i / \delta} \tag{S58}$$

where N_i is the permeation flux and $\Delta f_i = f_i - f_{i\delta}$ is the difference in the partial fugacities between the upstream $\left(f_i\right)$ and downstream $\left(f_{i\delta}\right)$ faces of the membrane layer of thickness δ. The membrane permeation selectivity, S_{perm}, is defined as the ratio of the component permeabilities

$$S_{perm} = \frac{N_1/\Delta f_1}{N_2/\Delta f_2} = \frac{\Pi_1}{\Pi_2} \tag{S59}$$

The solution of eqs (S55), (S56), and (S57) requires discretization of the membrane layer into slices, typically about 100 in number. Combination of the discretized partial differential eqs along with algebraic equations describing mixture adsorption equilibrium, results in a set of differential-algebraic equations (DAEs), which are solved using BESIRK.[76] BESIRK is a sparse matrix solver, based on the semi-implicit Runge-Kutta method originally developed by Michelsen,[77] and extended with the Bulirsch-Stoer extrapolation method.[78] Use of BESIRK improves the numerical solution efficiency in solving the set of DAEs. The evaluation of the sparse Jacobian required in the numerical algorithm is largely based on analytic expressions.[79] Further details of the numerical procedures used in this work, are provided by Krishna and co-workers;[79-82] interested readers are referred to our website that contains the numerical details.[80]

9.5 Water/ethanol permeation across DDR membrane

Membrane permeation simulations for 5/95 water/ethanol mixtures across a DDR membrane at 300 K were undertaken. The input parameters used in the simulations are:

Framework density: $\rho = 1760$ kg m^{-3};

membrane thickness δ = 50 μm;

M-S diffusivity for water: $Đ_1 = 1\times10^{-10}$ m^2 s^{-1}

M-S diffusivity for ethanol: $Đ_1 = 1\times10^{-11}$ m^2 s^{-1}

The ratio of partial fugacities in upstream compartment $f_1/f_2 = 5/95$.

The partial fugacities in the downstream compartment are maintained vanishingly small: $f_1 = f_2 = 2$ Pa.

The water/ethanol mixture adsorption equilibrium in DDR requires the use of the RAST in order to quantify the deviations from thermodynamic ideality. The CBMC data for mixture adsorption, in Campaigns A and B were used to determine the Margules parameters. In Figure S55, the RAST model calculations are compared with the CBMC simulated data for both Campaigns A and B. The Margules fits are of good accuracy.

Figure S67a shows calculations of the elements of the matrix of thermodynamic correction factors. It is clear that the off-diagonal elements are of significant importance.

The continuous solid lines in Figure S67b show the component permeabilities for water and ethanol for steady-state permeation of 5/95 water/ethanol mixtures across a DDR membrane at 300 K with varying total upstream fugacity, $f_t = f_1 + f_2$ with values ranging from 1 kPa to 100 kPa. The mixture adsorption equilibrium is determined using the RAST, taking due account of thermodynamic coupling, quantified by $\begin{bmatrix} \Gamma_{11} & \Gamma_{12} \\ \Gamma_{21} & \Gamma_{22} \end{bmatrix}$. The dashed lines in Figure S67b are obtained in simulations in which the thermodynamic coupling effects are ignored and $\Gamma_{ij} = \delta_{ij}$. Neglecting thermodynamic coupling effects results in

significant underestimation of the ethanol permeabilities. The corresponding values of the permeation selectivity, $S_{perm} = \frac{N_1/\Delta f_1}{N_2/\Delta f_2} = \frac{\Pi_1}{\Pi_2}$ are shown in Figure S67b. Neglect of thermodynamic coupling results in severe overestimation of the water/ethanol permeation selectivity.

For the specific choice of total upstream fugacity = 10 kPa, the simulation results for transient permeation of 5/95 water/ethanol mixtures across a DDR membrane at 300 K are shown in Figure S67d. Noteworthily, the water flux exhibits a pronounced overshoot during the early stages of the transient approach to steady state. If thermodynamic coupling effects are ignored, the transient overshoots in the water flux is not observed.

Transient overshoots in the fluxes of the more mobile species have been reported in a number of experimental studies of binary mixture permeation. Geus et al.[83] report experimental data on transient 50/50 CH_4/nC_4H_{10} mixture permeation across an MFI membrane; the flux of the more mobile CH_4 exhibits a pronounced overshoot during the approach to steady state. The experimental data of Bakker[84] for transient permeation H_2/nC_4H_{10} mixture across an MFI membrane shows a maximum in the flux of the more mobile H_2. For permeation of nC6/2MP mixtures across an MFI membrane, Matsufuji et al.[85] report experimental data showing overshoots in the nC6 flux during transient approach to steady-state. The experimental data of Matsufuji et al.[86] for transient permeation of (a) 50/50 m-xylene/p-xylene, and (b) 24/50/25 p-xylene/m-xylene/o-xylene mixtures across MFI membrane show a maximum in the flux of p-xylene which is the most mobile of the three xylene isomers. For nC_4H_{10}/iso-C_4H_{10} mixture permeation across a MFI membrane, curious overshoots and undershoots, in the transient retentate and permeate concentrations have been reported in the experiments of Courthial et al.[87]

Thermodynamic non-idealities have a significant influence on the permeation fluxes. In order to demonstrate this Figure S68a,b present simulation of steady-state permeation of 5/95 water(1)/ethanol(2) mixture across a DDR membrane at 300 K. In (a) the component permeabilities are plotted as function of the total upstream fugacity. In (b) the permeation selectivity is plotted as a function of the total upstream fugacity. The continuous solid lines are simulations taking using the RAST. The dashed lines are obtained

in simulations using the IAST. For both scenarios, the thermodynamic coupling effects are duly accounted for. Due to thermodynamic non-idealities, the water permeabilities are significantly enhanced. The ethanol permeabilities are practically unaffected by thermodynamic non-idealities. We note that the inclusion of thermodynamic non-idealities and use of RAST result is significant enhancements in the permeation selectivities in favor of water.

Figure S68c compares the RAST and IAST simulations of transient permeation of 5/95 water(1)/ethanol(2) mixture across a DDR membrane at 300 K; the total upstream fugacity is maintained at 10 kPa.

9.6 Water/ethanol permeation across CHA membrane

Membrane permeation simulations for 5/95 water/ethanol mixtures across a CHA membrane at 300 K were undertaken. The input parameters used in the simulations are:

Framework density: $\rho = 1444$ kg m^{-3};

membrane thickness δ = 50 μm

M-S diffusivity for water: $Đ_1 = 1\times10^{-10}$ m^2 s^{-1}

M-S diffusivity for ethanol: $Đ_1 = 1\times10^{-11}$ m^2 s^{-1}

The ratio of partial fugacities in upstream compartment $f_1/f_2 = 5/95$.

The partial fugacities in the downstream compartment are maintained vanishingly small: $f_1 = f_2 = 2$ Pa.

The water/ethanol mixture adsorption equilibrium in CHA requires the use of the RAST. The CBMC data for mixture adsorption, in Campaigns A and B were used to determine the Margules parameters. In Figure S53, the RAST model calculations are compared with the CBMC simulated data for both Campaigns A and B. The Margules fits are of good accuracy.

The continuous solid lines in Figure S69a show the component permeabilities for water and ethanol for steady-state permeation of 5/95 water/ethanol mixtures across a CHA membrane at 300 K with varying

total upstream fugacity, $f_t = f_1 + f_2$ with values ranging from 1 kPa to 100 kPa. The mixture adsorption equilibrium is determined using the RAST, taking due account of thermodynamic coupling, quantified by $\begin{bmatrix} \Gamma_{11} & \Gamma_{12} \\ \Gamma_{21} & \Gamma_{22} \end{bmatrix}$. The dashed lines in Figure S69a are obtained in simulations in which the thermodynamic coupling effects are ignored and $\Gamma_{ij} = \delta_{ij}$. Neglecting thermodynamic coupling effects results in significant underestimation of the ethanol permeabilities. The corresponding values of the permeation selectivity, $S_{perm} = \frac{N_1/\Delta f_1}{N_2/\Delta f_2} = \frac{\Pi_1}{\Pi_2}$ are shown in Figure S69b. Neglect of thermodynamic coupling results in severe overestimation of the water/ethanol permeation selectivity.

For the specific choice of total upstream fugacity = 10 kPa, the simulation results for transient permeation of 5/95 water/ethanol mixtures across a CHA membrane at 300 K are shown in Figure S69c. Noteworthily, the water flux exhibits a pronounced overshoot during the early stages of the transient approach to steady-state. If thermodynamic coupling effects are ignored, the transient overshoots in the water flux is not observed.

Thermodynamic non-idealities have a significant influence on the permeation fluxes. In order to demonstrate this Figure S70a,b present simulation of steady-state permeation of 5/95 water(1)/ethanol(2) mixture across a CHA membrane at 300 K. In (a) the component permeabilities are plotted as function of the total upstream fugacity. In (b) the permeation selectivity is plotted as a function of the total upstream fugacity. The continuous solid lines are simulations taking using the RAST. The dashed lines are obtained in simulations using the IAST. Due to thermodynamic non-idealities, the water permeabilities are significantly enhanced. The ethanol permeabilities are less influenced by thermodynamic non-idealities. For both scenarios, the thermodynamic coupling effects are duly accounted for. We note that the inclusion of thermodynamic non-idealities and use of RAST result is significant enhancements in the permeation selectivities in favor of water.

Figure S70c compares the RAST and IAST simulations of transient permeation of 5/95 water(1)/ethanol(2) mixture across a CHA membrane at 300 K; the total upstream fugacity is maintained at 10 kPa.

9.7 Water/ethanol permeation across ZIF-8 membrane

Membrane permeation simulations for 5/95 water/ethanol mixtures across a ZIF-8 membrane at 300 K were undertaken. The input parameters used in the simulations are:

Framework density: $\rho = 924$ kg m^{-3};

membrane thickness δ = 50 μm

M-S diffusivity for water: $Đ_1 = 1\times10^{-10}$ m^2 s^{-1}

M-S diffusivity for ethanol: $Đ_1 = 1\times10^{-11}$ m^2 s^{-1}

The ratio of partial fugacities in upstream compartment $f_1/f_2 = 5/95$.

The partial fugacities in the downstream compartment are maintained vanishingly small: $f_1 = f_2 = 2$ Pa.

The water/ethanol mixture adsorption equilibrium in ZIF-8 requires the use of the RAST. The CBMC data for mixture adsorption, in Campaigns A and B were used to determine the Margules parameters. In Figure S57, the RAST model calculations are compared with the CBMC simulated data for both Campaigns A and B. The Margules fits are of good accuracy.

Thermodynamic non-idealities have a significant influence on the permeation fluxes. In order to demonstrate this Figure S71a,b present simulation of steady-state permeation of 5/95 water(1)/ethanol(2) mixture across a ZIF-8 membrane at 300 K. In (a) the component perrmeabilities are plotted as function of the total upstream fugacity. In (b) the permeation selectivity is plotted as a function of the total upstream fugacity. The continuous solid lines are simulations taking using the RAST. The dashed lines are obtained in simulations using the IAST. For both scenarios, the thermodynamic coupling effects are duly accounted for. Due to thermodynamic non-idealities, the water permeabilities are significantly enhanced.

The ethanol permeabilities are practically unaffected by thermodynamic non-idealities. We note that the inclusion of thermodynamic non-idealities and use of RAST result is significant enhancements in the permeation selectivities in favor of water.

9.8 Water/ethanol permeation across LTA-4A membrane

Membrane permeation simulations for 5/95 water/ethanol mixtures across a LTA-4A membrane at 333 K were undertaken. The input parameters used in the simulations are:

Framework density: $\rho = 1529$ kg m^{-3};

membrane thickness δ = 50 μm;

M-S diffusivity for water: $Đ_1 = 1 \times 10^{-10}$ m^2 s^{-1}

M-S diffusivity for ethanol: $Đ_1 = 1 \times 10^{-11}$ m^2 s^{-1}

The ratio of partial pressures in upstream compartment $p_1 / p_2 = 5/95$.

The partial pressures in the downstream compartment are maintained vanishingly small: $p_1 = p_2 = 2$ Pa.

For the choice of total upstream pressure = 2.1 kPa, the simulation results for transient permeation of 5/95 water/ethanol mixtures across a LTA-4A membrane are shown in Figure S72. Noteworthily, the water flux exhibits a pronounced overshoot during the early stages of the transient approach to steady-state. If thermodynamic coupling effects are ignored, the transient overshoots in the water flux is not observed.

9.9 List of Figures for Maxwell-Stefan Modeling of Membrane Permeation

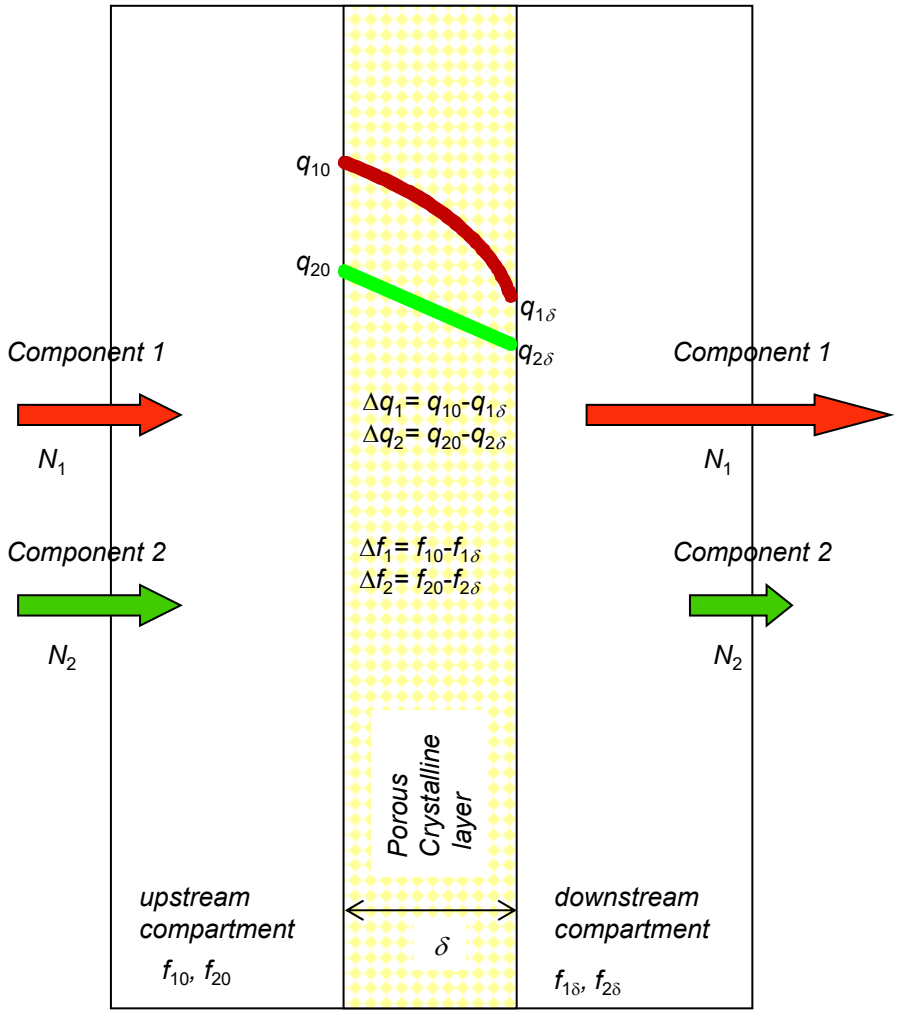

Figure S66. Schematic of membrane permeation unit.

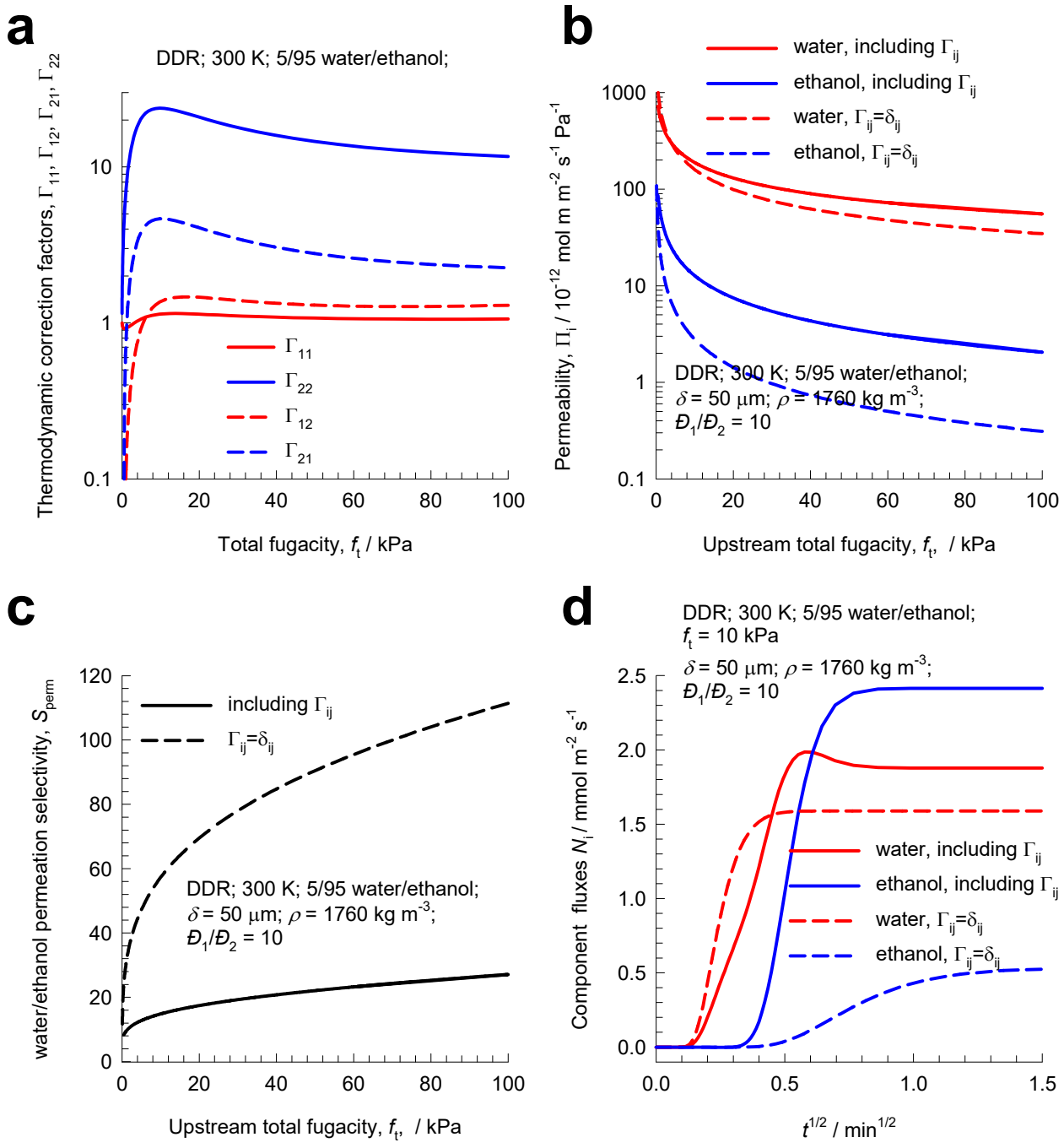

Figure S67. (a) Thermodynamic correction factors for 5/95 water(1)/ethanol(2) mixture across a DDR membrane at 300 K. (b, c) Simulation of steady-state permeation of 5/95 water(1)/ethanol(2) mixture across a DDR membrane at 300 K. In (b) the component permeabilities are plotted as function of the total upstream fugacity. In (c) the permeation selectivity is plotted as a function of the total upstream fugacity. (d) Simulations of transient permeation of 5/95 water(1)/ethanol(2) mixture across a DDR membrane at

300 K; the total upstream fugacity is maintained at 10 kPa. The mixture adsorption equilibrium is determined using the RAST. The continuous solid lines are simulations taking due account of thermodynamic coupling, quantified by $\begin{bmatrix} \Gamma_{11} & \Gamma_{12} \\ \Gamma_{21} & \Gamma_{22} \end{bmatrix}$. The dashed lines are obtained in simulations in which the thermodynamic coupling effects are ignored and $\Gamma_{ij} = \delta_{ij}$.

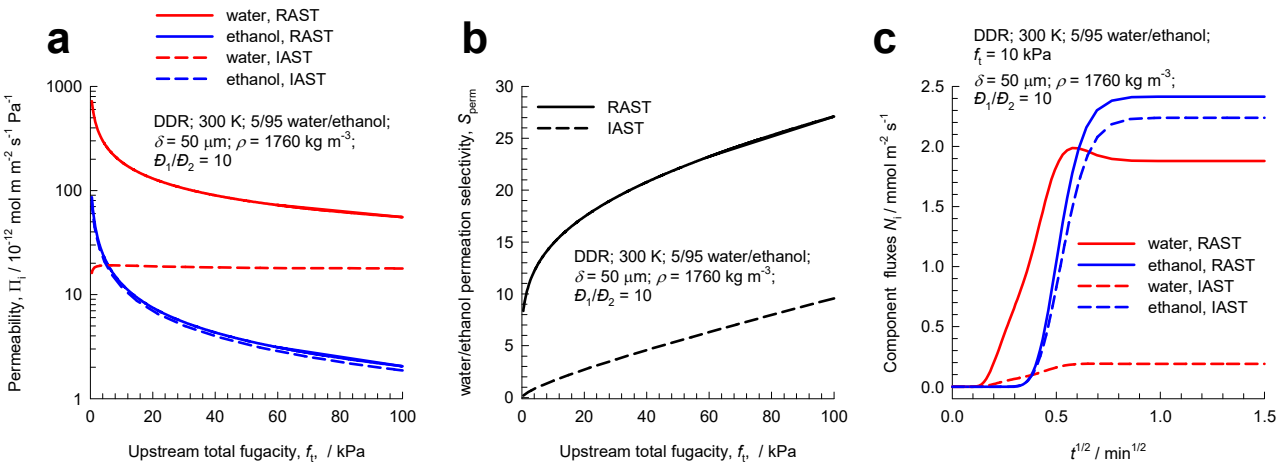

Figure S68. (a, b) Simulation of steady-state permeation of 5/95 water(1)/ethanol(2) mixture across a DDR membrane at 300 K. In (a) the component permeabilities are plotted as function of the total upstream fugacity. In (b) the permeation selectivity is plotted as a function of the total upstream fugacity. (c) Simulations of transient permeation of 5/95 water(1)/ethanol(2) mixture across a DDR membrane at 300 K; the total upstream fugacity is maintained at 10 kPa. The continuous solid lines are simulations taking using the RAST. The dashed lines are obtained in simulations using the IAST. For both scenarios, the thermodynamic coupling effects are duly accounted for.

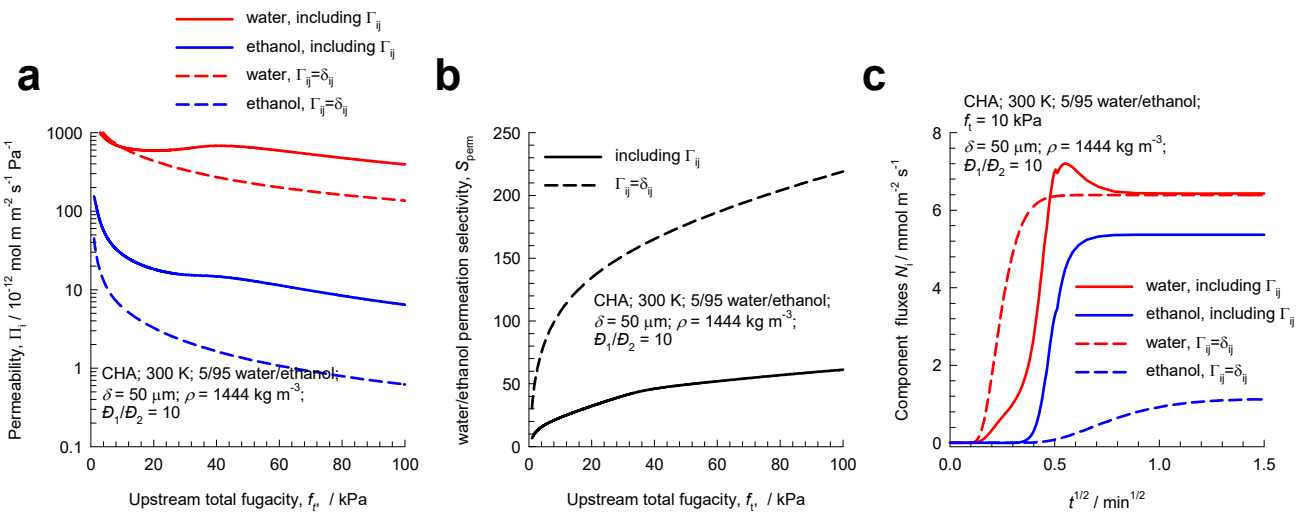

Figure S69. (a, b) Simulation of steady-state permeation of 5/95 water(1)/ethanol(2) mixture across a CHA membrane at 300 K. In (a) the component permeabilities are plotted as function of the total upstream fugacity. In (b) the permeation selectivity is plotted as a function of the total upstream fugacity. (c) Simulations of transient permeation of 5/95 water(1)/ethanol(2) mixture across a CHA membrane at 300 K; the total upstream fugacity is maintained at 10 kPa. The mixture adsorption equilibrium is determined using the RAST. The continuous solid lines are simulations taking due account of thermodynamic coupling, quantified by $\begin{bmatrix} \Gamma_{11} & \Gamma_{12} \\ \Gamma_{21} & \Gamma_{22} \end{bmatrix}$. The dashed lines are obtained in simulations in which the thermodynamic coupling effects are ignored and $\Gamma_{ij} = \delta_{ij}$.

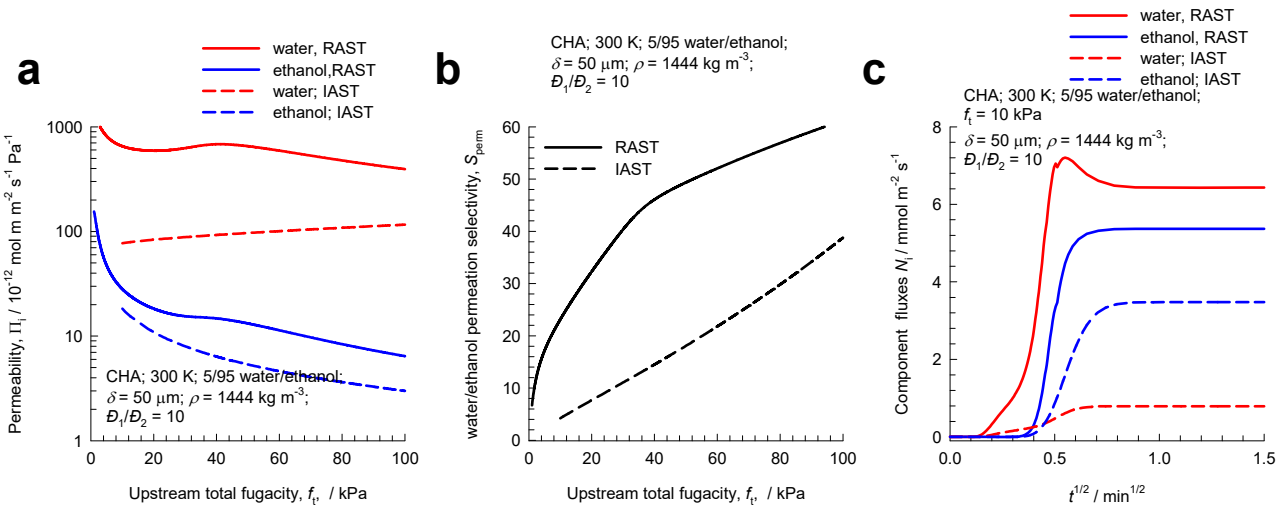

Figure S70. (a, b) Simulation of steady-state permeation of 5/95 water(1)/ethanol(2) mixture across a CHA membrane at 300 K. In (a) the component permeabilities are plotted as function of the total upstream fugacity. In (b) the permeation selectivity is plotted as a function of the total upstream fugacity. (c) Simulations of transient permeation of 5/95 water(1)/ethanol(2) mixture across a CHA membrane at 300 K; the total upstream fugacity is maintained at 10 kPa. The continuous solid lines are simulations taking using the RAST. The dashed lines are obtained in simulations using the IAST. For both scenarios, the thermodynamic coupling effects are duly accounted for.

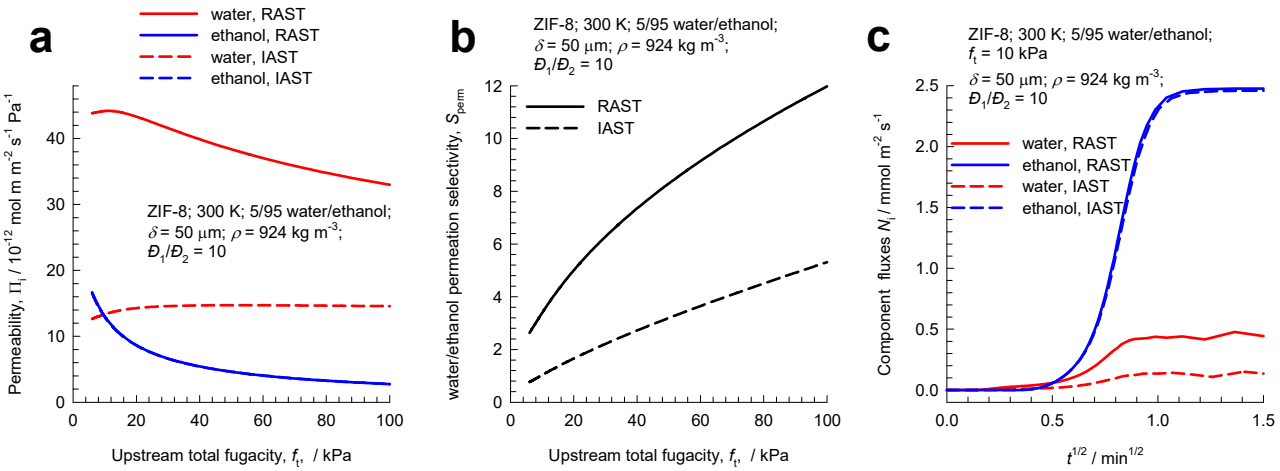

Figure S71. (a, b) Simulation of steady-state permeation of 5/95 water(1)/ethanol(2) mixture across a ZIF-8 membrane at 300 K. In (a) the component permeabilities are plotted as function of the total upstream fugacity. In (b) the permeation selectivity is plotted as a function of the total upstream fugacity. (c) Simulations of transient permeation of 5/95 water(1)/ethanol(2) mixture across a CHA membrane at 300 K; the total upstream fugacity is maintained at 10 kPa. The continuous solid lines are simulations taking using the RAST. The dashed lines are obtained in simulations using the IAST. For both scenarios, the thermodynamic coupling effects are duly accounted for.

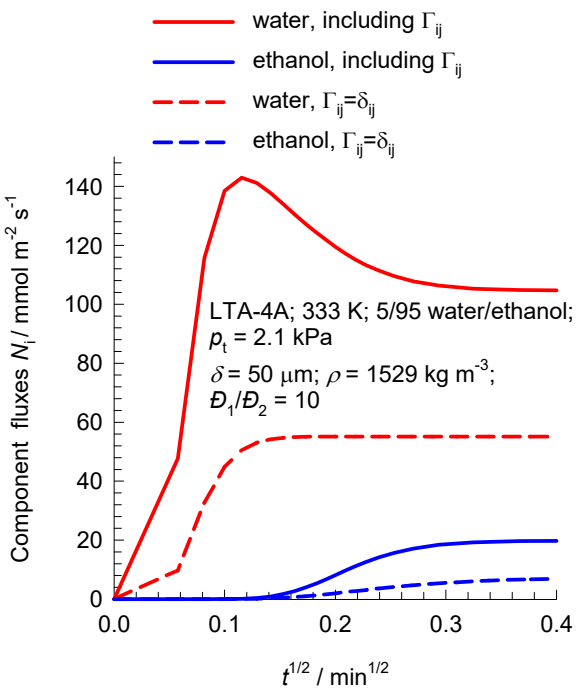

Figure S72. Simulations of transient permeation of 5/95 water(1)/ethanol(2) mixture across a LTA-4A membrane at 333 K; the total upstream pressure is maintained at 2.1 kPa. The mixture adsorption equilibrium is determined using the RAST. The continuous solid lines are simulations taking due account of thermodynamic coupling, quantified by $\begin{bmatrix} \Gamma_{11} & \Gamma_{12} \\ \Gamma_{21} & \Gamma_{22} \end{bmatrix}$. The dashed lines are obtained in simulations in which the thermodynamic coupling effects are ignored and $\Gamma_{ij} = \delta_{ij}$.

10 Nomenclature

Latin alphabet

A	surface area per kg of framework, $m^2\ kg^{-1}$
b	Langmuir-Freundlich constant, $Pa^{-\nu}$
C	constant used in eq (S38), $kg\ mol^{-1}$
$D_{i,self}$	self-diffusivity of species i, $m^2\ s^{-1}$
f_i	partial fugacity of species i, Pa
f_t	total fugacity of bulk fluid mixture, Pa
n	number of species in the mixture, dimensionless
P_i^0	sorption pressure, Pa
q_i	molar loading of species i, $mol\ kg^{-1}$
q_t	total molar loading of mixture, $mol\ kg^{-1}$
$q_{i,sat}$	molar loading of species i at saturation, $mol\ kg^{-1}$
$q_{sat,mix}$	saturation capacity of mixture, $mol\ kg^{-1}$
R	gas constant, 8.314 $J\ mol^{-1}\ K^{-1}$
S_{ads}	adsorption selectivity, dimensionless
S_{diff}	diffusion selectivity, dimensionless
S_{perm}	permeation selectivity, dimensionless
T	absolute temperature, K
V_p	pore volume, $m^3\ kg^{-1}$
x_i	mole fraction of species i in adsorbed phase, dimensionless
y_i	mole fraction of species i in bulk fluid mixture, dimensionless

Greek letters

μ_i	molar chemical potential, J mol^{-1}
θ	fractional pore occupancy, dimensionless
ν	Freundlich exponent, dimensionless
π	spreading pressure, N m^{-1}
ρ	framework density, kg m^{-3}
Φ	surface potential, mol kg^{-1}

Subscripts

i,j	components in mixture
i	referring to component *i*
t	referring to total mixture
sat	referring to saturation conditions

Superscripts

0	referring to pure component loading

11 References

(1) Olson, D. H.; Camblor, M. A.; Vallaescusa, L. A.; Kuehl, G. H. Light hydrocarbon sorption properties of pure silica Si-CHA and ITQ-3 and high silica ZSM-58. *Microporous Mesoporous Mater.* **2004**, *67*, 27-33.

(2) Hedin, N.; DeMartin, G. J.; Roth, W. J.; Strohmaier, K. G.; Reyes, S. C. PFG NMR self-diffusion of small hydrocarbons in high silica DDR, CHA and LTA structures. *Microporous Mesoporous Mater.* **2008**, *109*, 327-334.

(3) Ruthven, D. M.; Reyes, S. C. Adsorptive separation of light olefins from paraffins. *Microporous Mesoporous Mater.* **2007**, *104*, 59-66.

(4) Khalighi, M.; Chen, Y. F.; Farooq, S.; Karimi, I. A.; Jiang, J. W. Propylene/Propane Separation Using SiCHA. *Ind. Eng. Chem. Res.* **2013**, *52*, 3877-3892. https://doi.org/10.1021/ie3026955.

(5) Gies, H. Studies on clathrasils IX: Crystal structure of decadodecasil 3 R, the missing link between zeolites and clathrasils. *Z. Kristallogr.* **1986**, *175*, 93-104.

(6) Chui, S. S. Y.; Lo, S. M. F.; Charmant, J. P. H.; Orpen, A. G.; Williams, I. D. A Chemically Functionalizable Nanoporous Material $[Cu_3(TMA)_2(H2O)_3]_n$. *Science* **1999**, *283*, 1148-1150.

(7) Yang, Q.; Zhong, C. Electrostatic-Field-Induced Enhancement of Gas Mixture Separation in Metal-Organic Frameworks: A Computational Study. *ChemPhysChem* **2006**, *7*, 1417-1421.

(8) Krishna, R.; van Baten, J. M. Hydrogen Bonding Effects in Adsorption of Water-alcohol Mixtures in Zeolites and the Consequences for the Characteristics of the Maxwell-Stefan Diffusivities. *Langmuir* **2010**, *26*, 10854-10867. https://doi.org/10.1021/la100737c.

(9) Krishna, R.; van Baten, J. M. Mutual slowing-down effects in mixture diffusion in zeolites. *J. Phys. Chem. C* **2010**, *114*, 13154-13156. https://doi.org/10.1021/jp105240c.

(10) Krishna, R.; van Baten, J. M. Highlighting Pitfalls in the Maxwell-Stefan Modeling of Water-Alcohol Mixture Permeation across Pervaporation Membranes. *J. Membr. Sci.* **2010**, *360*, 476-482. https://doi.org/10.1016/j.memsci.2010.05.049.

(11) Kuhn, J.; Castillo-Sanchez, J. M.; Gascon, J.; Calero, S.; Dubbeldam, D.; Vlugt, T. J. H.; Kapteijn, F.; Gross, J. Adsorption and Diffusion of Water, Methanol, and Ethanol in All-Silica DD3R: Experiments and Simulation. *J. Phys. Chem. C* **2009**, *113*, 14290-14301.

(12) Rick, S. W. A Reoptimization of the Five-site Water Potential (TIP5P) for use with Ewald Sums. *J. Chem. Phys.* **2004**, *120*, 6085-6093.

(13) Chen, B.; Potoff, J. J.; Siepmann, J. I. Monte Carlo Calculations for Alcohols and Their Mixtures with Alkanes. Transferable Potentials for Phase Equilibria. 5. United-Atom Description of Primary, Secondary, and Tertiary Alcohols. *J. Phys. Chem. B* **2001**, *105*, 3093-3104.

(14) Kiselev, A. V.; Lopatkin, A. A.; Shul'ga, A. A. Molecular statistical calculation of gas adsorption by silicalite. *Zeolites* **1985**, *5*, 261-267.

(15) Mayo, S. L.; Olafson, B. D.; Goddard, W. A. DREIDING: A Generic Force Field for Molecular Simulations. *J. Phys. Chem.* **1990**, *94*, 8897-8909.

(16) Yang, Q.; Zhong, C. Understanding Hydrogen Adsorption in Metal-Organic Frameworks with Open Metal Sites: A Computational Study. *J. Phys. Chem. B* **2006**, *110*, 655-658.

(17) Jorgensen, W. L.; Maxwell, D. S.; Tirado-Rives, J. Development and Testing of the OPLS All-Atom Force Field on Conformational Energetics and Properties of Organic Liquids. *J. Am. Chem. Soc.* **1996**, *118*, 11225-11236.

(18) Zhou, M.; Wang, Q.; Zhang, L.; Liu, Y. C.; Kang, Y. Adsorption Sites of Hydrogen in Zeolitic Imidazolate Frameworks. *J. Phys. Chem. B* **2009**, *113*, 11049-11053.

(19) Xu, Q.; Zhong, C. A General Approach for Estimating Framework Charges in Metal-Organic Frameworks. *J. Phys. Chem. C* **2010**, *114*, 5035-5042.

(20) Frenkel, D.; Smit, B. *Understanding Molecular Simulations: From Algorithms to Applications*. 2nd Edition, Academic Press: San Diego, 2002; pp

(21) Gutierrez-Sevillano, J. J.; Calero, S.; Krishna, R. Selective Adsorption of Water from Mixtures with 1-Alcohols by Exploitation of Molecular Packing Effects in CuBTC. *J. Phys. Chem. C* **2015**, *119*, 3658-3666. https://doi.org/10.1021/jp512853w.

(22) Gutierrez-Sevillano, J. J.; Calero, S.; Krishna, R. Separation of Benzene from Mixtures with Water, Methanol, Ethanol, and Acetone: Highlighting Hydrogen Bonding and Molecular Clustering Influences in CuBTC. *Phys. Chem. Chem. Phys.* **2015**, *17*, 20114-20124. https://doi.org/10.1039/C5CP02726H.

(23) Zhang, C.; Yang, X. Molecular dynamics simulation of ethanol/water mixtures for structure and diffusion properties. *Fluid Phase Equilib.* **2005**, *231*, 1-10.

(24) Krishna, R.; Van Baten, J. M. Water/Alcohol Mixture Adsorption in Hydrophobic Materials: Enhanced Water Ingress caused by Hydrogen Bonding. *ACS Omega* **2020**, *5*, 28393-28402. https://doi.org/10.1021/acsomega.0c04491.

(25) Smith, W.; Forester, T. R.; Todorov, I. T. The DL_POLY Molecular Simulation Package. http://www.cse.clrc.ac.uk/msi/software/DL_POLY/index.shtml, Warrington, England, March 2006.

(26) Myers, A. L.; Prausnitz, J. M. Thermodynamics of Mixed Gas Adsorption. *A.I.Ch.E.J.* **1965**, *11*, 121-130.

(27) Ruthven, D. M. *Principles of Adsorption and Adsorption Processes*. John Wiley: New York, 1984; pp 1-433.

(28) Talu, O.; Myers, A. L. Rigorous Thermodynamic Treatment of Gas-Adsorption. *A.I.Ch.E.J.* **1988**, *34*, 1887-1893.

(29) Siperstein, F. R.; Myers, A. L. Mixed-Gas Adsorption. *A.I.Ch.E.J.* **2001**, *47*, 1141-1159.

(30) Krishna, R.; Van Baten, J. M. Elucidation of Selectivity Reversals for Binary Mixture Adsorption in Microporous Adsorbents. *ACS Omega* **2020**, *5*, 9031-9040. https://doi.org/10.1021/acsomega.0c01051.

(31) Krishna, R.; Van Baten, J. M. Using Molecular Simulations for Elucidation of Thermodynamic Non-Idealities in Adsorption of CO_2-containing Mixtures in NaX Zeolite. *ACS Omega* **2020**, *5*, 20535-20542. https://doi.org/10.1021/acsomega.0c02730.

(32) Krishna, R.; Van Baten, J. M. Investigating the Non-idealities in Adsorption of CO_2-bearing Mixtures in Cation-exchanged Zeolites. *Sep. Purif. Technol.* **2018**, *206*, 208-217. https://doi.org/10.1016/j.seppur.2018.06.009.

(33) Krishna, R.; van Baten, J. M. Using the Spreading Pressure to Inter-Relate the Characteristics of Unary, Binary and Ternary Mixture Permeation across Microporous Membranes. *J. Membr. Sci.* **2022**, *643*, 120049. https://doi.org/10.1016/j.memsci.2021.120049.

(34) Krishna, R.; van Baten, J. M. Segregation effects in adsorption of CO_2 containing mixtures and their consequences for separation selectivities in cage-type zeolites. *Sep. Purif. Technol.* **2008**, *61*, 414-423. https://doi.org/10.1016/j.seppur.2007.12.003.

(35) Krishna, R.; Van Baten, J. M. How Reliable is the Ideal Adsorbed Solution Theory for Estimation of Mixture Separation Selectivities in Microporous Crystalline Adsorbents? *ACS Omega* **2021**, *6*, 15499–15513. https://doi.org/10.1021/acsomega.1c02136.

(36) Krishna, R.; van Baten, J. M.; Baur, R. Highlighting the Origins and Consequences of Thermodynamic Nonidealities in Mixture Separations using Zeolites and Metal-Organic Frameworks. *Microporous Mesoporous Mater.* **2018**, *267*, 274-292. http://dx.doi.org/10.1016/j.micromeso.2018.03.013.

(37) Krishna, R. Occupancy Dependency of Maxwell−Stefan Diffusivities in Ordered Crystalline Microporous Materials. *ACS Omega* **2018**, *3*, 15743-15753. https://doi.org/10.1021/acsomega.8b02465.

(38) Talu, O.; Zwiebel, I. Multicomponent Adsorption Equilibria of Nonideal Mixtures. *A.I.Ch.E.J.* **1986**, *32*, 1263-1276.

(39) Sochard, S.; Fernandes, N.; Reneaume, J.-M. Modeling of Adsorption Isotherm of a Binary Mixture with Real Adsorbed Solution Theory and Nonrandom Two-Liquid Model. *A.I.Ch.E.J.* **2010**, *56*, 3109-3119.

(40) Mittal, N.; Bai, P.; Siepmann, I.; Daoutidis, P.; Tsapatsis, M. Bioethanol Enrichment using Zeolite Membranes: Molecular Modeling, Conceptual Process Design and Techno-Economic Analysis. *J. Membr. Sci.* **2017**, *540*, 464-476.

(41) Calleja, G.; Jimenez, A.; Pau, J.; Domínguez, L.; Pérez, P. Multicomponent Adsorption Equilibrium of Ethylene, Propane, Propylene and CO_2 on 13X Zeolite. *Gas Sep. Purif.* **1994**, *8*, 247-256.

(42) Kaur, H.; Marshall, B. D. Real adsorbed solution theory model for the adsorption of CO_2 from humid gas on CALF-20. *ChemRxiv* **2023**, 1-18. https://doi.org/10.26434/chemrxiv-2023-2cp2c.

(43) Sakuth, M.; Meyer, J.; Gmehling, J. Vapor Phase Adsorption Equilibria of Toluene + 1-Propanol Mixtures on Y-Zeolites with Different Silicon to Aluminum Ratios. *J. Chem. Eng. Data* **1995**, *40*, 895-899.

(44) Sakuth, M.; Meyer, J.; Gmehling, J. Measurement and Prediction of Binary Adsorption Equilibria of Vapors on Dealuminated Y-zeolites (DAY). *Chem. Eng. Process.* **1998**, *37*, 267-277.

(45) Fleys, M.; Thompson, R. W. Monte Carlo Simulations of Water Adsorption Isotherms in Silicalite and Dealuminated Zeolite Y. *J. Chem. Theory Comput.* **2005**, *1*, 453-458.

(46) Newalkar, B. L.; Jasra, R. V.; Kamath, V.; Bhat, S. G. T. Sorption of water in aluminophosphate molecular sieve $AlPO_4$-5. *Microporous Mesoporous Mater.* **1998**, *20*, 129-137.

(47) Pillai, R. S.; Jasra, R. V. Computational Study for Water Sorption in AlPO4-5 and AlPO4-11Molecular Sieves. *Langmuir* **2010**, *26*, 1755-1764.

(48) Halasz, I.; Kim, S.; Marcus, B. Uncommon Adsorption Isotherm of Methanol on a Hydrophobic Y-zeolite. *J. Phys. Chem. B* **2001**, *105*, 10788-10796.

(49) Di Lella, A.; Desbiens, N.; Boutin, A.; Demachy, I.; P., U.; Bellat, J. P.; Fuchs, A. H. Molecular simulation studies of water physisorption in zeolites. *Phys. Chem. Chem. Phys.* **2006**, *8*, 5396-5406.

(50) Narasimhan, L.; Boulet, P.; Kuchta, B.; Schaef, O.; Denoyel, R.; Brunet, P. Molecular Simulations of Water and Paracresol in MFI Zeolite - A Monte Carlo Study. *Langmuir* **2009**, *25*, 11598-11607.

(51) Chmelik, C.; Bux, H.; Caro, J.; Heinke, L.; Hibbe, F.; Titze, T.; Kärger, J. Mass transfer in a Nanoscale Material Enhanced by an Opposing Flux. *Phys. Rev. Lett.* **2010**, *104*, 085902.

(52) Krishna, R.; van Baten, J. M. A rationalization of the Type IV loading dependence in the Kärger-Pfeifer classification of self-diffusivities. *Microporous Mesoporous Mater.* **2011**, *142*, 745-748.

(53) Tsotsalas, M.; Hejcik, P.; Sumida, K.; Kalay, Z.; Furukawa, S.; Kitagawa, S. Impact of Molecular Clustering inside Nanopores on Desorption Processes. *J. Am. Chem. Soc.* **2013**, *135*, 4608-4611.

(54) Pera-Titus, M.; Fité, C.; Sebastián, V.; Lorente, E.; Llorens, J.; Cunill, F. Modeling Pervaporation of Ethanol/Water Mixtures within 'Real' Zeolite NaA Membranes. *Ind. Eng. Chem. Res.* **2008**, *47*, 3213-3224.

(55) Krishna, R. Separating Mixtures by Exploiting Molecular Packing Effects in Microporous Materials. *Phys. Chem. Chem. Phys.* **2015**, *17*, 39-59. https://doi.org/10.1039/C4CP03939D.

(56) Krishna, R. Elucidation and Characterization of Entropy Effects in Mixture Separations with Micro-porous Crystalline Adsorbents. *Sep. Purif. Technol.* **2019**, *215*, 227-241. https://doi.org/10.1016/j.seppur.2019.01.014.

(57) Krishna, R.; van Baten, J. M. Entropy-based Separation of Linear Chain Molecules by Exploiting Differences in the Saturation Capacities in Cage-type Zeolites. *Sep. Purif. Technol.* **2011**, *76*, 325-330. https://doi.org/10.1016/j.seppur.2010.10.023.

(58) Skoulidas, A. I.; Sholl, D. S.; Krishna, R. Correlation effects in diffusion of CH_4/CF_4 mixtures in MFI zeolite. A study linking MD simulations with the Maxwell-Stefan formulation. *Langmuir* **2003**, *19*, 7977-7988.

(59) Chempath, S.; Krishna, R.; Snurr, R. Q. Nonequilibrium MD simulations of difusion of binary mixtures containing short n-alkanes in faujasite. *J. Phys. Chem. B* **2004**, *108*, 13481-13491.

(60) Krishna, R. Describing the Diffusion of Guest Molecules inside Porous Structures. *J. Phys. Chem. C* **2009**, *113*, 19756-19781. https://doi.org/10.1021/jp906879d.

(61) Krishna, R. Diffusion in Porous Crystalline Materials. *Chem. Soc. Rev.* **2012**, *41*, 3099-3118. https://doi.org/10.1039/C2CS15284C.

(62) Krishna, R.; van Baten, J. M. Onsager coefficients for binary mixture diffusion in nanopores. *Chem. Eng. Sci.* **2008**, *63*, 3120-3140.

(63) Hansen, N.; Keil, F. J. Multiscale modeling of reaction and diffusion in zeolites: from the molecular level to the reactor. *Soft Mater.* **2012**, *10*, 179-201.

(64) Krishna, R.; van Baten, J. M. An Investigation of the Characteristics of Maxwell-Stefan Diffusivities of Binary Mixtures in Silica Nanopores. *Chem. Eng. Sci.* **2009**, *64*, 870-882.

(65) Krishna, R.; van Baten, J. M. Unified Maxwell-Stefan Description of Binary Mixture Diffusion in Micro- and Meso- Porous Materials. *Chem. Eng. Sci.* **2009**, *64*, 3159-3178.

(66) Krishna, R.; van Baten, J. M. Diffusion of alkane mixtures in zeolites. Validating the Maxwell-Stefan formulation using MD simulations. *J. Phys. Chem. B* **2005**, *109*, 6386-6396.

(67) Krishna, R.; van Baten, J. M. Influence of segregated adsorption on mixture diffusion in DDR zeolite. *Chem. Phys. Lett.* **2007**, *446*, 344-349.

(68) Krishna, R.; van Baten, J. M. Insights into diffusion of gases in zeolites gained from molecular dynamics simulations. *Microporous Mesoporous Mater.* **2008**, *109*, 91-108.

(69) Krishna, R.; van Baten, J. M. Describing Mixture Diffusion in Microporous Materials under Conditions of Pore Saturation. *J. Phys. Chem. C* **2010**, *114*, 11557-11563.

(70) Krishna, R.; van Baten, J. M. A molecular dynamics investigation of the diffusion characteristics of cavity-type zeolites with 8-ring windows. *Microporous Mesoporous Mater.* **2011**, *137*, 83-91. https://doi.org/10.1016/j.micromeso.2010.08.026.

(71) Krishna, R.; van Baten, J. M. Maxwell-Stefan modeling of slowing-down effects in mixed gas permeation across porous membranes. *J. Membr. Sci.* **2011**, *383*, 289-300. https://doi.org/10.1016/j.memsci.2011.08.067.

(72) Krishna, R.; Van Baten, J. M. Using Molecular Simulations to Unravel the Benefits of Characterizing Mixture Permeation in Microporous Membranes in Terms of the Spreading Pressure. *ACS Omega* **2020**, *5*, 32769−32780. https://dx.doi.org/10.1021/acsomega.0c05269.

(73) Peng, P.; Shi, B.; Lan, Y. A Review of Membrane Materials for Ethanol Recovery by Pervaporation. *Separ. Sci. Technol.* **2011**, *46*, 234-246.

(74) Sato, K.; Aoki, K.; Sugimoto, K.; Izumi, K.; Inoue, S.; Saito, J.; Ikeda, S.; Nakane, T. Dehydrating performance of commercial LTA zeolite membranes and application to fuel grade bio-ethanol production by hybrid distillation/vapor permeation process. *Microporous Mesoporous Mater.* **2008**, *115*, 184-188.

(75) Sato, K.; Sugimoto, K.; Shimosuma, N.; Kikuchi, T.; Kyotani, T.; Kurata, T. Development of practically available up-scaled high-silica CHA-type zeolite membranes for industrial purpose in dehydration of N-methyl pyrrolidone solution. *J. Membr. Sci.* **2012**, *409-410*, 82-95.

(76) Kooijman, H. A.; Taylor, R. A dynamic nonequilibrium model of tray distillation columns. *A.I.Ch.E.J.* **1995**, *41*, 1852-1863.

(77) Michelsen, M. An efficient general purpose method of integration of stiff ordinary differential equations. *A.I.Ch.E.J.* **1976**, *22*, 594-597.

(78) Bulirsch, R.; Stoer, J. Numerical treatment of ordinary differential equations by extrapolation methods. *Numer. Math.* **1966**, *8*, 1-14.

(79) Krishna, R.; Baur, R. Modelling Issues in Zeolite Based Separation Processes. *Sep. Purif. Technol.* **2003**, *33*, 213-254.

(80) Krishna, R.; Baur, R. Diffusion, Adsorption and Reaction in Zeolites: Modelling and Numerical Issues. http://krishna.amsterchem.com/zeolite/, University of Amsterdam, Amsterdam, 1 January 2015.

(81) Krishna, R.; van Baten, J. M. Investigating the potential of MgMOF-74 membranes for CO_2 capture. *J. Membr. Sci.* **2011**, *377*, 249-260.

(82) He, Y.; Krishna, R.; Chen, B. Metal-Organic Frameworks with Potential for Energy-Efficient Adsorptive Separation of Light Hydrocarbons. *Energy Environ. Sci.* **2012**, *5*, 9107-9120.

(83) Geus, E. R.; van Bekkum, H.; Bakker, W. J. W.; Moulijn, J. A. High-temperature Stainless Steel Supported Zeolite (MFI) Membranes: Preparation, Module Construction, and Permeation Experiments. *Microporous Mater.* **1993**, *1*, 131-147.

(84) Bakker, W. J. W. *Structured systems in gas separation*. Ph.D. Dissertation, Delft University of Technology, Delft, 1999.

(85) Matsufuji, T.; Watanabe, K.; Nishiyama, N.; Egashira, Y.; Matsukata, M.; Ueyama, K. Permeation of Hexane Isomers Through an MFI Membrane. *Ind. Eng. Chem. Res.* **2000**, *39*, 2434-2438.

(86) Matsufuji, T.; Nishiyama, N.; Matsukata, M.; Ueyama, K. Separation of Butane and Xylene Isomers with MFI-type Zeolitic Membrane Synthesized by a Vapor-Phase Transport Method. *J. Membr. Sci.* **2000**, *178*, 25-34.

(87) Courthial, L.; Bandot, A.; Tayakout-Fayolle, M.; Jallut, C. Transient Method for Mass-Transfer Characterization Through Supported Zeolite Membranes: Extension to Two Components. *A.I.Ch.E.J.* **2013**, *59*, 959-970.